

Imperial College London
Department of Materials

Hierarchical Strengthening of Polycrystal-Inspired Lattice Materials

Jedsada Lertthanasarn

A thesis submitted in partial fulfilment of the requirements for the degree of
Doctor of Philosophy at Imperial College London,
November 2021

Blank

Abstract

Architected lattice materials offer excellent specific properties, ideal for high-performance and weight-critical applications. However, high-strength lattice materials also often exhibit a significant and catastrophic post-yielding collapse due to buckling and plastic yielding of struts, leading to a trade-off between the strength and stability, and compromising the energy absorption capacity. The mimicry of crystalline strengthening features in the lattice architecture at the mesoscale offers effective ways of improving the energy absorption capacity and eliminating the post-yield collapse of high-strength architected lattice materials. Such crystal-inspired lattice materials are called meta-crystals.

This PhD thesis aims to establish the relationship between the intrinsic crystalline microstructure, the extrinsic architected mesostructure, and the mechanical behaviour of meta-crystals, in particular the separate and synergistic strengthening of intrinsic and extrinsic hierarchical features at different length scales. The mechanical behaviours of metallic polycrystal-like meta-crystals were studied by quasi-static compression experiments with digital image correlation (DIC) analyses, hardness testing, and finite element analysis (FEA). The as-printed and post-processed meso- and microstructures of the meta-crystals were characterised via X-ray computed tomography (x-CT), scanning electron microscope (SEM) imaging, electron backscatter diffraction (EBSD) analysis, electron dispersive x-ray spectroscopy (EDX) analysis, and in the transmission electron microscope (TEM). The meta-crystals investigated contained varying numbers of meta-grains, different strut diameters, were fabricated from different base materials, and were subjected to different post-processing treatments. The experiments were designed to deconvolute the strengthening contributions from the crystalline microstructure and architected features at different length scales, as well as the synergistic strengthening across the hierarchical structures.

The study showed that the presence of defects can overwhelm the strengthening contributions from the crystal-inspired architecture and the intrinsic crystalline microstructure, particularly when the base material has low ductility and work

hardening. The influence of surface processing defects such as lack-of-fusions is especially detrimental compared to internal porosities and such defects need to be minimised. Excessive effects from the processing defects lead to premature fracture of struts rendering the strengthening architecture ineffective. The influence of defects can be minimised via optimisation of the processing parameters, altering the microstructure, or increasing the strut diameter. The examination of various base materials such as Ti-6Al-4V, 316L, and IN718 meta-crystals highlighted the role of the base material in minimising the influence of the processing defects. Additionally, the base materials' properties also affected the efficacy of the polycrystal-like architecture, with precipitation-hardenable alloys such as IN718 shown to be the most ideally suited to enable the combined strengthening induced by both the intrinsic and extrinsic features. Optimising the crystalline microstructure of as-printed IN718 enabled meta-crystals with exceptional strength and energy absorption capacity. A theoretical framework for the strength of polycrystal-like meta-crystals was also developed by characterising the hierarchical features of the IN718 meta-crystals, providing a basis for future designs.

Statement of Originality

I declare that the work contained in this thesis is my own carried out in the Department of Materials, Imperial College London from October 2017 to November 2021, under the supervision of Dr. Minh-Son Pham. No part of this work has been submitted for any other degree, diploma or any other qualifications. Information derived from published and unpublished work of others has been appropriately acknowledged and referenced.

Copywrite Declaration

The copywrite of this thesis rests with the author and is made available under a Creative Commons Attribution Non-Commercial No Derivatives licence. Researchers are free to copy, distribute or transmit the thesis on the condition that they attribute it, that they do not use it for commercial purposes and that they do not alter, transform or build upon it. For any reuse or redistribution, researchers must make clear to others the licence terms of this work.

Acknowledgements

This study would not have been possible without the following people, whose combined efforts have helped and inspired me during my four years in London.

Firstly, I would like to thank my supervisor, Dr Minh-Son Pham. Thank you for having the confidence and trust in me to work on this fascinating project. I could not have asked for a better opportunity to do a PhD study. Throughout my studies, you were always patient and kind, knowledgeable and creative, encouraging and supportive. I know how hard you worked for all of us, thank you.

The talented and dynamic research group that you have assembled have also been invaluable. A big thank you to the group for your technical and moral support; I will miss our weekly group meetings. In particular, I would like to mention my 2017 cohorts whom I became good friends with: Ale, Bogdan, and Minsoo. I have thoroughly enjoyed our experiences together in and out of London, and my time here would not have been the same without you. Ale and Bogdan also provided the TEM micrographs and the ThermoCalc simulations in this thesis. My gratitude extends to my friends and colleagues outside of the research group. All of you have directly or indirectly contributed to my studies.

I would also like to acknowledge Dr Sarat Babu (Betatype Ltd.) and Dr Sergey Adjamskiy (Additive Laser Technology of Ukraine) for kindly fabricating the Ti-6Al-4V and Inconel 718 meta-crystal samples, respectively.

Most importantly, I would like to thank my parents, my brother, and my sister, for the sacrifices that they have made. I hope that you are proud of what we have accomplished.

*J. Lertthanasarn
November 2021*

Contents

Abstract	iii
Statement of Originality	v
Copywrite Declaration	v
Acknowledgements	vi
List of Figures	x
List of Tables	xiv
Nomenclature	xv
1. Introduction	1
1.1. Background and motivation	1
1.2. Aims and objectives	2
1.3. Overview of the thesis	3
1.4. Publications and conference talks	4
2. Literature Review	7
2.1. Metallurgical strengthening in polycrystalline alloys	7
2.1.1. Structure of crystalline solids	7
2.1.2. Crystal plasticity	9
2.1.3. Overview of strengthening mechanisms	10
2.2. Additive manufacturing	17
2.2.1. Technologies	17
2.2.2. Laser powder bed fusion	19
2.2.3. Designs enabled by additive manufacturing	33
2.3. Cellular solids	37
2.3.1. Static mechanical properties of cellular solids	38
2.3.2. Architected lattice materials	43
2.3.3. Meta-crystals	51
2.4. Conclusions	55
3. Experimental and Analytical Methods	57
3.1. Polycrystal-inspired meta-crystal design	57
3.2. Sample fabrication and post-processing	59
3.2.1. Meta-crystals fabrication	59
3.2.2. Heat-treatments	61
3.3. Mechanical testing and analysis	61

3.3.1. Tensile testing of bulk specimens	61
3.3.2. Compression behaviour of meta-crystals	62
3.3.3. Hardness testing of meta-crystals	64
3.3.4. Finite element modelling	65
3.3.5. ThermoCalc	65
3.4. Characterisation and analysis	66
3.4.1. X-ray computed tomography (x-CT)	66
3.4.2. Microstructure characterisation and analysis	67
4. Influence of Processing Defects	69
4.1. Introduction	69
4.2. Experimental procedure	71
4.3. Results	71
4.3.1. Printing quality: geometric accuracy and internal defects	71
4.3.2. Microstructure	75
4.3.3. Mechanical properties	77
4.4. Discussions	81
4.4.1. The influence of processing defects on the boundary strengthening in Ti-6Al-4V meta-crystals	81
4.4.2. The effect of the crystalline microstructure	82
4.4.3. Enabling the strengthening effects of the polycrystal-like architecture	84
4.5. Conclusions	84
5. Influence of the Base Material	87
5.1. Introduction	87
5.2. Experimental procedure	89
5.3. Results	90
5.3.1. Characterisation of the fabricated meta-crystals	90
5.3.2. Microstructure	92
5.3.3. Mechanical properties	94
5.4. Discussions	99
5.4.1. Material-dependent mechanical behaviours of meta-crystals	99
5.4.2. Tolerance of the base material to processing defects	102
5.5. Conclusions	104
6. Enabling a synergy of metallurgical and architectural strengthening in meta-crystals	107
6.1. Introduction	107

6.2. Experimental procedure	109
6.3. Results	110
6.4. Constitutive formulations	121
6.5. Discussions	125
6.6. Conclusions	128
7. Conclusions and Future Works	131
7.1. Conclusions	131
7.2. Recommendations for future works	134
References	136
Appendices	157

List of Figures

Figure 1 Common crystal structures of metals: face-centred cubic lattice, body-centred cubic lattice, and hexagonal close packed lattice unit cells.	8
Figure 2 Schematics representation of an edge and a screw dislocation. OO' is the dislocation line, b is the Burgers vector, and s is the positive line direction.	10
Figure 3 Precipitation hardening of coherent and incoherent precipitates.	13
Figure 4 Stages of strain hardening of a single crystal. Plot of hardening rate versus the flow stress showing 4 distinct stages of strain hardening.	15
Figure 5 Schematic of a typical laser powder bed fusion process.	19
Figure 6 Key processing parameters (block capitals) and terminologies (italics) in L-PBF.	21
Figure 7 Representative geometry showing different regions which can be printed with different processing parameters.	23
Figure 8 Gas porosity in L-PBF.	24
Figure 9 Surface defects in L-PBF parts.	25
Figure 10 Power-velocity processing window for Ti-6Al-4V produced via L-PBF under constant hatch spacing and layer thickness showing boundaries for lack-of-fusion (LOF) and keyhole pores formation.	26
Figure 11 Internal porosity formation mechanism in L-PBF.	27
Figure 12 Overpotential electrochemical polishing surface modification technique to improve the surface roughness of additively manufactured parts. The change in surface roughness and removal thickness over polishing time.	29
Figure 13 Internal porosity reduction by hot isostatic pressing (HIP) in L-PBF Ti-6Al-4V specimen. Porosity is highlighted in red.	30
Figure 14 Microstructure and texture in FeCrAl alloy fabricated via L-PBF. EBSD IPF-build direction maps of the as-printed specimen of sections parallel (left) and perpendicular (right) to the build direction.	32
Figure 15 Polymer pentamode lattice material fabricated by dip-in three-dimensional DLW optical lithography.	34

Figure 16 Non-mechanical lattice material enabled by metal AM.	35
Figure 17 The cellular structure of wood. An SEM micrograph of soft maple showing pores or vessels (V) and wood fibres (F).	37
Figure 18 Overview of potential cellular solids metamaterials applications.	38
Figure 19 Typical compressive stress-strain response of bending- vs. stretching-dominated structures.	39
Figure 20 The Gibson-Ashby scaling relationships for cellular solids of different unit-cell topologies.	40
Figure 21 Examples of different unit-cell topologies and their coordination number.	42
Figure 22 Strut failure modes.	45
Figure 23 BCC unit-cells with uniform (a) struts and tapered (b) struts.	46
Figure 24 Cellular microstructure of inclined AlSi10Mg strut fabricated by AM.	50
Figure 25 Nickel octet truss nanolattice material at increasing magnifications.	51
Figure 26 Analogous deformation behaviours between stretching-dominated lattice materials and single crystal micropillars.	52
Figure 27 The hierarchical lattice structure of meta-crystals.	53
Figure 28 Compressive deformation response of polycrystal-inspired meta-crystals.	54
Figure 29 Polycrystal-inspired meta-crystal architecture.	58
Figure 30 Ti-6Al-4V meta-crystals with 0.5 mm strut diameter fabricated via L-PBF. Courtesy of Betatype Ltd.	60
Figure 31 Quasi-static compression test rig with DSLR camera set-up for DIC analysis.	63
Figure 32 Typical compressive stress-strain response of stretching-dominated lattice materials with key properties defined.	64
Figure 33 The average percentage difference in the theoretically calculated and the measured relative density (ρ) for all as-print meta-crystals with 0.5 and 0.8 mm strut diameters.	72
Figure 34 Internal processing defects in meta-crystals.	73

Figure 35 Fracture surfaces of struts.	75
Figure 36 SEM micrographs and EBSD maps (IPF-build direction/out of page) showing the etched surface of the as-printed and annealed microstructure.	76
Figure 37 The normalised stress-strain responses of the 1, 4, 16, 64 MGs Ti-6Al-4V meta-crystals with 0.5 mm strut diameter..	77
Figure 38 The total energy absorbed up to 60% nominal strain (densification) by the 0.5 and 0.8 mm meta-crystals in as-printed and annealed conditions.	78
Figure 39 DIC showing the deformation of the 16 MGs meta-crystals under increasing compressive strain.	79
Figure 40 The normalised stress-strain responses of the 1, 4, 16, 64 MGs Ti-6Al-4V meta-crystals with 0.8 mm strut diameter.	80
Figure 41 SEM micrographs showing processing defects in meta-crystals fabricated from 316L, IN718, and Ti-6Al-4V.	91
Figure 42 Quantification of internal porosity in the node and strut regions of 316L, IN718, and Ti-6Al-4V meta-crystals.	92
Figure 43 EBSD maps showing the grain structure in the node and strut regions.	94
Figure 44 The mechanical behaviour of meta-crystals with different base materials.	95
Figure 45 The relationships between the mechanical properties of meta-crystals with the number of MGs.	96
Figure 46 DIC analysis of the meta-crystals under compression at the first stress drop.	98
Figure 47 SEM micrographs showing strut deformation.	99
Figure 48 The scaling relationship between the stiffness and the relative density. The ideal stretching-dominated lattice materials (dashed line) versus experimental data for meta-crystals of IN718 (x markers), Ti-6Al-4V (o markers) and 316L (+ markers).	100
Figure 49 Hierarchical structures of meta-crystals. The structures and strengthening features of meta-crystals at multiple length scales.	108
Figure 50 Compressive properties of lattice structures. Comparison of the normalised yield stress versus the normalised energy absorption up to densification (where reported) for various unit-cell topologies and base materials.	110
Figure 51 Compressive response of meta-crystals.	111

Figure 52 Correlations between the equivalent MG size and mechanical properties of as-printed and heat-treated meta-crystals.	113
Figure 53 Meso-scale deformation of as-printed and heat-treated meta-crystals struts.	115
Figure 54 SEM micrographs revealing processing defects in the meta-crystals.	117
Figure 55 Grain structure and deformation in the node and strut regions of a heat-treated meta-crystal.	118
Figure 56 The effect of the heat-treatment on the microstructure of meta-crystals.	120
Figure 57 Strength contributions induced by fractal structure sources.	127
Figure 58 Potential combination of the polycrystal-like architecture with meta-precipitates to disrupt the known location of the localised deformation bands.	134

List of Tables

Table 1 Categorisation of additive manufacturing technologies and the applicable classes of materials.	18
Table 2 Typical layer thickness and minimum feature size achievable in different metal AM technologies	20
Table 3 Summary of the meta-crystals investigated.	59
Table 4 L-PBF processing parameters for 316L, Ti-6Al-4V, IN718 meta-crystals. Nb. “-” indicates not applicable.	60
Table 5 Sample preparation procedures for 316L, Ti-6Al-4V, and IN718 lattice materials for microstructure characterisation. Follow procedure for the grinding and polishing sequentially in descending order.	67
Table 6 The theoretical and measured relative densities of meta-crystals with different base materials and number of MGs.	90
Table 7 Parameters for as-printed IN718.	119
Table 8 Additional parameters for heat-treated IN718	121

Nomenclature

AM	Additive Manufacturing
BC	Boundary condition
BD	Build direction
BCC	Body-centred cubic
CAD	Computer-aided design
CAE	Complete Abaqus environment
DED	Direct energy deposition
DIC	Digital image correlation
DLP	Digital light processing
EB-PBF	Electron beam powder bed fusion
EBSD	Electron backscatter diffraction
EDX	Electron dispersive x-ray spectroscopy
FCC	Face-centred cubic
FDM	Fused deposition modelling
FE	Finite element
GND	Geometrically necessary dislocations
HAGB	High angle grain boundaries
HAZ	Heat affected zones
HCP	Hexagonal closed-packed
HEA	High entropy alloys
HIP	Hot isostatic press
HX	Heat exchangers
IN718	Inconel 718
L-PBF	Laser powder bed fusion
LENS	Laser engineering net shape
LOF	Lack-of-fusion
MG	Meta-grain
MPC	Multi-point constraint
PBF	Powder bed fusion
PLA	Polylactic-acid
SE	Secondary electron
SEM	Scanning electron microscopy
SLA	Stereolithography
SLS	Selective laser sintering
TEM	Transmission electron microscopy
UTS	Ultimate tensile strength
x-CT	X-ray computed tomography

Blank

Chapter 1

Introduction

1.1. Background and motivation

Making lighter, stronger, and tougher materials has been a perpetual goal for many scientists and engineers in materials, mechanics, and structures. Throughout history, the discovery and development of such materials have empowered civilisations. From the rise of large-scale societies in the bronze age, to the industrial revolution with the mass production of iron and steel and, more recently, the growth of the aerospace industry with the commercialisation of titanium by the Kroll process, materials research has always been vital. Currently, significant research interest is shown to lattice materials - a type of material that has inherently low densities and can be architected to have defined properties [1]. This makes lattice materials desirable in many high-performance and weight-critical applications such as the aerospace, biomedical, and energy industries.

Lattice materials are a subset of mechanical metamaterials. Their mechanical properties not only depend on the intrinsic properties of the fabricated material (base material) but also the engineered mesoscale architecture [2–4]. The architecture of a lattice material typically consists of a periodically-ordered network of struts. This architecture can be engineered to give lattice materials superior specific strength [5], locally tailored properties [6], and multifunctionality [7]. With advancements in additive manufacturing (AM) technologies, increasingly complex and intricate architectures can be fabricated at higher quality, further pushing the capabilities of lattice materials [8–13]. The

capabilities are further extended in metal AM, where the processing parameters provide an additional degree of freedom for tailoring the microstructure [14,15]. The capacity for local tailoring of the microstructure and architecture provides an opportunity for complete spatial control over the mechanical properties of metallic lattice materials, with optimised structures across length scales.

Struts in high strength lattice architectures predominantly deform by axial stretching or compression rather than bending [16]. Such lattice materials offer exceptional specific strength [17] but often suffer from a significant and catastrophic collapse after yielding. While this instability is uncommon in bending-dominated lattice materials, their strengths are comparatively lower [18,19]. The strength-stability trade-off of lattice materials leads to undesirable energy absorption capacity [1,20,21] and is considered a significant limitation of lattice materials. However, a recently proposed crystal-inspired design approach was able to overcome this trade-off. The novel design mimics the crystalline microstructure from engineering alloys in the lattice architecture to induce significant strengthening and increase in the energy absorption capacity of the lattice material [22]. Such crystal-inspired lattice materials are called meta-crystals. Metallic meta-crystals contain a fractal crystal structure across length scales: the intrinsic crystalline material and the architected crystal-like mesoscale structure.

1.2. Aims and objectives

Poly(lactic-acid) (PLA) meta-crystals demonstrated the effectiveness of the crystal-inspired approach with architectures mimicking crystalline grains, precipitates, and phases [22]. The proof-of-concept study confirmed that the compressive mechanical properties of the meta-crystals improved with the inclusion of such strengthening architectures. However, the approach has not been demonstrated with metallic base materials. Since many industrial applications demand for metallic parts due to the suitability for structural applications, it is necessary to understand the behaviour metallic meta-crystals. In addition, the use of alloys as the base material opens exciting opportunities in combining both the strengthening induced by crystal-like architecture

and metallurgical hardening to design lightweight, high strength and damage-tolerant materials.

The main goal of this study is to further explore the potential of the crystal-inspired approach, specifically metallic polycrystal-like lattice materials. We aim to investigate the separate and synergistic influence of fractal features at each length scale and study the underlying mechanisms in the deformation and strengthening of meta-crystals. This will range from the intrinsic crystalline features (such as dislocation cells, precipitates, crystal phase, polygrains) to the crystal-like mesostructure (including processing defects, the lattice parameters and macro-polygrain architectures). The investigation intends to reveal how such variables affect the way the fractal architecture interacts with the deformation shear bands to strengthen and stabilise the structure after plastic yield. With the potential for microstructural tailoring via AM, deconvoluting the contribution from the hierarchical features provides an opportunity to combine all the strengthening sources both at the metallurgical and structural levels for synergistic strengthening across length scales.

We hope that this work will provide a foundation for the design of hierarchical meta-crystals with exceptional specific strength and energy absorption capacity. Combined with the inherent versatility of lattice materials, meta-crystals can be suitable for a wide range of high-performance applications.

1.3. Overview of the thesis

This thesis contains seven chapters, organised as follows:

Chapter 1 provides the background and scope of the thesis by situating the research in a broader context. The chapter establishes the motivation and aim of the work and outlines the research conducted. Publications and conference talks resulting from the work in this thesis are listed.

Chapter 2 critically reviews relevant literature, providing a relevant background to this study. The review focuses on three main topics: metallurgical strengthening in polycrystalline alloys, additive manufacturing, and lattice materials.

Chapter 3 describes the methods and methodologies used to conduct the research.

Chapter 4 studies the influence of processing defects on the compressive mechanical properties of meta-crystals fabricated via L-PBF. Ti-6Al-4V meta-crystals were investigated due to the low elongation to failure, which amplifies the influence of the processing defects. The study investigated as-printed and annealed meta-crystals with 0.5 and 0.8 mm strut diameters.

Chapter 5 discusses the influence of the intrinsic metallurgical microstructure of the base material on the behaviour of meta-crystals. The mechanical behaviour and crystalline microstructure of the same polygrain-like meta-crystals fabricated from 316L stainless steel, Ti-6Al-4V, and IN718 meta-crystals are examined and discussed.

Chapter 6 rationalises and develops the work of the previous two chapters in a detailed investigation of IN718 meta-crystals. The study characterised the fractal structures (both intrinsic crystal and artificial polycrystal features) at multiple length scales to deconvolute their strengthening contributions and examine their synergistic effects. This established a theoretical framework to develop high performing fractal meta-crystals for critical load-bearing conditions.

Chapter 7 concludes the findings of this study in a broader context and provides an outlook for future research.

1.4. Publications and conference talks

The work contained in this thesis has been reported in The following peer-reviewed publications. In chronological order:

- I. Pham, M., Liu, C., Todd, I. and Lertthanasarn, J., 2019. Damage-tolerant architected materials inspired by crystal microstructure. *Nature*, 565(7739), pp.305-311.
- II. Lertthanasarn, J., Liu, C. and Pham, M., 2021. Synergistic effects of crystalline microstructure, architected mesostructure, and processing defects on the mechanical behaviour of Ti6Al4V meta-crystals. *Materials Science and Engineering: A*, 818, p.141436.

- III. Liu, C., Lertthanasarn, J. and Pham, M., 2021. The origin of the boundary strengthening in polycrystal-inspired architected materials. *Nature Communications*, 12(1).
- IV. Lertthanasarn, J., Liu, C. and Pham, M., 2021. Influence of the base material on the mechanical behaviors of polycrystal-like meta-crystals. *Journal of Micromechanics and Molecular Physics*, p.2150004.

The following manuscript is in preparation for submission to a peer-reviewed journal:

- V. Lertthanasarn, J., Liu, C., Dovgvy, B., and Pham, M., 2021. Crystal-inspired hierarchical meta-materials with exceptional strength and energy absorption capacity. *manuscript in preparation*

Manuscripts number II, IV, and V make up the bulk of chapters 5, 4, and 6, respectively.

The following manuscript is not within the scope of this thesis, but was completed as a result of collaborative work:

- VI. Iantaffi, C., Leung, C.L.A., Chen, Y., Guan, S., Atwood, R.C., Lertthanasarn, J., Pham, M., Meisnar, M., Rohr, T., Lee, P., 2021. Oxidation-induced mechanisms during directed energy deposition additive manufactured titanium alloy builds. *Additive Manufacturing Letters*, 1, p.100022.

Additionally, the work contained in this thesis have also been presented in the following conferences:

- I. Lertthanasarn, J., Liu, C. and Pham, M., 2019. Polycrystal-inspired mechanical metamaterials. *Euromat 2019*, Stockholm, Sweden, September 2019
- II. Lertthanasarn, J., Liu, C. Hernández-Nava, E. Todd, I. and Pham, M., 2020. Polycrystal-inspired hierarchical lattice materials. *TMS 2020*, San Diego, US, February 2020

Blank

Chapter 2

Literature Review

This chapter discusses three topics relevant to understanding the mechanical behaviours of crystal-inspired lattice material. The first topic is the fundamentals of metallurgical strengthening (in polycrystalline alloys) that is the inspiration for the meta-crystal approach. This section provides a brief overview of the structure of crystalline solids and the crystal defects, the crystal plasticity, and the strengthening mechanisms in polycrystalline alloys. The second topic is on additive manufacturing as it is the most effective way to fabricate the intricate and potentially complex architectures of the meta-crystals. This section begins by introducing different additive manufacturing technologies, before focusing on recent research in laser-powder bed fusion (and the base materials considered in this study, microstructure, and imperfections). Lastly, the bulk of the literature review is on the third topic: architected lattice materials. This section critically reviews state-of-the-art research in lattice materials and explores the potential issues of existing lattice materials that the crystal-inspired approach can overcome.

2.1. Metallurgical strengthening in polycrystalline alloys

2.1.1. Structure of crystalline solids

Crystals are orderly arrangements of atoms in space. Crystallographers had postulated early in the 1700s that crystalline solids are a three-dimensional array of closely stacked unit-cells, which developed on previous ideas of spherical and polyhedral units by

Bergman, Huygens, Hooke, and Kepler. Quantitative work in crystallography was later instigated by Haüy with an expression for the measurable angles between crystal faces of a given solid [23]. However, a more complete understanding of crystalline solids and their plastic behaviour was not established until much later, when von Laue discovered the diffraction of x-rays by crystals in 1912 [24]. X-ray diffraction analysis confirmed the three-dimensional long-range periodic arrangement of atoms in metals and enabled numerous investigations in crystallography.

The crystal structure of metals is represented as a lattice where the atoms and interatomic bonds coincide with the lattice points and the connections between them. The smallest repeating entity in the crystal structure is the lattice unit cell. From all combinations of equal and unequal axes and interaxial angles of the lattice, there are 14 types of unit cells, known as the Bravais lattices [25]. Defining the unit cell is useful as it reflects the symmetry that governs the elastic and plastic response of the crystal structure. The three most common unit cells found in metal are the face-centred cubic (FCC) lattice, the body-centred cubic (BCC) lattice, and the hexagonal close-packed (HCP) lattice as shown in Figure 1.

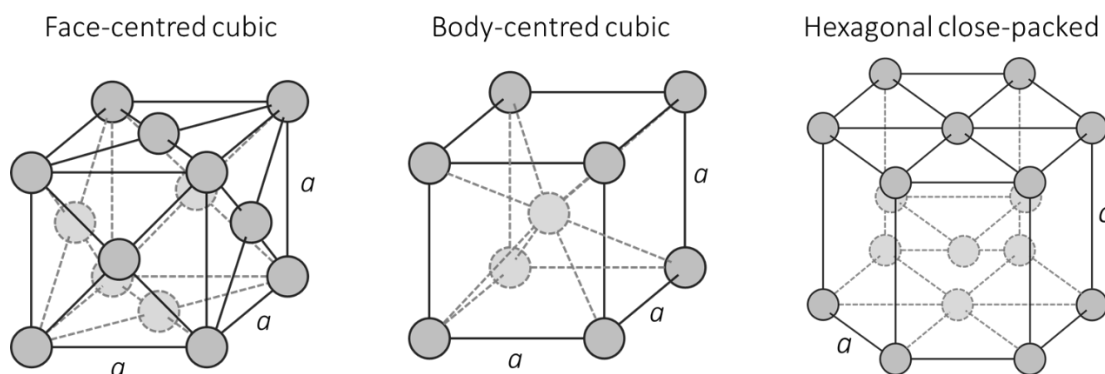


Figure 1 | Common crystal structures of metals: face-centred cubic lattice, body-centred cubic lattice, and hexagonal close packed lattice unit cells.

Crystalline solids can deform elastically and plastically. The elastic response is related to the balanced forces between the constituent atoms. Under small strain, the applied external stress upsets the balance between the attractive forces and the short-range repulsive forces; equilibrium is restored with the removal of the applied stress. The plastic response is locally heterogeneous and requires defects in the crystal lattice to

initiate and develop. Plastic deformation is therefore structure-sensitive; it is highly dependent on the defects or imperfections in the crystal lattice.

Crystal defects are spatial deviations from the perfect lattice. There are many types of defects, with increasing dimensionality ranging from points to lines to planes to volumes. Point defects are localised to a few atoms and include vacancies (missing atoms from lattice sites) and interstitials (extra atoms between lattice sites). Most known line defects are dislocations. Line crystallographic defects are dislocations that are classified into edge and screw type. Planar defects include grain boundaries, twin boundaries, antiphase boundaries, and stacking faults. [26,27]

2.1.2. Crystal plasticity

Dislocations are the main carriers of plasticity in crystalline solids. Two idealised and limiting forms of dislocations are edge and screw dislocations (Figure 2). For edge dislocations, an extra half-plane of atoms extends from dislocation line OO' in the positive z -direction, leading to distortion in the perfect lattice. The magnitude and direction of the distortion are defined by the Burgers vector, \mathbf{b} , which can be determined from the Burgers circuit. An edge dislocation is when the \mathbf{b} vector is perpendicular to the dislocation line, OO' , whereas a screw dislocation is when \mathbf{b} is parallel to OO' . Plastic deformation through dislocation movement is termed glide or slip. Slip occurs on preferred planes and directions, together called slip systems, which varies depending on the crystal structure. Slip initiates when the resolved shear stress (determined from the geometrical relationship between the tensile axis, the slip plane normal, and the slip direction) reaches the critical value. An edge dislocation can also move perpendicular to the slip plane by a process called climb. Movement by climb is diffusion-controlled and is, therefore, more frequent at higher temperatures. [28,29]

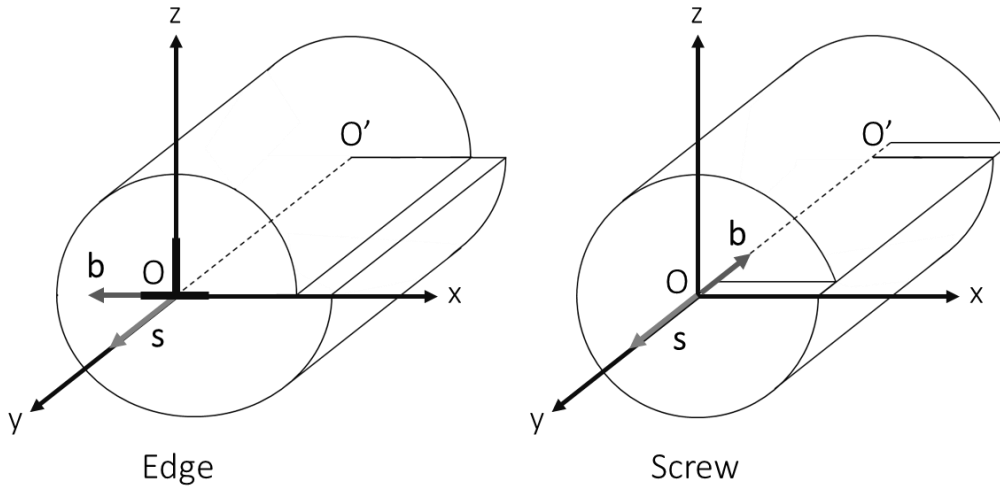


Figure 2 | Schematics representation of an edge and a screw dislocation. OO' is the dislocation line, b is the Burgers vector, and s is the positive line direction. (Figure adapted from [27]).

Dislocations are often of a mixed nature, partially consisting of an edge component and a screw component. There can also be steps in the dislocation line, known as kinks (contained in the slip plane) and jogs (any step in the dislocation line), that affects the motion of dislocations. Dislocations can also dissociate into partial dislocations to lower their energies, provided that the total b is conserved in the process [30]. Partial dislocations lead to stacking faults, while the intersection of two Shockley partials on different $\{111\}$ planes can form a Lomer-Cottrell lock and the dislocation becomes sessile. [27,28,31]

Other forms of plastic deformation are mechanical twinning and martensitic transformation. Mechanical twinning results from applied shear stress on the crystal lattice, which forms mirror-image atomic positions on either side of the twin boundary. Twinning also occurs on specific crystallographic planes and directions for each crystal structure. Twinning is favoured when the condition for slip is restricted; it occurs more readily at lower temperatures and higher strain rates. In stress-induced martensitic transformation, the sheared region transforms into another crystal structure. [27,29]

2.1.3. Overview of strengthening mechanisms

As dislocations are the main carriers of plasticity at low temperatures, the strength of a crystalline solid is inversely related to the dislocation mobility. The most fundamental

resistance to dislocation motion is the intrinsic lattice resistance, which stems from two sources: the Peierls-Nabarro resistance and the phonon drag. The Peierls-Nabarro resistance is related to the movement of the dislocation core through the discrete lattice [32,33], whereas the phonon drag is the interaction between a moving dislocation and the thermal waves from the lattice vibration. The intrinsic lattice resistance varies with the crystal structure, the dislocation type, and the temperature. For example, the lattice resistance of BCC metals is high for screw dislocations, whereas the resistances of FCC and HCP metals are low for both edge and screw dislocations [27]. Where the lattice resistance is low, various extrinsic mechanisms can be utilised to reduce dislocation mobility in the crystal. Some of the most effective extrinsic strengthening mechanisms in engineering alloys include solid solution strengthening, precipitation strengthening, strain hardening, and grain boundary strengthening.

Solid-solution strengthening

An effective way to strengthen pure metal is to introduce additional constituents in the form of a solid-solution. A solid-solution forms when atoms of two or more elements occupy various sites of a given crystal structure as a single phase. The proportion of the solute atoms that can be dissolved in the host lattice is its solubility. There are two types of solid-solutions: substitutional (where the solute atoms occupy the lattice points of the host lattice) and interstitial solid-solution (where the solute atoms are much smaller than the solvent atoms and occupy the space between the lattice points of the host lattice). There are several factors, as outlined by Hume-Rothery, that govern the formation of substitutional solid-solutions [34–37]. The formation of solid-solutions are more favourable when the atomic sizes of the solute and the solvent differ by less than 15%, their crystal structures are similar, they have a strong chemical affinity to each other, and that the relative valence of the solvent is lower than that of the solute. The incorporation of such solute atoms creates a size or a modulus misfit (or both) which results in a local attraction or repulsion to the dislocations. The size misfit elastically interacts with the dislocation while the modulus misfit affects the line energy of the dislocation via bonding interactions. Other mechanisms from electrical and chemical interactions also contribute to solid-solution strengthening.

The dispersion of substitutional and interstitial solid solutions can be considered random, although there is evidence that solute atoms aggregate around dislocations, stacking faults, and grain boundaries [28]. The average spacing of the solute atoms governs the degree of their interactions with dislocations. Both solid-solutions can also be partially- or fully-ordered, forming a superlattice. The constituent atoms in a superlattice occupy specific sites in the unit-cell. In a superlattice, dislocations dissociate into pairs, separated by an antiphase boundary. This is to maintain the long-range order of the lattice; the first dislocation upsets the ordering, and the second dislocation restores the atoms into their preferred sites.

Precipitation strengthening

Additional constituents can also be incorporated in the form of precipitates. Precipitates are second phase particles finely dispersed in the metallic matrix. For an alloy system to be precipitation-hardenable, the second phase must have an appreciable maximum solubility of several percent at elevated temperatures, but the solubility limit should decrease rapidly with decreasing temperature [38]. This is a necessary condition for precipitation hardening via the typical two-stage heat treatment. For the heat treatments, first, the alloy is solution-treated and quenched such that all of the second component is in supersaturated solid-solution, then, the alloy is aged at a lower temperature to nucleate and grow precipitates. Precipitates grow from lattice regions with solute segregation or local clustering [39,40]. The plastic resistance of coherent precipitates generally increases with the precipitate size [27], which increases with ageing time (Figure 3a). However, ageing beyond the critical precipitate size leads to a loss of coherency between the precipitates and the matrix. The plastic resistance decreases due to dislocations bowing around the precipitates rather than shearing it. The plastic resistance continues to decrease as the precipitate size increases thereafter. This is termed over-ageing. In addition to the size of the precipitates, the degree of strengthening also depends on the coherency, shape, volume fraction, distribution and spacing of the precipitates in the matrix.

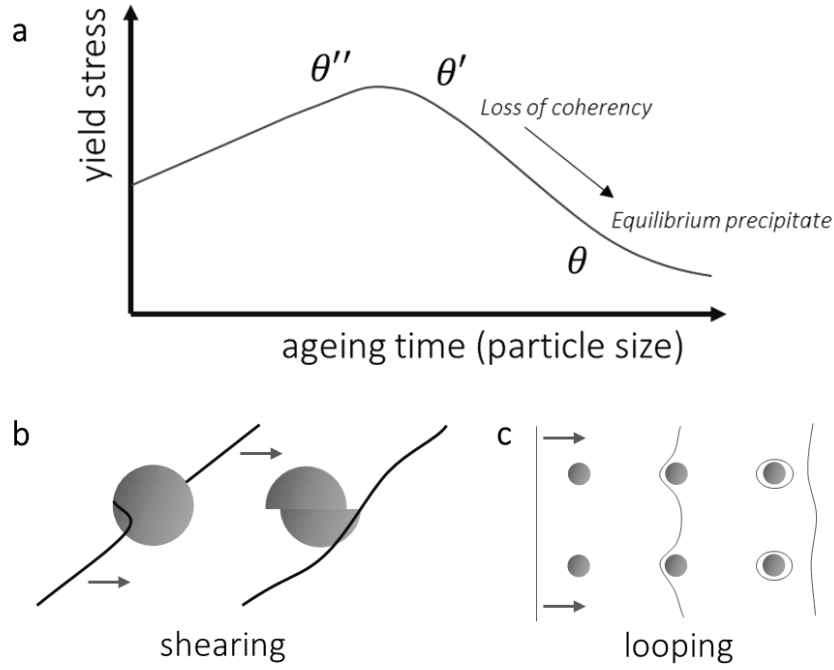


Figure 3 | Precipitation hardening of coherent and incoherent precipitates. a, Variation of yield stress with ageing heat treatment time (precipitate size). Schematics of a dislocation **b**, shearing a precipitate and **c**, looping around precipitates based on the Orowan mechanism. (Figure adapted from [28])

Precipitates impede dislocation motion via several mechanisms: stacking-fault strengthening, atomic-order strengthening, coherency strengthening, and modulus misfit strengthening. More than one mechanism can be relevant for each precipitate particle. In all cases of precipitate shearing (Figure 3b), there is also plastic resistance associated with the formation of new interfaces [41]. However, this resistance is relatively small compared to more dominant mechanisms. Stacking-fault strengthening is significant when there is a large difference between the stacking-fault energies of the precipitate and the matrix [42]. Depending on the relative difference between the stacking fault energies, there will either be a repulsive interaction between the dislocation and the particle from contact up to the halfway point, or there will be attractive interaction from the halfway point up the edge of the particle. Atomic-order strengthening is related to the shearing of chemically ordered superlattice domains [41,43]. As previously discussed, a dislocation passing through a superlattice creates an antiphase boundary that can be restored by a second dislocation moving on the same plane. For coherency strengthening and elastic misfit strengthening, the interactions between the precipitates and nearby dislocations are analogous to the mechanisms in

solid-solution strengthening. Coherency strengthening results from a size misfit between the precipitates and the matrix which creates a stress field that interacts with nearby dislocations [44]. Elastic misfit strengthening arises from differences in the shear or bulk modulus affecting the line tension of the dislocation, and more stress is required to shear the precipitates [45].

When the precipitates are incoherent with the matrix, either due to the size or the difference in the crystal structure, dislocations will bow around the particle rather than cut through it. The stress required to bow a dislocation line between precipitates increases with smaller precipitate spacings. As a dislocation percolates through a field of precipitates, it leaves behind a dislocation loop around each particle, in a mechanism described by Orowan (Figure 3c) [46]. The structure resulting from the formation of multiple dislocation loops around a precipitate can be considered similar to a dislocation cell, and the strengthening mechanism shifts from an Orowan-type to a Hall-Petch type relationship. The Orowan mechanism can also apply to dispersion hardening, which is a similar strengthening feature to precipitation hardening but the second phase particles have very little to no solubility in the matrix. Such particles are therefore more thermally stable at higher temperatures and are resistant to over-ageing.

Dislocation forest hardening due to straining (i.e., Strain hardening)

Dislocation forest hardening (i.e., strain hardening) is a phenomenon where the stress required to cause plastic deformation by slip continually increases with increasing strain. The interaction of dislocations with other dislocations and crystalline defects reduces their mobility and increases the plastic resistance. As the dislocation density increases with strain through various multiplication processes, the plastic resistance evolves with continual straining. The evolution of the strain hardening process is very complex and is often described in four distinct stages (Figure 4). Such stages directly relate to single-crystal FCC metals; however, the characteristics of the processes are expected to be similar in BCC and HCP metals as well. Polycrystalline metals only show stages III and IV, and occasionally stage II.

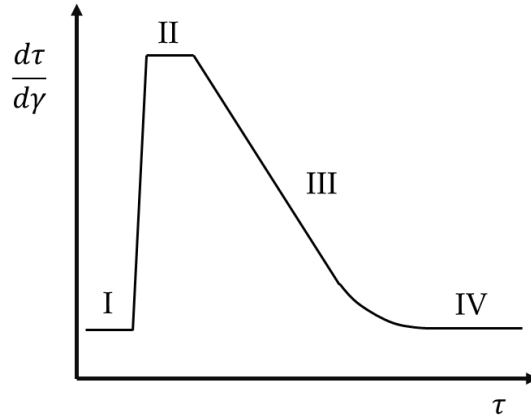


Figure 4 | Stages of strain hardening of a single crystal. Plot of hardening rate versus the flow stress showing 4 distinct stages of strain hardening. (Figure adapted from [47])

The first stage of the strain hardening process is called *easy glide*. It is a low strain hardening rate stage associated with deformation on a single slip system. A small but finite hardening rate is observed in this stage due to the accumulation of edge dislocations [48]. Stage II is characterised by a relatively high *linear hardening* behaviour, corresponding to geometrical storage of dislocations in cells (high-density networks of dislocations). The behaviour in stage II is mainly related to the interaction of dislocations of different slip systems, that is, the short-range interaction of mobile dislocations on a slip with dislocations that intersects the slip plane [49]. In stage III, the strain hardening rate decreases with increasing strain, often called *dynamic recovery*. The recovery behaviour in stage III can be related to the activation of cross slips, which permits dislocation pile-ups to escape and screw segments on different slip planes to annihilate [47]. The behaviour of stage III is highly temperature dependant due to the mechanisms associated. Stage IV corresponds to a small sustained hardening rate at very large strains [50], caused by the accumulation of dipoles and loops left from dynamic recovery.

Grain boundary strengthening

Grain boundaries are high energy lattice regions located between differently orientated crystallographic domains. While the grain boundaries themselves have little inherent strength [51,52], grain boundary strengthening arises due to hindrance to dislocation motion between the grains. There are two ways in which grain boundaries increase the plastic resistance of polycrystalline materials. Firstly, compatible deformation of an

aggregate of grains requires the activation of different slip systems in different grains. Five independent slip systems are required for a polycrystalline aggregate to undergo a change of shape [53], otherwise, low ductility is exhibited. Assuming similar strains in individual grains to the overall strain, the orientation average (average of the reciprocal of the Schmid factor of the grain aggregates) can be determined using the principle of virtual work [54]. In FCC polycrystalline aggregates, the average orientation factor is approximately 3.1.

The second way that grain boundaries increase the plastic resistance is related to the grain size. An empirical relationship between the grain size and the tensile yield stress was first established by Hall [55] and Petch [56]; the plastic resistance increases with a smaller grain size. There are two interpretations of the grain size dependence of the flow stress in polycrystals. The first is based on observations that isolated slip in individual grains did not lead to general yield, but required slip percolation across grain boundaries. Slip percolation occurs through a mechanism whereby dislocation pile-ups at the boundaries of the soft grain induce a stress concentration to nucleate new slip in the harder adjacent grains. Pile-ups at the boundaries also induces back-stress on approaching dislocations on the same plane, increasing the plastic resistance upon further loading in the same direction. The second interpretation of grain size dependence is related to the presence of geometrically necessary dislocations (GNDs) at the boundaries [57]. The production of GNDs at the boundaries are necessary to maintain compatibility between neighbouring grains if individual grains are to deform in their most favourable slip systems. Thus, smaller grain sizes lead to higher dislocation densities (and plastic resistance).

2.2. Additive manufacturing

The second topic of the literature review is on additive manufacturing (AM). Lattice materials are difficult to fabricate using traditional manufacturing methods due to their intricate mesostructure. This is especially true for meta-crystals with semi-periodic architectures that mimic strengthening features from metallurgy. Meta-crystals are only effectively realisable by AM and, therefore, it is important to consider how the processing method affects its mechanical behaviour.

2.2.1. Technologies

Additive manufacturing is the process of creating objects by joining materials together, usually in a layer-by-layer manner [58]. The technique was conceived as a rapid prototyping technology [59] but, in recent years, has transformed into a rapid manufacturing technology suitable for industrial applications [60]. AM provides several advantages over traditional subtractive manufacturing technologies. In particular, enabling the fabrication of complex near-net-shape parts with minimal waste and short lead times [61]. Besides the economic and environmental benefits, AM enables designs which were previously limited by manufacturing capabilities, leading to improved performances across industries [10,62,63]. AM also enables mass customisation. Parts can be tailored to individuals or functions at lower costs [64].

Many different AM technologies exist today, which can be broadly categorised as vat polymerisation, material extrusion, material jetting, binder jetting, powder bed fusion (PBF), direct energy deposition (DED), and sheet lamination [65]. Each category of AM have unique characteristics making AM a very versatile technology. Across the categories, objects can be fabricated from polymer, composite, metal, and ceramics, with resolutions ranging from several hundred nanometres to several metres. A brief description of different AM technologies and the applicable classes of materials in each category are shown in Table 1 (Nb., not an exhaustive list of AM technologies).

Table 1 | Categorisation of additive manufacturing technologies and the applicable classes of materials.

Categories	Technologies	Description	Materials
Vat polymerisation	Stereolithography (SLA)	Cures photopolymer resin using a laser/UV/visible light in a layer-by-layer manner. DLP uses a projector and therefore cures the entire layer simultaneously.	Plastics
	Direct light processing (DLP)		Plastics
	Continuous DLP		Plastics
Material extrusion	Fused deposition modelling (FDM)	Extrudes and deposits material along a path layer-by-layer. Requires significant support material	Plastics, ceramics, composites
Material jetting	Material jetting	Droplets of molten polymer or metal is jetted and cured/solidified layer-by-layer. For nanoparticle jetting, the metal powder is suspended in a photopolymer for deposition and subsequently sintered.	Plastics, metals
	Nanoparticle jetting		Metals
Binder jetting	Binder jetting	Binding adhesive is deposited onto the material layer-by-layer. Printed parts require post-processing to remove binding agent and increase density.	Ceramics, metals
Powder bed fusion	Laser PBF (L-PBF)	A thin layer of metal powder is distributed on the build platform and the desired geometry (cross-section) is melted with a laser or an electron beam. The process repeats in a layer-by-layer manner to create the solid part.	Metals
	Electron beam PBF (EB-PBF)		Metals
Direct energy deposition	Laser engineering net shape (LENS)	The metal powder or wire is deposited as it is melted with a laser or an electron beam. The melt pool is encased in inert atmosphere.	Metals
	Electron beam AM (EBAM)		Metals
Sheet lamination	Laminated object manufacturing (LOM)	Sheets of material are laminated together using heat and pressure and cut into the desired geometry. The part is built layer-by-layer	Polymers, composites

2.2.2. Laser powder bed fusion

Thanks to fine spot size and the presence of powder that serves as supporting structure, laser powder bed fusion (L-PBF) was predominantly used to fabricate intricate structures such as the lattice materials in this project. Therefore, L-PBF will be the focus of more in-depth reviews and discussions in the following sections.

L-PBF is one of the most common metal AM technology for metals. Similar to other powder bed systems, L-PBF is a layer-by-layer fabrication process. A thin layer of metal powder ($\sim 20\text{ }\mu\text{m}$ up to $100\text{ }\mu\text{m}$ [66]) is distributed onto a substrate build plate and selectively melted and consolidated using a focused laser beam (laser power can range from 20 W to 1 kW [66]). The laser, directed by a pair of mirrors, traces the cross-sectional geometry of the part at that layer at speeds of up to 15 m/s. Once the layer is complete, the build plate lowers by one layer thickness and the process repeats until the end of the print. The build plate is typically covered in an inert gas flow (typically Ar or N) throughout the print to prevent oxidation (the oxygen content is maintained at less than 0.1% [67]) and to remove process emissions [68]. A schematic of the process is shown in Figure 5 [69].

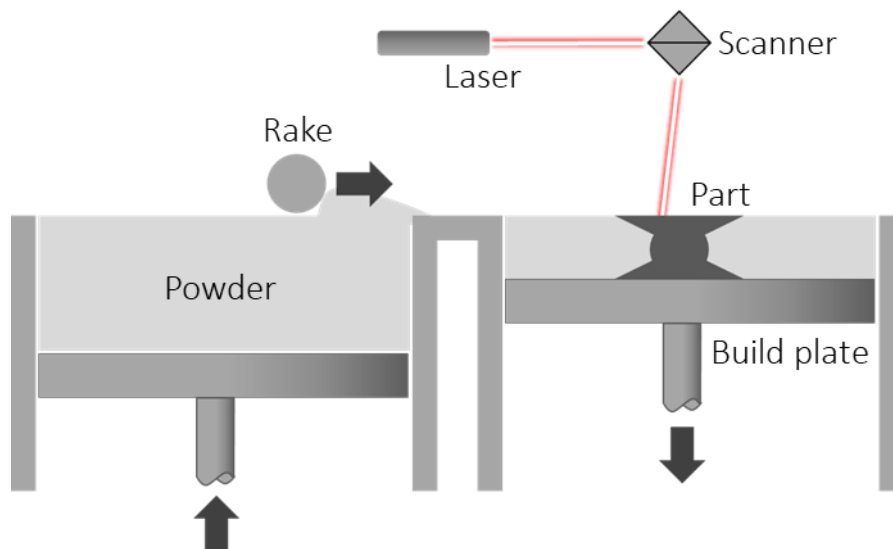


Figure 5 | Schematic of a typical laser powder bed fusion process. Figure adapted from [69].

Several technologies are similar to L-PBF but with slight fundamental variations. This includes electron beam powder bed fusion (EB-PBF), selective laser sintering (SLS), and

direct energy deposition (DED). Key differences in the processing conditions between EB-PBF and L-PBF are the energy source (electron beam vs. laser), the build atmosphere (vacuum vs. inert atmosphere), and the substrate temperature (elevated vs. low) [70]. For SLS, the laser sinters the powder rather than fully melting the powder [71]. For DED, the material is consolidated as it is being deposited, rather than having a powder bed. DED utilises both powder and wire feedstock, while the energy source can be an electron beam, a laser, or a plasma arc [72]. A comparison of the typical feature sizes achievable by various technologies is shown in Table 2.

Table 2 | Typical layer thickness and minimum feature size achievable in different metal AM technologies

Technology	Layer thickness (μm)	Beam diameter (μm)
L-PBF [73,74]	~10-50	~55-180
EB-PBF [75]	~50-70	~100-200
DED powder fed [76] (wire fed [77])	250 (3000)	~380 (16000)

2.2.2.1. Processing parameters

There are two main distinctions in L-PBF: continuous wave and modulated scanning. This relates to the method of delivering the laser energy to melt the material; the laser beam can be continuous [78] or rapidly pulsed along the scan track [14]. For both techniques, numerous parameters govern the L-PBF process. These processing parameters affect the formation of defects and the microstructure of the as-printed parts and, therefore, have a significant influence on their mechanical properties [79–83]. The ‘optimal’ processing parameters vary depending on many factors such as the geometry of the part, the AM system, and the base material used. With insufficient knowledge of the relationship between the processing parameters and the resultant melt pool dynamics under different conditions, processing parameters are often determined empirically and iteratively for each job. *In-situ* monitoring with a closed-loop control system of the process parameters could potentially alleviate this issue in the future [84–86]. A schematic representation of key processing parameters in continuous wave scanning is shown in Figure 6, including other relevant terminologies. For modulated

laser, the point distance (distance between pulses) and exposure time (duration of each pulse) are also important parameters.

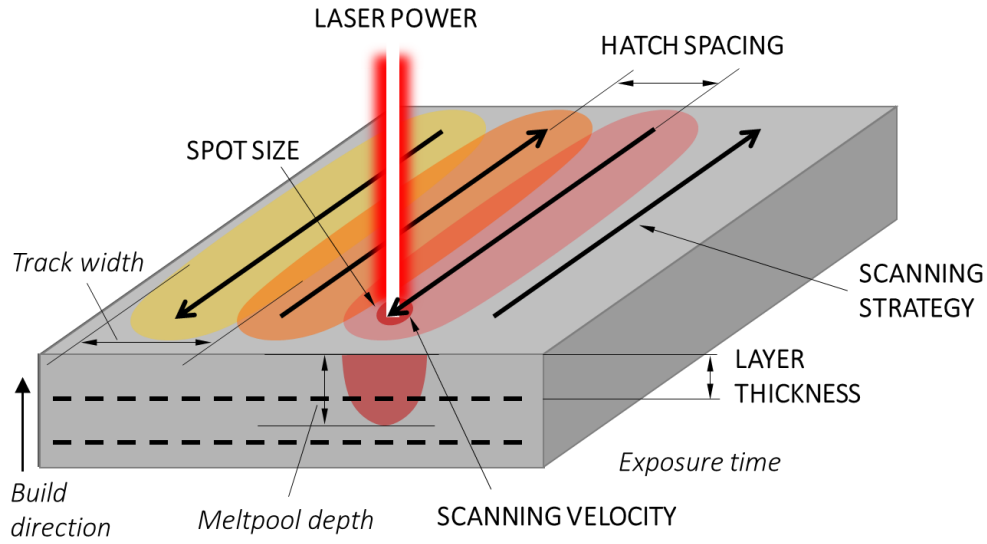


Figure 6 | Key processing parameters (block capitals) and terminologies (italics) in L-PBF.

The scanning strategy is the raster path that the laser traces to cover the infill area. The strategy shown in Figure 6 is the *meander* scanning strategy, where the scan direction reverses at the edge of the part. There are many other scanning strategies. Each one utilises different techniques such as partitioning of the infill area into islands, rotation between layers, different combinations of scanning directions, etc. to influence the thermal history in the part. The separation distance between adjacent scan paths is the hatch spacing. This is smaller than the track width (or melt pool width) so that each successive pass of the laser partially remelts the previous track, essentially welding adjacent tracks together. Similarly, the melt pool depth needs to be greater than the layer thickness to partially remelt the previous layer.

The outlined processing parameters dictate the location, amount, and rate of energy delivery into the material, thus the thermal profile in the consolidated part. This led to researchers describing the influence of the processing parameters using a single metric: the input energy density, E_D (Eq. 2.1, where P is the laser power, v is the scan velocity, d is the beam diameter) [87,88]. Alternatively, the linear energy density ($\frac{P}{v}$) [89] and the volumetric energy density ($\frac{P}{v \cdot d \cdot t}$, where t is the layer thickness) [90] have also been used.

While parts built with the same E_D sometimes show similar density [87,91–95], oftentimes, it has also been shown that there are significant variations in the microstructure [96–98], density [96,99,100], surface morphology [101], and properties [102]. The metric is insufficient as the sole descriptor of the processing parameters as many variables are omitted (such as the geometrical parameters, material properties, and part geometry). Additionally, the metric disregards how individual parameters affect the melt pool dynamics, its sizes and geometries despite maintaining a constant E_D [88,90,99].

$$E_D = \frac{P}{vd} \quad (2.1)$$

It is more useful to consider the processing parameters as laser parameters (spot size, power, scanning velocity, exposure time, and pulse distance) and geometrical parameters (hatch spacing, scanning strategy, layer thickness). Laser parameters govern the melt pool geometry and dimensions, whereas the geometrical parameters affect how the melt pools stack and overlap with one another. Of course, this does not consider variables unrelated to the processing parameters and therefore remains a simplistic generalisation of the process dynamics. Such information would provide a more accurate description of the process; for example, the melt pool geometry is also affected by the absorptivity and the specific heat capacity of the base material [103].

The processing parameters can vary within the same part depending on the region being built. Typically, parts are discretised as upskin, downskin, border, and infill regions Figure 7. Varying the parameters for different regions maximises the processing efficiency while ensuring geometrical fidelity and consolidation under different boundary conditions (thermal conductivity, support material, etc.).

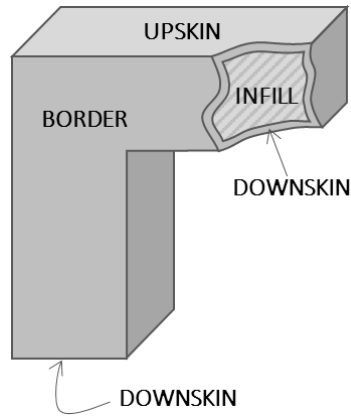


Figure 7 | Representative geometry showing different regions which can be printed with different processing parameters.

2.2.2.2. Processing defects

Defects are unintended deviations from the design in the part. Different types of defects include geometrical defects (e.g., warping, staircase effect, partially melted powder, dimensional inaccuracies), internal defects (e.g., pores and cracks), and chemical defects (e.g., inclusions and oxides). Most defects are detrimental to the mechanical integrity of the part and should therefore be minimised [69,79,104–106]. There are generally three sources for defects to be created or transferred into the print: from the feedstock powder, during the L-PBF process, and during the post-processing treatment [107]. Therefore, poor feedstock quality, improper selection of process parameters, unsuitable alloy composition, and inappropriate post-processing treatments can all introduce defects in the part.

Defects introduced via the feedstock powder

The main type of defect that is introduced through the feedstock powder is gas porosity. Gas pores are created in the powder particles during production, particularly during gas atomisation processes [108], and is retained in the part during printing (Figure 8). The amount of porosity retained depends on the processing parameters. Refinements of the processing parameters can ensure gas bubbles escape the melt pool surface leading to near defect-free deposits [107]. Gas pores are typically $<100\ \mu\text{m}$ in size (most tend to be $<10\ \mu\text{m}$) and spherical in appearance [79,81,109–111] which, compared to other types of

defects, are much smaller and are expected to be less detrimental to the mechanical properties of printed parts. Gas porosity can also be introduced during processing such as through evaporation of volatile elements [112].

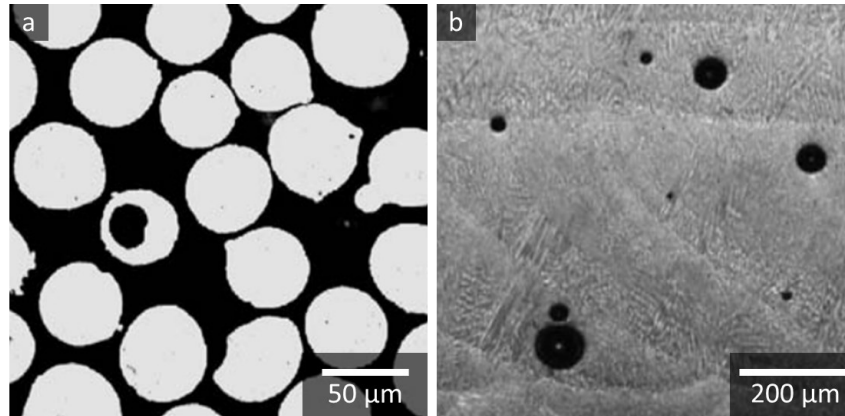


Figure 8 | Gas porosity in L-PBF. a, Optical image showing porosity inside Inconel 718 powder particle and b, SEM image showing the retained gas porosity by L-PBF. (Reproduced with permission from Springer [81])

Defect formation during processing

Defects formed during the L-PBF process account for most of the defects found in additively manufactured parts. Every type of defect (geometrical, internal, and chemical defects) can be introduced at this stage, and most can be minimised through the processing parameters.

Geometrical defects include part warping, dimensional inaccuracies, and surface defects. Warping defects are thermally induced. High temperature gradients and repeated heating and cooling cycles can lead to distortion in certain geometries such as thin-walled structures [113–115]. Large thermal gradients (up to 10^7 K/min) in L-PBF due to smaller melt pool, faster scanning velocity, and lower substrate temperatures make part warping a greater concern compared to other metal AM processes [116,117]. For geometrical and dimensional accuracies, L-PBF is generally very good due to the small particle and laser spot size, however, locally over- and under-consolidation can occur in thin and intricate features; for example, the circularity of lattice struts can vary with build inclination angle [118,119]. Surface defects such as the staircase effect (discretisation of geometry into slices), partially melted particles, and surface lack of

fusion increases the surface roughness of printed parts (Figure 9) [120]. Often, these behave like notches and induce stress concentrations, detrimentally affecting the fatigue and tensile properties of printed parts [106,121]. Optimisation of processing parameters such as the layer thickness and the laser power can reduce the surface roughness.

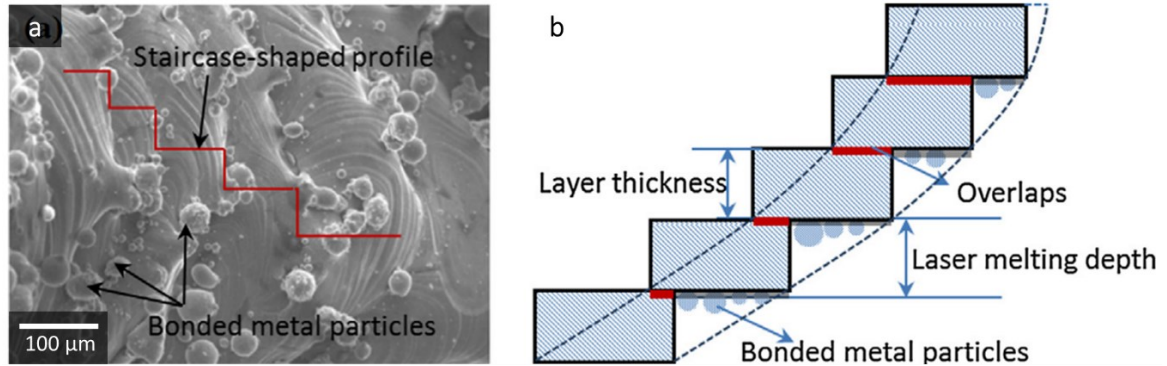


Figure 9 | Surface defects in L-PBF parts. **a**, an SEM micrograph showing the staircase-shaped profile and partially melted powder particles on the surface of a lattice strut and **b**, a schematic showing the mechanism for creating such defects. (Reproduced with permission from Elsevier [120])

In addition to surface defects, sub-surface pores also significantly affect the fatigue life of printed parts [122–124]. The two main types of internal porosities are lack-of-fusion (LOF) and keyholing, which typically corresponds to too little and too much laser energy input, respectively. This is clearly depicted in the power-velocity processing window (Figure 10) [107]. However, it should be noted that the energy density alone is insufficient for predicting defect formation [125], as the metric does not account for geometrical parameters nor determine the melt pool geometry [126], as discussed in section 2.2.2.1. With the remaining variables held constant in this scenario (such as hatch spacing, layer thickness, base material, and part geometry), the processing window shown is therefore case-specific. For example, the heat accumulation and energy dissipation in parts with non-uniform geometries vary due to different conductivity (fully consolidated part vs support structure vs powder) and interlayer cooling time, which will lead to spatially-dependent processing windows. This is evident with increased porosity at larger build heights and shorter interlayer cooling times [127].

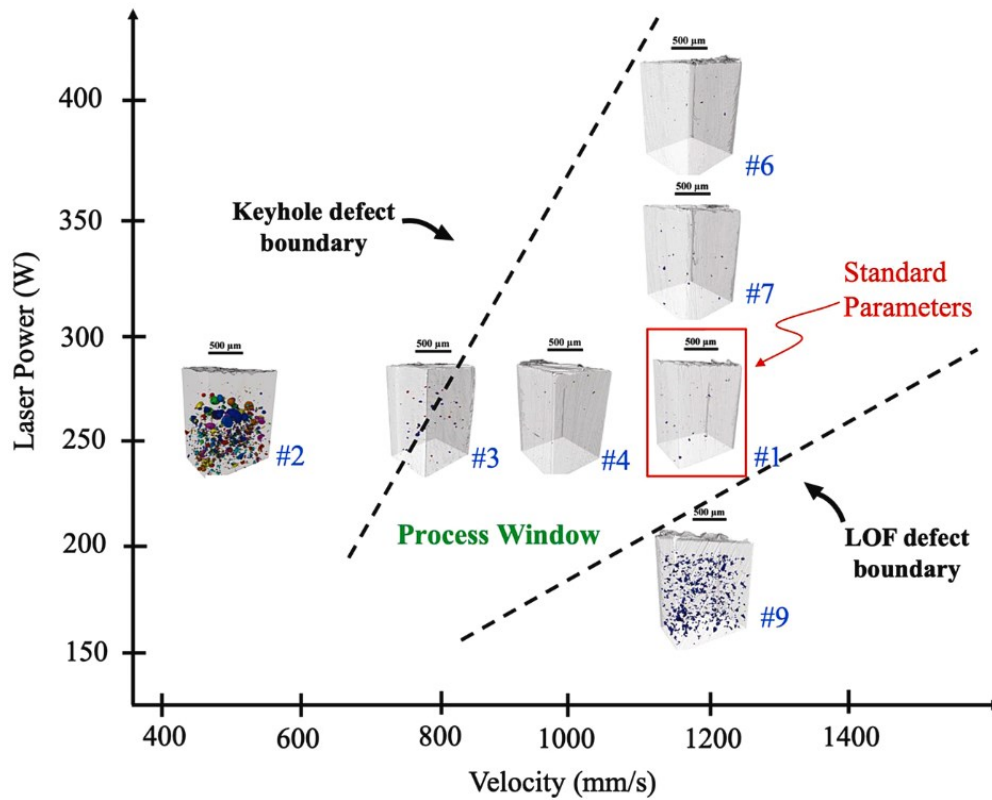


Figure 10 | Power-velocity processing window for Ti-6Al-4V produced via L-PBF under constant hatch spacing and layer thickness showing boundaries for lack-of-fusion (LOF) and keyhole pores formation. (Reproduced from [107], which was published under a CC BY NC ND license).

LOF pores and keyhole pores affect the mechanical properties of printed parts differently. Up to 1% of keyhole porosity was shown to have little effect on the tensile strength or elongation to failure of printed parts [128], whereas 1% of LOF porosity significantly reduced both the tensile strength [129] and elongation to failure [130]. LOF pores had a particularly detrimental effect on the fatigue properties; such pores were often identified as the primary sites for crack initiation, especially in machined samples [121,131–133]. The varying effects on the mechanical properties are due to differences in the morphologies of LOF and keyhole pores. While both types of pores can be relatively large, LOF pores tend to be irregular in shape [134] and keyhole pores tend to be more spherical [80]. This is the result of their formation mechanisms. LOF pores form due to insufficient overlap between neighbouring melt pools (both between layers and between tracks) [108,135], whereas keyhole pores form due to laser ‘drilling’ (excessing laser energy density creates an elongated melt pool and a vapour cavity that is ‘pinched-off’

and trapped by the Marangoni flow) [107,136–138]. Schematics of the formation mechanisms for LOF and keyhole pores are shown in Figure 11.

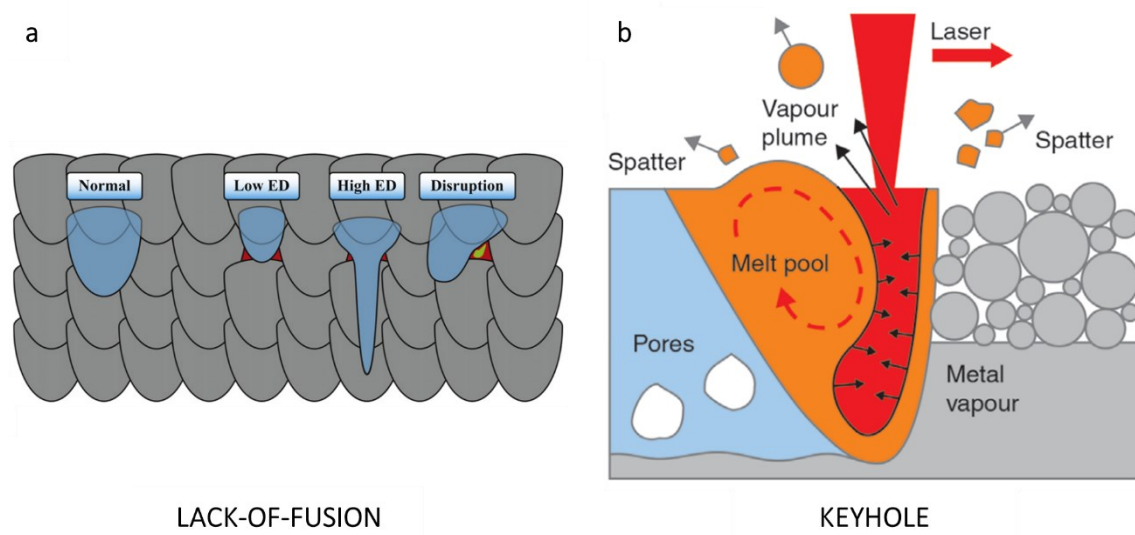


Figure 11 | Internal porosity formation mechanism in L-PBF. a, Lack-of-fusion porosity formation due to insufficient overlaps between adjacent melt pools. (Adapted from [134], published under a creative commons CC-BY open access license). **b,** Keyhole porosity formation due to excessive energy input. (Adapted from [139])

Cracking is another significant defect that can occur during processing besides porosity formation. The two main cracking mechanisms are solidification cracking and liquation cracking. Solidification cracking, also known as 'hot tearing', occurs at the terminal stage of solidification in the melt pool. There, enclosing dendritic growth can trap the remaining liquid in the constricted interdendritic region, which then becomes crack initiation points when subjected to thermal stresses from rapid solidification [140]. It was shown in fusion welding that alloy systems with steeper solidification gradients (i.e., a large change in temperature with respect to a change in the fraction of solid) at the terminal stage are more susceptible to solidification cracking [141,142]. This was shown to also be applicable in L-PBF despite the differences in the cooling rate [143]. On the other hand, liquation cracking occurs in the heat-affected zone (HAZ that is the region adjacent to the melt pool that are also significantly heated). During solidification, chemical segregation can lead to regions with lower melting temperatures (eutectic compounds or solute-enriched regions). Local melting of lower temperature regions in the HAZ coupled with the induced thermal stresses from the surrounding solids can

lead to liquation cracking [144]. As chemical segregation can be related to the temperature range between the liquidus and solidus temperatures, alloys with a wider freezing range are more susceptible to liquation cracking [143]. Other forms of cracking mechanisms include ductility-dip cracking [145], and strain-age cracking [146]. Strain-age cracking occurs in precipitation-hardenable alloys. Strain-age cracking mostly occur during post-processing heat treatments, but can also happen in fabrication. The HAZ effectively undergoes ageing heat treatment leading to an increase in strength and a reduction in ductility. If the stress relaxation from the elevated temperature occurs too slowly, the residual stress in the part can induce a strain that exceeds the reduced ductility leading to cracking [146,147].

A chemical defect that can occur during processing is due to the vaporisation of volatile elements. When processing alloys that contain one or more volatile elements, the rate of vaporisation of the elements are likely different [148], resulting in a change in the chemical composition of the as-printed part. Sufficient changes in the composition can lead to the formation of different phases [112] as well as changes to the mechanical properties of the part [149]. Additionally, vaporisation has also been linked to the formation of spherical gas pores in the consolidated material [112].

Post-processing treatments

Post-processing treatments of additively manufactured parts is done to alter the as-printed microstructure and/or to remove the processing defects; both serve the same purpose of improving the as-print mechanical properties. As discussed, surface roughness and large, irregular pores are the most detrimental sources of defects. While both types of defects are lessened by process parameters optimisation, it is often insufficient, hence post-processing treatments are required.

Several techniques have been applied to improve the surface roughness of parts, the most accurate and controllable is machining. Machining significantly improves the fatigue life, tensile strength, and elongation to failure of AM parts [121,150,151]. However, post-process machining is severely limited by the part geometry. As AM enables freeform fabrication, the geometry of many AM parts such as lattice structures

or parts with internal channels cannot be post-processed by machining. This also limits shot peening and blasting techniques [152]. An alternative surface modification technique for parts with internal geometries is electrochemical polishing. This is an effective method for improving the surface roughness of parts resulting in mirror-like finish, however, excess material is inevitably removed during the process leading to a change in the part dimensions [153–155]. For intricate geometries such as lattice struts, this would result in a significant change in its structural integrity. A modified overpotential electrochemical polishing method was proposed to achieve a surface roughness of $0.18\text{ }\mu\text{m}$ while only reducing the thickness of lattice struts by $\sim 70\mu\text{m}$ (Figure 12) [156].

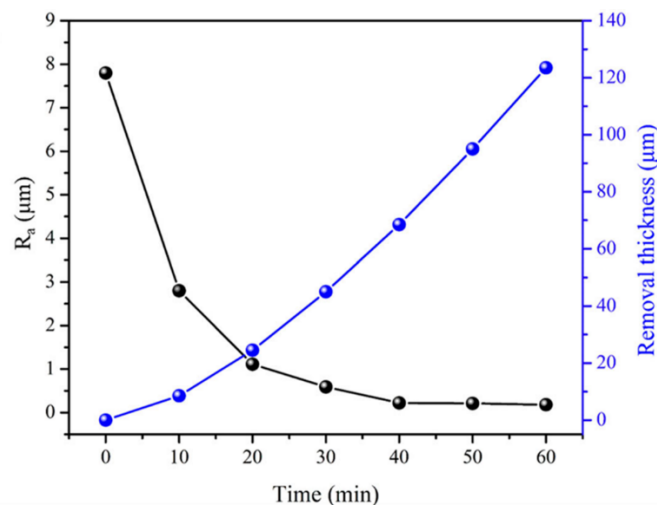


Figure 12 | Overpotential electrochemical polishing surface modification technique to improve the surface roughness of additively manufactured parts. The change in surface roughness and removal thickness over polishing time. (Reproduced from [156], published under a creative commons CC-BY license).

For internal porosity and cracks, hot isostatic pressing (HIP) is a widely used technique. During HIP, the part is held at elevated temperatures and pressures in inert gas atmosphere. The reduced yield stress and increased diffusivity at elevated temperatures allow pores to collapse and, under ideal conditions, enables bonding of pore and crack interfaces [157]. Analysis of parts by xCT showed that most internal porosity closed after HIP (Figure 13), with the exception of near-surface pores [158]. It was suggested that the remaining near-surface pores were exposed to the exterior by micro-cracks and therefore persisted through the HIP process [159]. Persistent pores after HIP in other studies were

also attributed to the entrapped Ar inside the pore [160]. A different study showed that gas pores do close during HIP and that the entrapped gas is absorbed into the material. However, subsequent heat treatments of HIPped parts can regrow such gas pores, but not LOF pores [79]. The HIPping process also simultaneously heat-treats the part, which reduce internal stresses and improve mechanical properties from the as-print condition [140].

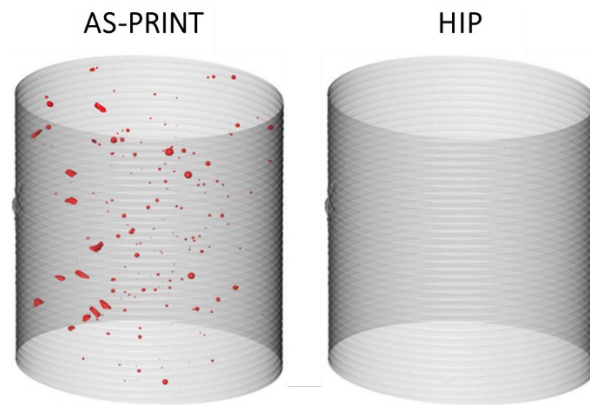


Figure 13 | Internal porosity reduction by hot isostatic pressing (HIP) in L-PBF Ti-6Al-4V specimen. Porosity is highlighted in red. (Adapted from [158], published under Creative Commons Attribution 4.0 International License)

2.2.2.3. Materials and microstructures

A limited number of alloy systems have been effectively processed by L-PBF. These include Al-alloys [161], Ti-alloys [162], HEAs [163], stainless steels [164], and nickel-based superalloys [165]. Certainly not all alloys are ‘printable’; in those, large quantities of defects are formed in the as-printed part. Alloys used in L-PBF were initially adapted from those used in laser welding due to the similarities between the two processes. More recently, however, increasing efforts are given to developing new alloys specific to L-PBF to fully exploit its unique processing conditions [143,166,167].

The as-printed microstructures produced by L-PBF are unique due to the rapid cooling, extremely high thermal gradient and repeated thermal cycling of the part during processing [140,168–170]. More excitingly, the thermal history is directly influenced by the processing parameters, which presents an opportunity for extensive spatial control over the as-print microstructure of the part [83]. Typically, the microstructures of AM-produced parts are dominated by highly textured columnar grains (Figure 14)

[73,143,171–173]. Epitaxial growth followed by competitive grain growth in AM creates high aspect ratio grains aligned to the primary heat-flux direction (i.e., the build direction) [174,175]. Dendritic/cellular subgrain structures are commonly observed in cubic alloys, with the cell size (or the primary dendrite arm spacing) directly related to the cooling rate during processing [176,177], where finer cells are observed at faster cooling rates. Chemical segregation to the interdendritic/cellular regions also occurs during dendritic/cellular growth [163]. Moreover, the cell boundaries contain dense dislocation structures, understood to significantly increase the plastic resistance analogous to deformation cells [164]. The phases present in L-PBF-produced parts can be different from their wrought counterpart due to the rapid cooling. Rapid cooling can produce metastable phases such as the α' martensites in Ti-6Al-4V alloy [178] and suppress the precipitation of strengthening γ' while forming non-equilibrium Laves in Inconel 718 [179]. Additionally, phase transformations can occur for the consolidated material in the HAZ, as shown in DED [180,181] and EB-PBF [182].

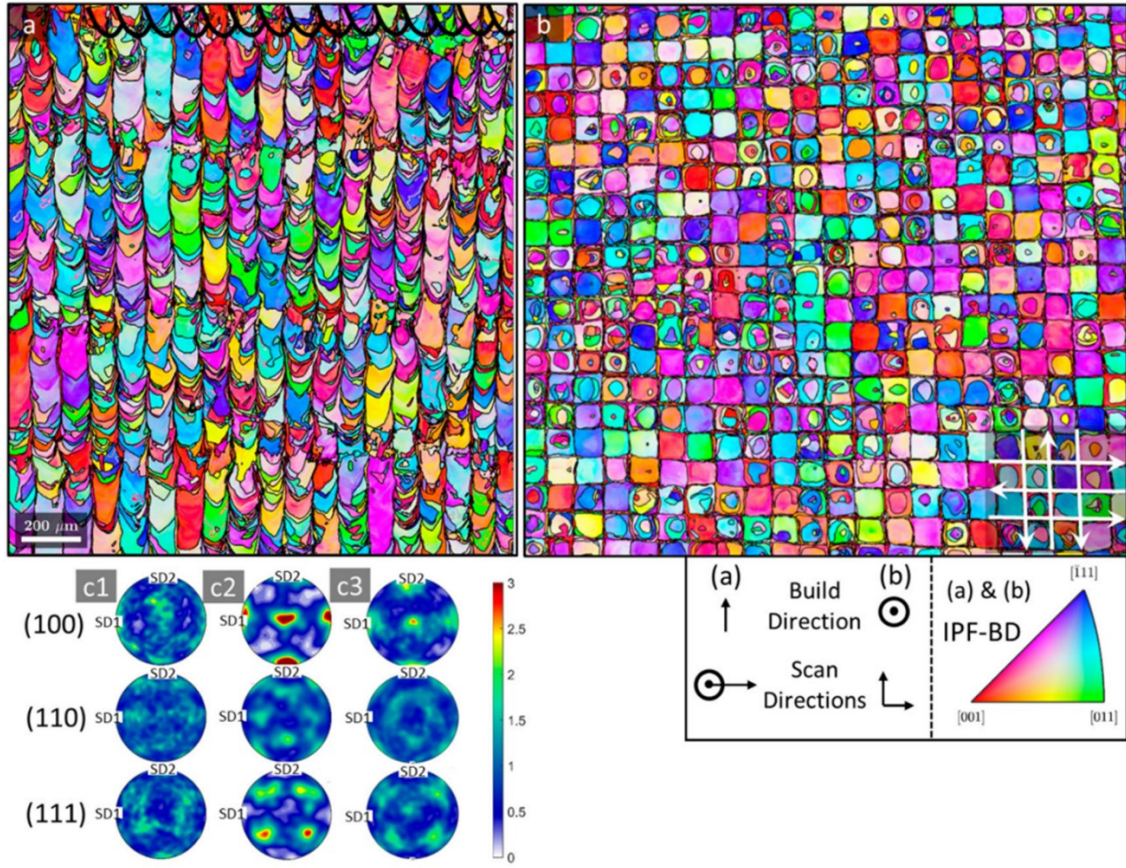


Figure 14 | Microstructure and texture in FeCrAl alloy fabricated via L-PBF. EBSD IPF-build direction maps of the as-printed specimen of sections parallel (left) and perpendicular (right) to the build direction. (Reproduced from [143], published under a creative commons CC-BY license).

The scanning strategy [172,183,184] and the ratio between the thermal gradient (G) and the liquid-solid interface velocity (R) [185–187] both significantly affect the grain structure, specifically the grain morphology and size. Texture control was shown in DED by rapidly changing the electron heat source from point to line to alternate between epitaxial growth and equiaxed nucleation [83]. Changing from the conventional raster fill to the point fill alters the G and R parameters to increase constitutional undercooling, transitioning the solidification mode from columnar to equiaxed. With nucleation in the undercooled region, the microstructure consists of more randomly oriented equiaxed fine grains and no texture [14]. The point fill method also allows for control of the grain size. Increasing the spacing between the points increases the cooling rate and thus the undercooling, and a larger undercooling leads to a higher nucleation density which results in finer equiaxed grains [188]. Changing the scan direction between layers alters the heat gradient direction, therefore where epitaxial growth is pertinent, both the grain

morphology and texture are affected. Changing the scan direction between layers strengthened the $\langle 111 \rangle$ fibre texture in L-PBF of pure tantalum [189], changed the preferential orientation from $\langle 001 \rangle$ to $\langle 110 \rangle$ in L-PBF of a Ti-alloy [190], and resulted in a cube texture around the build direction in DED of IN718 [191].

2.2.3. Designs enabled by additive manufacturing

A major advantage of AM is the capability for freeform fabrication. This had a significant impact in the field of metamaterials (i.e., materials that have new properties thanks mainly to their architectures), enabling new designs and improved performances. In this section, designs of mechanical and non-mechanical metamaterials enabled by AM will be discussed, except for load-bearing cellular solids, which will be covered in greater detail in section 2.3.1.

Pentamode materials were conceptually proposed in 1995 [192]; a material that has an extremely large bulk modulus compared to its shear modulus, sometimes referred to as 'meta-fluids', since their behaviour is similar to that of isotropic fluids. A study demonstrated the feasibility of this design by using lithography to fabricate a polymer lattice material that has a bulk to shear modulus of ratio of approximately 1000 (Figure 15) [193]. A different study applied pentamode lattice materials as an elasto-mechanical core-shell cloak, which was successful in elastically 'hiding' objects when compressed [194].

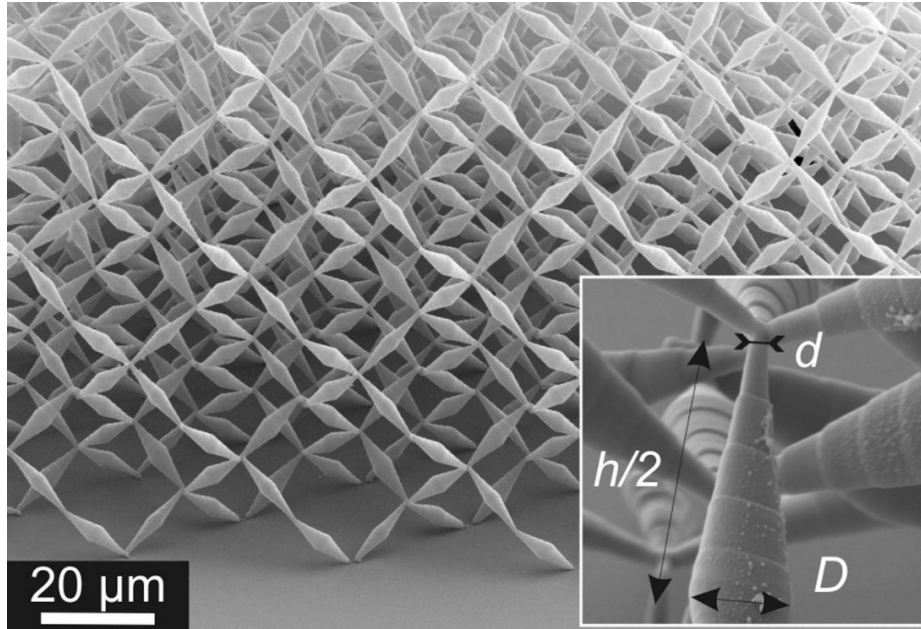


Figure 15 | Polymer pentamode lattice material fabricated by dip-in three-dimensional DLW optical lithography. (Reproduced from [193] with permission from AIP Publishing)

Lattice materials with a tuneable Poisson ratio have also been proposed. Through variation in strut geometry, Poisson ratios between -0.7 and 0.5 at up to 50% tensile deformation was achievable [195]. Lattice materials with a Poisson ratio of -1, known as dilational metamaterials, have also been designed. These are the opposite of pentamode lattices, with a small bulk-to-shear modulus ratio, the lattices preserve their geometric proportions under deformation [196]. Lattice materials that respond to magnetic fields have also been developed. Constructed with hollow struts infilled with magnetorheological fluid suspensions, the effective stiffness of the field responsive lattice material can be controlled in real-time with remotely applied magnetic fields [4].

Metal AM has had a significant effect on the design and performance of heat exchangers (HX). With AM, HXs are designed with intricate internal channels that optimise fluid flow and heat flux performance with much less geometrical constraints as encountered in conventional manufacturing techniques. Geometrical variations in the internal structures were shown to significantly affect the HX performance. As demonstrated with a manifold-microchannel HX, conceived through a multi-objective optimisation algorithm, the design achieved almost a 60% increase in gravimetric heat transfer density compared to conventional wavy-fin designs [2]. Similarly, an additively manufactured

HX consisting of manifold-microchannels, fabricated as a single component, showed a 40% improvement in gravimetric heat transfer density compared to conventional plain fin HX [197]. In a different study, AM enabled the variation in geometry of wavy microchannels. The difference in geometry dictated whether the flow was allowed to accelerate and separate from the walls or not, and therefore influenced both the pressure loss and heat transfer coefficient on the internal surface [198]. In addition to the ability to incorporate novel geometry, the inherent surface roughness of PBF parts also improved the heat transfer performance of HX [199]. For passive cooling applications, topology optimisation produced freeform designs only realisable through metal AM. Topology optimised passive cooler designs for LED lamps yield a 26% lower package temperature using 12% less material compared to lattice-fin design (Figure 16a) [200].

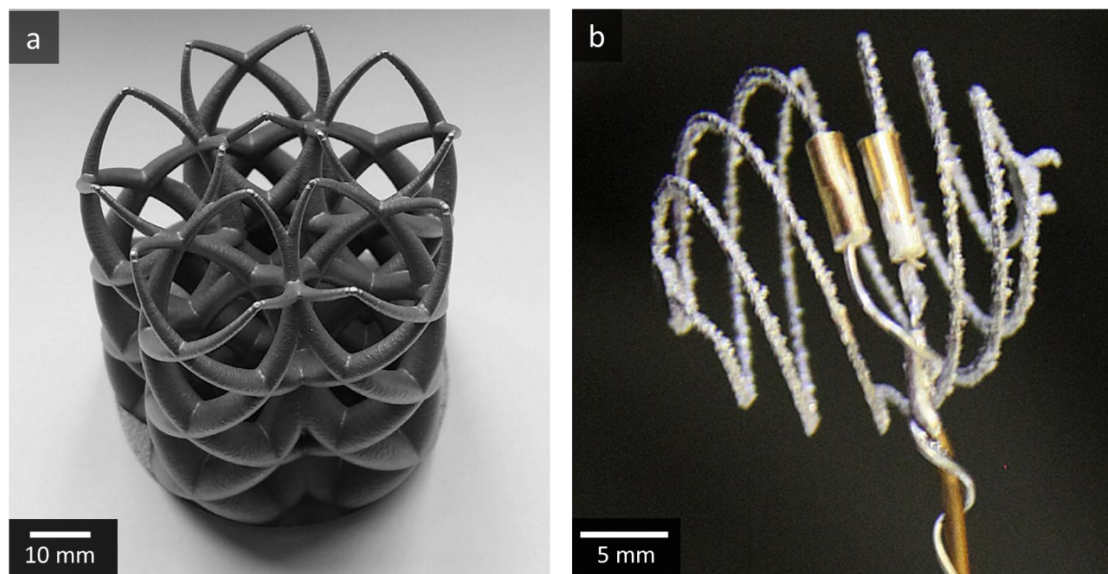


Figure 16 | Non-mechanical lattice material enabled by metal AM. a, Passive cooling lattice-fin design of a heatsink for LED lamps. (Reproduced from [200] with permission from Elsevier) b, High-performance freeform antenna fabricated from Ti-6Al-4V. (Reproduced from [201] with permission from IEEE)

As with the impact of optimised internal channels in HX, optimisation of the enclosed channel flow field in fuel cells also improved its performance. Micro fuel cells fabricated from stainless steel were extremely durable, robust and chemically and thermally stable, while the enclosed geometry resulted in significantly higher power and current densities compared to conventional open groove designs [202]. The increase in geometrical freedom with metal AM has also improved the performance of quantum devices. A functional prototype of a cold atom source module for quantum sensors was produced

from an Al-alloy using L-PBF [63]. A significant advantage of this AM-enabled prototype is its efficiency; the lower power consumption minimises the required resources for operation. Also for a quantum device, a magnetic shielding component and a vacuum chamber were manufactured from Ni- and Ti-alloys using L-PBF [203]. Both performances indicated that AM is suitable for the fabrication of such devices, allowing future designs to have increased integration between systems, resulting in a reduction in size, weight, and assembly complexity.

2.3. Cellular solids

Cellular solids is a class of metamaterial with an internal architecture consisting of space-filling compartments or *cells*. The geometry of the cells can be *closed* (enclosed by solid faces) or *opened* (no partitioning between neighbouring cells), and the cells can be assembled in space *stochastically* or *periodically* [1]. This leads to a range of architectures such as honeycombs (closed-cells, periodic), foams (closed-cells, stochastic), and lattice materials (opened-cells, periodic). Cellular solids are also commonly found in nature, examples include coral, wood (Figure 17 [204]), and bone. The cellular architecture gives this class of materials a unique combination of properties which are typically low density [205], have good thermal [206] and acoustic [207] insulating properties, and have good energy absorbing capacities [208]. This makes cellular solids suitable for a variety of applications such as lightweight structural components, packaging, buoyancy, insulation, etc. Examples of potential applications for cellular solids are shown in Figure 18.

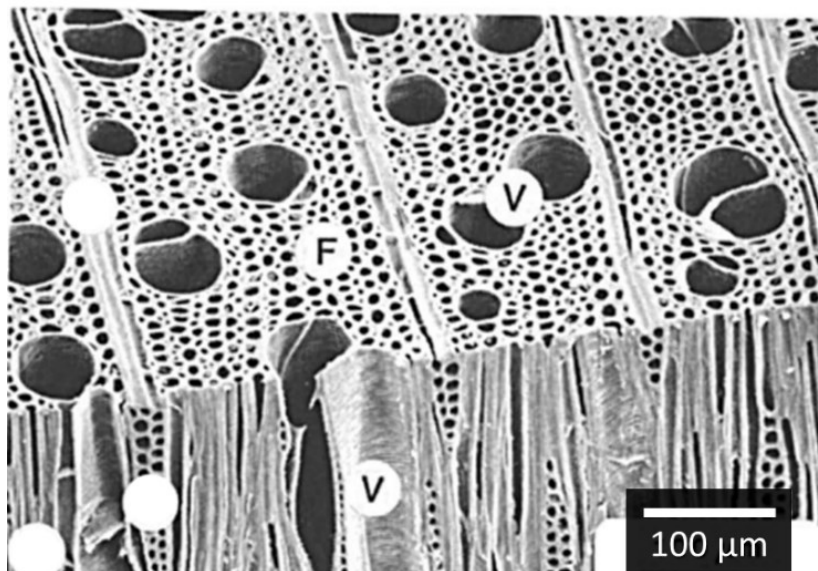


Figure 17 | The cellular structure of wood. An SEM micrograph of soft maple showing pores or vessels (V) and wood fibres (F). (Reproduced with permission from ACS Publications) [204]

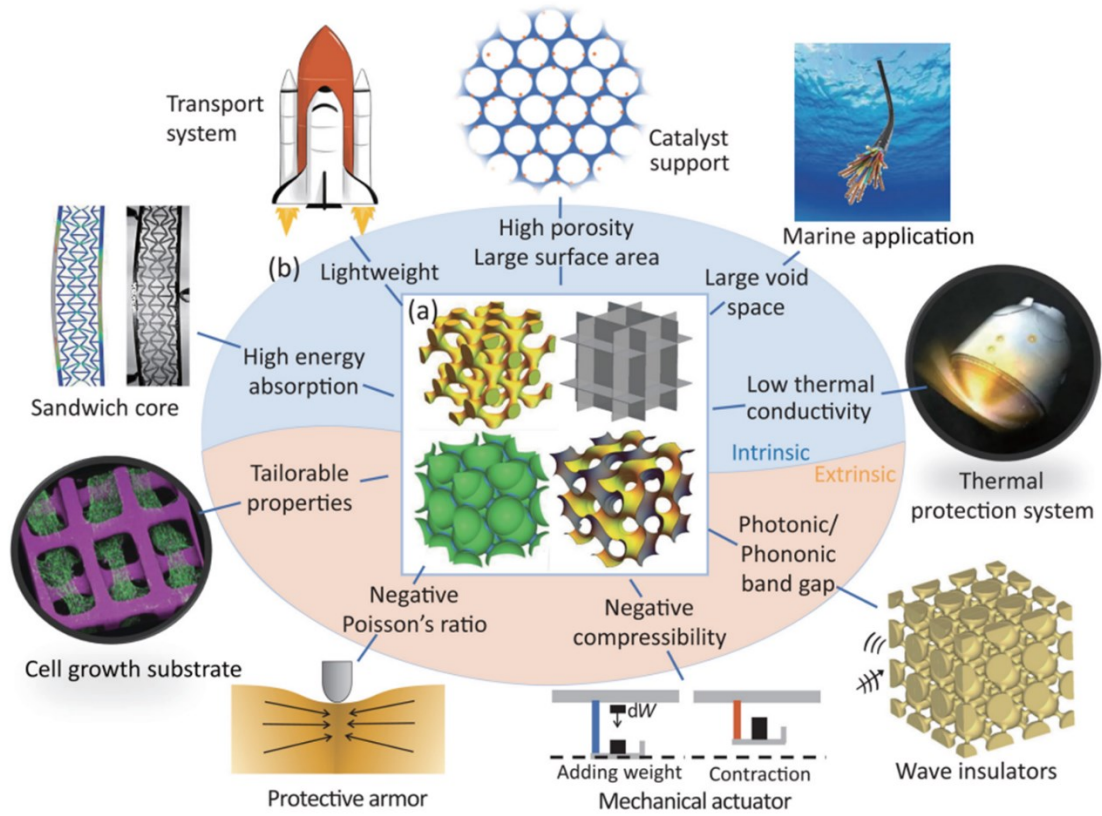


Figure 18 | Overview of potential cellular solids metamaterials applications. (Reproduced from [209] with permission from AIP Publishing).

2.3.1. Static mechanical properties of cellular solids

2.3.1.1. The Gibson-Ashby model

The most important characteristic of any cellular solid is its relative density ($\bar{\rho}$), defined as the ratio of the measured mass density of the cellular solid (ρ^*) to the mass density of the base material (ρ_s) (Eq. 2.2) (i.e., the fraction of the solid volume to the nominal volume, referred to as the volume fraction).

$$\bar{\rho} = \frac{\rho^*}{\rho_s} \quad (2.2)$$

In terms of the mechanical properties, another important characteristic of cellular solids is the compressive deformation behaviour. The two distinctive deformation behaviours observed in cellular solids are the uniaxial compression/stretching of struts and the bending of struts/cell walls, which are referred to as stretching-dominated and bending-

dominated structures, respectively [210]. There are generally three distinct regimes in the compressive deformation behaviours of cellular solids: 1.) the linear elastic regime, 2.) the stress plateau regime, and 3.) the densification regime [1,211] (Figure 19). The biggest differences between stretching- and bending-dominated structures lie in the stress plateau regime; generally, stretching-dominated structures exhibit greater peak stresses, but also suffer mechanical instabilities thereafter [106,212–214] (Figure 19b shows one initial post-yield softening, however, repeated softening/hardening cycles are possible with different stretching-dominated materials). This is a direct consequence of the axial compression of struts instead of bending, which provides greater stiffness and strength but fails by buckling and therefore exhibit a sudden loss in load-bearing capacity. The behaviours make stretching-dominated cellular solids ideal for lightweight structural applications and bending-dominated cellular solids ideal for energy-absorbing applications.

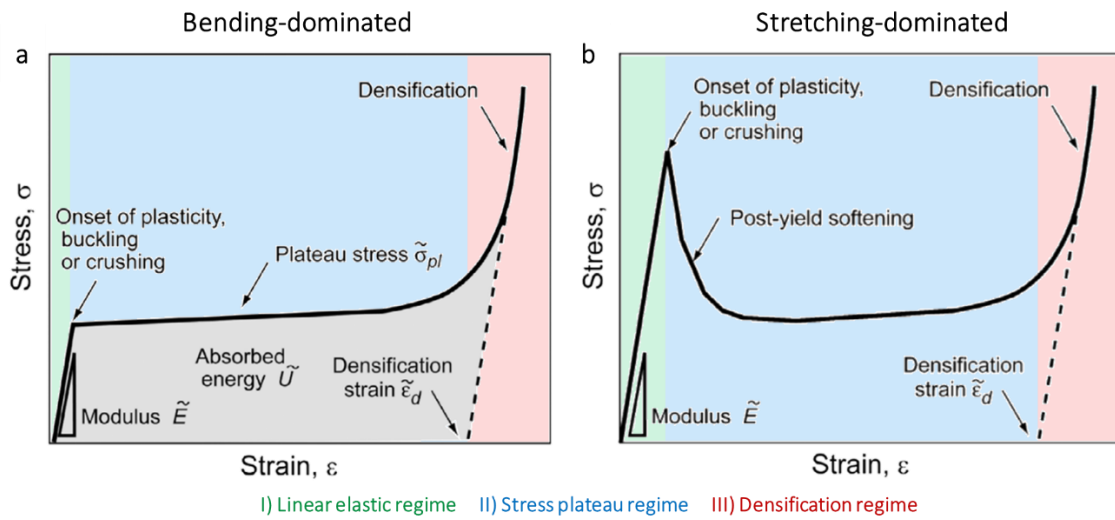


Figure 19 | Typical compressive stress-strain response of bending- vs. stretching-dominated structures. Three distinct regimes are highlighted in different colours: the linear elastic regime (green), the stress plateau regime (blue), and the densification regime (red). (Adapted from [211] with permission from John Wiley & Sons).

A semi-empirical scaling relationship between the mechanical properties of foams and their $\bar{\rho}$ was initially proposed by Gibson and Ashby [1,16,210]. This has later been applied to other cellular solids such as lattice materials with good accuracy. The general scaling relationship for the stiffness and strength with $\bar{\rho}$ is shown in Eqs. 2.3 and 2.4, where E is the elastic modulus and σ is the yield stress (Nb., the superscript * denotes

the properties of the cellular solid, whereas the subscript S denotes the properties of the base material). The power n and m depends on the deformation behaviour of the cellular solid, with n and m equal 1 for stretching-dominated structures and $n = 2$ and $m = 1.5$ for bending-dominated structures.

$$\frac{E^*}{E_s} \propto \left(\frac{\rho^*}{\rho_s}\right)^n \quad (2.3)$$

$$\frac{\sigma^*}{\sigma_s} \propto \left(\frac{\rho^*}{\rho_s}\right)^m \quad (2.4)$$

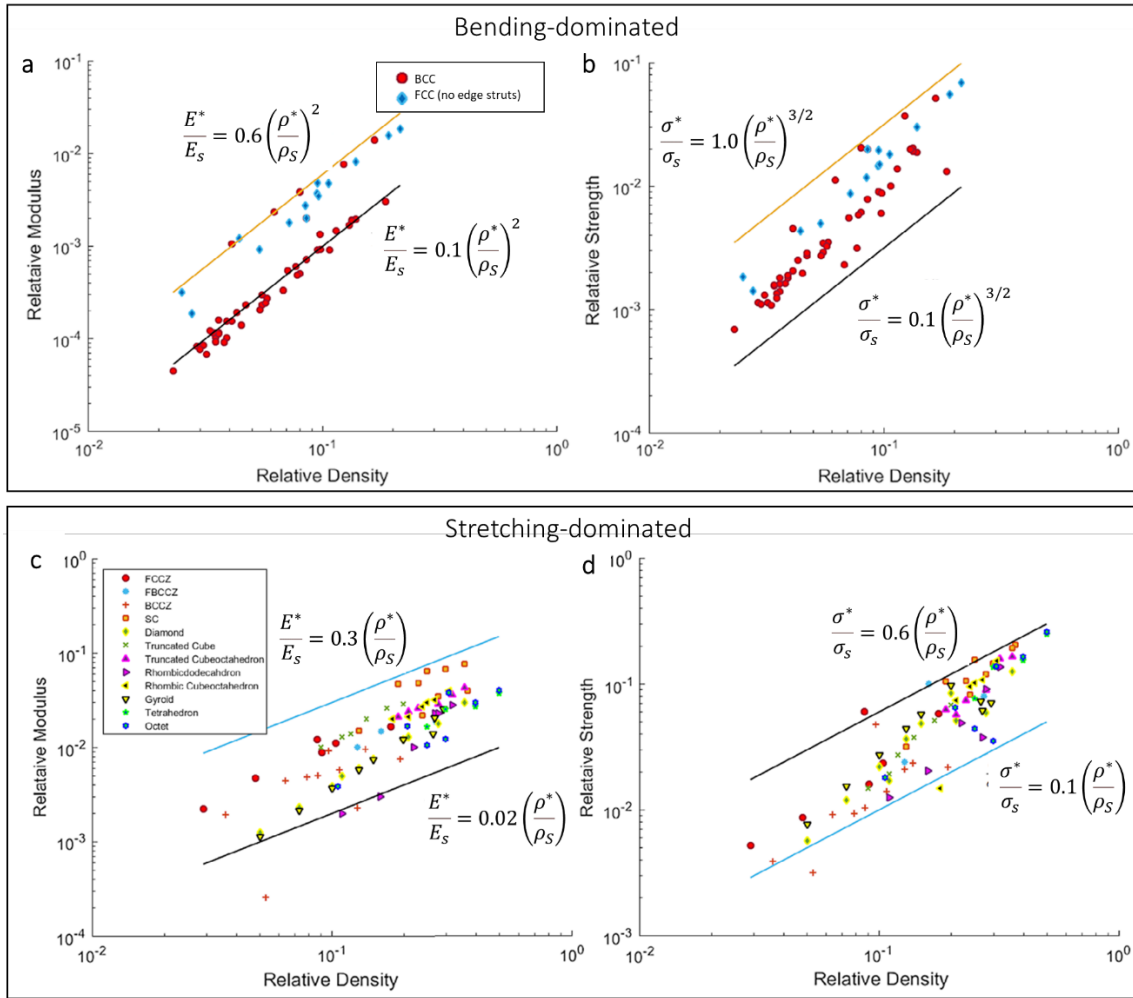


Figure 20 | The Gibson-Ashby scaling relationships for cellular solids of different unit-cell topologies. Plots **a**, **c**, the relative modulus and **b**, **d**, the relative strength vs. the relative density for bending- and stretching-dominated structures, respectively. (Adapted from [215] with permission from John Wiley & Sons).

The accuracy of the models have been verified by numerous studies [12,216–218]; plots of the relative modulus and the relative strength vs. the relative density of various cellular solids with different topologies are shown in Figure 20 and compared to the Gibson-Ashby model [215]. The models were shown to be fairly accurate, discrepancies between the estimated values and experimentally obtained values were attributed to inconsistencies from fabrication. For example, the differences in the values were attributed to the residual stress and the struts surface roughness in gyroid lattice materials fabricated from 316L stainless steel [120] and AlSi10Mg [219]. Elsewhere, with Ti-6Al-4V BCC structures, the reasoning was systematic manufacturing errors in L-PBF and the model was adjusted with correctional constants to reduce the error [220].

2.3.1.2. Maxwell’s criterion for categorising lattice materials

The compressive deformation behaviour of a cellular solid is related to the geometric properties of its architecture. In stochastic foams, neighbouring cells are unlikely to have the same number of vertices, edges, and faces and, hence, connectivity and so the geometrical characterisation of its architecture quickly becomes complex. Various topological laws have been proposed to aid in the understanding of stochastic cellular materials. For example, Euler’s law states that most foams, regardless of the shape, have on average five edges per face [221]. The Aboav-Weaire law states that the more number of sides a cell has, the fewer the number of sides its immediate neighbour has on average [222]. It was shown using topological arguments that stochastic foams are predominantly bending-dominated [223]. On the other hand, opened-cell strut-based lattice materials can exhibit either deformation modes depending on their unit-cell topologies.

The deformation behaviour of the lattice material is affected by the average degrees of freedom of the struts, which can be determined using Maxwell’s stability criterion for space trusses (Eq. 2.5, where s is the number of trusses and n is the number of joints) [16]. Maxwell’s criterion is originally used to determine the structural rigidity of pin-jointed frames, as a necessary condition of static and kinematic determinacy. Maxwell’s criterion implies that the frame is unstable (and is a mechanism) when $M < 0$, the frame is statically determinate when $M = 0$, and the frame is statically indeterminate when $M >$

0 [224–226]. Since lattice materials have fixed joints (where s is the number of struts and n is the number of nodes), this implies that the existing degrees of freedom at the nodes when $M < 0$ leads to bending in the struts, hence bending-dominated. Whereas when $M \geq 0$, the structure is rigid and the struts only carry axial loads, hence stretching-dominated. The criterion is a necessary, but not sufficient, condition for rigidity as it does not account for states of self-stress and mechanisms in statically indeterminate structures (e.g. stressed struts in the absence of external load due to change in length of another strut) [227,228].

$$M = s - 3n + 6 \quad (2.5)$$

In the case of periodic lattice materials, the nodes are similarly situated (i.e., the remainder of the structure appears the same when viewed from any node in any orientation [229]) and the structural rigidity can be considered in terms of the coordination number of the unit-cell, Z (the average number of nearest neighbouring nodes in the unit cell). It was shown that the coordination at each node in an infinite periodic structure is at least 12 for the structure to be rigid [16]. Several examples of different unit-cell topologies are shown in Figure 21 with the respective coordination number; the diamond, simple cubic, and BCC topologies are bending-dominated, whereas the octet truss and tetrakaidecahedral topologies are stretching-dominated [230].

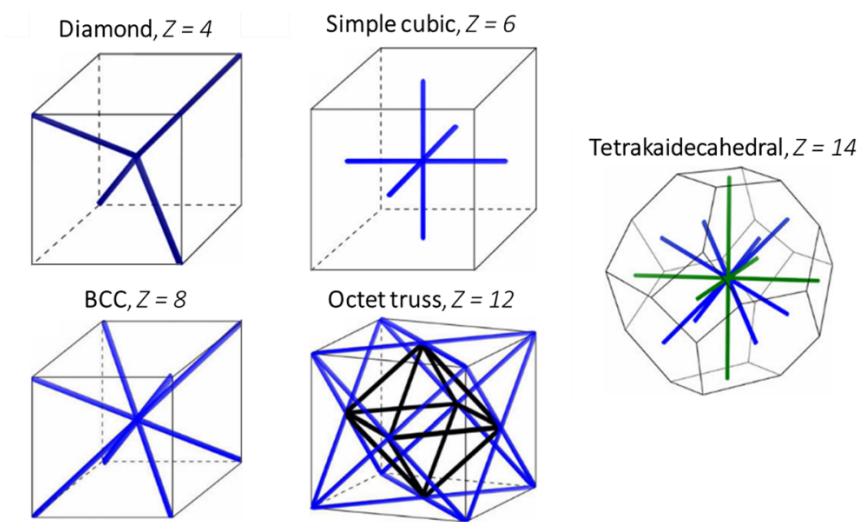


Figure 21 | Examples of different unit-cell topologies and their coordination number. (Reproduced from [230] with permission from the Royal Society).

While Maxwell's criterion is a valuable preliminary predictor for the deformation behaviour of periodic lattice materials, it has been shown to be inaccurate in some cases. Imperfect struts due to fabrication defects can prevent struts from contributing to the rigidity of the structure and the deformation behaviour of the structure can change. Additionally, it has been shown that the loading direction with respect to the unit-cell topology is also influential to the deformation behaviour, specifically struts aligned to the loading direction carry greater loads and tend to buckle more readily. For example, stretching-dominated behaviour was observed in structures that were classified as bending-dominated by Maxwell's criterion [231].

2.3.2. Architected lattice materials

Structurally efficient architected lattice materials are widely researched due to their considerable potential in industrial applications. Differently from foams, architected lattice materials have specifically designed mesostructures to obtain the desired mechanical properties. This section focuses on the influential variables affecting the mechanical properties of architected lattice materials.

2.3.2.1. Unit-cell parameters

The $\bar{\rho}$ was shown to influence the failure modes of the struts (plastic yielding and buckling). Initially, the failure modes were believed to be solely due to the properties of the base material, however, it was shown through modelling that the failure mode of a stretching-dominated octet-truss lattice transitioned from buckling to yielding as $\bar{\rho}$ increased from 10 to 20%. This was validated from the *in-situ* tomography data and from the force-displacement behaviour obtained through mechanical testing [232]. A different study showed that low $\bar{\rho}$ (5%) octet-truss lattices exhibited rigid-body node rotation due to buckling of struts, whereas high density (50%) octet-truss lattices exhibited more homogenous stable deformation due to plastic yielding. FE analysis indicated that in lower density lattices plastic hinges formed at the strut centre and around the nodes, while in higher density lattices the plastic yielding only occurred near the nodes which then propagates throughout the struts as the nominal strain increased [233]. It should be noted that in both studies $\bar{\rho}$ was increased by changing the strut diameter and keeping

the cell size is kept constant. Therefore, the transition of failure modes of the structure might possibly be due to differences in the strut geometry rather than differences in $\bar{\rho}$.

Numerous studies have explored the influence of the geometrical parameters such as strut length, cross-section, diameter, and cell size on the modulus, strength, and energy absorption capability of architected lattice materials. Firstly, the effect of the unit-cell shape will be discussed. In addition to non-symmetry, unit-cells which are elongated in one or more principal directions will result in anisotropic mechanical behaviours of the lattice materials. While this is more common in foams, due to difficulties in controlling the cell shapes, it can be beneficial in architected lattice materials for specific loading scenarios such as orthopaedic implants. In BCC lattice materials, longer cell length in the loading direction showed greater elastic modulus and peak strength [234,235]. However, this may be due to increased alignment of strut to the loading direction specifically in BCC topologies [236].

Another influential parameter is the *strut aspect ratio*, $R_S = l/d$, where l is the strut length and d is the strut diameter. A decrease in R_S in 316L stainless steel BCC lattice materials resulted in a steep increase in both normalised stiffness and strength, while the densification strain decreased. As R_S decreases from 12.3 to 6.0, the normalised stiffness and strength increased by 445% and 330%, respectively, while the densification strain decreased by 150% [237]. Furthermore, the stress-strain response and the optical images indicated that the failure modes and collapse behaviour remained the same for different R_S ; the struts failed by plastic yielding rather than buckling despite the relatively slender nature of the struts, as similarly reported in [235]. However, the failure mode changed to strut buckling at very large R_S (Figure 22). Additionally, it was shown by FEA that in plastic yielding, deformation propagated from the edge of the node region in to the strut, whereas in buckling, localised plastic hinges form adjacent to the nodes and at the centre of the struts [233]. This significantly affects the specific energy absorption of the lattice material.

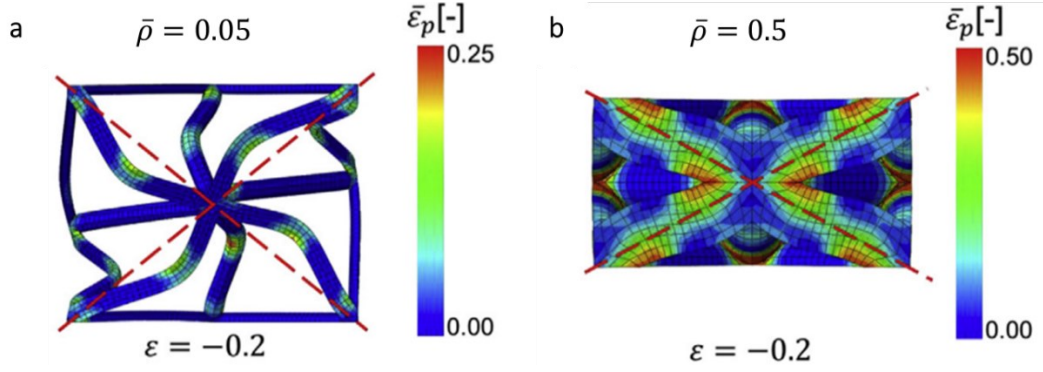


Figure 22 | Strut failure modes. a, Strut buckling and rigid body rotation of node for struts with large R_S . b, Plastic yielding of struts with low R_S . (Adapted from [233] with permission from Elsevier).

For non-circular strut cross-sections, the mechanical properties of the lattice material are affected by the characteristic length of the cross-section, since both the bending stiffness and the critical buckling load depend on the second moment of area. In some cases, the cross-section geometry is limited by the fabrication technique. For example, electrodeposition techniques tend to produce hollow struts [238], and assembly techniques tend to have struts with square cross-sections [239]. While the absolute stiffness of lattices with hollow struts is lower than lattices with solid struts of the same $\bar{\rho}$, its specific stiffness is greater [240]. The compressive mechanical behaviours of BCC lattice structures with three different strut cross-section geometries were explored (circular, semi-circular, and U-shape). With the cross-section geometry oriented to have the highest stiffness in the bending direction, semi-circular and U-shape struts exhibited strengths twice that of circular struts [241]. The mechanical properties of BCC and octet-truss lattice materials with larger strut diameters near the nodes compared to the centre were also investigated [18,233]. The studies revealed that a slight reduction (20%) in diameter towards the centre gave the highest strength (Figure 23), but further reductions in diameter reduced the strength to below that of uniform struts. Additionally, struts with a larger diameter near the centre exhibited significantly lower strength than struts which tapers inward at the centre. Pyramidal lattice materials containing curved struts with square cross-sections showed 30% lower specific strength compared to straight struts, but 150% greater specific energy absorption [242].

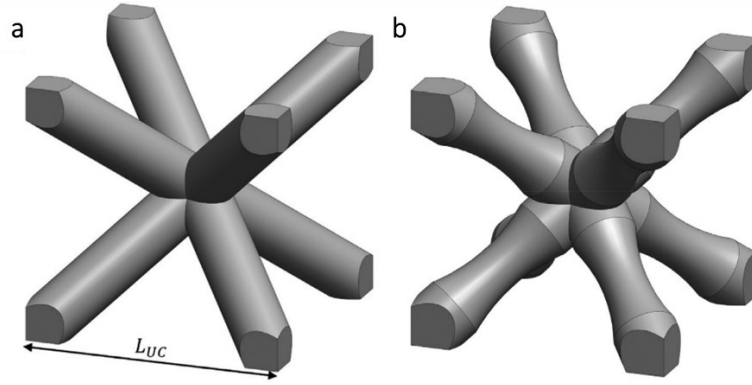


Figure 23 | BCC unit-cells with uniform (a) struts and tapered (b) struts. (Reproduced from [18] with permission from Elsevier).

2.3.2.2. Outer boundary effects

The physical constraints near the boundaries of the lattice material are less than the constraints on the inner regions (due to lower edge connectivity), leading to different mechanical responses between the regions. When the size of the lattice material is much larger than the size of the unit-cell, this effect tends to zero as the mechanical response converges to that of the bulk structure. It was originally suggested for metallic foams that the size effect is significant when the ratio of specimen size to unit-cell size is less than four and becomes negligible when the ratio rises to seven [1,243,244]. For architected lattice materials, it was shown that a minimum of 4 unit-cells was required in each direction to ensure size-independent mechanical properties [245].

The addition of a surface architecture (i.e., a *skin* or a *shell* encasing the lattice material) can also affect the properties of a lattice material. Surface architectures are often required for irregularly-shaped lattice materials. Except for conformal lattice materials, irregularly shaped lattice materials have numerous *open* struts (struts not supported at an end) at the boundaries that do not contribute to their strengths [246]. It was shown that the presence of a solid shell improved the stiffness of BCC and gyroid lattice materials, whereas net-like skins only improved the stiffness of BCC lattice materials [247]. Another study showed that the presence of the shell architecture only on the top and bottom surfaces (surfaces in contact with the loading platens) also improved the strength of BCC lattice materials. The increase in strength was attributed to the additional resistance to horizontal lattice sliding on the loading platens and the relative

displacements between different portions of the lattice structure during deformation [248]. Besides the benefits to the mechanical performance, surface architectures also aid in the aerodynamic performance, thermal insulation, shape maintenance, and the build quality of overhanging features.

2.3.2.3. Loading conditions

A study investigated the dynamic response of 316L stainless steel BCC lattice materials and single struts at strain rates from 10^{-3} to 6000 s^{-1} via drop weight tests and Split Hopkinson bar tests [249]. The dynamic response was oscillatory and exhibited increased peak stress compared to quasi-static loading. The oscillatory behaviour was believed to be due to the elastic wave which developed during initial contact and is reflected within the lattice block and increased peak stress was due to the base material's strain rate sensitivity. The failure mode did not change at different strain rates. In a different study, a 30% increase in strength of the octet truss lattice material was observed when the strain rate increased from 10^{-3} to 10^3 s^{-1} which was attributed to the strain rate sensitivity of the base material [233]. Investigation of the specific energy absorption at various strain rates of heat-treated Ti-6Al-4V FCC lattices showed that the energy absorbed during quasi-static compression was the lowest at 9.29 J/mm^3 , this value then increased to the peak energy absorbed at 13.52 J/mm^3 at a strain rate of 0.313 s^{-1} and thereafter decreased to 10.35 J/mm^3 at a strain rate of 1 s^{-1} [250]. The study did not explain why the highest energy absorption was at the intermediate strain rate. Blast loading analyses of lattice materials with different unit-cell topologies were performed using a ballistic pendulum [251]. While the deformation mode remained unchanged for all strain rates, the blast loading response showed a doubling of the strength which will improve energy absorption performance. Inertial effects were considered to be insignificant as no lateral stabilisation against buckling occurred. The performance enhancement due to shock waves that form during impact (as observed in foams [252]) was also considered but the impact velocity was shown to never reach the critical velocity for shock wave development. The increase in performance was then attributed to the strain rate sensitivity of the base material.

Lattice materials can also exhibit anisotropic mechanical responses. For unit-cell topologies that are symmetrical about the principal planes, the mechanical anisotropy partly arises from the processing defects, since the formation of some defects is dependent on the build direction (e.g., higher surface roughness on the downskin). Certainly, non-symmetrical topologies also exhibit anisotropic mechanical behaviours, with the highest stiffness and strengths shown when loaded parallel to the strut axes [253]. An approach for predicting the yield surface of lattices subjected to uniaxial and biaxial stresses analytically based on classical beam theory was developed and showed good agreement with FEA results [235]. The plastic collapse surfaces of octet-truss [254] and BCC [255] lattice materials have also been derived analytically and experimentally. The compressive strength was much higher than the shear strength for BCC lattice materials and therefore, as the load angle increases from pure compression to pure shear the strength of the lattice block decreases. However, it was shown in another study that the mechanical response of BCC lattices under shear loading has low repeatability [255]. The shear response of tests performed on specimens with the same geometry showed variations up to 220% in the peak stress. It was suggested that shear loading is heavily affected by structural imperfections from processing. The fatigue behaviour of lattice materials is also sensitive to processing imperfections. The fatigue limit of AlSi7Mg BCC and FCC lattice materials were shown to be limited by the fatigue limits of *hot spots* (i.e., local geometrical imperfections), as identified by x-CT scans [256]. Similarly, surface-based lattice materials showed superior fatigue resistance over strut-based lattice materials due to a lack of stress concentration points at nodal locations [257].

2.3.2.4. Effects from processing

Various processing defects, such as those discussed in section 2.2.2.2, can be present in AM metallic lattice materials which affects its mechanical behaviour. Processing of lattice materials by PBF is mostly limited by the difficulty in fabricating intricate overhanging struts [70]. Lattice strut quality differs significantly depending on the build angle. Comparison of designed strut cross-section with fabricated strut cross-section shows that vertically built struts are most accurate whereas horizontal struts are the least accurate [119,258,259]. There also appears to be more partially melted powder bonded

to the underside of the horizontally built struts due to over-melting, thus, increasing the surface roughness. L-PBF was employed to fabricate 'diamond' lattices from AlSi10Mg with cell sizes ranging from 3 up to 7 mm and reported no defects or broken cells within the structure [260]. Deformation and sagging of struts became apparent when cell size was increased above 7 mm even with the self-supporting topology of the diamond structure. 316L stainless steel BCC lattice materials fabricated via L-PBF reported that micro-struts built at 45° to the horizontal exhibit yield stress values ~5% lower than strands built vertically [248]. 316L stainless steel struts built parallel to the build direction showed no distortion [261]. Ti-6Al-4V struts built at inclination less than 20° exhibited flaws in the geometry [253].

A significant increase in the internal porosity of AlSi10Mg lattice material was observed with both the laser power and the scan speed [262]. Analysis of EB-PBF produced Ti-6Al-4V struts with diameters ranging between 0.45 mm and 2 mm showed that fine struts (≤ 0.6 mm) tend to be oversized while coarse struts (≥ 1 mm) are slightly undersized. The beam parameters and powder size were constant and, therefore, the deviations were attributed to the fractions of contouring and hatching areas for different diameters. The strut surface roughness of EB-PBF produced Ti-6Al-4V was shown not to vary significantly (~ 100 μm) with the strut diameter between 0.56 to 1.8 mm [263]. However, in L-PBF produced Ti-6Al-4V struts, it was shown that the roughness significantly increased from ~ 25 μm to ~ 60 μm when the thickness is reduced from 1 mm to 0.25 mm [264].

PBF also leads to variations in the microstructure of metallic lattice materials due to differences in the heat flux direction and thermal gradient resulting from the intricate geometry. The heat flux direction is typically aligned to the build direction in bulk specimens; however, this becomes more aligned to the strut direction in lattice materials. As a result, large columnar grains aligned to the strut axis have been observed in vertical and inclined 316L [171,233] and Ti-6Al-4V [265] struts. The grain sizes were also observed to be much smaller in the node than in the struts [233,266]. Additionally, the solidification cells were observed to be much finer near the upskin of the inclined AlSi10Mg struts (Figure 24) [267]. The stark difference in the cell size was attributed to

different cooling rates: low conductivity towards the unmelted powder in zone B and high conductivity towards the consolidated material in zone A. Another study on 4130 steel lattice material similarly showed two distinct zones in the microstructure of inclined struts. However, the difference in the upper zone from the lower zone in this study was attributed to high-temperature tempering effects from reheating during deposition of the upper layer [268].

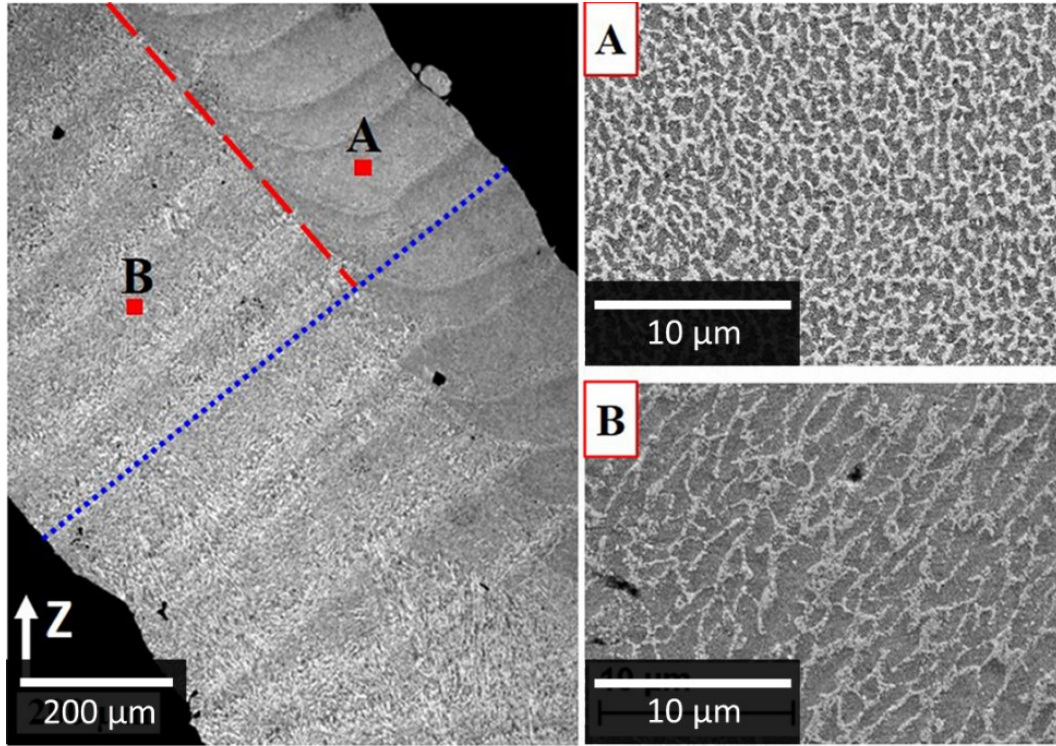


Figure 24 | Cellular microstructure of inclined AlSi10Mg strut fabricated by AM. Inset A and B shows variations in the cell size in different regions of the inclined strut; finer cells observed near the upper surface and coarser cells observed near the lower surface. Build direction is Z. (Reproduced from [267] with permission from Elsevier)

2.3.2.5. Nanolattice materials

A special class of lattice materials showing exciting properties is the nanoscale lattice material. Such lattice materials are fabricated via a multi-step process typically consisting of lithography of a polymer scaffold that is used for electrodeposition and later removed by etching or pyrolysis. This process tends to produce hollow struts with very thin walls resulting in exceptionally low $\bar{\rho}$, for example, a hollow-strut nickel nanolattice with 2 μm unit-cell size and 300-400 nm strut diameters was achieved,

resulting in a $\bar{\rho}$ of 0.9 mg/cm³ (Figure 25) [269]. Such nanolattice materials exhibited extreme mechanical properties [217,269–272]. Copper octet truss nanolattices with an average grain diameter of approximately 2 μ m (the strut cross-section mostly consist of a single grain) showed greater normalised compressive yield strength than that of the base material [5]. This was attributed to the size effect present in single-crystal metals with sub-micron dimensions. Alumina octet-truss nanolattices showed complete recovery to their original shape after compressions in excess of 50% strain. Brittle fracture was suppressed due to a very small strut thickness to strut radius ratio, which led to deformation by elastic shell buckling instead [13]. Titanium nitride octahedral nanolattices were subjected to multiple loading cycles without fracture whilst attaining a tensile strength of 1.75 GPa, which was attributed to the low probability of existing defects in the nano-scale struts [273].

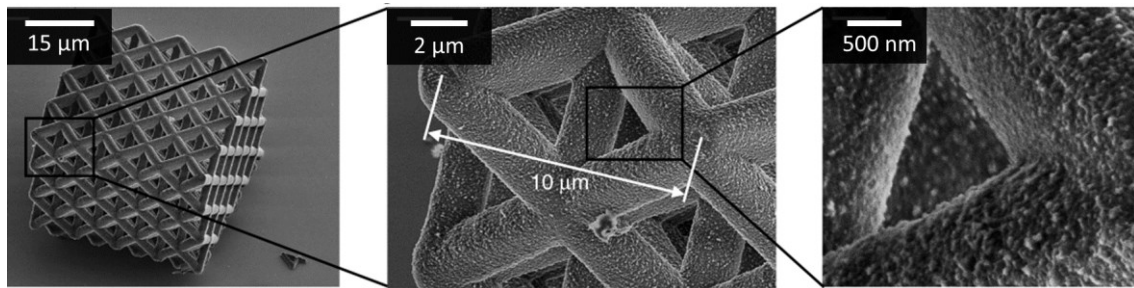


Figure 25 | Nickel octet truss nanolattice material at increasing magnifications. (Adapted from [269] which was published under a CC BY license)

2.3.3. Meta-crystals

Meta-crystals are also a special class of architected lattice materials, designed to overcome one of the biggest weaknesses of stretching-dominated structures. That is, high-strength stretching-dominated lattice materials exhibit much more localised deformations compared to bending-dominated lattice materials [262]. Struts in stretching-dominated structures are subjected to compressive and tensile loads rather than bending, which often leads to buckling failure. Once a critical stress is reached, buckling failure occurs on specific planes and directions depending on the lattice topology and the loading direction, and corresponds to the sudden loss in strength, as seen in the compressive stress-strain response (Figure 26a). The sudden loss in strength

is highly undesirable as it limits the energy absorption capacity and applicability of the lattice material. The localised deformation and loss in strength can also occur due to localised plastic hinge formation in the strut. After the initial loss in strength, increasing nominal strain leads to successive collapse of other lattice planes, resulting in the serrated post-yield behaviour in the plateau region (Figure 26b). The localised deformation bands were observed to be analogous to the slip behaviour in single-crystal materials (Figure 26c), which also shows similar serrated post-yield stress-strain responses once a critical resolved shear stress is reached.

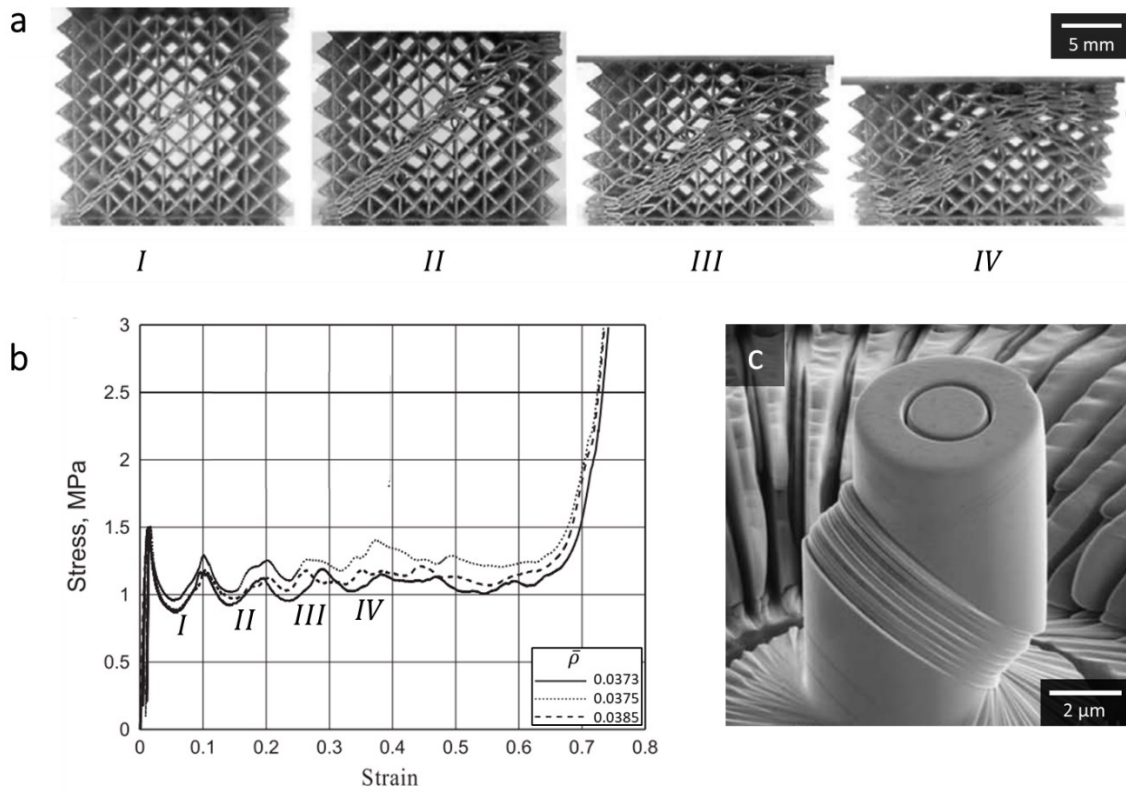


Figure 26 | Analogous deformation behaviours between stretching-dominated lattice materials and single crystal micropillars. a, Formation of localised deformation bands with increasing nominal strain in BCCZ lattice material. **b,** The compressive stress-strain response of lattice material shown in (a) with the corresponding stages of deformation indicated. (Reproduced from [255] with permission from Elsevier). **c,** The compressive deformation behaviour of a single crystal micropillar. (Reproduced from [274] with permission from Elsevier).

With similarities in the deformation behaviour and mechanical response of stretching-dominated lattice materials and single-crystal materials, it was postulated that analogous strengthening features from crystalline materials can also be adopted in the lattice materials' architectures to enhance the strength and eliminate the post-yield

collapse. Such crystal-inspired lattice materials are named meta-crystals. Additionally, metallic meta-crystals contain a fractal structure across length scales: the intrinsic atomic lattice and microstructure of the crystalline material and the architected lattice and polycrystal-like feature of the mesoscale structure (Figure 27). The feasibility and effectiveness of this approach were demonstrated with PLA meta-crystals containing architectures mimicking crystalline features (as discussed in section 2.1.3) such as grain boundaries, precipitate particles, and multiphase microstructures [22]. It was shown that the strengthening features improved the mechanical properties of the meta-crystals, in particular the post-yield behaviour. Reducing the meta-grain (MG) size increases the yield stress while also reducing the magnitude of the initial stress drop. The presence of meta-precipitates also improved the yield stress and the plateau stress, with localised deformation bands bypassing the meta-precipitates. The two-phase meta-crystal with BCC (soft phase) and FCC (hard phase) lattice topologies exhibited similar strengths to strong single-phase FCC lattice materials while improving the toughness thanks to the localised deformation in the BCC phase.

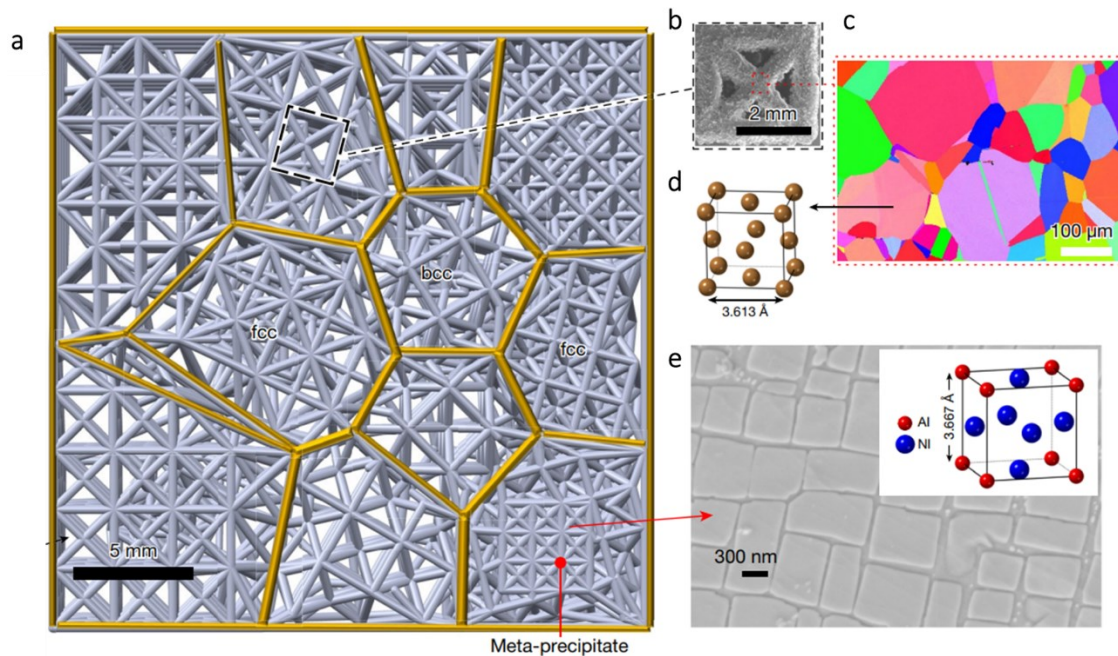


Figure 27 | The hierarchical lattice structure of meta-crystals. **a**, Crystal-inspired lattice architecture with meta-grains, meta-phases, and meta-precipitates. **b**, The FCC uni-cell of the lattice material with **c**, a polycrystalline microstructure and **d**, an intrinsic FCC unit-cell of atoms. **e**, the intrinsic γ/γ' precipitates in nickel superalloys with the unit-cell illustrated in the inset. [22]

2.3.3.1. Polycrystal-inspired lattice materials

Meta-crystals with polycrystal-like architectures are the main focus of the investigations in this thesis and are, therefore, elaborated further in this section. The polycrystal-inspired meta-crystals contain lattice domains of different orientations, each analogous to crystalline grains, called meta-grains (MGs). DIC analysis during compression of a PLA meta-crystal containing 2 MGs showed that the deformation band was deflected at the MG twin boundary, similar to a twinned bicrystal (Figure 28a). It was further shown that with an increasing number of MGs, the localised deformation shear bands became much more shortened and uniformly distributed in the lattice structure (Figure 28c). This led to a Hall-Petch-like relationship [55,56] between the normalised (by $\bar{\rho}$) yield stress and the size of the MG in the lattice material (Figure 28b).

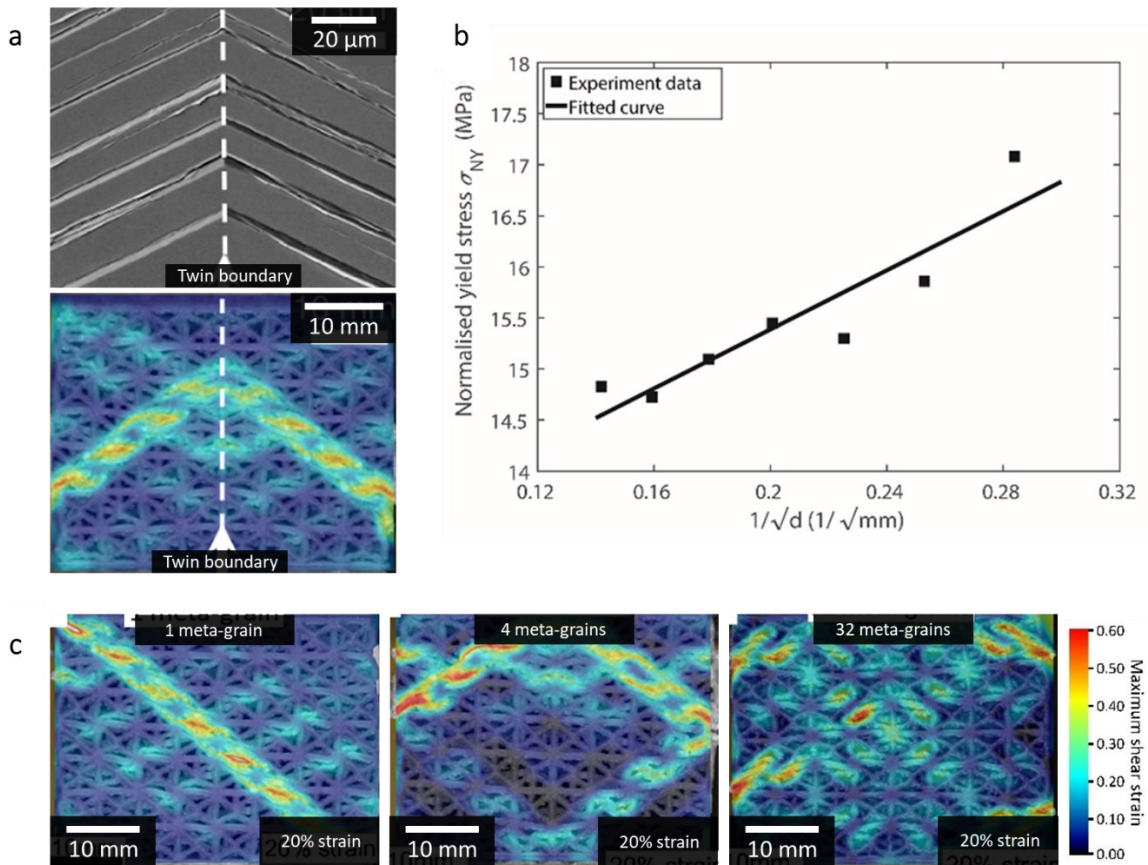


Figure 28 | Compressive deformation response of polycrystal-inspired meta-crystals. a, Deformation of a twinned bicrystal compared to the deformation in a 2 MGs meta-crystal. **b,** The Hall-Petch-like relationship between the normalised yield stress and the size of the MG. **c,** Homogenisation of deformation with an increasing number of MGs. (Micrograph of the twinned bicrystal reproduced from [275] with permission from Elsevier)

The location and the orientation of the deformation band depend on the lattice topology and the loading direction [276]. In 1 MG FCC meta-crystals (i.e., no strengthening architecture), shearing is governed by the buckling of $\langle 001 \rangle$ struts and, therefore, the strength varies depending on the unit-cell orientation with respect to the loading direction, similar to the orientation-dependent slip behaviour in crystalline materials. With additional MGs, the strength of the meta-crystal is also governed by the type of the MG boundary. The type of the MG boundary (e.g., twist or tilt) correlates to its coherency (i.e., the number of connecting struts). This directly relates to the strength of the boundary and its effectiveness in impeding and deflecting the localised deformation bands [276].

2.4. Conclusions

Lattice materials are widely researched due to their excellent and tailorable specific properties. The mechanical properties of lattice materials are continually improving thanks to advances in AM, enabling more intricate geometries to be fabricated with fewer processing defects. Numerous studies have investigated a wide range of lattice materials, providing a comprehensive understanding of the variables affecting their mechanical properties. This includes the influences of the microstructure, the processing defects, the lattice parameters, and the loading conditions.

Meta-crystals are lattice materials with architectures mimicking strengthening features from crystalline materials such as precipitates and grains. Meta-crystals are designed to overcome the trade-off between strength and mechanical stability common in architected lattice materials by distributing the localised deformation bands, which was demonstrated to be effective using PLA meta-crystals. However, the eventual aim to implement meta-crystals in real-world applications necessitates the investigation of metallic meta-crystals. While traditional lattice materials have been investigated with different metallic base materials, it is still unclear how the meta-crystals will behave with different base material properties and with the presence PBF-specific processing defects. It is important to understand how such variables affect the mesoscale deformation in meta-crystals and, consequently, affect the strengthening mechanisms of the polycrystal-

like architecture. Additionally, metallic meta-crystals contain a hierarchical lattice structure with fractal-like strengthening features. This presents an exciting opportunity for optimisation of all strengthening features, and potentially achieve synergistic strengthening across length scales.

Chapter 3

Experimental and Analytical Methods

3.1. Polycrystal-inspired meta-crystal design

As discussed in §2.3, grain boundaries play two roles in polycrystals, both relating to acting as barriers to dislocation slip. Firstly, compatible deformation in polycrystals requires activation of different slip systems in different grains, increasing the plastic deformation resistance. Secondly, the internal stress built up from dislocation pile-ups at boundaries to initiate new slip in ‘harder’ grains means that there is an empirical relationship between grain size and yield stress for a given volume, specifically smaller grains increase the plastic yield resistance as described by the Hall-Petch relationship.

To study the effect of the size of meta-grains only, the meta-crystals were designed such that all lattice orientations in meta-grain domains were inclined at the same angle with respect to the loading direction, and only the size of meta-grains was varied. This removes any variation in strengths due to the mechanical anisotropy of differently-oriented lattice domains, which is analogous to the variation in the stress required to activate different slip systems in different grains. As such, the main strengthening mechanism mimicked in the polycrystal-like architecture is the meta-grain size effect. For this, the meta-crystals in this study all have the same volume, which are cuboid with side lengths of 40 mm, and were divided into 1, 2, 4, 8, 16, 32, and 64 lattice subdomains (named meta-grains or MGs). The partition of the volume into MGs are as shown in Figure 29b (red lines). The MGs were infilled with an FCC-like lattice structure, rotated such that adjacent MGs were misoriented from each other but have the same inclined

angle to the loading direction, Figure 29a. The misorientations were created through a $\pm 45^\circ$ rotation about the global x-axis followed by a $\pm 45^\circ$ rotation about the global y-axis.

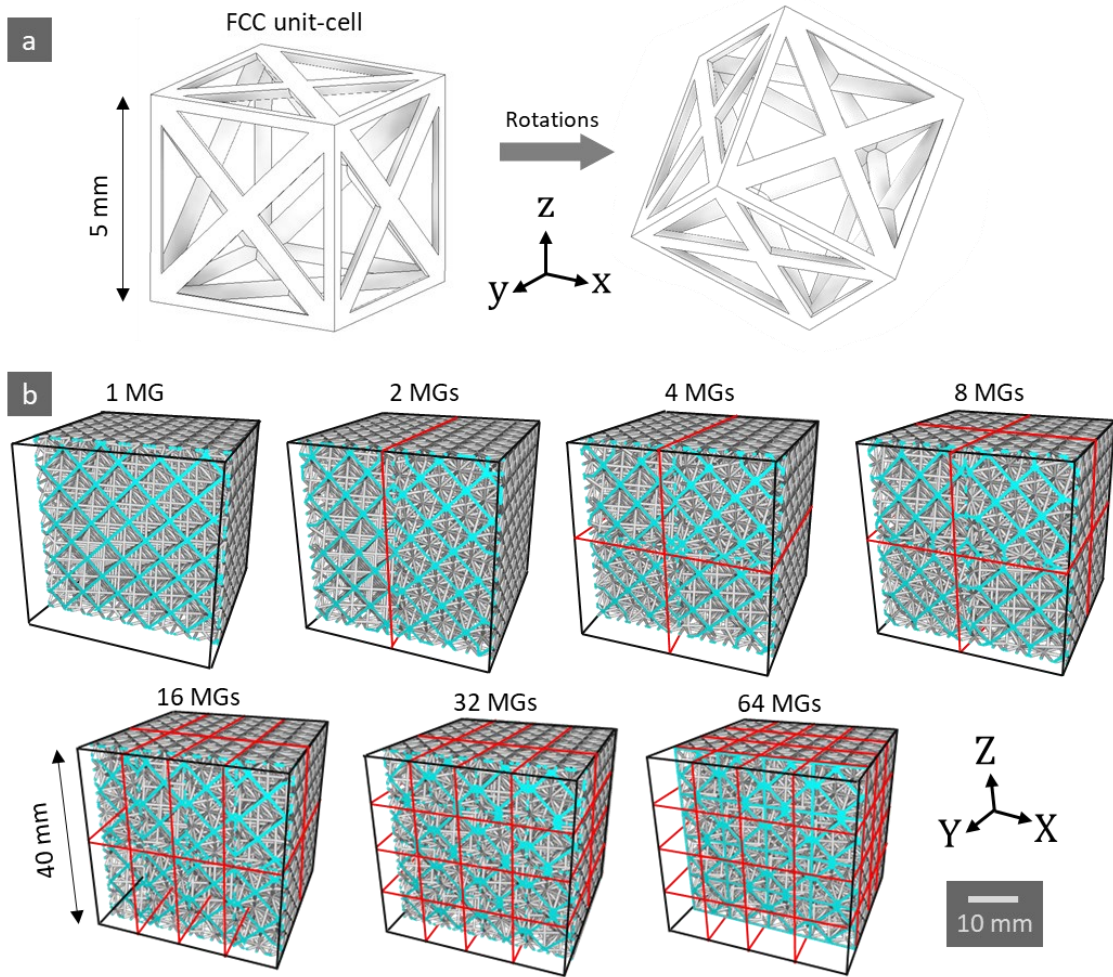


Figure 29 | Polycrystal-inspired meta-crystal architecture. **a**, FCC-like unit cells with 5 mm side lengths rotated about the x and y-axis. All meta-grains are periodically infilled with rotated FCC unit-cells which are similarly inclined to the z-axis (loading direction). **b**, Partition of the lattice volume into 1, 2, 4, 8, 16, 32, and 64 domains. Neighbouring domains are misoriented to each other to create meta-grains.

The infilled FCC unit cell is similar to the octet-truss architecture, a common stretching-dominated topology, which maximises the strength of the architecture. All unit cells have 5 mm edge length and either 0.5 mm or 0.8 mm strut diameters (strut diameter is consistent in each meta-crystal group). Infilling rotated FCC unit cells into cuboidal domains requires ‘trimming’ of struts at the MG boundaries. This creates open struts (struts not supported at the trimmed end). Therefore, a square planar lattice with an edge length of 5 mm encased each MG and acted as ‘attraction’ points for the open struts. The open struts were attracted to the nearest node on the square lattice to remove any

mechanically redundant members. The square lattice was kept in the fabricated samples for added support.

The computer-aided design (CAD) models of the meta-crystals created using the software nTopology Element are as shown in Figure 29b. The models are sectioned to reveal the internal lattice orientations. The size of the MG is represented by the equivalent size (d), which is equal to the diameter of a sphere with the same volume as the MG. All variations of the meta-crystals investigated in this study are shown in Table 3.

Table 3 | Summary of the meta-crystals investigated.

Base material	Number of meta-grains	Strut diameter (mm)	Unit-cell dimensions (mm)	Lattice dimensions (mm)	Post-processing
316L	1, 2, 4, 8	0.8	5x5x5	40x40x40	None
Ti-6Al-4V	1, 2, 4, 8, 16, 32, 64	0.5			None
	1, 2, 4, 8, 16, 32, 64	0.5			Annealed
	1, 2, 4, 8, 16, 32, 64	0.8			None
	1, 2, 4, 8, 16, 32, 64	0.8			Annealed
IN718	1, 2, 4, 8, 16, 32	0.8			None
	1, 2, 4, 8	0.8			Solution annealed + Aged

3.2. Sample fabrication and post-processing

3.2.1. Meta-crystals fabrication

316L stainless steel, Ti-6Al-4V, and IN718 meta-crystals were fabricated using pre-alloyed powders via laser powder bed fusion (L-PBF). Imperial College London and Betatype Ltd. fabricated the 316L and Ti-6Al-4V meta-crystals, respectively, using the Renishaw AM250 printer. Additive Laser Technologies fabricated the IN718 meta-crystals using an ALT Alfa-150 printer. Table 4 summarises the relevant processing parameters used for each base material. The printing parameters were selected to ensure a high print quality based on previous optimisations of the alloy and the geometry of the meta-crystals. The 316L and IN718 meta-crystals were built parallel to the loading

direction, while the Ti-6Al-4V meta-crystals were rotated to minimise overhanging struts. Ti-6Al-4V meta-crystals with 0.5 mm strut diameters are shown in Figure 30.

Table 4 | L-PBF processing parameters for 316L, Ti-6Al-4V, IN718 meta-crystals. Nb. “-” indicates not applicable.

Base Material	Region	Printing Parameters								
		Spot Size (μm)	Layer Thickness (μm)	Count	Power (W)	Point Distance (μm)	Exposure Time (ms)	Scan Velocity (mm/s)	Hatch Spacing (μm)	Layer Rotation (°)
316L	Borders	70	50	2	110	60	100	600	100	-
	Infill			-	200	60	80	750	110	67
	Upskin			1	160	50	110	455	110	-
	Downskin			1	100	40	80	500	60	-
IN718	Borders	125	50	1	180	-	-	500	100	-
	Infill			-	200	-	-	1000	100	67
	Upskin			1	200	-	-	1100	90	-
	Downskin			3	150	-	-	1000	80	-
Ti-6Al-4V	Borders	75	60	4	160	20	30	667	10	-
	Infill			-	200	60	70	857	95	67
	Upskin			1	200	90	100	900	65	-
	Downskin			1	175	75	50	1500	65	-

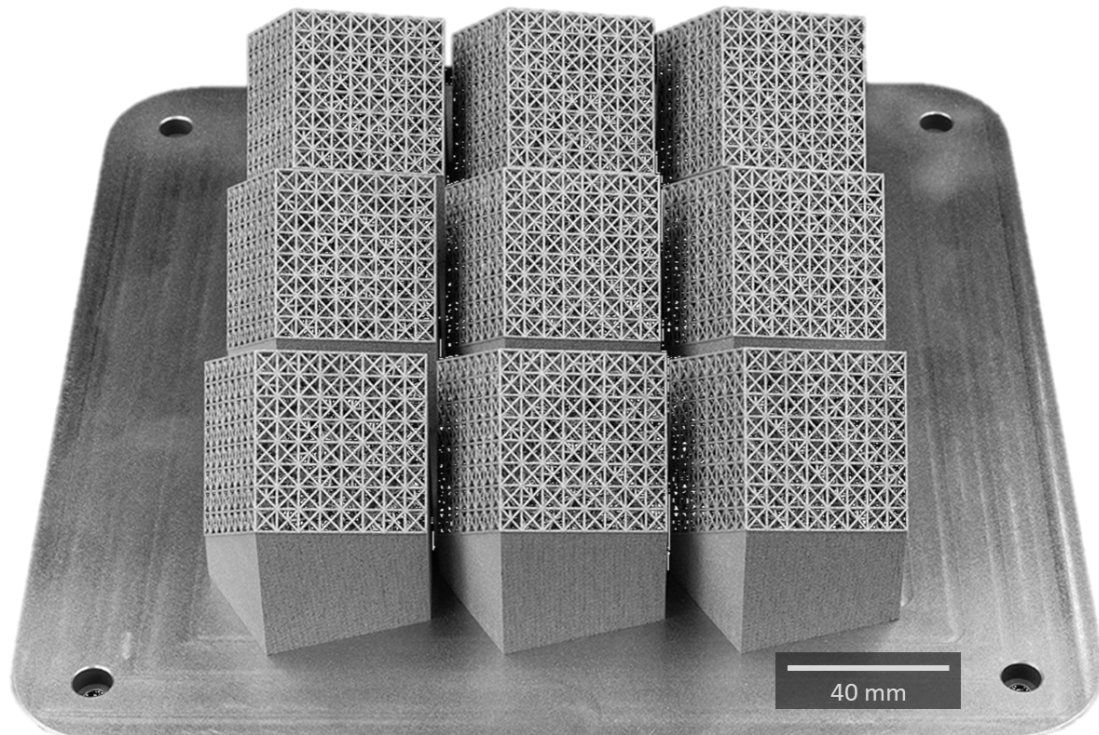


Figure 30 | Ti-6Al-4V meta-crystals with 0.5 mm strut diameter fabricated via L-PBF. Courtesy of Betatype Ltd.

3.2.2. Heat-treatments

While there was no heat treatment done for 316L meta-crystals because the alloy is not precipitation-hardenable and has excellent ductility in the LPBF condition [277,278] , selected Ti-6Al-4V and IN718 meta-crystals underwent heat treatments (Table 3). The purposes of the heat treatments differed for the base materials. The annealing heat treatment aimed to relieve internal stresses and increase the ductility of the Ti-6Al-4V meta-crystals, while the solution annealing and ageing heat treatment aimed to increase the yield and UTS of the IN718 meta-crystals via precipitation hardening. The heat treatment procedures are as follows:

Ti-6Al-4V

The heat treatments of the Ti-6Al-4V meta-crystals were conducted inside a vacuum furnace to minimise oxidation. The procedure began with heating at a rate of 20°C/min, followed by dwelling at 1050°C (above the β -transus temperature) for 2 hrs to homogenise the microstructure, and ends with furnace cooling under vacuum [259,279].

IN718

This heat treatment is based on the modified procedure proposed by Gallmeyer for IN718 parts fabricated via L-PBF [179]. The procedure consisted of two stages and was conducted in Ar atmosphere to minimise oxidation. Firstly, the meta-crystals were solution treated at 1020°C for 15 minutes to dissolve unwanted phases but retain the solidification substructure. This was followed by water quenching and ageing at 720°C for 24 hours to precipitate strengthening γ' and γ'' phases. The samples were air-cooled afterwards.

3.3. Mechanical testing and analysis

3.3.1. Tensile testing of bulk specimens

IN718 dogbone specimens were tensile tested at room temperature using Instron TTDL 5004 at a strain rate of 10^{-3} s^{-1} following ISO 189201 standards. DIC analysis using the

software GOM Correlate was used for strain measurement. The test were conducted on 18 samples with 70 mm gauge length and 8 mm gauge diameter. The samples were fabricated with an additional 1 mm to the diameter, which was removed via machining prior to testing.

3.3.2. Compression behaviour of meta-crystals

3.3.2.1. Quasi-static compression testing

The deformation behaviour of the meta-crystals were characterised via quasi-static compression tests. With the exception of the heat-treated IN718 meta-crystals due to their high strength, all tests were conducted using an Instron 6620 universal testing machine equipped with a 250 kN load cell. The heat-treated IN718 meta-crystals tests were conducted using in an Instron 8806 equipped with a 2.5 MN load cell. All tests were conducted at a strain rate of 10^{-3} s^{-1} along the global Z-direction of the meta-crystals. Castrol multipurpose high-temperature grease was applied between the steel compression platens and the meta-crystals to reduce friction. A schematic representation of the test rig is shown in Figure 31.

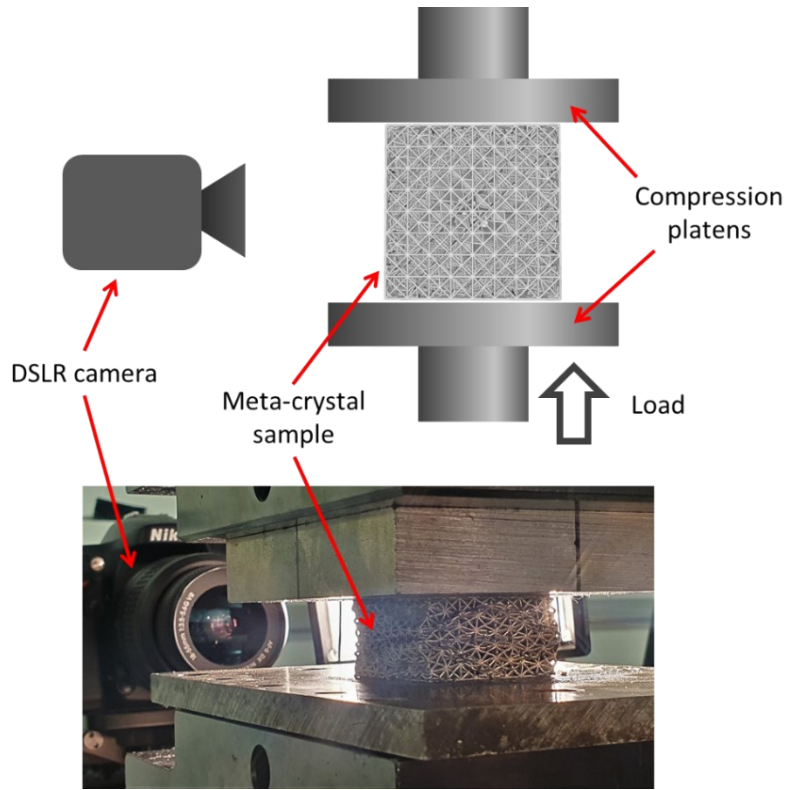


Figure 31 | Quasi-static compression test rig with DSLR camera set-up for DIC analysis.

3.3.2.2. Analysis of the mechanical data

For stress calculations, the load data obtained via the load cell was divided by the global contact area of the meta-crystals (measured using Vernier callipers). All stresses reported are then normalised by the measured relative density, $\bar{\rho}$, of the meta-crystals unless stated otherwise. The measured $\bar{\rho}$ of each meta-crystal was calculated from its nominal volume (measured using Vernier callipers), its mass (measured using a digital scale with an accuracy of 0.01 g), and the density of the base material (taken from literature: Ti-6Al-4V [280], IN718 [281], 316L [282]), as opposed to the theoretical $\bar{\rho}$ which is determined from the CAD models. All of the measurement values used are the average of three repeated measurements.

A MATLAB script was created to calculate the elastic modulus, yield stress, peak stress, stress drop percentage, stress drop magnitude, energy absorption capacity using the stress-strain data (Appendix A). The properties are defined as shown in Figure 32.

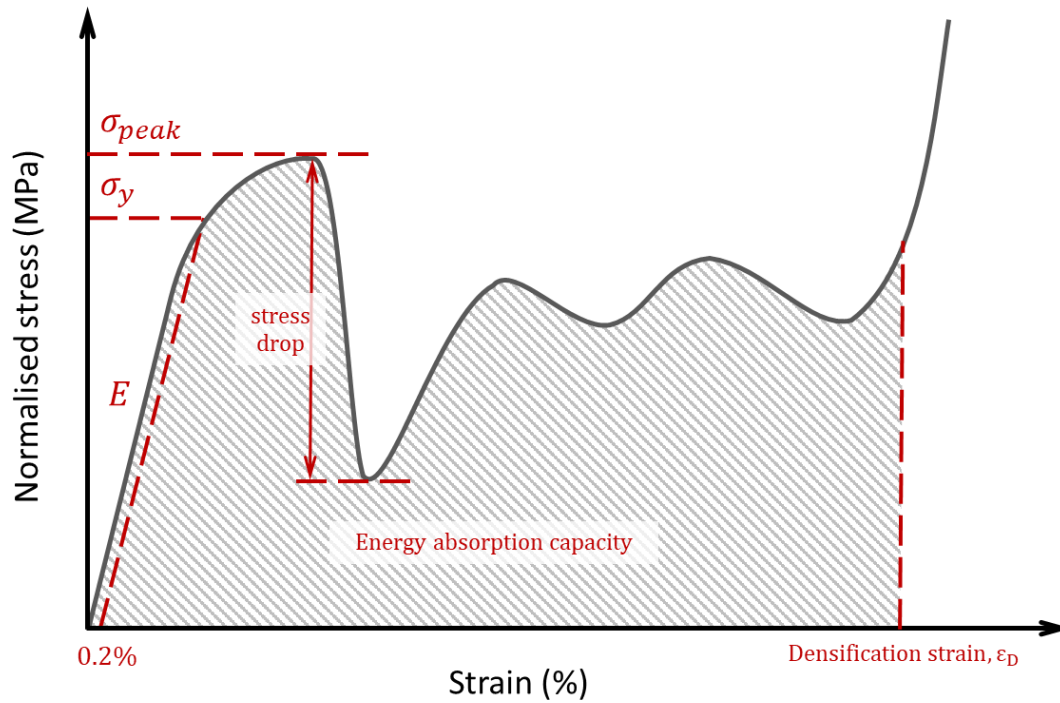


Figure 32 | Typical compressive stress-strain response of stretching-dominated lattice materials with key properties defined.

3.3.2.3. Digital image correlation (DIC)

A Nikon DSLR camera captured the surface deformation behaviour of the meta-crystals during the compression test in 1-second intervals. The deformation field was analysed by digital image correlation (DIC) using the software DaVis. A subset with a size of 101 x 101 pixels (equivalent to 0.39 mm², or approximately 1-2 pixels per strut diameter) was used to analyse the images sized 6000 x 4000 pixels (pixel size of 3.89 μ m) with a step size of 25 pixels.

3.3.3. Hardness testing of meta-crystals

Hardness measurements were taken for all samples. Measurements were taken at the cross-section of the samples, revealed by planar grinding. A Buehler Wilson VH1202 hardness testing machine was used to obtain the Vickers hardness at a load of 1 kg and an indentation time of 10 s. Six measurements were taken in each of the node and strut regions sectioned parallel and perpendicular to the build direction for as-printed and heat-treated meta-crystals.

3.3.4. Finite element modelling

The compressive behaviours of meta-crystals were modelled by finite element (FE) analysis using the Abaqus/Explicit solver. The beam models were imported into Abaqus CAE as a wire part, on which a circular section was applied. The parts were meshed with beam elements (B31), <001> struts contained five elements and $\frac{1}{2}$ <101> struts contained three elements. A smooth-step displacement controlled boundary condition (BC) was applied on a reference point that is tied (multi-point constraint, MPC) to the nodes on the top surface of the models. The nodes on the bottom surface were also tied (MPC) to a reference point that was held stationary using an encastre BC. Interactions were specified using the general contact with no friction and 'hard' contact. The material behaviour was approximated with an elastic-plastic bi-linear curve using tensile data obtained from the bulk specimen. A mass scaling factor of 64 was applied to the models.

3.3.5. ThermoCalc

Precipitation module TC-Prisma using thermodynamic TCNI8 and mobility MOBNI2 databases was used to investigate the evolution of γ' , γ'' , δ , and Laves phases during heat treatment of IN718. Following the solution annealing, the heat treatment simulations were performed in non-isothermal mode, assuming a disordered FCC (A1) matrix. γ' and γ'' were assumed to form in the bulk of the sample, while δ and Laves phases were set to form at the grain boundaries.

To best approximate the simulation conditions of the as-printed samples, EBSD results for the grain analysis of parallel section were used, with an average grain size of 56 μm and an aspect ratio of 3.6. The dislocation density in the matrix was set to $0.86 \times 10^{14} \text{m}^{-2}$, obtained from measurements of LPBF manufactured IN718 after annealing [179].

3.4. Characterisation and analysis

3.4.1. X-ray computed tomography (x-CT)

Ti-6Al-4V and IN719 meta-crystals were x-CT scanned at the National History Museum in London to study the quality of internal lattice struts, including the internal porosity. The x-CT scan parameters were 210 kV and 10W with 1 second exposure, 8-frame averaging and 1 mm of tin for filtration. The Ti-6Al-4V meta-crystals were scanned prior to testing at two magnifications, with voxel resolutions of 30 μm and 10 μm . The 30 μm scan captured the entire meta-crystal while the 10 μm captured a small section in more detail. The IN718 meta-crystals were scanned before and after testing with a voxel resolution was 22 μm .

3.4.1.1. Analysis of x-CT data

The print quality was quantified from the x-CT tomographic data using ImageJ, which included measuring the consolidated volume, pores, surface roughness, and strut diameter. For consistency, the same image processing procedure was followed in ImageJ. This included creating a *substack* of relevant images, *cropping* relevant areas, adjusting *brightness* and *contrast*, *thresholding*, converting to *binary*, and *despeckling* to remove noise. Converting to binary allows the area of the image representing consolidated volume and the internal porosity to be calculated using the *Analyze Particles* function, the data from which was extracted and processed in Excel. A simple macro was written to iteratively process every image in the stack. To calculate the surface roughness, cropped cross-sectional images of struts parallel, perpendicular, and at 45° to the build direction were processed using the plug-in *analyze_stripes* [283]. The extracted data were again processed in Excel to give the mean roughness, R_a , and the root mean squared roughness, R_q . Finally, to calculate the strut diameter, the strut outline and centre of mass data was extracted from cropped cross-sectional images of struts parallel, perpendicular, and at 45° to the build direction. A MATLAB script (Appendix A) was created to analyse the extracted data to give the minimum, mean, and

maximum diameter along its axis (only the mean diameter for struts perpendicular to the build direction).

3.4.2. Microstructure characterisation and analysis

3.4.2.1. Sample preparation

The specifics of the sample preparation procedure for microstructural characterisation depended on the base material, the characterisation technique, and the aim of the investigation. Detailed summary of the procedures used for scanning electron microscopy (SEM) and electron backscatter diffraction (EBSD) is shown in Table 3. For all procedures, the samples were mounted in Technovit 5071 dissolvable cold mount resin to avoid damaging the samples' struts. The resin was dissolved after the grinding and polishing procedure with acetone in an ultrasonic cleaner for 1-3 hrs.

Table 5 | Sample preparation procedures for 316L, Ti-6Al-4V, and IN718 lattice materials for microstructure characterisation. Follow procedure for the grinding and polishing sequentially in descending order.

Material	Grinding			Polishing			Etching	Comments
	SiC Grit	Force (N)	Time (s)	Sol.	Force (N)	Time (min)		
316L	600	15	60 x 2	OP-S Water	10 10	30 5	None	Same procedure for SEM and EBSD.
	800	15	Until plane					
	1200	10	60					
	2000	10	60					
	4000	10	60					
Ti-6Al-4V	600	15	90 x 2	OP-S* Water	15 15	20 5	Kroll's reagent, 10 seconds	For EBSD of as-printed samples, alternate between polishing and etching 6 times.
	800	15	Until plane					
	1200	15	60 x 2					
	2000	15	60 x 2					
	4000	15	60 x 2					
IN718	600	10	60 x 2	OP-S Water	5 5	40 5	Kalling's reagent, 40 seconds	Etching required only to reveal cellular substructure in SEM. Not required for EBSD.
	800	10	Until plane					
	1200	5	60 x 2					
	2000	5	60 x 2					
	4000	5	60 x 2					

SiC papers and Struers MD-Chem pads were used for grinding and polishing. Substantial grinding was done to remove sectioning damage. After fine grinding, samples were inspected under the optical microscope for large scratches. The grinding

process was repeated from 1200 grit onwards if the samples were deemed unacceptable. The OP-S solution (0.25 μm colloidal silica) used to polish Ti-6Al-4V samples required a chemical-mechanical polish and, therefore, the OP-S solution (denoted with an asterisk *) was mixed with H_2O_2 and H_2O (in the ratio of 7:3:10 by vol. OP-S: H_2O_2 : H_2O). The grinding and polishing times varied slightly depending on the number of samples and the relative surface area of the lattice material exposed. The Ti-6Al-4V samples were etched using Kroll's reagent (92:5:3 by vol. of H_2O :HF: HNO_3) by immersion for 10 seconds whereas the IN718 samples were etched using Kalling's reagents (1:20:20 by vol. CuCl_3 : HCl: $\text{C}_2\text{H}_6\text{O}$) by swabbing for 40 seconds.

Thin foils for TEM were prepared by twin-jet electropolishing in a solution of 10 % perchloric acid in methanol applying 20 kV at -5 °C with a Struers TenuPol-5.

3.4.2.2. Microscopy

Scanning Electron Microscope (SEM)

SEM micrographs were captured by secondary electron imaging using a Zeiss Gemini Sigma300 FEG SEM system with an accelerating voltage of 5 and 10 keV, and an aperture size of 30 μm . The chemical composition was measured using electron dispersive x-ray spectroscopy (EDX) detector.

Electron backscatter diffraction (EBSD) maps were acquired using a Bruker Argus high-definition backscatter detector. An accelerating voltage of 20 keV with an aperture size of 120 μm and a pixel size ranging between 0.1-0.5 μm were used. GND analyses were performed on selected EBSD maps using the Adaptive Domain Misorientation Approach in MATLAB [284]

Transmission electron microscopy (TEM)

TEM investigations were carried out using a Jeol JEM-2100F microscope operating at 200 kV. The EDX line scan was obtained in Jeol 2100F using Oxford Instrument EDX detector for with 1 million counts.

Chapter 4

Influence of Processing Defects

4.1. Introduction

This chapter explores the significance of the processing defects on the mechanical behaviour of polycrystal-inspired meta-crystals. For this, Ti-6Al-4V meta-crystals fabricated via L-PBF were investigated, as the effect of defects will be amplified by the low elongation to failure of the base material. Additionally, Ti-6Al-4V is one of the most widely used titanium alloys today due to its excellent properties and good producibility [285]. Investigation of defects in Ti-6Al-4V parts have shown that the surface roughness is the most detrimental to the mechanical performance, particularly the fatigue performance [286]. While defects can be minimised by optimising the processing parameters [161], it remains challenging to fabricate metallic parts with intricate structures. Such challenges may limit the contributions from the architecture and the intrinsic microstructure of the base material.

Titanium is an allotropic material with an α -HCP phase at room temperature and a β -BCC phase above the transus. Ti-6Al-4V is an $\alpha+\beta$ titanium alloy that has good corrosion resistance and significantly higher strength than commercially pure titanium. Ti-6Al-4V is classically used in airframes and aerospace engines, due to its excellent specific properties, though it has more recently found applications in dental and orthopaedic implants as well due to its biocompatibility [287–289].

Typically, three main microstructures can be obtained in Ti-6Al-4V depending on the thermo-mechanical processing method: fully equiaxed, fully lamellar, and bi-modal

(mixed of equiaxed α and lamellar $\alpha+\beta$). Within the fully lamellar type, the microstructure varies greatly with the cooling rate from above the β transus (975-995 °C depending on the grade of the alloy). At low cooling rates, nucleation and growth of α lamellae from the β boundary form colonies within the prior β grains. The lamellae become finer as the cooling rate increases. Additional nucleation occurs at existing α plates and grows perpendicularly to that plate to form the basketweave or the Widmanstätten structure. At very high cooling rates, as in L-PBF, diffusionless transformation occurs to form acicular α' martensites, which is a very fine needle-like microstructure. [285,290,291]

Ti-6Al-4V alloy processed via L-PBF have been extensively investigated. Studies reported that as-printed Ti-6Al-4V shows comparable or superior strengths to wrought and HIPped parts, but inferior ductility [292–294]. This is attributed to the acicular α' martensitic microstructure of as-printed Ti-6Al-4V. In between the α' laths are limited amounts of the remaining prior- β grains, which can be seen to be large columnar grains prior to the transformation. This typical as-printed microstructure can be avoided in-situ with modifications to the processing parameters. A study obtained lamella and equiaxed $\alpha+\beta$ microstructures by increasing the laser/material interaction time, leading to improved ductility but lower strengths [168]. A different study obtained an ultra-fine $\alpha+\beta$ microstructure (through decomposition of the α' martensite) by tuning the layer thickness, focal offset distance, and the energy density, resulting in improved ductility and high strengths [290]. Alternatively, post-processing heat treatments can also obtain the $\alpha+\beta$ microstructure [178,295].

Meta-crystals fabricated from Ti-6Al-4V contain a hierarchical lattice structure: the atomic lattice types of BCC (body-centred cubic, β) and HCP (hexagonal close-packed, α' or α) structures, crystalline polygrain microstructure, and architected lattice of face-centred cubic (FCC) and polygrain-like mesostructures. The compressive behaviours of the as-printed meta-crystals were investigated before varying the intrinsic crystalline microstructure and strut diameters to minimise the effects of the processing defects. Firstly, heat treatment was used to alter the crystalline microstructure from α' to ($\alpha+\beta$), reducing the internal stresses and increasing the elongation to failure of the base

material. Secondly, the study increased the strut diameter from 0.5 to 0.8 mm to reduce the stress concentration from the defects. Finally, both methods were applied simultaneously to investigate their combined effects. The study discusses how the measures effectively enabled the crystal-inspired approach to design damage-tolerant Ti-6Al-4V meta-crystals.

4.2. Experimental procedure

Four sets of polycrystal-like meta-crystals with 1, 2, 4, 8, 16, 32, and 64 MGs were fabricated (section 3.2.1). Each set differed by strut diameter and post-processing treatment, specifically: 0.5 mm/as-printed, 0.5 mm/annealed, 0.8 mm/as-printed, and 0.8 mm/annealed. The as-printed meta-crystals were characterised by x-CT (section 3.4.1) prior to mechanical testing. Heat treatments were conducted in a vacuum furnace (section 3.2.2). Mechanical behaviours of the meta-crystals were investigated via quasi-static compression tests with DIC analyses (sections 3.3.2.1 and 3.3.2.3), one compression test was conducted on each meta-crystal set. Following the mechanical testing, the meso- and microstructure of the meta-crystals were characterised by electron microscopy, via SE imaging and EBSD analysis. The fracture surfaces of the struts were also captured in the SEM (section 3.4.2).

4.3. Results

4.3.1. Printing quality: geometric accuracy and internal defects

Figure 33 shows the difference between the measured and theoretical $\bar{\rho}$ of the as-printed meta-crystals. The difference provides an indication of the print quality of the lattice material: the higher the difference, the lower the print quality. Tomographic and microscopic observations revealed that deviations from the theoretical relative density resulted mainly from the geometric inaccuracy from the design and surface defects (Figure 34c and d). There were negligible differences between the as-printed and the annealed meta-crystals since no change in shape occurred during the heat treatment.

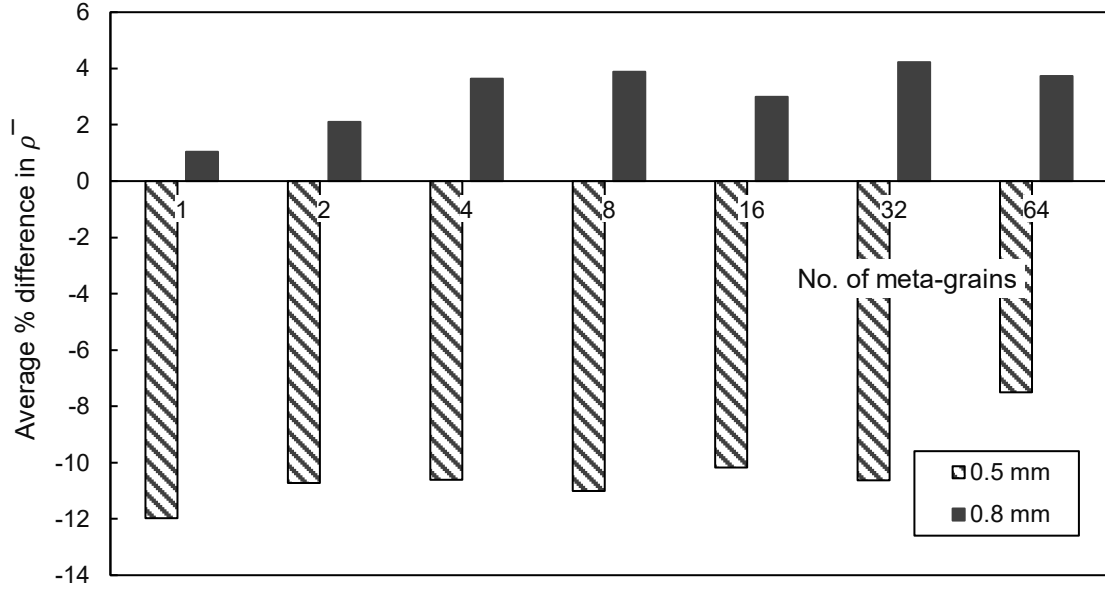


Figure 33 | The average percentage difference in the theoretically calculated and the measured relative density ($\bar{\rho}$) for all as-print meta-crystals with 0.5 and 0.8 mm strut diameters.

Figure 33 suggests that the print quality of the meta-crystals with 0.8 mm diameter struts was better than those with 0.5 mm diameter struts, as the absolute difference between the $\bar{\rho}$ is smaller. This was corroborated by representative micrographs of the 0.5 and 0.8 mm diameter struts in Figure 34a and b, where the porosity, the surface roughness, and the geometrical deviations of the two strut diameters are clearly distinctive. The quantity of internal pores is much higher for the smaller diameter struts in both the node and the strut regions. Figure 34a and b revealed that most of the pores observed are non-spherical lack-of-fusion pores, which also appears to be the cause of the high surface roughness (lack-of-fusion occurs at the surface of the struts). The 0.5 mm struts also showed a much more irregular surface, sharp notches on the free surface, and large deviations in the diameter (from the nominal dimension) along the length of the strut. Such notch-like defects are stress concentrators and can significantly weaken the struts. The decrease in the roughness with an increase in strut diameter was consistent with the findings reported elsewhere [296]. There were no clear trends in the quality of prints with increasing numbers of MGs.

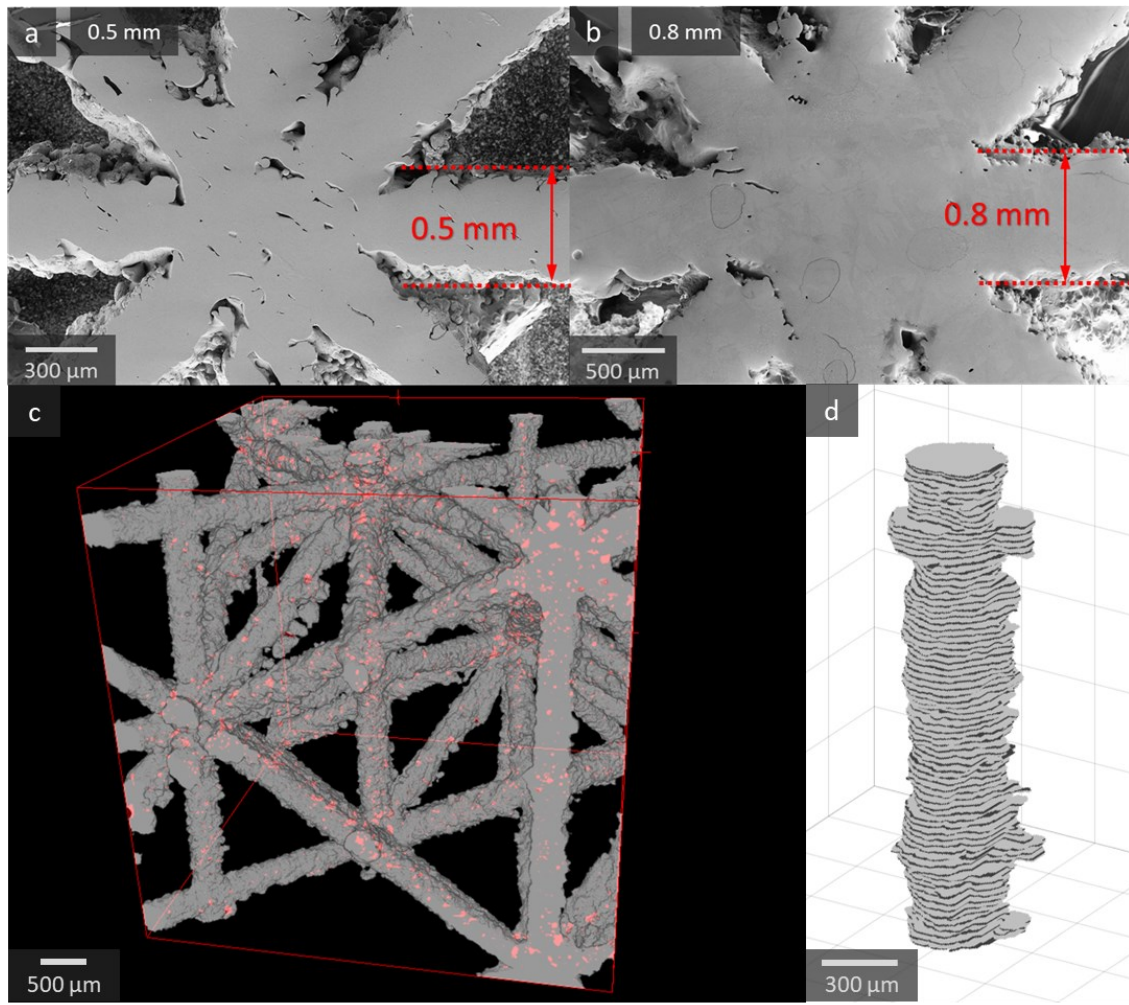


Figure 34 | Internal processing defects in meta-crystals. **a, b,** SEM micrographs showing a longitudinal section of the 0.5 mm and 0.8 mm diameter struts with the red dotted lines depicting designed strut diameter for comparison. **c, d,** 3D reconstruction of x-CT data for analysis of internal pores (highlighted in red) and the variation in strut cross-section.

x-CT scans were acquired for further quantification of the defects (particularly internal pores). Only meta-crystals with 0.5 mm diameter struts were scanned due to their higher density of defects. As with the previous analysis of the $\bar{\rho}$, the x-CT data also revealed a similar difference between the theoretical and actual volume of the lattice, consistent with the observations shown in Figure 33. Compared to the theoretical volume from the computer models, the real volume was approximately 24% smaller. To obtain more details, the x-CT data of some struts were analysed at a higher resolution. The volumes of randomly selected struts measured from the x-CT data were consistently less than the theoretical volumes by 21.5% on average, approximately double the difference given by

the measured $\bar{\rho}$ but slightly smaller than the overall difference determined from the x-CT data of the entire structure. The latter suggests that the volume of the struts was less than the design, while the volume of nodes was greater than the design. This is also seen in the SEM images in Figure 34a and b which shows oversized nodes. The oversized nodes are likely caused by adjacent struts overlapping at the intersection and, therefore, increasing the strut diameter leads to more overlaps (i.e., larger nodes and shorter strut lengths). In addition to the volume of the struts, the volume of internal pores in the 0.5 mm strut was also calculated from the processed x-CT data (Figure 34c). The average volume fraction of the internal pores is 0.32%, showing little deviations between different MG designs and strut orientations, as the build-direction was not parallel to the global Z-direction. The average minimum diameter of the struts ranged from 0.44 ± 0.04 mm (e.g., Figure 34d).

With failure occurring at the least consolidated area, the SEM images of the fracture surfaces confirm the severity of the reduction in diameter (Figure 35b). Low consolidation was due to lack-of-fusion near the free surface and was the major reason for the failure of struts, especially in smaller diameter struts. Additionally, the faceted fracture surface with tearing ridges and little evidence of ductile microvoids in the as-printed strut indicates fast fracture (Figure 35c), whereas the fracture surface of annealed struts shows more evidence of ductile microvoids dimples (Figure 35d), indicating the annealing was able to regain some ductility. The fracture features in Figure 35d are at a similar scale to the α lamellae in Figure 36b and d suggesting interlamellar fracture.

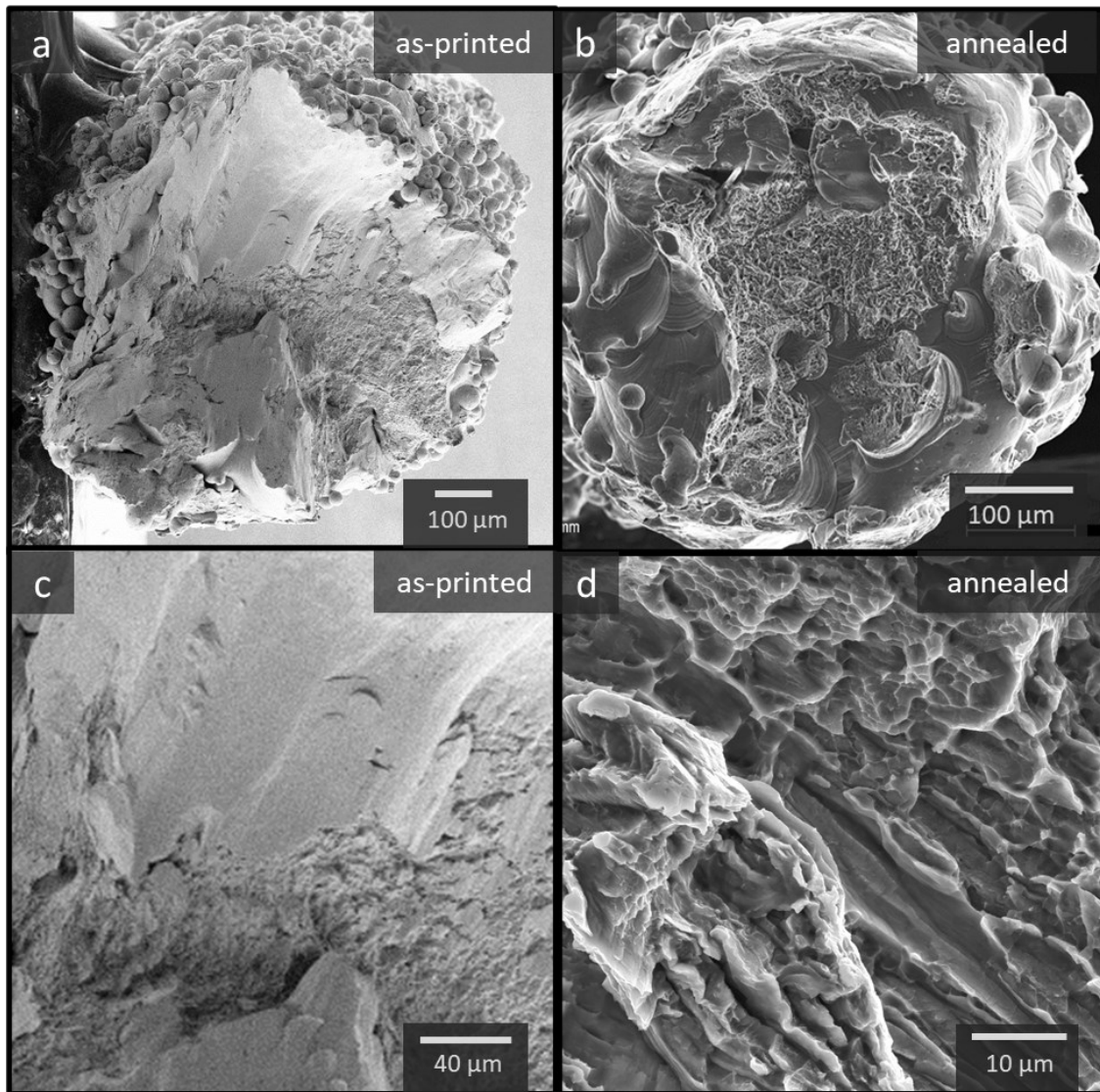


Figure 35 | Fracture surfaces of struts. **a, b**, 0.8 mm/as-printed and 0.5 mm/annealed struts showing low consolidation areas and **c, d**, close-ups of the respective surfaces showing different fracture morphologies.

4.3.2. Microstructure

The microstructure was revealed by chemical etching of sectioned struts from the as-printed and annealed meta-crystals (Figure 36a and b). The as-printed microstructure of Ti-6Al-4V comprises of very fine acicular martensites α' (Figure 36a), consistent with that reported in the literature [259,297]. The α' martensite is responsible for the brittleness of the as-print Ti-6Al-4V. In comparison, the annealed microstructure is much coarser, note the differences in scale (Figure 36a and c versus b and d). The annealing heat treatment dissolved acicular α' martensites and transformed them into β at temperatures above the transus temperature. Upon slow cooling in the vacuum furnace,

β transformed to larger α lamella colonies, leaving small fractions of β between the lamellae (Figure 36b and d). The resulting microstructure can help to regain ductility at the expense of strength. There was no texture observed at the current magnification (Figure 36c and d), however, it is widely reported that the as-printed microstructure is textured with columnar prior- β grains along the build direction [162,290].

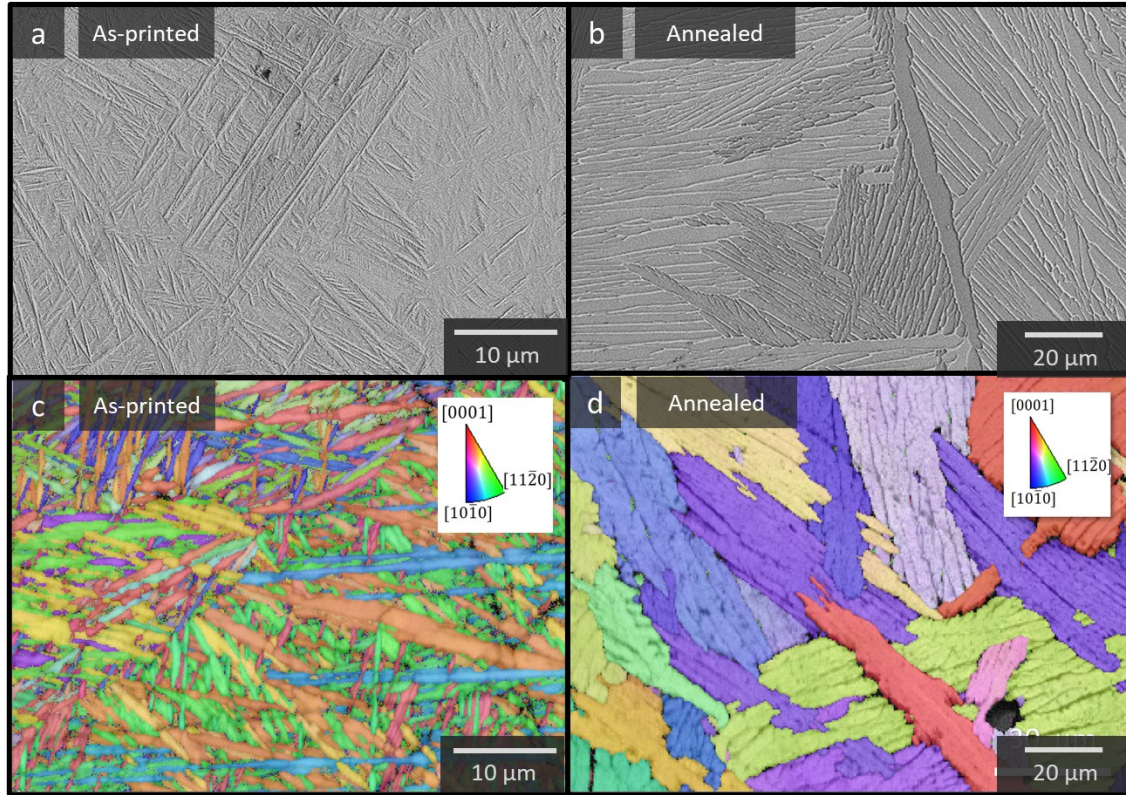


Figure 36 | SEM micrographs and EBSD maps (IPF-build direction/out of page) showing the etched surface of the as-printed and annealed microstructure. a, c, as-printed meta-crystals and b, d, annealed meta-crystals. Nb. the SEM micrographs and EBSD maps are not of the same region.

While there was a clear difference in the microstructure between as-printed and annealed conditions of the same strut diameter, the variation of the strut diameter from 0.5 mm to 0.8 mm did not result in significant differences in the microstructure for both as-printed and annealed conditions. This is similar to the previously reported microstructure of Ti-6Al-4V struts where only a small difference between the lath thickness was observed between the 0.5 and 1 mm sample diameters, although a bigger difference was observed with larger struts [264].

4.3.3. Mechanical properties

The stress-strain curves of the as-printed titanium meta-crystals with 0.5 mm diameter struts are shown in Figure 37a (stress was normalised by the relative density). The 0.5 mm/as-printed meta-crystals shows a slight improvement in the energy absorption capacity with increasing the number of MGs (25% increase from 1 to 64 MGs) (Figure 38) in agreement with a previous study on meta-crystals fabricated by a PLA [22]. Nevertheless, the improvement was insignificant and much less in comparison to PLA meta-crystals. The 0.5 mm/as-printed still exhibited classic stretching-dominated lattice mechanical behaviour: sharp post-yield stress drop and subsequently unstable responses. Increasing the number of MGs did not noticeably improve the strength, nor the post-yield behaviour.

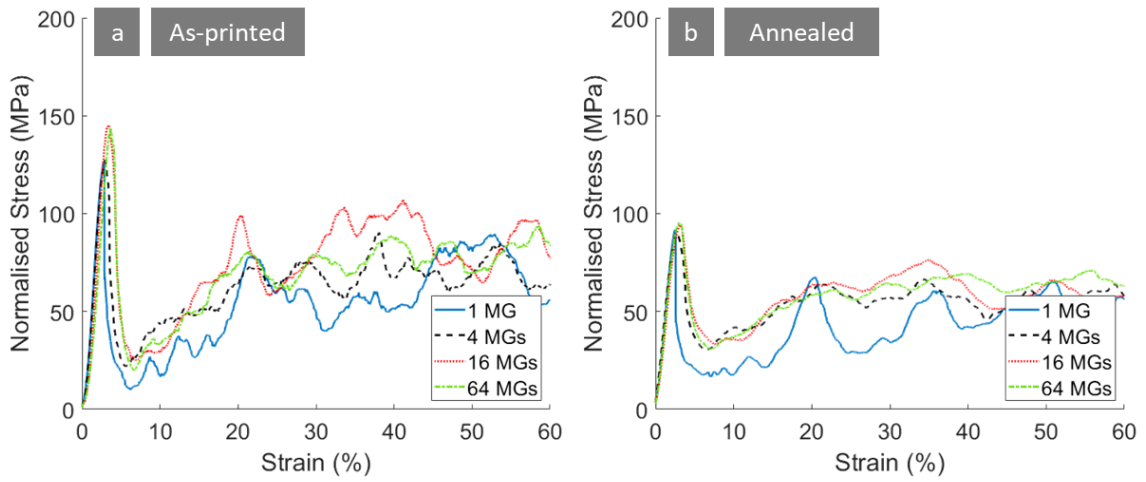


Figure 37 | The normalised stress-strain responses of the 1, 4, 16, 64 MGs Ti-6Al-4V meta-crystals with 0.5 mm strut diameter. a, as-printed and b, annealed meta-crystals.

This lack of significant improvement was also highlighted in the DIC analysis of the deformation (Figure 39), which shows the deformation under increasing compressive strain in the meta-crystals containing 16 MGs. The analysis of the 0.5 mm/as-printed meta-crystal revealed that the MG boundaries did not arrest or deflect the initial localised deformation band, suggesting that the stress concentration induced by the deformation band was too high for the MG boundaries and, therefore, failed to eliminate the initial collapse behaviour of the meta-crystal. The deformation bands also formed on arbitrary planes and orientations in contrast to that predicted previously in [298]. The

unstable response and little hardening in the post-yield behaviour were attributed to the successive crumbling of lattice planes (Figure 39).

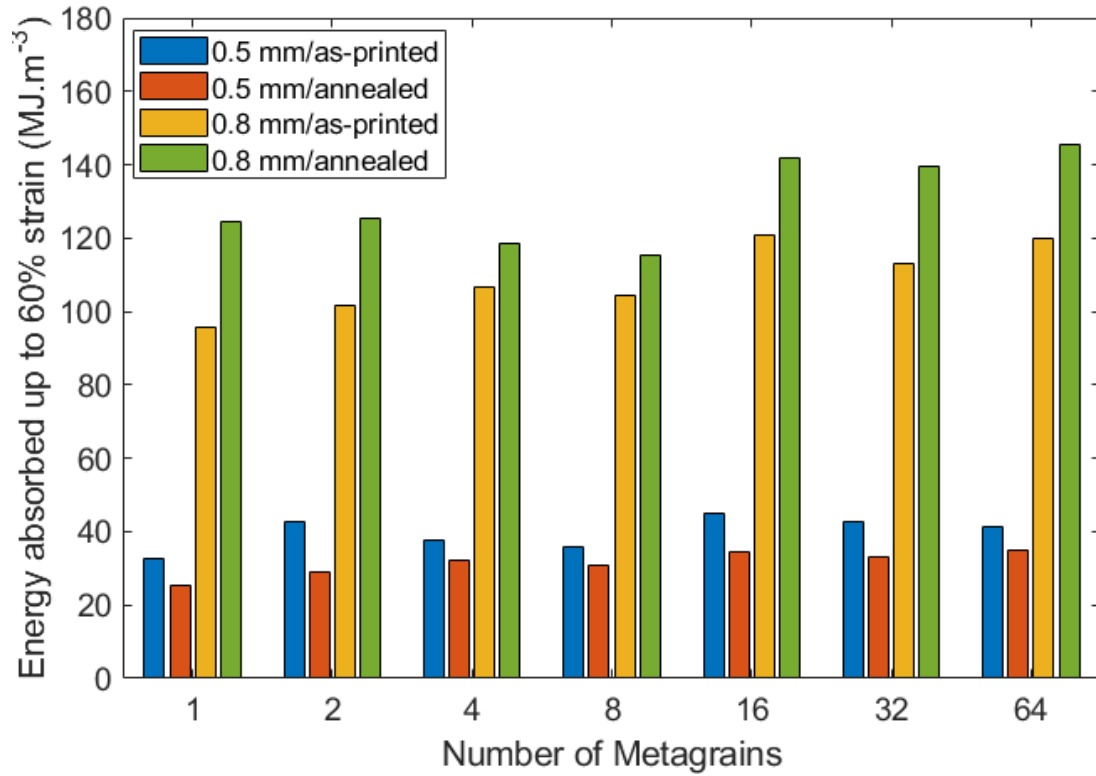


Figure 38 | The total energy absorbed up to 60% nominal strain (densification) by the 0.5 and 0.8 mm meta-crystals in as-printed and annealed conditions.

Section 4.3.1 shows that increasing the strut diameter can lead to higher strut quality (Figure 33 and Figure 34). Figure 40a and Figure 38 indeed shows that there is a clearer trend where the strength (Note the difference in the scale) and the energy absorption capacity improved with a reduction in the size of MGs for the 0.8 mm/as-printed meta-crystals i.e., the contribution of MG boundary strengthening was enhanced. The deformation of the 0.8 mm/as-printed meta-crystals showed formations of secondary deformation bands following the initial collapse despite the ill-defined and crumbled planes (perpendicular to the loading direction) in some locations (Figure 39, third row). It should be noted that there the presence of the square lattice at the MG boundaries, with additional struts aligned to the loading direction, may potentially increase the strength of the meta-crystals with more MGs, in particular those with 0.8 mm struts.

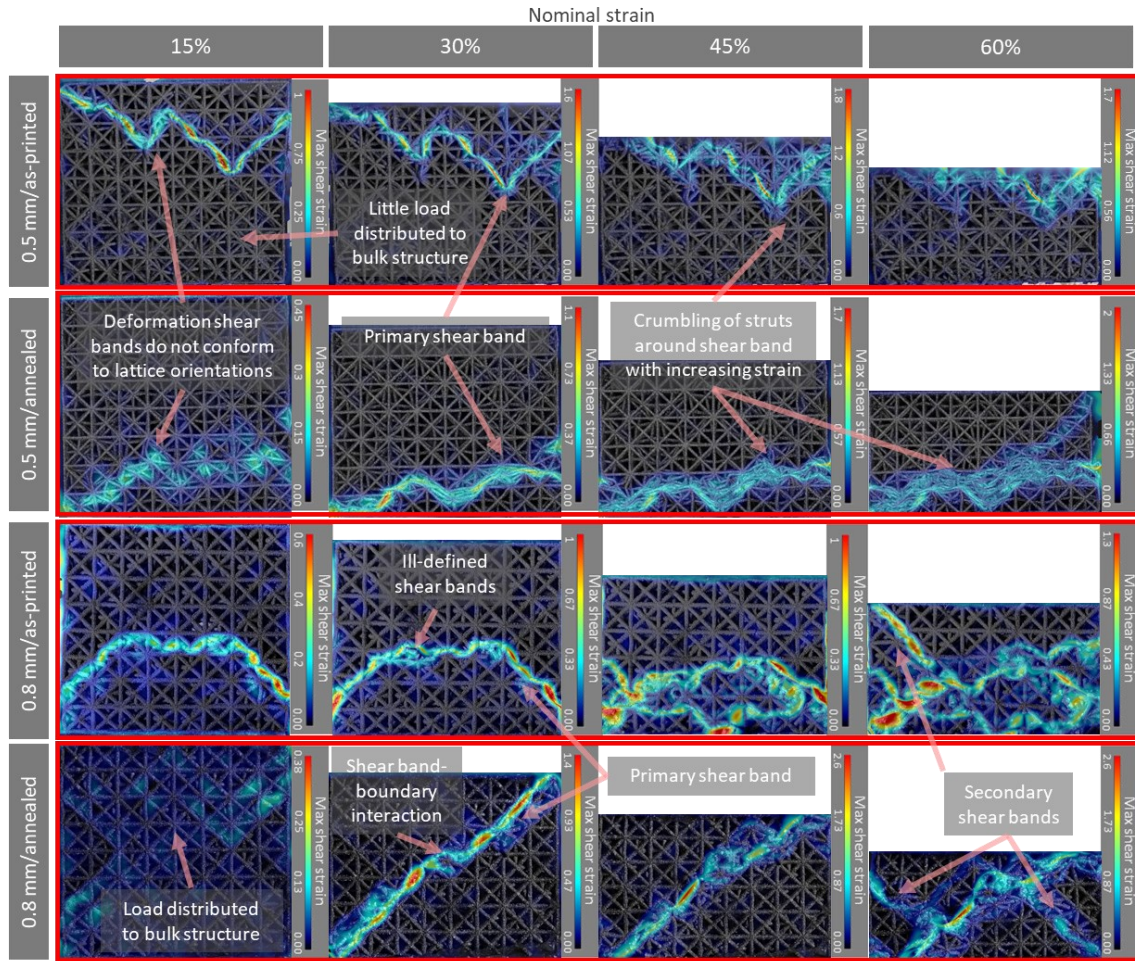


Figure 39 | DIC showing the deformation of the 16 MGs meta-crystals under increasing compressive strain. From left to right of the same row: Deformation fields at 15 %, 30 %, 45 % and 60 %. First and second rows: the meta-crystal with the 0.5 mm strut diameter of the as-printed and annealed conditions, respectively. Third and fourth rows: the meta-crystal with the 0.8 mm strut diameter of the as-printed and annealed conditions, respectively

Heat treatment was done to study the effect of intrinsic crystalline microstructure on the significance of the defects, in particular, to verify if the MG boundary strengthening was enhanced. Annealing heat-treatment significantly reduced the yield strength of the 0.5 mm/annealed meta-crystals, suggesting the residual stress was successfully removed in annealed struts and also the transformation from brittle α' to more ductile $(\alpha+\beta)$ microstructure (Figure 36). In addition, the relative magnitude of the initial stress drop of the 0.5 mm/annealed meta-crystals lessened and their post-yield behaviour became less erratic compared to the as-printed meta-crystals (Figure 37b). The annealing also enhanced the contribution of MGs with a more noticeable increase in the energy absorption capacity, despite a lower average energy absorption capacity compared to

the 0.5 mm/as-printed due to the lower yield stress (Figure 38). However, deformation of the 0.5 mm/annealed meta-crystals still showed crumbling of struts after the formation of the initial localised bands (Figure 39, second row), indicating the process defect is the predominant factor governing the behaviour of the meta-crystals.

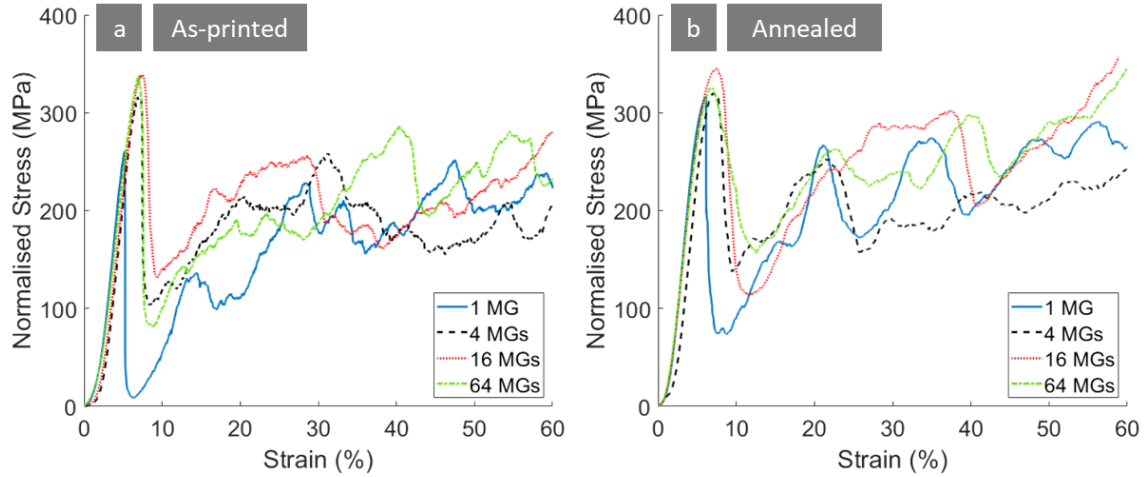


Figure 40 | The normalised stress-strain responses of the 1, 4, 16, 64 MGs Ti-6Al-4V meta-crystals with 0.8 mm strut diameter. a, as-printed and b, annealed meta-crystals.

The synergistic effect of both increasing the strut diameter and heat-treatment was demonstrated by the 0.8 mm/annealed meta-crystals (Figure 40b). The transformation of α' to more a ductile ($\alpha+\beta$) microstructure reduced the initial stress drop that is the biggest instability after plastic yield (Figure 37b). The post-yield stability was also improved in particular for 64 MGs (Figure 40b). The energy absorption capacity did not increase (even slightly decreased) with increasing the number of MGs to 8, but clearly improved for larger numbers (16, 32 and 64) of MGs (Figure 38). The DIC analysis of the 0.8mm/annealed 16 MGs meta-crystal shows an interaction between the MG boundaries and localised deformation bands, helping to slow down the propagation and promoting the formation of secondary deformation bands (Figure 39, fourth row). Although the energy absorption capacity did not increase with the small increase in the number of MGs, the magnitude and gradient of the initial stress drop decreased significantly. For example, Figure 40b shows that the stress drop was almost halved for the 64 MGs. Although it was not shown in Figure 40b, this was also seen for the 32 MGs. The less significant and sudden stress drop was thanks to interactions between the primary

localised deformation band and the boundaries of MGs, suggesting an increasingly influential role of the architecture in the meta-crystals containing ($\alpha+\beta$) microstructure.

4.4. Discussions

4.4.1. The influence of processing defects on the boundary strengthening in Ti-6Al-4V meta-crystals

The addition of MG boundaries was able to deflect and scatter localised deformation bands, increasing the strength and the damage tolerance of architected materials made from polylactic acid (PLA) [22]. However, when such meta-crystals were fabricated from Ti-6Al-4V by L-PBF, the effectiveness of the MG boundaries was significantly reduced due to the differences in the intrinsic microstructure and the processing quality. PLA struts are much more elastically compliant and can be fabricated with higher geometric accuracy, helping to mask the adverse effect induced by processing defects and enable an influential role of MG boundaries in improving the strength and post-yield stability of meta-crystals. In contrast, Ti-6Al-4V struts were fabricated with much lower accuracy, in particular, insufficient fusion occurred at the free surface of struts (Figure 33 and Figure 34a, b) and variations in the strut and node geometries. While a study reported that the internal porosity causes strut fracture rather than the lack-of-fusion defects, the reported internal porosity volume fractions of 1.12% and 2.01% (for 0.6 mm and 0.8 mm struts, respectively [299]) were much higher than the internal porosity 0.34% observed in the 0.5 mm struts in the present study. In addition, other studies reported that lack-of-fusion porosity less than 1% typically do not affect the static mechanical performance [111,300]. The surface defects were therefore more damaging for the meta-crystals in this study. In particular during buckling, where the defects compounded the already high bending stress on the surface of the struts. The loss of load-bearing area also led to large stress concentration which caused fast fracture of the remaining consolidated material, explaining the smooth fracture surface observed for the as-printed struts (Figure 35a and c).

The increase in the strut diameter was shown to help achieve better strut quality (Figure 33, Figure 34a and b, Figure 35a, and b) consistent with a previous study [296]. In addition, increasing the strut diameter (d) while keeping the lattice spacing constant reduces the slenderness ratio $R = L/r$, where L is the length of strut and r is the radius of gyration ($r = d/4$). The slenderness ratio of $\langle 001 \rangle$ struts (most susceptible to buckling for the studied FCC lattice [301]) with diameters of 0.5 mm and 0.8 mm are 40 and 25, respectively. Since these are less than the transition slenderness ratio (R_{trans}) of 60.3 (determined using Eq. 4.1), the critical stress for buckling was approximated using Johnson's parabolic formula (Eq. 4.2) [302].

$$R_{trans} = \sqrt{\frac{2\pi^2 E}{K^2 \sigma_y}} \quad (4.1)$$

$$\sigma_{crit} = \frac{P_{crit}}{A} = \sigma_y - \left(\frac{\sigma_y K L}{2\pi r}\right)^2 \left(\frac{1}{E}\right) \quad (4.2)$$

Where $K = 0.9$ is the effective length factor, $E = 98.5 \text{ GPa}$ is the elastic modulus [178], $L = 5 \text{ mm}$ and σ_y is the yield stress with $\sigma_y = 736 \text{ MPa}$ [151].

The calculated critical buckling stress for the 0.8 mm struts was ~665 MPa compared to ~555 MPa for the 0.5 mm struts. However, the peak strengths of the meta-crystals with thicker struts were ~3x greater than the meta-crystals with the thinner struts (Figure 38a and Figure 40a). Such differences reflect the influence of defects. The larger struts were less affected by the role of notch-like asperities as stress concentrators (Figure 33 and Figure 34), minimising the effect of processing defects.

It should also be noted that for cuboid MGs, with the preference to shearing on the $\frac{1}{2}\{100\}$ plane, the number of available parallel shear planes are limited, and the strength is therefore more influenced by the presence of defects in that plane (i.e., for cuboidal MGs which are elongated in the loading direction, there are multiple parallel shear planes which could potentially buckle).

4.4.2. The effect of the crystalline microstructure

The deformation behaviour of the meta-crystals design is governed by the hierarchical lattice structure inside the base material, namely the atomic lattice and intrinsic

crystalline microstructure. Ti-6Al-4V fabricated by powder bed fusion is known to be very brittle [290]. The rapid cooling in L-PBF resulted in near fully α' martensitic HCP microstructure which was observed in the studied Ti-6Al-4V struts (Figure 36a). Together with the high thermal gradient (estimated up to 10^7 K/m) in L-PBF, fine solidification microstructure containing dense dislocations is often formed in as-printed alloys, e.g. 316L as shown in [303]. Such microstructure leads to high strength, but low ductility [289]. Together with the predominant notch-like defects, the brittleness of as-built struts caused successive and fast crumbling of lattice struts on planes perpendicular to the loading direction (Figure 37a).

Heat treatment resulted in a microstructure transformation from brittle α' to a different microstructure that is more ductile and contains two crystal lattice types: α -HCP and β -BCC (Figure 35b, d, and Figure 36b). The heat treatment should also alter the intrinsic polygrain microstructure and relieve the internal stresses built up during processing to regain ductility with the expense of lowering the yield strength (Figure 37b). Such changes in crystalline structure should help to minimise the tendency for fast fracture and enable an influential role of polygrain-like architected mesostructure. However, the 0.5 mm/annealed meta-crystals only showed that the magnitude of the collapse reduced thanks to the decreased yield strength, but the meta-crystals still crumbled successively in a layer-by-layer manner (Figure 39, second row). Although a slightly bigger improvement was seen in the energy absorption capacity with an increasing number of MGs, the change in the intrinsic microstructure by heat-treatment was still insufficient for the given as-print quality of the meta-crystals. This is expected as a previous study showed that the ductility with coarse lamellar ($\alpha+\beta$) only marginally increased by ~6% compared to acicular α' martensite microstructure [15]. Additionally, a previous study reported a significant increase in the oxygen content (~0.19 to ~0.23 wt.%) of L-PBF Ti-6Al-4V with a reduction in strut diameter from 1 mm to 0.5 mm [264], such increase enhances the strength with a significant loss in ductility of Ti-6Al-4V [304,305]. While the heat-treatment was able to change α' to more ductile ($\alpha+\beta$) microstructure, given the predominant role of notch-like defects and potential embrittlement effect due to oxygen, the ($\alpha+\beta$) microstructure still showed insufficient total elongation to failure. Therefore,

the benefits of microstructural change due to the heat-treatment of Ti-6Al-4V meta-crystals for the 0.5 mm struts were limited.

4.4.3. Enabling the strengthening effects of the polycrystal-like architecture

Sections 4.4.1 and 4.4.2 show that the quality of the lattice struts can greatly affect the efficacy of Ti-6Al-4V meta-crystals. It may not be effective to use hot isostatic pressing (HIP) to remove defects in lattice materials as the most severe defects found were notch-like defects on the free surface, which are known to not be removed by HIP [158]. Effective ways to reduce the surface roughness would be through electrochemical etching [153] and, more conveniently, through process parameters optimisation. Section 4.4.1 shows that a better choice of the strut dimensions can be effective in achieving good quality lattice struts. Figure 40b highlights that once the quality of struts was improved, the polycrystal-like architected mesostructure in combination with the change in crystalline microstructure noticeably improved the post-yield instability and reduced the loss in strength via increasing the number of MGs. These improvements are significant as any loss in strength makes the materials less desirable for loading-bearing and safety-critical applications. This finding confirms the validity of the meta-crystal approach and highlights the strong dependence of the base material's properties. Most importantly, it emphasizes the influential role of each hierarchical lattice structure at a given length scale. The extension of the hierarchy by adding polycrystal-like architected mesostructures and the strong dependence on the base material provides added opportunities in designing lightweight materials with more tuneable properties. One of the most exciting directions of research is to radically change the crystalline microstructure by printing meta-crystals with alloys of different lattice structures, with other *printable* alloys such as high entropy alloy [174] and 316L steel [303,306] or IN718.

4.5. Conclusions

The separate and synergistic effects of each hierarchical feature on the mechanical behaviour of additively manufacturing Ti-6Al-4V meta-crystals were studied. The

predominance of the process defects and the brittleness due to the martensitic α' in the as-printed condition caused the fast fracture of struts, reducing the effects of polycrystal-like architected mesostructures. In particular, the lack-of-fusion defects on struts' free surfaces were found to be influential. Such defects led to notch-like stress concentration and significantly reduced the load-bearing areas, causing overload and the fast fracture of consolidated struts. Increasing the strut diameter not only effectively enhanced the quality of as-printed struts but also reduced the roles of notch-like defects. This quality improvement in combination with the transformation of α' to $(\alpha+\beta)$ microstructure thanks to heat treatment enabled effective synergistic contributions from the crystalline microstructure and polycrystal-like architected mesostructure to significantly improve the energy absorption of Ti-6Al-4V meta-crystals. This present study highlights the influential role of each length scale feature in the hierarchical structure ranging from atomic lattices (α -HCP and β -BCC), the crystalline lamellar microstructure of the base material, architected lattice and crystal-like architected mesostructure in controlling the mechanical strength and energy absorption capacity of lightweight architected materials.

Blank

Chapter 5

Influence of the Base Material

5.1. Introduction

Lattice materials with the same architecture but different base materials and microstructures exhibit dissimilar deformation behaviours [1]. For example, heat-treatment of AlSi10Mg BCC lattice materials led to localised deformation band formation instead of fracture, resulting in a significantly higher energy absorption [307]. The differences in behaviour were due to a change in the Si morphology, which prevented shear failure in the as-fabricated lattice due to crack propagation along the α -Al/Si eutectic microstructure. Similarly, heat-treatment and hot isostatic pressing treatment of diamond Ti-6Al-4V lattices changed the microstructure to a lamellar $\alpha + \beta$ -phase which lowered the strength but significantly increased ductility, making the lattice material more suited to dynamically loaded applications [308].

While the effect of the base material's yield strength and stiffness have been thoroughly reported (e.g., via the scaling laws in Eqs. 2.3 and 2.4), there have not been studies which optimise the base material to specific lattice architectures in different applications. Additionally, it was shown in chapter 4 that the combination of the processing defects and the base material's properties can greatly influence the mechanical behaviour of meta-crystals. Therefore, this study investigated the effect of different base material on the mechanical behaviour of polycrystal-inspired meta-crystals, in particular the post-yield behaviour. The meta-crystals in this study were fabricated from three different metallic alloys Ti-6Al-4V, Inconel 718 (IN718), and 316L stainless steel via L-PBF. The

alloys were chosen thanks to their *printability*, their varied mechanical properties, and their wide uses in critical load-bearing applications such as in the aerospace [309] and the medical industries [310]. However, despite their *printability*, variations in the as-printed meso-structures, such as the quantity and type of defects, are still expected. Additionally, the influence of the processing defects varies with different lattice architecture and base material. Meta-crystals with smaller diameter struts and a brittle base material did not significantly benefit from the strengthening architecture [106]. Materials that are more tolerant to defects will ensure effective strengthening from the architecture.

Additively manufactured 316L is widely reported to consist of a single phase FCC austenite, has high strength and excellent ductility thanks to twinning induced plasticity [277,278]. IN718 is a nickel-based superalloy primarily strengthened by coherent γ' / γ'' precipitates. The nominal base composition is 51Ni-21Fe-19Cr-5Nb-3Mo-1Ti; the addition of Nb helps to overcome cracking during welding [311] and L-PBF. The microstructure of wrought IN718 consists of the austenite FCC- γ matrix with three intermetallic precipitate phases: ordered ($L1_2$) FCC- γ' with the composition $Ni_3(Al, Ti, Nb)$, BCT- γ'' with the composition Ni_3Nb , and orthorhombic δ also with the composition Ni_3Nb . The morphologies of the γ' and γ'' precipitates are distinct, with the γ' appearing spherical or cuboidal and γ'' appearing disc-shaped (or oblate spheroid) [312,313]. δ precipitates are comparatively larger, with a needle-like morphology and mostly found at the grain boundaries [314]. The microstructure of as-printed IN718 differs from the wrought state somewhat. In particular, the matrix is mostly free of γ' / γ'' precipitates but contains considerable amounts of brittle Laves phase (with the composition $(Ni, Cr, Fe)_2(Nb, Mo, Ti)$) that is detrimental to the mechanical properties of AM IN718 [315]. The Laves precipitates are located in the intercellular regions, which also contain high dislocation densities [316] and higher concentrations of low solubility elements (such as Nb, Mo, Ti, C) due to segregation [317]. Similar to most AM microstructure, IN718 also shows epitaxial and competitive growth of grains, resulting in large columnar grains aligned to the build direction and mechanical anisotropy [315]. Due to the columnar grain structure, the mechanical properties of as-printed parts are highly anisotropic. For as-printed samples, Ti-6Al-4V has the highest yield strength ranging from ~960-1195

MPa, followed by IN718 with ~720-900 MPa and lastly 316L with ~450-590 MPa. The UTS of Ti-6Al-4V ranges between ~1040-1270 MPa, while IN718 ranges between 1117-1143 MPa, and 316L ranges between 640-700 MPa. Ti-6Al-4V has a far lower elongation to failure than IN718 and 316L with reported values between ~4.9-6.5% [288,293,318] compared to ~19.2-25.9% [73,319,320] and ~36-59% [164,321], respectively.

The range of properties provided by the chosen alloys will enable an extensive investigation on the effects of the base material's properties on the strengthening behaviour of meta-crystals. Although there were previous studies of lattice materials fabricated by the three alloys (Ti-6Al-4V [259], IN718 [322], and 316L [237]), no efforts have been for polycrystal-like meta-crystals. Therefore, in this study, meta-crystals containing increasing numbers of polygrain-like subdomains were investigated for each of the alloys to study the effects of crystalline microstructure and architected mesostructures on the mechanical behaviour of meta-crystals. The effects of different material properties during the deformation of the struts were reported and discussed. Furthermore, the fabrication defects were characterised and their influence on the deformation behaviour were also analysed. The study elucidated how different base material properties of the three alloys accommodated the processing defects and interacted with the polycrystal-like architecture to enable significant hardening at the macroscale for structural applications.

5.2. Experimental procedure

One set of quasi-static compression test was conducted on Ti-6Al-4V, IN718, and 316L meta-crystals with 1, 2, 4, and 8 MGs (sections 3.3.2.1 and 3.3.2.3). All meta-crystals in this study have 0.8 mm strut diameters. The meso- and microstructure of the meta-crystals were characterised by electron microscopy, via SE imaging and EBSD analysis (section 3.4.2). Hardness measurements were also captured in struts parallel and perpendicular to the build direction in the undeformed and deformed regions (section 3.3.3).

5.3. Results

5.3.1. Characterisation of the fabricated meta-crystals

Table 6 summarises the meta-crystals investigated in this study, including the theoretical and calculated relative densities ($\bar{\rho}$) of the fabricated meta-crystals. The $\bar{\rho}$ measured from the fabricated meta-crystals were consistently larger than the theoretically calculated $\bar{\rho}$ from the models, indicating that the consolidated geometries were overall larger than the design. The 316L and IN718 meta-crystals showed up to ~30% increase in $\bar{\rho}$, whereas the fabrication of the Ti-6Al-4V meta-crystals were geometrically far more accurate with an average increase of 1.9%. Higher geometric accuracy of the Ti-6Al-4V meta-crystals could be due to the fewer number of overhangs compared to the IN718 and 316L meta-crystals as a result of using different build directions. There appears to be no consistent correlation with the relative difference of $\bar{\rho}$ with the number of MGs. Since the stiffness and strength of lattice materials are proportional to its relative density, all mechanical properties of the meta-crystals were normalised by the measured $\bar{\rho}$, unless stated otherwise. Also shown in Table 6 is the equivalent MG size, given as the diameter of a sphere with the same volume as each MG.

Table 6 | The theoretical and measured relative densities of meta-crystals with different base materials and number of MGs.

Base material	Number of MGs	Equivalent MG size, d (mm)	Theoretical relative density	Measured relative density	Relative difference (%)
Inconel 718	1	49.6	0.215	0.268	24.9
	2	39.4	0.220	0.264	19.9
	4	31.3	0.226	0.254	12.2
	8	24.8	0.228	0.259	13.7
Ti-6Al-4V	1	49.6	0.215	0.215	0.2
	2	39.4	0.220	0.224	1.9
	4	31.3	0.226	0.235	3.7
	8	24.8	0.228	0.233	1.9
316L	1	49.6	0.215	0.274	27.8
	2	39.4	0.220	0.285	29.5
	4	31.3	0.226	0.293	29.5
	8	24.8	0.228	0.296	29.9

The fabrication quality can be qualitative analysed from SEM micrographs as shown in Figure 41. It can be seen that the node regions were over-consolidated, especially the corner nodes (of the unit-cell) where more struts overlap. The increase in consolidated mass in node regions are likely responsible for the differences in the measured and theoretical $\bar{\rho}$. The additional mass is not only redundant but might also be detrimental to the strength of the lattice materials. The over-consolidated nodes increase the risk of having a localised deformation in the far smaller strut regions, resulting in early fracture. Another form of imperfection seen in Figure 41a, b and c are the struts' surface roughness. This is a combination of the discretisation of geometry, partially-melted powder particles, and lack-of-fusion at the free surface. Less surface roughness is seen in the IN718 and the 316L struts compared to the Ti-6Al-4V struts, which suggests a trade-off between the surface finish quality and the geometric accuracy of struts.

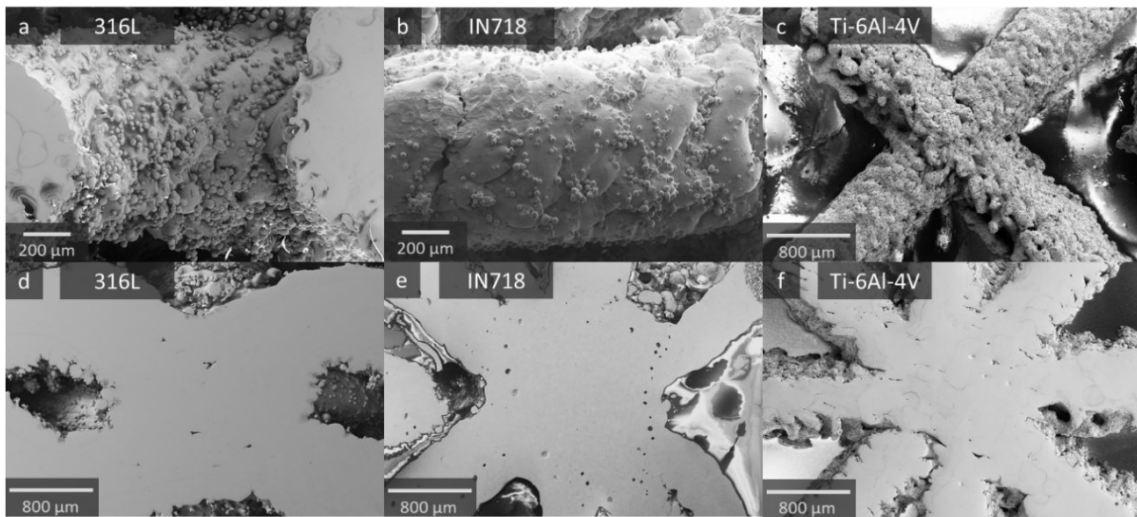


Figure 41 | SEM micrographs showing processing defects in meta-crystals fabricated from 316L, IN718, and Ti-6Al-4V. a, b, c, Surface roughness on lattice struts due to partially melted powder particles, stair-step effect, and lack-of-fusion. d, e, f, Internal defects in the nodes including various pores and cracks.

The cross-sections in Figure 41d, e, and f shows the internal imperfections in the printed struts such as internal pores. Analyses of such micrographs showed that the average area fraction of pores is higher in the strut regions than the node regions in IN718 meta-crystals whereas the opposite is true in 316L and Ti-6Al-4V meta-crystals (Figure 42a). Overall, the area fraction of pores is highest in the IN718 meta-crystals, followed by Ti-6Al-4V then 316L. The fabricated IN718 meta-crystals also contained significantly more

round pores than the Ti-6Al-4V and 316L meta-crystals on average. Rounder pores are likely keyhole and entrapped gas pores (smaller) [323], while irregular pores are likely lack-of-fusion [324]. The pore size distribution was rather similar between the materials but are different in the node and the strut regions. The pore sizes are much more stochastic, skewing towards the smaller pores, in particular in the strut regions (Figure 42b, c). The different pore distributions in struts and nodes were more apparent in the 316L meta-crystals and less so in the IN718 meta-crystals. The IN718 meta-crystals contained much larger pores than the lattices of the other two materials, especially in the strut regions.

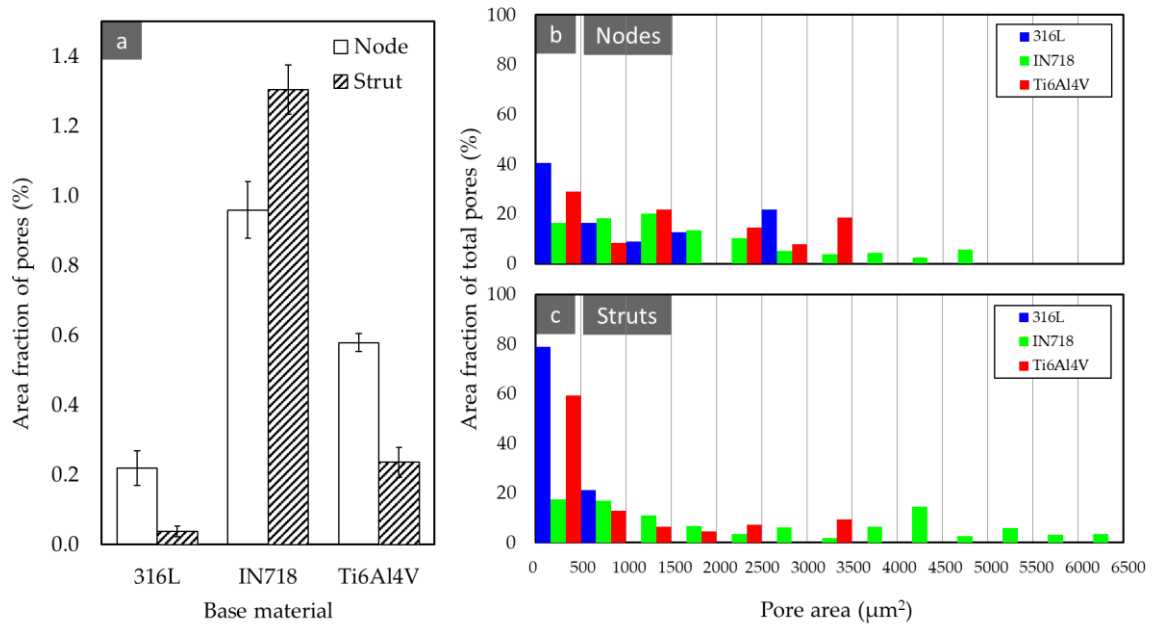


Figure 42 | Quantification of internal porosity in the node and strut regions of 316L, IN718, and Ti-6Al-4V meta-crystals. a, The average area fraction of pores in nodes and strut regions in 316L, IN718, and Ti64 meta-crystals. **b, c,** the distribution of pore size in each region.

5.3.2. Microstructure

The phases present in the as-printed alloys were consistent with those reported in literature [278,295,320]. While the matrix of IN718 was the FCC γ , as-printed IN718 also contained precipitates such as Laves and carbides in the interdendritic regions. Ti-6Al-4V was predominantly α' with small fractions of the prior- β phase between very fine acicular laths. Columnar grain structures (orientated towards the heat flux direction, which is a mix between the build direction and the strut orientation) can be seen in 316L

and IN718 nodes (Figure 43a and c), but not in Ti-6Al-4V due to the used high magnification (Figure 43e). However, it is commonly reported in literature that L-PBF Ti-6Al-4V forms large columnar prior- β grains in the heat-flux direction [162]. The columnar grain structure of 316L and IN718 breaks down in the boundary regions between the nodes and the struts (Figure 43c), a large number of pores were also observed in this region (Figure 42e). In Ti-6Al-4V, the solidification columnar grain structure of the prior- β was replaced by acicular laths via solid transformation from β to either α' or $(\alpha+\beta)$ upon further cooling [168]. This solid state transformation made the columnar microstructure less noticeable. For lattice material, the heat flux direction tends to align towards the strut orientation (Figure 43b and d), as the thermal conductivity of the consolidated material is higher than the powder [325]. Therefore, grains tend to elongate along the strut orientation, explaining why grains in 316L and IN718 were more oriented along the strut axis. As the architected lattice orientations in the MG are aligned to the same angle to the global-Z direction because of the used twin boundary, the average strut inclination was similar regardless of the number of MGs. Therefore, for 316L and IN718 meta-crystals built with the build direction being parallel to the Z, changing the number of MGs would not significantly affect the statistical distribution of grain microstructure. Since the Ti-6Al-4V meta-crystals were not built in the same orientation, there may be variations in its solidification microstructure (in particular the columnar grain microstructure) with varying the number of MGs. Nevertheless, the grain microstructure would be less prominent due to the $\beta \rightarrow \alpha$ solid phase transformation. Hence, for Ti-6Al-4V, there might be some strut orientation dependence of microstructure with varying number of MGs, but it might not be significant. Nevertheless, further study is needed to confirm this.

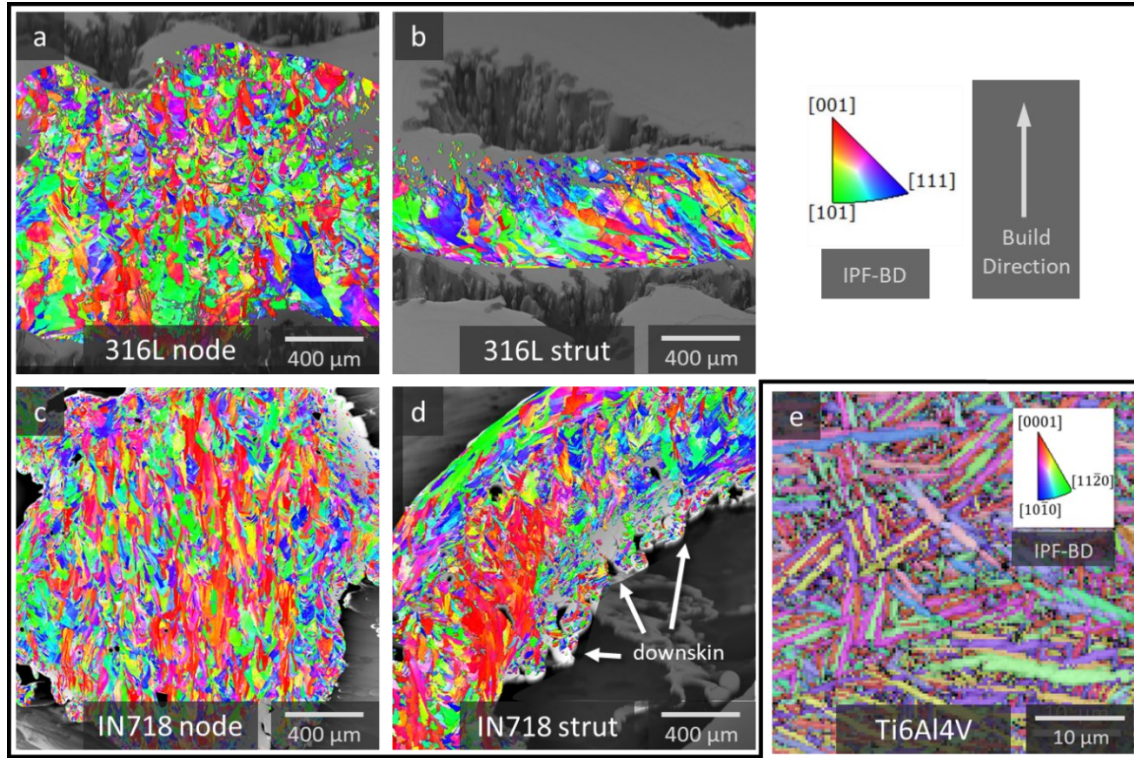


Figure 43 | EBSD maps showing the grain structure in the node and strut regions. a, b, 316L and c, d, IN718 meta-crystals showing coarse, columnar grain microstructure of FCC crystals. d, Ti-6Al-4V shows fine acicular laths of the α' martensite.

5.3.3. Mechanical properties

The compressive stress-strain response of the meta-crystals are shown in Figure 44a, b, and c. The hardness obtained after the compression tests in the node and strut regions on polished sections parallel and perpendicular to the build direction are shown in in Figure 44d. Despite the apparent columnar microstructure seen in 316L and IN718, the difference in the hardness parallel and perpendicular to the build direction (BD) was small; for the node regions, both alloys only showed a slightly higher hardness on sections perpendicular to the BD. The hardness range in the node was much smaller than the struts because 316L and IN718 hardened due to struts undergoing plastic deformation in the compression tests. No significant difference was seen between the Ti-6Al-4V nodes and the struts.

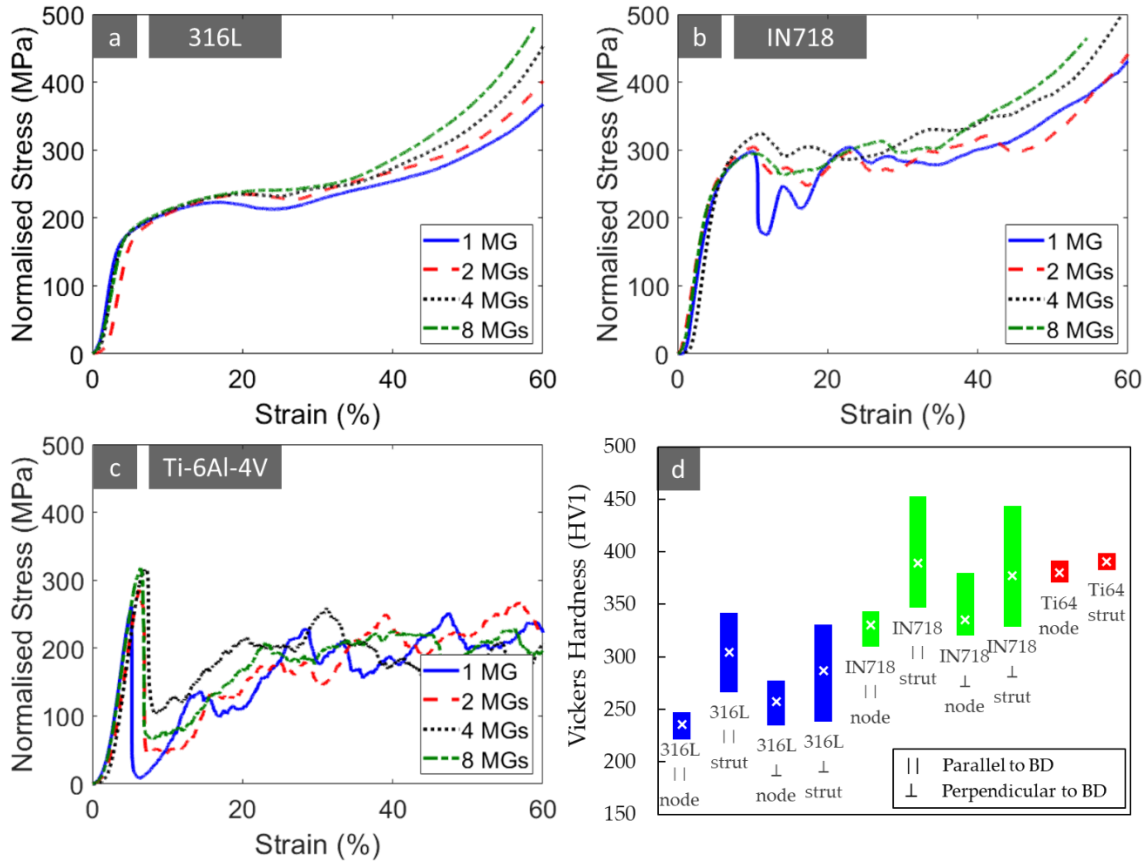


Figure 44 | The mechanical behaviour of meta-crystals with different base materials. a, b, c, The compressive stress-strain response of 316L, IN718, and Ti-6Al-4V meta-crystals with increasing number of MGs. **d,** Vickers hardness in the node and strut regions parallel and perpendicular to the build direction.

The effect of the base material on the meta-crystal's behaviour was significant, especially in the yield stress and the post-yield behaviour. Ti-6Al-4V meta-crystals showed the highest yield stress followed by IN718 and 316L meta-crystals regardless of the number of MGs. The hardness of the base material directly correlated with the yield stress of the meta-crystals, as expected (Figure 44d and Figure 45b). After yielding, the meta-crystals' responses differed considerably. 316L meta-crystals hardened right after the plastic yield with slight decrease in strength between 20-30% nominal strain for meta-crystals containing 1 and 2 MGs, but this decrease was completely avoided for 4 and 8 MGs (Figure 44a). IN718 meta-crystals suffered a much bigger post-yield loss in strength (at 5-10% strain) which was significantly minimised by increasing the number of MGs to 4 and 8 (Figure 44b and Figure 45d). Ti-6Al-4V meta-crystals showed the most undesirable behaviour with an almost complete loss in strength right after yield (Figure 44c and Figure 45d) and failed to recover the initial peak strength, including a much more

unstable post-yield response. The increase in the number of MGs were slightly beneficial, but could not completely eliminate this undesirable behaviour.

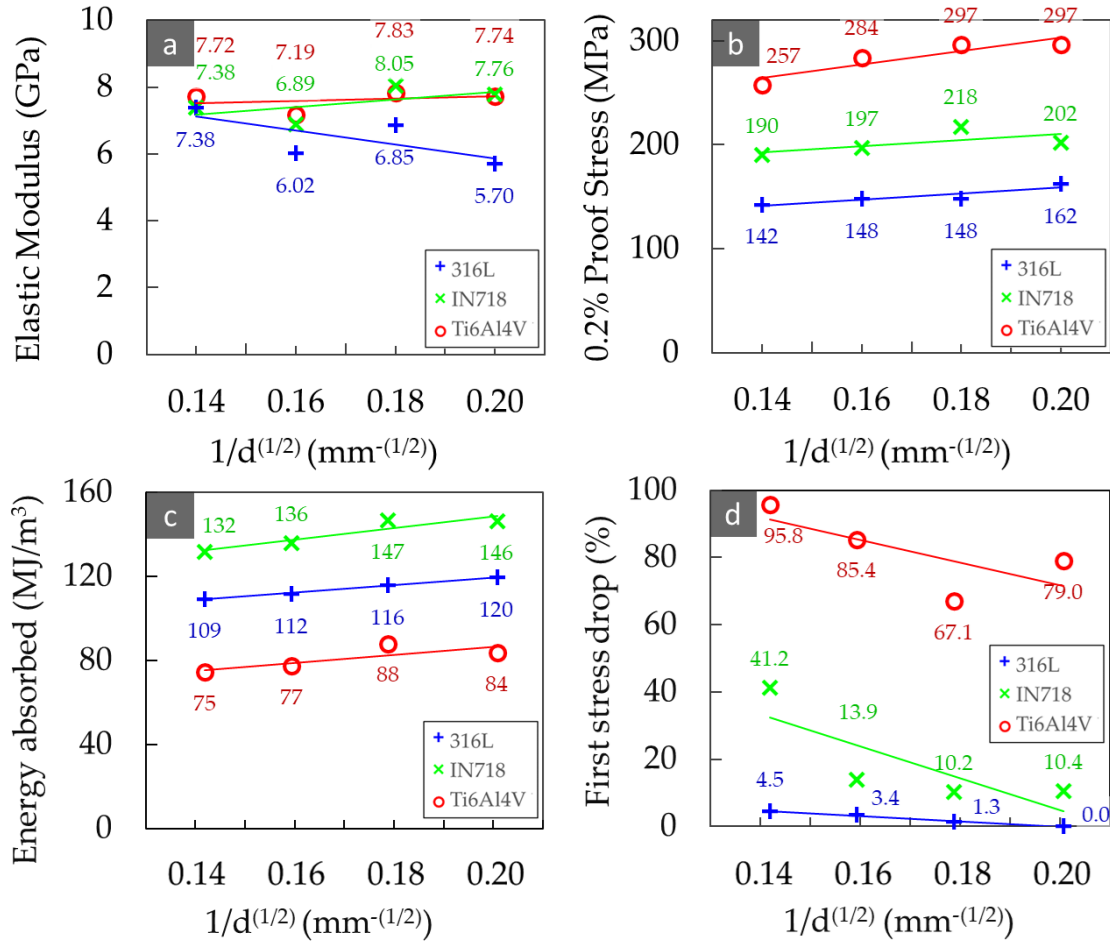


Figure 45 | The relationships between the mechanical properties of meta-crystals with the number of MGs. a, the apparent elastic modulus, **b,** the 0.2% proof stress, **c,** the total energy absorbed up to 50% total strain, and **d,** the percentage of the initial loss in strength with the inverse proportion of the square root of the MG size. Notes: 1) the first data point on the far left of each figure was of the single MG, 2) the apparent elastic modulus, 0.2% proof stress, and energy absorbed were normalised by relative density of the meta-crystal, and 3) the data were linearly fitted via the least squares regression.

While the elastic modulus of the meta-crystals negligibly changed with the size of MGs (Figure 45a), the effects of the polycrystal-inspired architecture on yield strength, energy absorption and post-yield stability were much more noticeable for all the alloys. Improvements were seen with the 0.2% proof stress (Figure 45b), total energy absorbed (Figure 45c), and marked reduction in the first stress drop (Figure 45d) with decreasing the MG size. However, the effect of the polycrystal-like architecture was different for different base materials, in particular concerning the post-yield stability that is most

reflected in the first stress drop: the higher the drop, the less stable the post-yield behaviour. There is little change in the post-yield stability in the 316L meta-crystals (Figure 45d) while the stability increasingly improved in IN718 and Ti-6Al-4V with a reduction in the size of MGs. DIC analysis revealed additional insights into underlying mechanisms responsible for the effects of polycrystal-like architecture on the deformation behaviour of the meta-crystals with the different base materials (Figure 46). The deformations in 316L meta-crystals were generally more distributed throughout the bulk structure followed by IN718, while in Ti-6Al-4V, deformations were highly localised in bands. Localised deformation bands formed in all MGs in 316L and IN718 meta-crystals, but only in some Ti-6Al-4V meta-crystals. For example, in the 4 MGs meta-crystals of Ti-6Al-4V, the deformation mostly did not conform to the lattice orientations in MGs but crumbled in planes perpendicular to the loading direction. The partition of the lattice material into multiple polycrystal-like domains (i.e., MGs) helped to break the long and dominant deformation bands into short and less severe ones in each MG. In addition, the MG mesostructure also helped to homogenize the distribution of the localised deformation bands. The shortening in the length and the homogenisation of the localised deformation bands thanks to the reduction of the size of MGs significantly reduce the post-yield stress drop, e.g. the stress drop in the 316L meta-crystals was eliminated entirely [326].

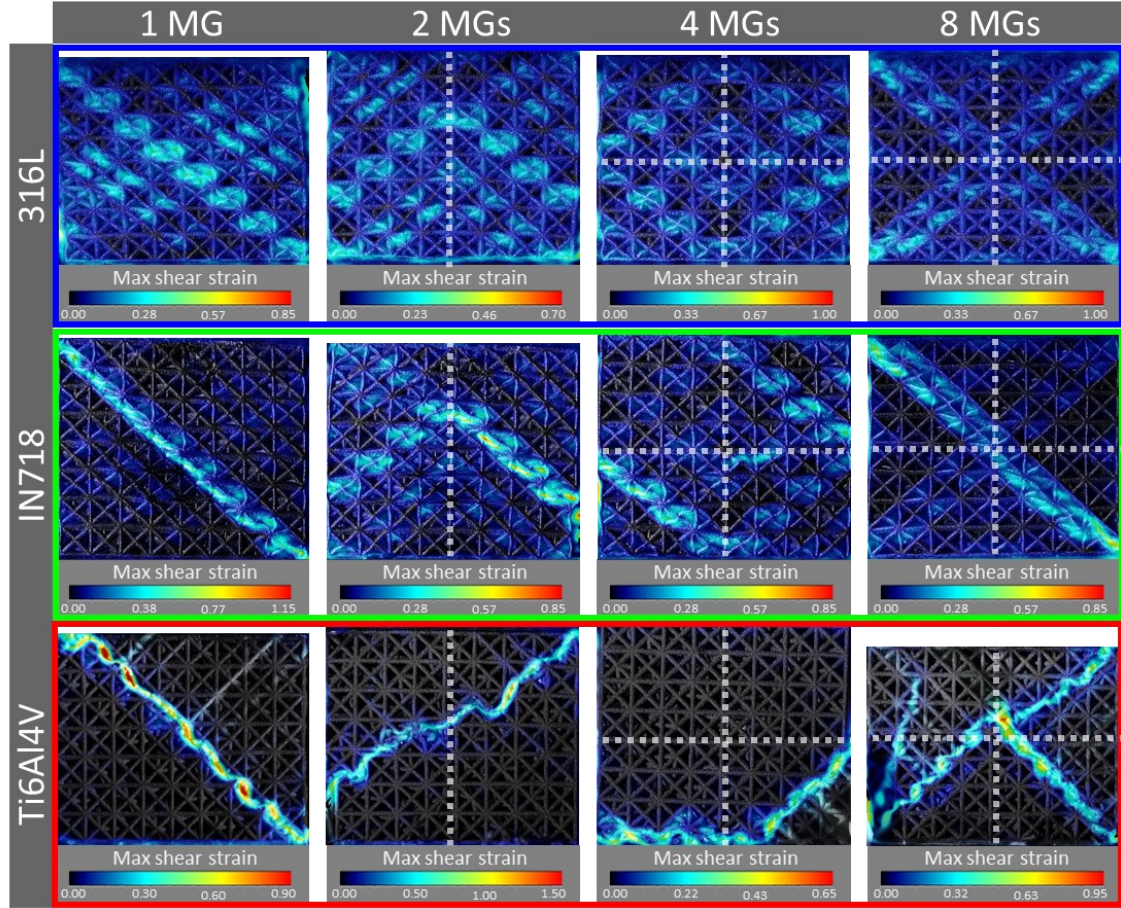


Figure 46 | DIC analysis of the meta-crystals under compression at the first stress drop. Top to bottom: 316L, IN718, and Ti6Al4V. Left to right: 1 MG, 2 MGs, 4 MGs, and 8 MGs. White dotted lines indicate MG boundaries.

The hardness measurements and the DIC suggest that deformation occurred only in the struts, not in the nodes. Deformed struts fabricated from 316L and IN718 are shown in Figure 47a and b. The micrographs show that deformation occurred as bending and plastic hinges near the ends of the struts, slightly offset from the nodes. Concerning the deformation of the base crystalline material in each strut, 316L struts mostly plastically deformed as shown in Figure 47a without fracturing into fragments. IN718 struts deformed similarly to 316L, however, damage initiated from defects present in these regions and eventually led to strut fracture (Figure 47b). The fracture behaviours of struts made out of 316L and IN718 were evidently ductile, as shown by the ductile dimples on the surface (Figure 47c). In contrast, the fracture of Ti-6Al-4V was brittle (Figure 47d) and struts tended to fracture with little plastic deformation, failing to distribute the load to bulk of the structure.

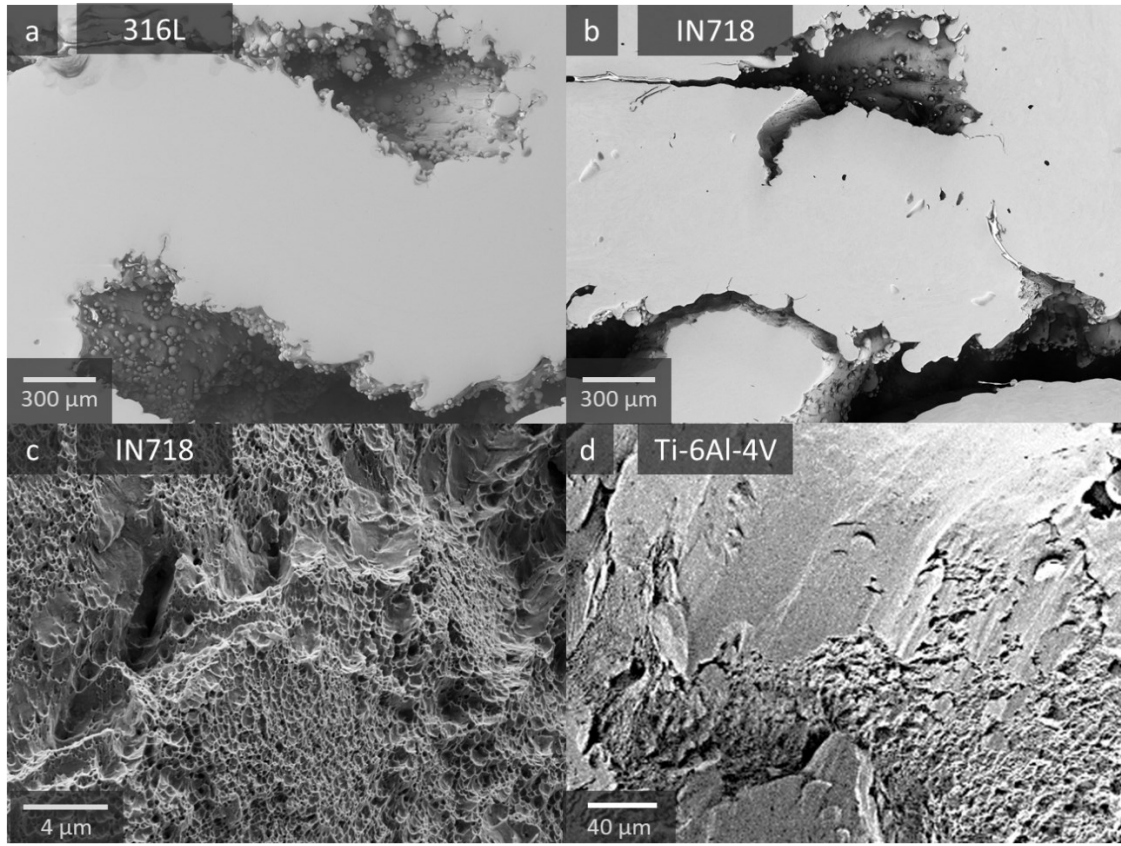


Figure 47 | SEM micrographs showing strut deformation. a, b, Plastic bending in 316L and crack propagation in IN718 struts. **c, d,** Fracture surfaces showing ductile dimples in IN718 and brittle behaviour in Ti-6Al-4V.

5.4. Discussions

5.4.1. Material-dependent mechanical behaviours of meta-crystals

The elastic moduli of 316L, IN718, and Ti-6Al-4V in the wrought condition are approximately 200 GPa [282], 200 GPa [281], and 114 GPa [280], respectively. Despite the variation of the base materials' intrinsic modulus, the elastic modulus (normalised by relative density) of the meta-crystals were shown to be very similar (~7 GPa), particularly for the 1 MG meta-crystals (Figure 45a). It has been shown that the stiffness of lattice materials are highly dependent on both the deformation behaviour of the unit cell (bending vs stretching) [231] and the Young's modulus of the base material [327,328]. Figure 48 shows the comparison of scaling relationship for the experimental measures of stiffness of the meta-crystals with the Gibson-Ashby theoretical relationship for ideal

stretching-dominated lattice materials (with $A=0.3$ and $m=1$ in Eqn. 2.3), which are of the order of the Hashin-Shtrikman upper bound for isotropic solid. The Ti-6Al-4V meta-crystals are closer to the ideal than 316L and IN718 meta-crystals. This was attributed to the redundant over-consolidated mass in the node regions of IN718 and 316L meta-crystals (Figure 41) and the lower measured relative densities for the Ti-6Al-4V meta-crystals (Table 6). Additionally, it can be seen that the reduction in the MG size appears to cause a slight reduction in the elastic modulus of the 316L meta-crystals, in particular after accounting for the variation in relative density (Figure 48). This reduction was rather insignificant given the strong dependence of stiffness on the processing defects. The MG size reduction had a negligible effect on the stiffness of IN718 and Ti-6Al-4V meta-crystals, suggesting that the reduction in the MG size with the used type of boundary did not have significant influence on the stiffness of the meta-crystals.

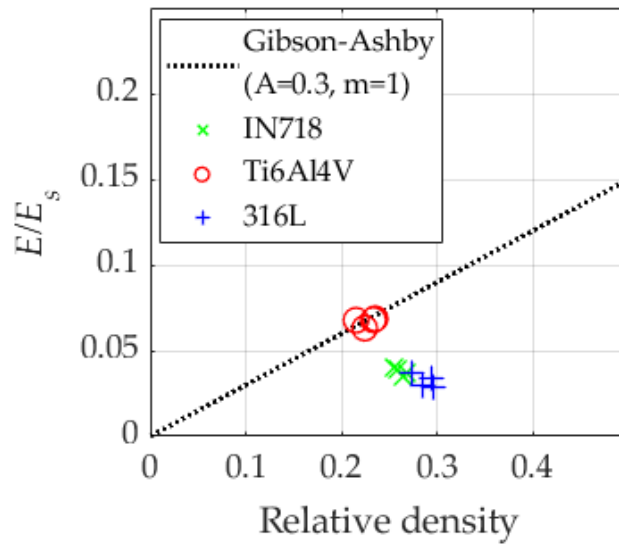


Figure 48 | The scaling relationship between the stiffness and the relative density. The ideal stretching-dominated lattice materials (dashed line) versus experimental data for meta-crystals of IN718 (x markers), Ti-6Al-4V (o markers) and 316L (+ markers).

While the base material did not significantly influence the linear elastic response of the meta-crystals, the post-yield behaviour was substantially affected. The architected FCC unit-cell in the meta-crystals is stretching-dominated [254] and, therefore, struts are subjected to significant axial stresses. However, the intrinsic plastic deformation of the base material can change the post-yield behaviour from the one of severe stress drops characteristic of the stretching-dominated (Figure 44c) to the other one of stable

deformation behaviour characteristic of the bending-dominated behaviour (Figure 44a and b). This is consistent with a previous study on IN625 that showed that nominally stretching-dominated structures can display behaviour similar to that of the bending-dominated thanks to the very high ductility of IN625 [212]. The ductility of the base materials used in this study are: ~36-59% in 316L [303], ~19.2-25.9% in IN718 [73,319,320], and ~4.9-6.5% in Ti-6Al-4V [288,293,318]. 316L has outstanding ductility in the as-printed condition thanks to dominant twinning-induced plasticity behaviour [303]. Such excellent ductility allowed struts to remain unfractured and to maintain the load bearing after the intrinsic plasticity of the base material (Figure 47a). In addition, the strength of the base material 316L increased due to work-hardening induced by the intrinsic crystal plasticity, explaining higher hardness measured in the struts than in the node regions (Figure 44d). The excellent ductility and work-hardening resulted in homogeneous deformation throughout the structure (Figure 46, top row) and a stable post-yield behaviour of 316L meta-crystals even for the single MG (Figure 44a). There were virtually insignificant stress drops after the plastic yield of 316L meta-crystals (Figure 44a and Figure 45d). Hence it was not necessary to introduce the polycrystal-like structure to reduce the post-yield stress in the 316L meta-crystals (Figure 45d). Nevertheless, the polycrystal-like structure led to more pronounced hardening with reduction in the MG size (Figure 44a) because the boundaries between MGs can stop and deflect the propagation of localised deformation bands (Figure 46, top row). The change in the stress-strain response from a stable behaviour (for 316L) to unstable behaviour with intermittent stress drops (for IN718 and Ti-6Al-4V) highlights the influential role of the base material in the post-yield behaviour (Figure 44a versus b, and c). In contrast to the behaviour of 316L, the extremely low ductility of Ti-6Al-4V due mainly to the large fraction of brittle α' martensitic lath in the as-print microstructure (Figure 43e) caused fast and brittle fracture of individual struts (Figure 47d), making catastrophic stress drop up to 95% - the strength was down to almost 0 MPa (Figure 44c and Figure 45d) for the single MG. Fast fracture of Ti-6Al-4V struts prevented load transfer and distribution throughout the lattice material, resulting in ill-defined bands that do not always follow the lattice orientations (Figure 46, bottom row). A reasonably good ductility for AM IN718 resulted in multiple stress drops after the plastic yield, most noticeable in the

meta-crystal with single MG (Figure 44b). Similar to 316L, the good ductility and work-hardening in the plastically deformed struts of IN718 enabled good stress distribution throughout the whole meta-crystal (Figure 46, middle row). The polycrystal-like structure plays significant roles in breaking down the dominant localised deformation band observed in the single MG (Figure 46, middle row, first image) into smaller and shorter localised deformation bands with reducing the MG size (Figure 46, middle row, 2nd – 4th columns), substantially eliminating the adverse effect of localised deformation bands on causing stress drop. As consequence, such influential roles helped to significantly reduce the stress drop from 41.2% seen in the single MG down to 10.4% in the 16 MGs (Figure 44b and Figure 45d), resulting in the most considerable improvement in the energy absorption and stability (Figure 44b, Figure 45c and d)

5.4.2. Tolerance of the base material to processing defects

Struts in compression can deform by buckling or plastic yielding, forming plastic hinges in either the joint between the nodes and struts (Figure 47a) or in the middle of the strut, depending on the strut aspect ratio (hinge forms in the middle of more slender struts). The most damaging defects are the large features on the strut's surface, such as lack-of-fusion as seen on the downskin of the strut in Figure 43d. Defects present on a surface that is under tension acts as crack initiation sites, as shown in Figure 47b. 316L and IN718 struts were ductile (Figure 47a-c) thanks to their FCC crystal lattices (Figure 43a-c), hence they were more tolerant to notch-like defects in particular in the downskin region. In contrast, Ti-6Al-4V was the very brittle behaviour (Figure 47d) and would snap right under bending at a very low strain, resulting in little plastic deformation of crystals in Ti-6Al-4V struts and the inferior behaviour of meta-crystals seen in Figure 44c and Figure 46. Insufficient crystal plasticity may explain the lack of hardening in fractured Ti-6Al-4V struts compared to IN718 and 316L struts (Figure 44d). Little plastic deformation (hence work-hardening) of Ti-6Al-4V is also supported by the difference in the hardness in the strut regions versus in the nodes, while such difference was significant in IN718 and 316L (Figure 44d). In addition to the low elongation of Ti-6Al-4V, the surface roughness of Ti-6Al-4V struts was also qualitatively observed to be much

higher than IN718 and 316L struts, further worsening the stress concentrating effect of the surface defects.

The fabrication quality of struts have been shown to correlate with the strut inclination to the build direction [212]. Although the lattice orientation varied between MGs, the lattice orientation in all MGs was aligned to the same angle to the Z direction as twin boundary was used in design. Since the 316L and IN718 meta-crystals were built parallel to the global Z-direction that was also the build direction, the processing defects would not be significantly dependent on the number of MGs. However, as the build direction of the Ti-6Al-4V meta-crystals were not parallel to the global Z-direction, there may be variations to the quantity of defects with different number of MGs. If any, the defect quantity would increase with the number of MGs as the internal structures were more complex. Nevertheless, Figure 45b, c and d show all meta-crystals were increasingly strengthened, confirming the effectiveness of the crystal-inspired design approach.

The internal porosity observed in the 316L and Ti-6Al-4V meta-crystals were mostly in the nodes. As deformation was localised in the struts, pores in the nodes would be uninfluential to the mechanical properties of the meta-crystals. While the pores in the struts were very small in diameter and the total porosity was less than 1% (previously shown to generally not affect the static mechanical performance [111,300]), the pores were irregular in shape, due to lack-of-fusion, which induces a higher stress concentration than rounder pores. In contrast, pores in IN718 struts were much rounder, suggesting that they were mostly due to keyholing and entrapped gasses. Additionally, a higher fraction of pores were observed in the struts than in the nodes of IN718 meta-crystals, opposite to the 316L and the Ti-6Al-4V meta-crystals (Figure 42a). This is likely due to the processing parameters selected, since the energy density of the IN718 border scans was much higher than for 316L and Ti-6Al-4V, the propensity for keyhole formation in the sub-surface regions is much higher. Also, since the fraction of border area is higher in the strut compared to the node, the quantity of pores was greater as well. The total porosity in IN718 was ~1.3% and the distribution of the pore sizes was much more uniform in both the nodes and the struts. Despite the large variation in the pore shape, size, and distribution in IN718 (and 316L) struts, internal porosity was seen

much more detrimental to the deformation and mechanical behaviour of Ti-6Al-4V meta-crystals. In addition to notch-like surface defects, the porosity in Ti-6Al-4V can contribute to early strut fracture, which induces a stress concentration effect on neighbouring struts, a knock-on effect that results in a crumbling behaviour of lattice planes as seen in Figure 46, third row. Meanwhile, IN718 and 316L were much more tolerant to pores thanks to the crystals' intrinsic hardening that resists further localised plastic deformation, enabling the strengthening effect of the architecture.

5.5. Conclusions

Meta-crystals mimicking polygrain crystalline materials were fabricated from 316L, IN718, and Ti-6Al-4V via L-PBF. The meta-crystals contained varying numbers (1, 2, 4 and 8) of MGs, which strengthens the meta-crystals through a grain boundary hardening-like approach. Architected MGs distributes and homogenises the local deformation localised deformation bands throughout the bulk structure, significantly improving the strength and post-yield stability of the meta-crystals. The base material's yield strength directly affected the strength of the 1 MG meta-crystals (before strengthening effect from the architected boundary). With the architected polycrystal-like boundaries, the yield stress and energy absorption increased with a reduction to the size of MGs observed for all base materials. The most significant improvement to the post-yield behaviour was seen in the IN718 meta-crystals, followed by the 316L then Ti-6Al-4V meta-crystals, due to the differences in the base material's properties. Higher ductility and work-hardening of the base material increased their tolerance to defects, such as the high surface roughness on the downskin of the struts and the large, irregularly shaped pores near the free surface. Defect tolerance prevents early strut fracture and enables the strengthening effects of the polycrystal-like architecture. This study showed that the combined effect of the metallurgical microstructure and polycrystal-like architectural design allows for synergistic strengthening of the meta-crystals to achieve high strength and damage-tolerant architected materials. In particular, meta-crystals fabricated by IN718 of only about 26% relative density

exhibited excellent normalised strength which was stable at about 300 MPa and good tolerance to damage.

Blank

Chapter 6

Enabling a synergy of metallurgical and architectural strengthening in meta-crystals

6.1. Introduction

The behaviour of meta-crystals was shown to be dependent on both the processing quality and the properties of the base material. For Ti-6Al-4V meta-crystals of the same architecture, processing defects from the laser powder-bed fusion (L-PBF) process, combined with the low elongation to failure of the alloy, overwhelmed the benefits of the polycrystal-like architecture [106]. The efficacy of the Ti-6Al-4V meta-crystals improved with heat-treatment by reducing the influence of defects. The influence of defects in lattice structures varies with the defect type and the base material properties. For 316L stainless steel meta-crystals, processing defects were far less influential due to the high ductility and there were effectively insignificant stress drops after the initial yielding and, therefore, it was not necessary to introduce the polycrystal-like structure. Additionally, 316L has a far lower yield strength compared to Ti-6Al-4V and IN718, which is reflected in the strength of the meta-crystals. On the other hand, IN718 polycrystal-like meta-crystals showed an excellent combination of specific strength and energy absorption capacity with increasing number of MGs. The efficacy of the polycrystal-like architecture was superior in IN718 compared to 316L and Ti-6Al-4V meta-crystals [329]. Moreover, IN718 exhibits good corrosion resistance and excellent static mechanical properties at temperatures ranging from -250 to 700°C [281]; the alloy is suitable for low-temperature applications such as cryogenic tankage [311], as well as

intermediate to high-temperature applications such as in aero engines and nuclear reactors [330–334]. With IN718 being precipitation-hardenable via heat-treatments, the alloy is ideally suited for polycrystal-like meta-crystals to ensure synergistic strengthening across length scales. The concept of hierarchical lattice structures in meta-crystals is shown in Figure 49.

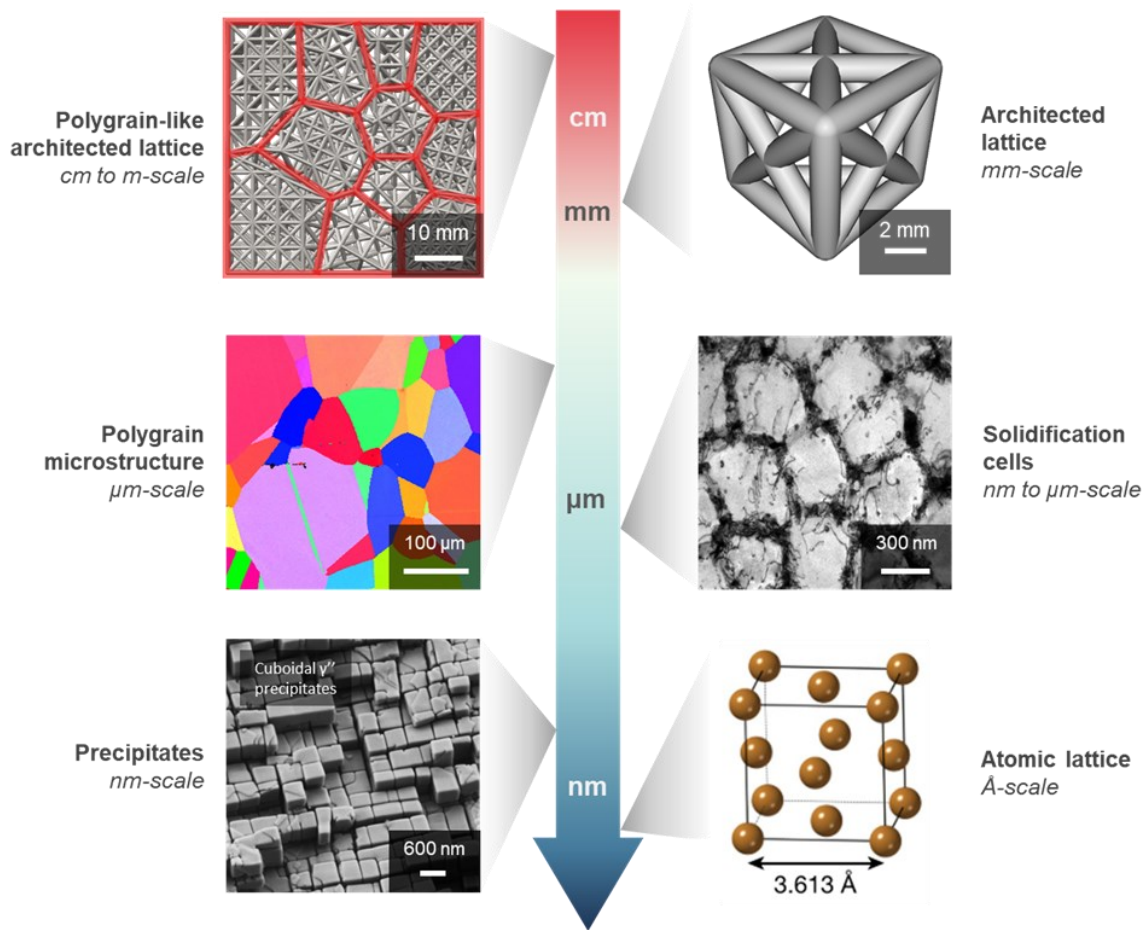


Figure 49 | Hierarchical structures of meta-crystals. The structures and strengthening features of meta-crystals at multiple length scales. From the polycrystal-like architecture (*m/cm*) to the polycrystal microstructure (μm) and the architected lattice *unit cell* (*mm*) to the intrinsic atomic lattice (*nm*), meta-crystals exhibit fractal-like self-similar structures. Similarly, strengthening features can be identified at each corresponding length scale, which serves to synergistically enhance the mechanical properties of the meta-crystals. (Polygrain-like architected lattice model created by Chen Liu and images of solidification cells and cuboidal precipitates captured by Alessandro Piglione)

The as-printed microstructure of IN718 differs from its wrought state, specifically, the matrix is free of γ'/γ'' precipitates but contains considerable amounts of brittle Laves phase. Heat treatments of AM IN718 can precipitate γ'/γ'' phases, as well as dissolve undesirable Laves and δ precipitates (depending on the heat treatment). The standard heat treatment of IN718, designed for conventionally-manufactured parts and consists

of solution annealing followed by double ageing [335], is commonly used for AM-produced parts [336,337]. However, it was shown that the standard annealing temperature fails to fully normalise the microstructure [338,339]. Additionally, the disappearance of the dislocation cells during the annealing stage reduces the strength of AM-produced parts [340]. It was also shown that AM IN718 has a faster ageing response than its wrought counterpart [340], therefore risking over-ageing. As such, modified heat treatment times and temperatures have been suggested [179], as well as no ageing [340] and direct ageing treatments [341], leading to different mechanical properties. This study follows the modified heat-treatment as suggested in [179], to retain the strengthening dislocation cellular substructure present in AM parts.

The influence of the crystalline microstructure and the extrinsic architecture on the mechanical behaviour of IN718 meta-crystals were investigated at each length scale (Figure 49). Doing so provides a better understanding of the contributions from each strengthening source and helps to develop a theoretical framework for the strength of hierarchical polycrystal-like lattice materials and, subsequently, providing the basis to understand the synergistic strengthening for design of lightweight, high strength and damage-tolerant materials.

6.2. Experimental procedure

As-printed and heat-treated meta-crystals containing 1, 2, 4, 8, 16, and 32 MGs with 0.8 mm strut diameter were fabricated for this study (courtesy of Additive Laser Technology of Ukraine) (section 3.2.1). Two sets of meta-crystals were heat-treated in Ar atmosphere (section 3.2.2). All meta-crystals were subjected to quasi-static compression tests with DIC analyses (sections 3.3.2.1 and 3.3.2.3). Two compression tests were conducted on each of the as-printed and heat-treated 1, 4, and 16 MGs meta-crystals. The as-printed and heat-treated 1 and 4 MGs meta-crystals were characterised by x-CT before and after mechanical testing (section 3.4.1). Hardness measurements were obtained in the undeformed and deformed struts and nodes of the as-printed and heat-treated meta-crystals (section 3.3.3). The meso- and microstructure of the as-printed and heat-treated meta-crystals were characterised by SE imaging, EBSD analysis, EDX analysis. TEM

micrographs were also obtained (section 3.4.2). FE analyses were conducted on the 1 and 4 MGs meta-crystals with the as-printed and heat-treated material properties obtained from tensile tests of bulk specimens (section 3.3.4).

6.3. Results

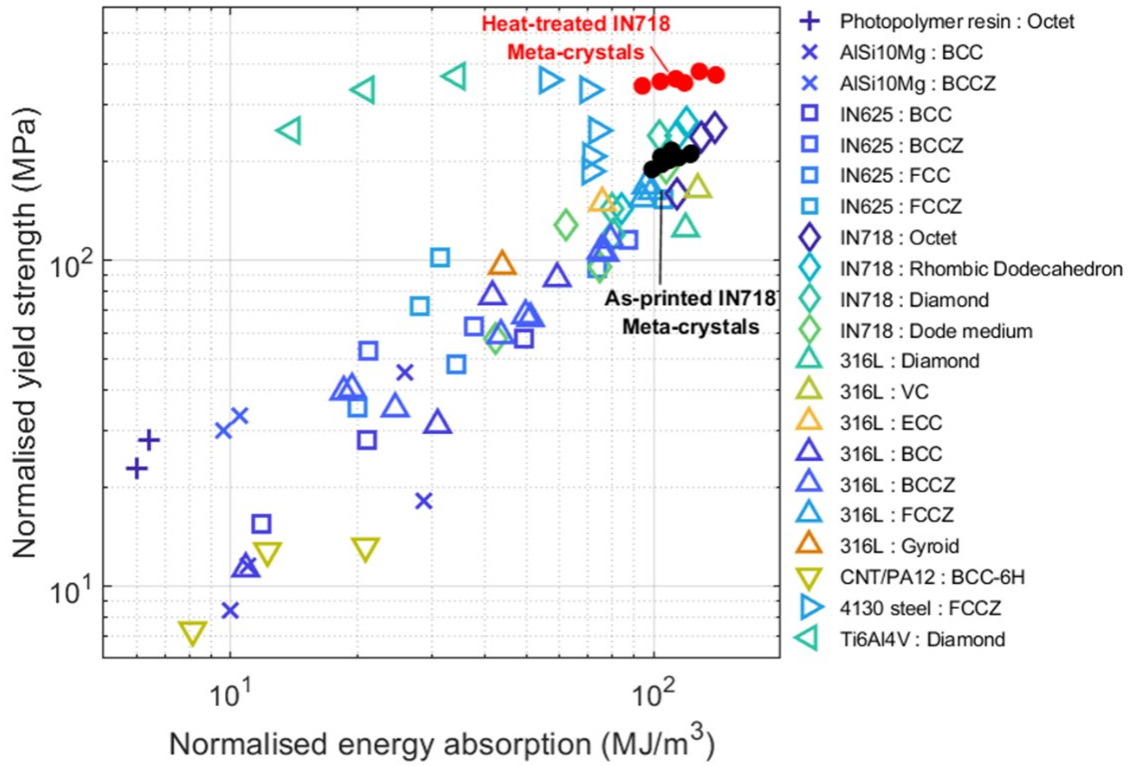


Figure 50 | Compressive properties of lattice structures. Comparison of the normalised yield stress versus the normalised energy absorption up to densification (where reported) for various unit-cell topologies and base materials. Properties were normalised by the relative density of the lattice structures. Where the densification strain is not applicable, the energy absorption is determined up to 40% nominal strain (as in this study). The marker colour corresponds to the unit-cell topology whereas the marker style corresponds to the base material. The synergistic strengthening of the architected structure and the optimised crystalline microstructure in this study showed an excellent combination of strength and energy absorption capacity (top-right corner). (References of lattice materials from top to bottom: [120,171,212,268,308,342–345]).

Figure 50 provides an overview in broad context of the yield strength vs. the energy absorption of lattice materials from literature for different base materials (marker symbol) and unit cell topologies (marker colour) in comparison to properties of the studied meta-crystals. There appears to be a correlation between the strength and energy absorption of lattice materials. Ti-6Al-4V and 4130 steel lattice materials did not conform to this trend, showing high strengths but poor energy absorption capacity. The figure

reveals that the heat-treated meta-crystals had the best combination of strength and energy absorption capacity (most top right corner in Figure 50) compared to the other considered lattice materials. The heat treatment had a significant effect on the strength, while the increasing number of MGs had a significant effect on the energy absorption capacity (the most top-right marker is heat-treated 32 MGs meta-crystal).

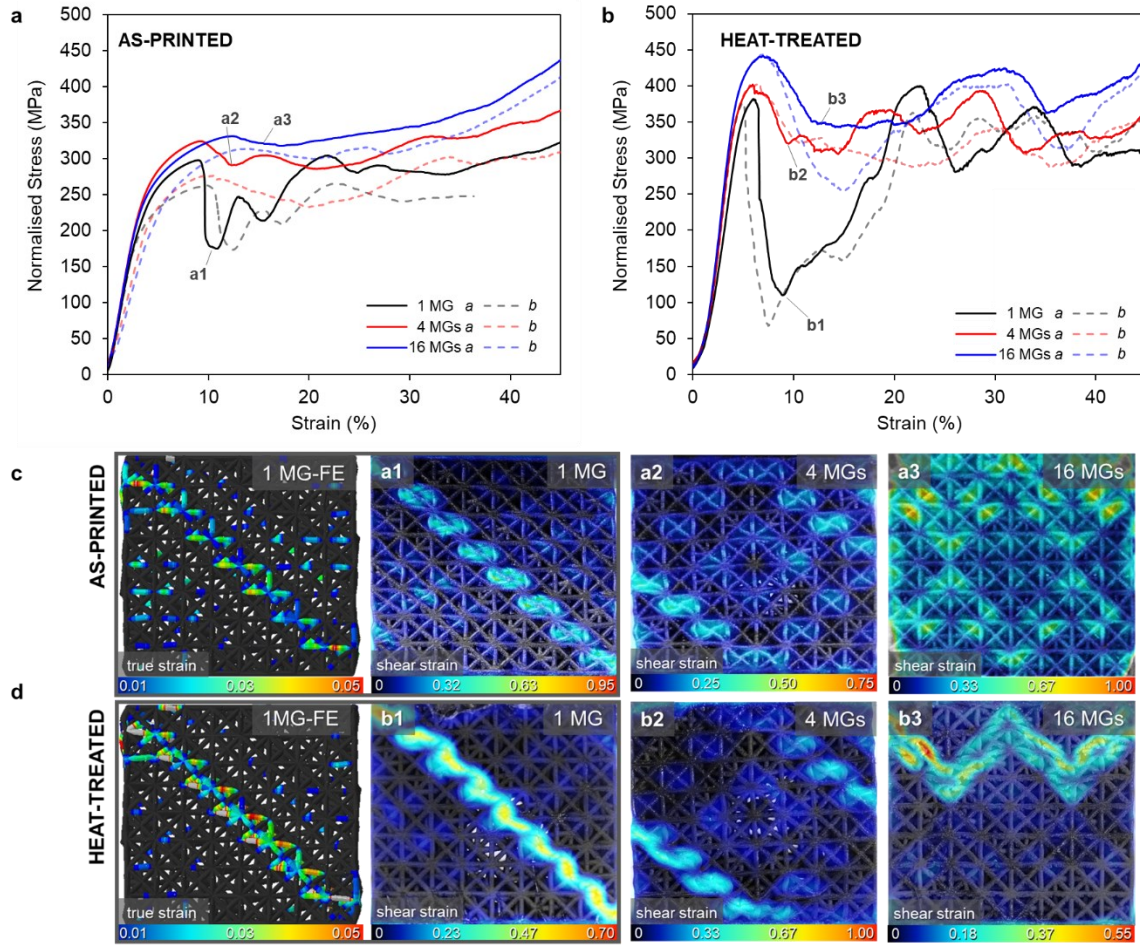


Figure 51 | Compressive response of meta-crystals. a-b, Normalised stress-strain curves of the as-printed and heat-treated meta-crystals (normalised by relative density); two sets of 1, 4, and 16 MGs as-printed and heat-treated meta-crystals shown. Additional 2, 8, and 32 MGs as-printed meta-crystals were also tested (Appendix D). All meta-crystals showed good repeatability, each showing similar post-yield behaviour. c, d, DIC analysis (1, 4, 16 MGs) and FE simulations (1 MG) showing the bulk deformation behaviour of the as-printed and heat-treated meta-crystals at approximately 10% nominal strain (as labelled on the stress-strain curves) which corresponds to the initial loss in strength.

The properties of the meta-crystals are analysed in more detailed by looking at the compressive mechanical response (normalised by the relative density) and the deformation behaviour of the meta-crystals. The stress-strain curve of the as-printed

meta-crystals (Figure 51a) highlights the strengthening effects of the architecture without the contribution from metallurgical precipitation hardening. The 0.2% proof strength, peak strength (maximum stress prior to the initial drop), post-yield stability, and the energy absorbed at 40% strain all improved with more MGs (reduction in MG size, D), with good repeatability (Figure 52). Compared to the 1 MG meta-crystals (no architected boundary strengthening of polycrystal-like features), the as-printed 16 MGs meta-crystals showed an average (of repeated tests) increase of 12.6% in the yield stress, 15.2% in the peak stress, 23.4% in the energy absorption, and most importantly a substantial decrease of 86.6% in the strength loss due to the first collapse. The 32 MGs meta-crystal effectively avoided the initial collapse synonymous with stretching-dominated lattices, without compromising the strength. The DIC analysis of the compression elucidates the effect of the MG boundaries on the deformation behaviour of the lattice; the MG architecture appears to homogenise the deformation throughout the bulk of the structure, by effectively distributing the localised deformation shear bands (Figure 51c). The number of shortened deformation shear band, therefore, increases with the number of MGs per meta-crystal, hence better redistributing the load and allowing more effective utilisation of the whole structure in load bearing after yielding. xCT data showed the localised deformation was not limited to the free surface observable by DIC, but extended through the thickness of the meta-crystal structure (Figure 53b, f and g). The deformation behaviour agreed with the observed behaviour from the finite element (FE) models; the logarithmic strain contours at 10% nominal strain show more homogenised deformation with more MGs (Figure 51c and d, Appendix E).

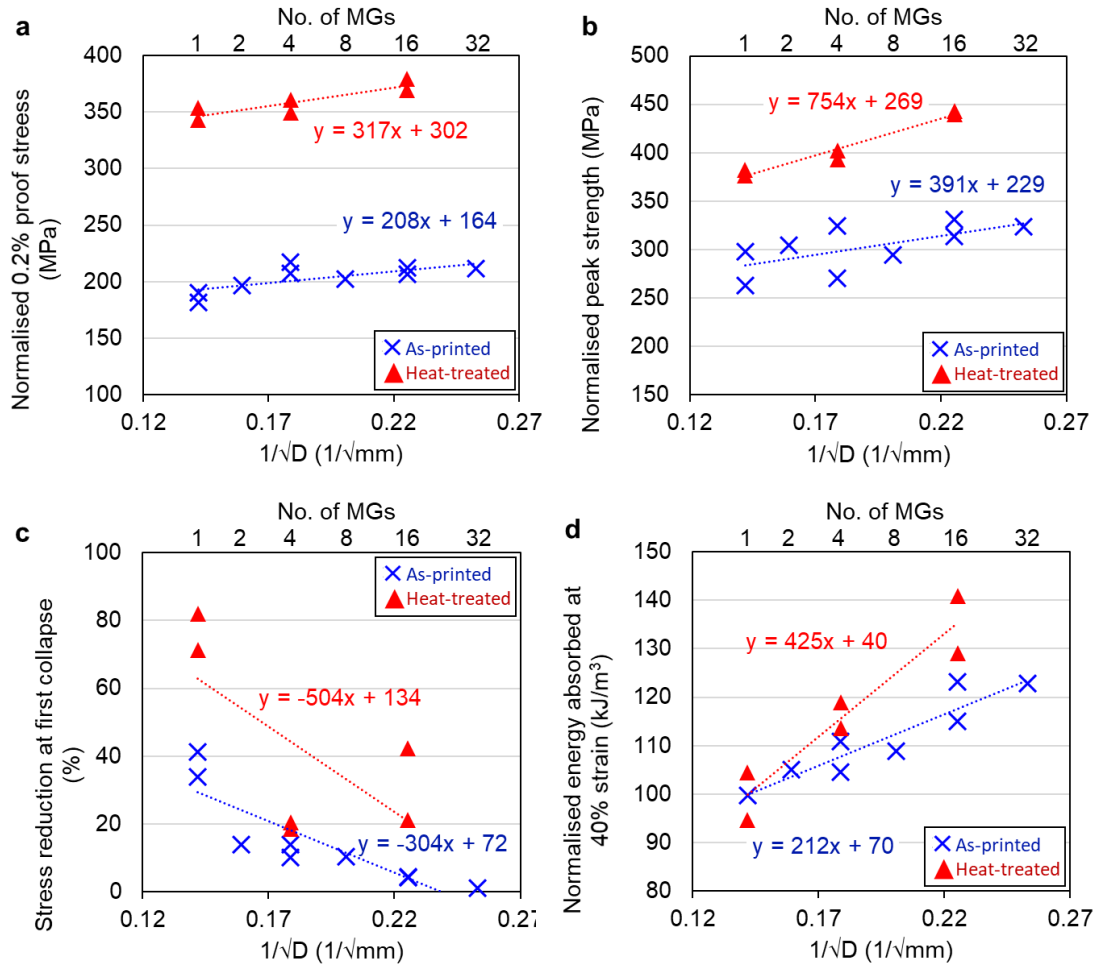


Figure 52 | Correlations between the equivalent MG size and mechanical properties of as-printed and heat-treated meta-crystals. a-b, The normalised 0.2% proof stress and the normalised initial peak strength increased with a reduction in the equivalent MG size. **c,** A reduction in the equivalent MG size effectively eliminated the collapse in the as-printed meta-crystals. The heat-treated meta-crystals showed a similar trend in significantly reducing the relative stress reduction during first collapse. **d,** The normalised energy absorbed by the meta-crystals up to 40% increases with more MGs for as-printed meta-crystals, and more significantly for the heat-treated meta-crystals.

The introduction of the precipitation hardening in the base material significantly improved the proof strength of the 1 MG meta-crystal by 162.5 MPa after the solution annealing + aging heat-treatment (Figure 51a, b and Figure 52a). The change in the microstructure (precipitation) after this heat treatment regime and its effects on IN718 was examined and discussed by Gallmeyer et. al. [179]. The use of the heat treatment on IN718 in this study substantially resulted in increase in the strength of the base material (Appendix C, and also reflected in the hardness measurement of the struts and the nodes Figure 53c). In detail, after the heat-treatment, the material's yield strength increased 62.4%, the hardness increased ~37.8%. This correlates with the 87.4% increase in the yield

strength of the 1 MG meta-crystals after heat-treatment. Although the fracture surface indicated that the fracture of the base material was still ductile (Figure 53f and g) the elongation to failure decreased by about 25.6%. Therefore, the shear band was more localised and intense (Figure 51d), hence more severe stress drop of the 1 MG meta-crystal (Figure 51b and Figure 52c), due to the loss in ductility of the base material. While as-printed struts were plastically deformed and remained unbroken after the first shear band, heat-treated struts were mostly broken (Figure 53f vs g). As expected, the introduction of meta-grain boundary strengthening via the polycrystal-like architecture helped to reduce the stress drop, and almost eliminated the drop for the 16 MG meta-crystal, substantially increasing the energy absorption, Figure 51b and Figure 52c, d. Although the effect of the heat-treatment on the failure of individual struts remained the same: most of the struts in localised shear band were broken and the distribution of shear bands was less homogenous (Figure 53g). The polycrystal-like architecture successfully mitigated the detrimental effect of the ductility loss and enabled a synergistic strengthening to improve both the peak stress and energy absorption with increasing number of MGs (16.4% and 35.6% increase respectively for the 16 MGs in comparison to the 1 MG meta-crystal).

The as-printed and the heat-treated 1MG meta-crystals both showed a non-negligible amount of hardening prior to the initial loss in strength, as opposed to immediate and catastrophic collapse after yield as observed with Ti6Al4V meta-crystals [106]. However, distinctive differences in the hardening behaviours of the as-printed and heat-treated meta-crystals were observed. The magnitude of hardening was greater in the as-printed condition, whereas the rate of hardening was greater in the heat-treated condition, when comparing the 1 MG meta-crystals. The relative increase from the proof to peak strength (meta-crystal hardening) of the as-printed 1 MG meta-crystal was 50.7%, while this was 8.9% for the heat-treated 1 MG meta-crystal (Figure 51a and b). However, the effect of the MG architecture on the hardening behaviour was greater in the heat-treated condition; the meta-crystal hardening of the as-printed 1 and 16 MGs were 50.7% and 54% compared to 8.9% and 17.9% of the heat-treated 1 and 16 MGs.

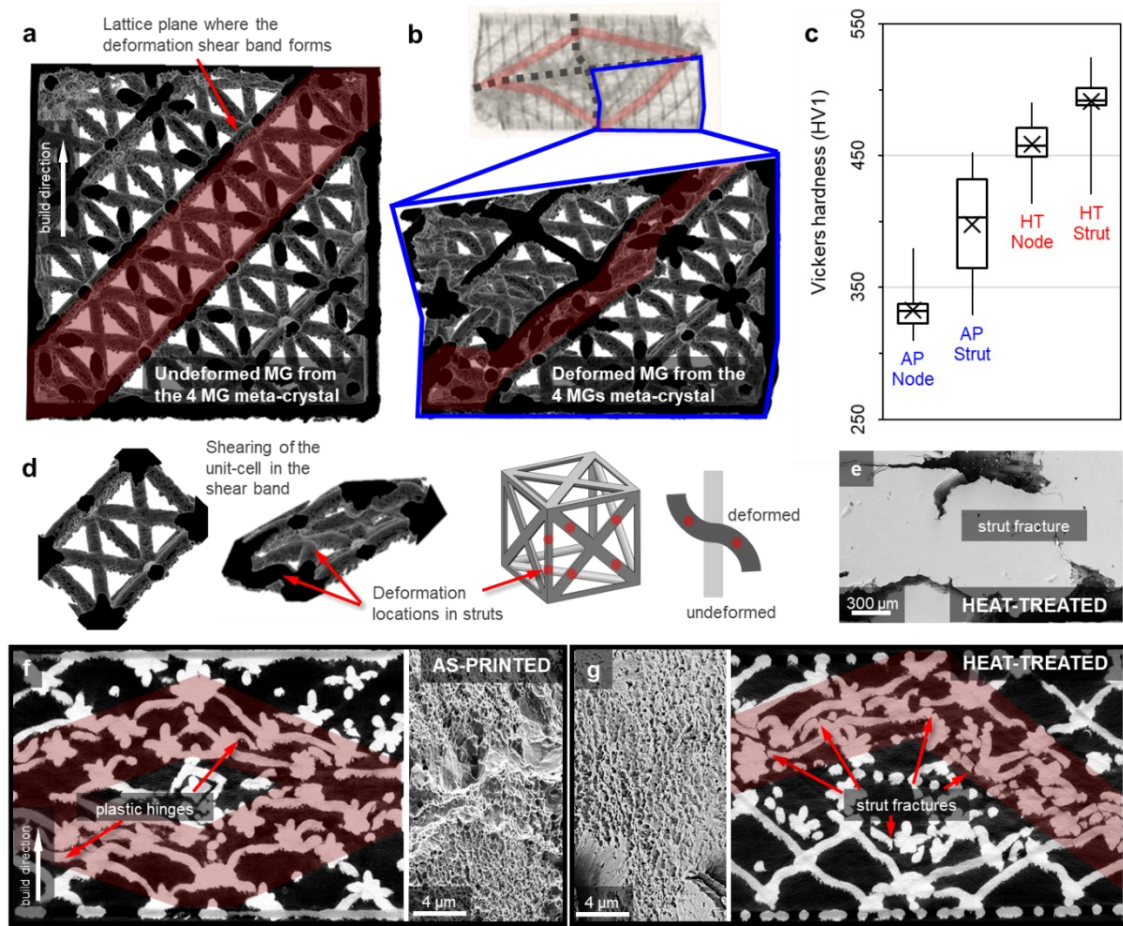


Figure 53 | Meso-scale deformation of as-printed and heat-treated meta-crystals struts. **a-b**, x-CT reconstruction of the undeformed and deformed meta-grain from the as-printed 4 MG meta-crystal showing location of deformation shear band. **c**, Vickers hardness of the as-printed and heat-treated meta-crystals in the node and strut regions taken after the compression test. X denotes the mean hardness. **d**, Shearing of unit-cell in the shear band leads to different deformation modes in the face and edge struts. Location of deformation localisation in strut highlighted. **e**, SEM micrograph showing crack propagation leading to strut fracture in a heat-treated meta-crystal. **f-g**, A slice taken from the post-mortem x-CT scans of the as-printed and heat-treated 4 MGs meta-crystals revealing differences in the deformation behaviour. Plastic hinge formation dominant in as-printed condition while strut fractures dominant in the heat-treated condition. Location of plastic hinge and strut fracture as indicated in d. The fracture surface of struts from the corresponding regions both show dimples indicating ductile fracture.

The deformation behaviour of individual struts was analysed to relate the processing defects and the microstructure to the overall behaviour of the meta-crystals. The deformation behaviour of struts differed in the as-printed and heat-treated condition. xCT observations revealed plastic hinge formation in both as-printed and heat-treated struts due to shearing of the critical deformation plane [301] (Figure 53a-b, f-g). The location of the plastic hinge differed between edge and face struts due to variations in the strut orientation and aspect ratio (Figure 53d). Decreased ductility after heat-treatment (Appendix C) led to more strut fractures at the same location (Figure 53f and

g), particularly in struts where the tensile surface was on the strut's downskin (Figure 53g). The strut orientation relative to the build direction significantly affected the print quality; the average strut diameter and surface roughness worsened with larger inclination angles (0° is parallel and 90° is perpendicular to the build direction). In struts inclined at 0° , 45° , 90° , the average diameters were 0.79 ± 0.01 , 0.80 ± 0.03 , and 0.85 ± 0.04 mm, and the average surface roughness (Ra) were 0.022 ± 0.003 , 0.042 ± 0.016 , 0.060 ± 0.028 mm, respectively (Figure 54a) (measured using a modified ImageJ plug-in analyze_stripes [283], section 3.4.1.1). Additionally, the downskin showed a higher surface roughness than the upskin, its appearance indicative of lack of fusion (Figure 54c). Lack of fusion were mainly observed near the free surface. Most internal pores observed were keyholes and a small fraction of entrapped gas, the former were mostly seen in the struts (Figure 54b) and in the boundaries between the node and strut (Figure 53e), and the latter were uniformly dispersed throughout the consolidated volume. The nodes and struts contain approximate 0.96% and 1.30% volume fraction of internal pores, with an average equivalent diameter of 18.4 ± 16.9 μm (assuming spherical pores). Struts underwent greater deformation than the nodes, as observed by the xCT (Figure 53d, f, and g) and supported by the higher average and the wider range of hardness in the strut regions (Figure 53c) and higher GNDs in the struts after deformation (Figure 55c and f). Typically, nodes act as rigid bodies during initial compression and therefore experience no deformation [233].

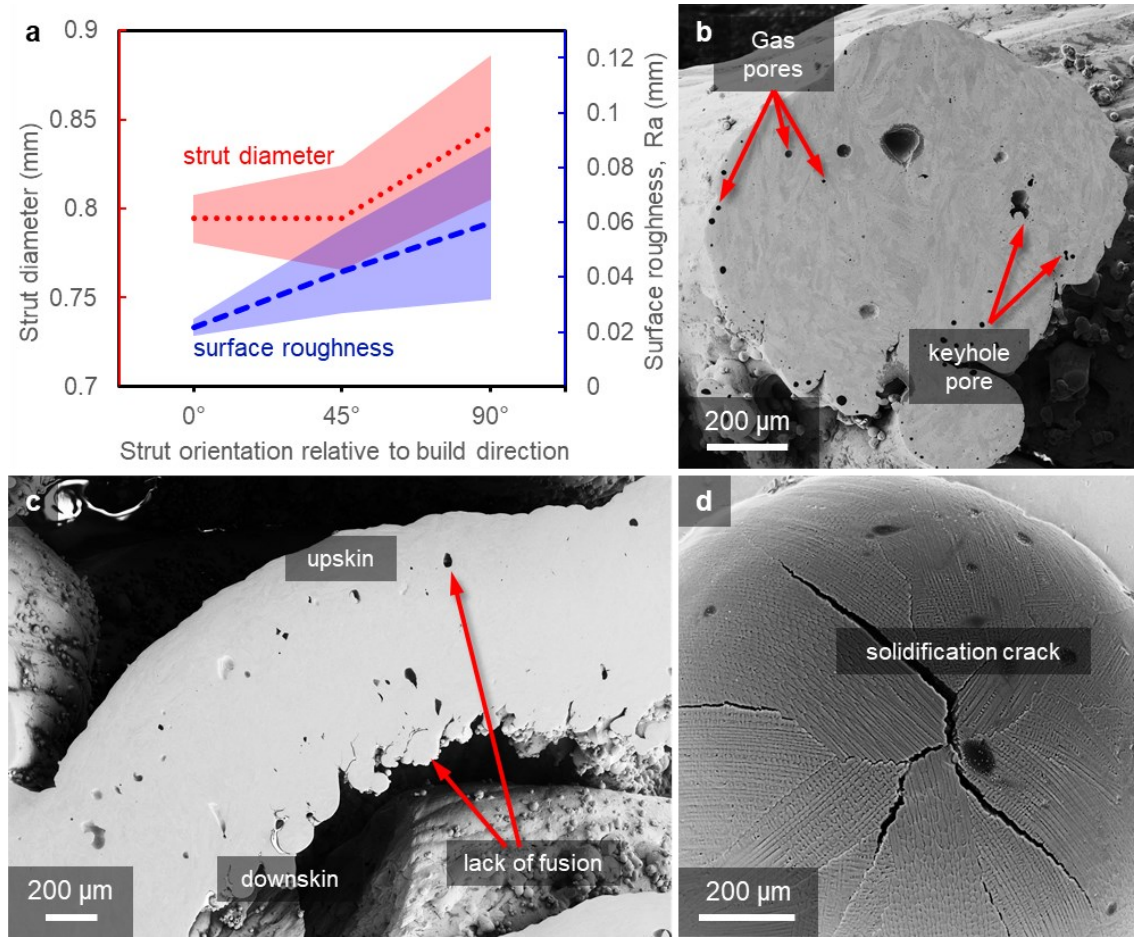


Figure 54 | SEM micrographs revealing processing defects in the meta-crystals. **a**, Mean strut diameter and surface roughness with increasing strut inclination angle obtained from the x-CT data. The geometrical accuracy of the struts worsened and became more varied with horizontally built struts compared to vertically built struts. **b**, **c**, Cross-section of strut showing keyhole, gas, and lack of fusion pores. Lack of fusion on the downskin of the strut led to a much higher surface roughness than the upskin. **d**, Solidification cracks in the intercellular regions with sharp crack tips which induces high stress concentrations.

EBSD maps were acquired in the node and struts of the as-printed and heat-treated meta-crystals to investigate microstructural characteristics including the grain size, shape, and texture. The EBSD measurements revealed an average grain diameter (d) of 47.9 μm in the node and 41.0 μm in the strut (based on high-angle grain boundaries, HAGBs, $>10^\circ$). No apparent change to the grain structure was observed after heat-treatment. Columnar grains were still visible in both the node and strut regions, although not as prominent as elsewhere observed in bulk specimens [337], while finer, more equiaxed grains were observed near the free surface and in the node boundaries (Figure 55a and d). The larger surface area to volume ratio of struts compared to the nodes (and therefore a higher cooling rate and G in the strut) leads to the smaller average grain size. Moreover, the crystallographic orientation of the columnar grains' primary axis (also $\langle 001 \rangle$ directions)

were influenced by both the build direction and the strut orientation. As a result, the microstructure was far less textured than the typical fibre texture observed in solid, bulk samples fabricated by AM. Heat-treatment also led the formation of a thin oxide layer that penetrated $<2\ \mu\text{m}$ below the free surface (Appendix G).

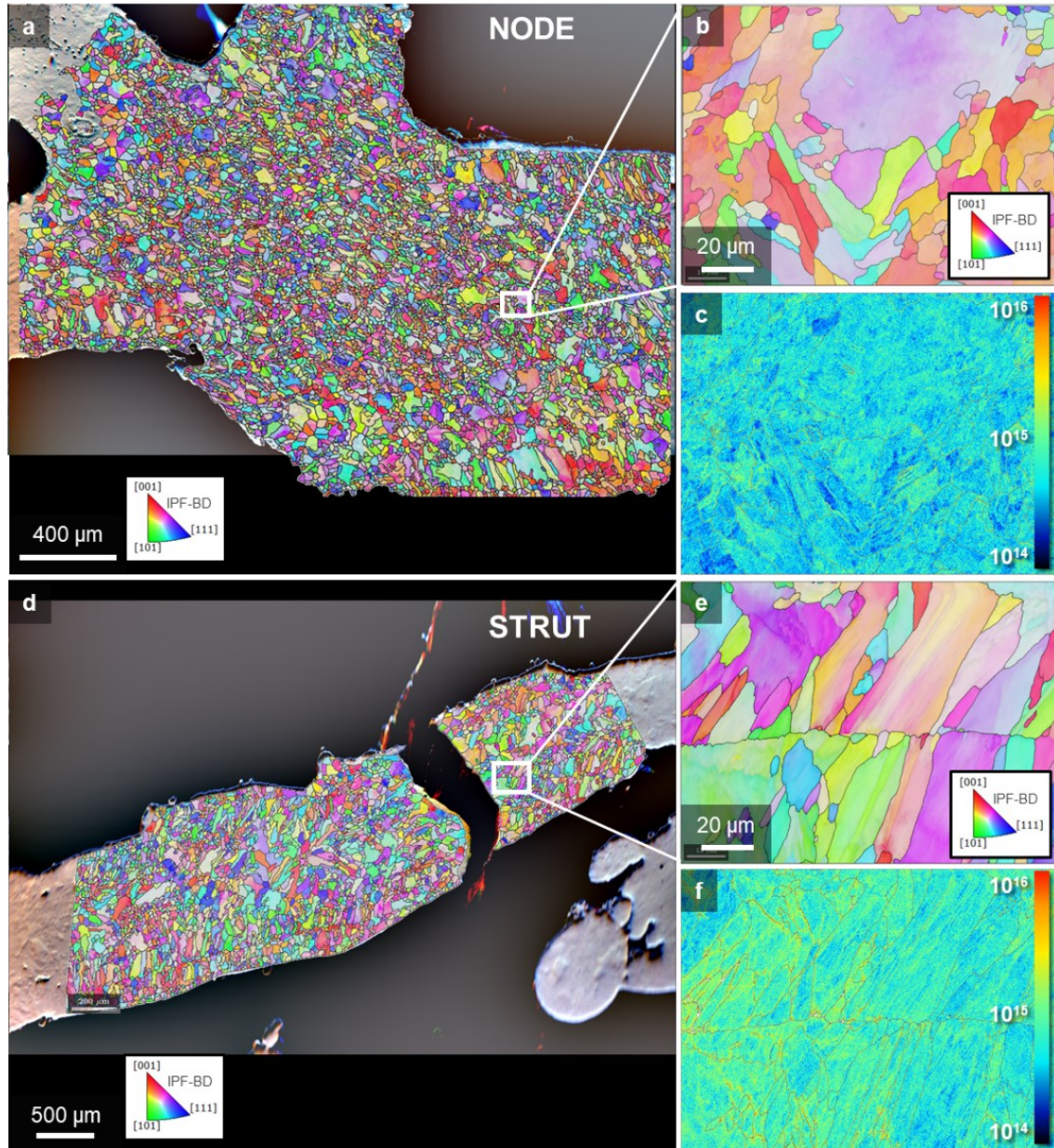


Figure 55 | Grain structure and deformation in the node and strut regions of a heat-treated meta-crystal. **a, d**, EBSD IPF-Z (into the page) maps of the node and strut regions. Build-direction was almost parallel to the Z direction. Grains near the free surface were typically smaller than those in the strut interior. Both regions showed weak crystallographic texture. **b-c, e-f**, High magnification EBSDs and the corresponding GND analysis in the node and strut regions. Higher levels of deformation observed in the strut region, while some deformation was observed in the node.

Characterisation of the subgrain structure revealed solidification cells in the as-printed condition. Differently from deformation cells, solidification cells have slender rod-like morphology (Figure 56a) due to continuous epitaxial growth, with the primary axis aligned to the local heat-flux direction during cooling. As the cooling rate directly affects the cell spacing [172], large variations in the cell spacing was observed in the struts due to the intricate geometry and complex thermal conditions. The average diameter (d_c) of cells was $0.85 \pm 0.27 \mu\text{m}$ (Figure 56b). Cell boundaries appeared to contain Laves and carbides (Figure 56c), as well as dense dislocation networks (Figure 56d). Chemical segregation was also observed between the boundary and the matrix, where the boundary was enriched in Nb with a slight increase in concentration of Ti (Figure 56e). The segregation was homogenised by the heat-treatment and the dislocation density decreased, despite the short solution annealing time which was supposed to preserve the dislocation networks. Cells were not apparent after heat-treatment; however, secondary phases were present in the prior cell boundaries (Figure 56g, h, and i), understood to predominantly be the δ -phase as predicted by the ThermoCalc simulation (Figure 56f). The heat-treatment also precipitated the strengthening γ' and γ'' phases, dispersed homogeneously throughout the matrix, which were not present in the as-printed condition (Figure 56g and h). The morphology of γ' and γ'' precipitates differed, [179] reported γ' as shorter and rounder while γ'' were more elongated, both were observed by SEM after heat-treatment (Figure 56i and j). The average equivalent diameter of the γ' and γ'' were $25 \pm 20 \text{ nm}$, consistent with the ThermoCalc simulation which predicted a mean diameter of 28 nm (Figure 56f). The volume fraction of γ' and γ'' phases were also consistent between the simulation and the SEM, ~14%. Evidence of precipitate shearing was also revealed in the bulk specimen by TEM (Figure 56i).

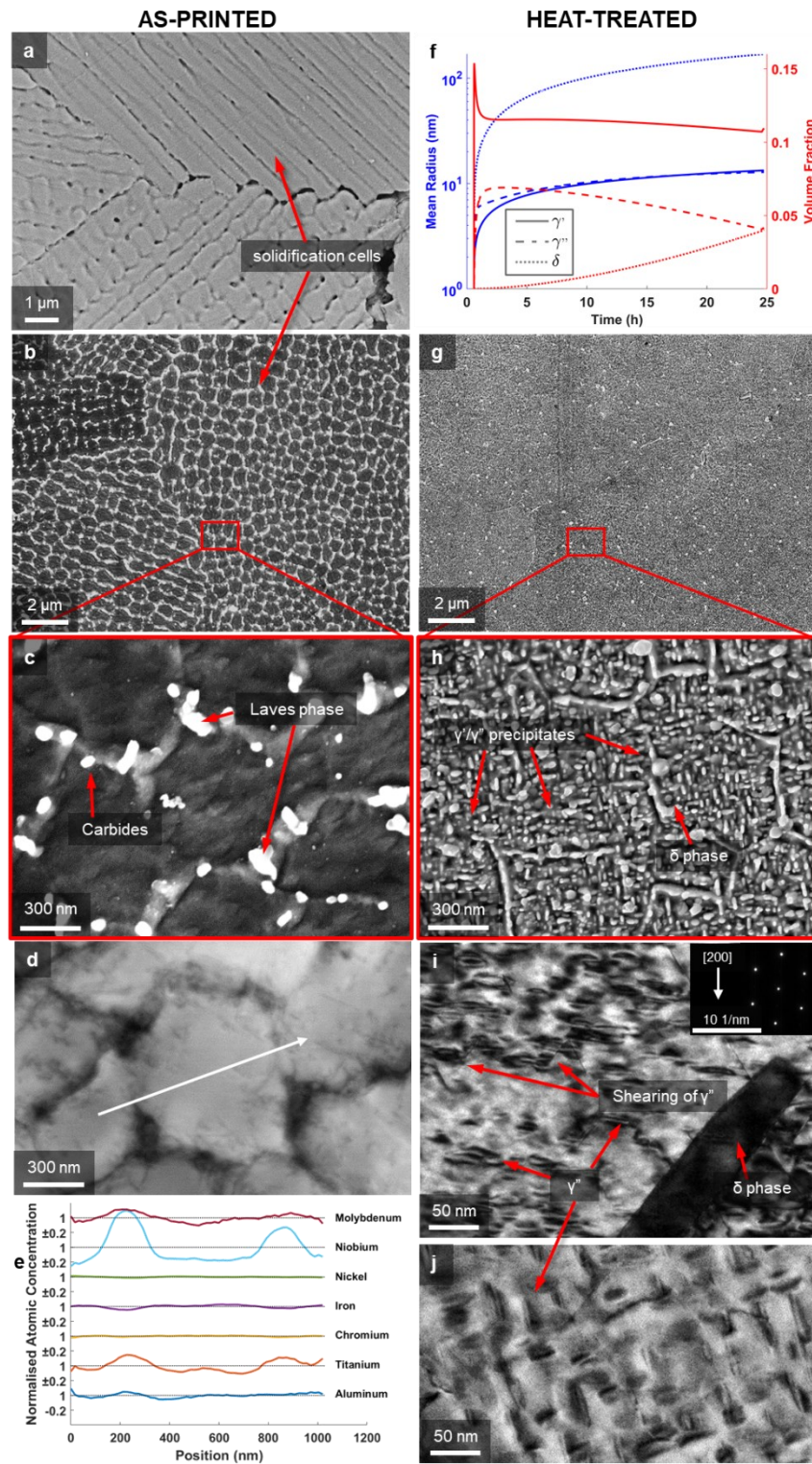


Figure 56 | The effect of the heat-treatment on the microstructure of meta-crystals. **a-c**, SEM micrograph showing orthogonal domains of rod-like solidification cells with Laves and carbides in the intercellular regions **d-e**, EDS line scan across cell boundary and interior showing chemical segregation. **f**, ThermoCalc simulation showing the effect of the heat-treatment on the mean radius and the volume fraction of the precipitates. (ThermoCalc simulations by Bogdan Dovgvyi) **g-h**, SEM micrographs revealing γ'/γ'' homogeneously dispersed with δ precipitates in the prior boundaries. **i-j**, TEM of γ'/γ'' with evidence of precipitate shearing. (TEM images captured by Alessandro Piglione).

6.4. Constitutive formulations

Strengthening of meta-crystals in this study were from both intrinsic crystalline microstructure and extrinsic architected meso-structures across different lengthscales. This section develops the constitutive laws for describing polygrain-like meta-crystals by deconvoluting the strengthening from each hierarchical structure. The strengthening sources were considered independently through well-established scaling laws.

The compressive yield strength of stretching-dominated structures, σ_y , scale linearly with the relative density, $\bar{\rho} = (\rho/\rho_s)$, (Eq. 6.1) [254]; where σ_{y_s} is the yield strength of the base material, m depends on the deformation behaviour (ranging from 1-1.5 as deformation changes from stretching to bending dominated behaviour), and C is a constant of proportionality which accounts for the influence of all geometrical information about the lattice except for the relative density [1,220]. This includes geometrical information such as the architected lattice topology, strut orientation, strut cross-section, and defects [346].

$$\sigma_y = C\sigma_{y_s}(\rho/\rho_s)^m = C\sigma_{y_s}\bar{\rho}^m \quad (6.1)$$

However, it is empirically determined and therefore lacks the required clarity when quantifying the contribution from the polygrain-like architecture. This necessitates an additional term to describe such designs. The effect of the architected boundaries was shown to inversely scale with the square root of the equivalent MG size (Figure 51b), analogous to the well-known Hall-Petch relationship of intrinsic polycrystal microstructure, which states that the yield strength is inversely proportional to the square root of the grain size (Eq. 6.2) [55,56]. Here, σ_{0_s} is the yield strength of single crystal (i.e., strength induced by the friction stress and solid solution) of Inconel 718, σ_{HP} is the strengthening from the Hall-Petch effect, k is the Hall-Petch coefficient, and d is the average grain size. Considering that a meta-grain is analogous to a crystalline grain, the scaling law for polycrystal-like meta-crystals can be written as Eq. 6.3, where K is the Hall-Petch-like constant and D is the equivalent MG size, $\bar{\rho}$ is the relative density $\bar{\rho} = (\rho/\rho_s)$, and $m = 1$.

$$\sigma_{y_s} = \sigma_{0_s} + \sigma_{HP} = \sigma_{0_s} + k/\sqrt{d} \quad (6.2)$$

$$\sigma_y = C(\sigma_{y_s} + K/\sqrt{D})\bar{\rho}^m \quad (6.3)$$

Strengthening contributions from the crystalline grains, solidification cells, and precipitates are encompassed by the intrinsic strength of the base material, σ_{y_s} in Eq. 6.3. For crystalline grain boundary strengthening, the Hall-Petch relationship is used (the first two terms of Eq. 6.4). To account for the contribution from solidification cells, an additional term (the third on the right-hand side of Eq. 6.4) accounting for the dislocation densities decorating the boundaries, was appended in Eq. 6.4 (where α is the proportionality factor, M is the Taylor factor, G is the shear modulus, b is the Burgers vector, and ρ is the immobile dislocation density). This was shown to be accurate for L-PBF CoCrFeNiMn alloy [347]. The dislocation density at the solidification cell boundaries can be related to the cell spacing according to the scaling law established for deformation cells (Eq. 6.5) [348,349], where λ_c is the dislocation cell diameter, which has been shown to fit well in previous studies [179,347].

$$\sigma_{y_s} = \sigma_{0_s} + \sigma_{HP} + \sigma_{cells} = \sigma_{0_s} + k/\sqrt{d} + \alpha M G b \sqrt{\rho} \quad (6.4)$$

$$\rho = 200/\pi\lambda_c^2 \quad (6.5)$$

Substituting Eqs. 6.4 and 6.5 into Eq. 6.3 gives the scaling relationship between the normalised compressive strength of as-printed IN718 polygrain-like meta-crystals and its hierarchical strengthening sources (Eq. 6.6), where C is the geometric constant of proportionality.

$$\sigma_y/\bar{\rho} = C(\sigma_{0_s} + k/\sqrt{d} + \alpha M G b \sqrt{200/\pi\lambda_c^2} + K/\sqrt{D}) \quad (6.6)$$

The base material's yield strength in the as-printed condition, as represented by $\sigma_{0_s} + k/\sqrt{d} + \alpha M G b \sqrt{200/\pi\lambda_c^2}$ in Eq. 6.6, can be calculated using the values in Table 7. This was calculated to be ~703 MPa, which is in very good agreement with the experimentally obtained yield stress of 755 ± 28 MPa from bulk samples (Appendix C). Note, the yield stress of a single crystal of 325 MPa [341] includes the friction stress and solid solution strengthening effects, which is higher in the as-printed condition due to rapid cooling.

Table 7 | Parameters for as-printed IN718.

Parameters	Definition	Value	Unit	References
$\sigma_{0,S}$	<i>Friction stress + Solid solution</i>	325	MPa	[341]
k	<i>Hall-Petch coefficient</i>	750	MPa · $\mu\text{m}^{1/2}$	[350]
α	<i>Proportionality factor</i>	0.5	-	[351]
G	<i>Shear modulus</i>	77	GPa	[281]
b	<i>Burgers vector</i>	0.2359	nm	[73]
M	<i>Taylor factor</i>	3.06	-	[349]
d	<i>Average grain size</i>	41.0	μm	EBSD analysis
λ_c	<i>Average cell diameter</i>	0.85	μm	SEM analysis
K	<i>Architected polycrystal coefficient</i>	892	MPa · $\text{mm}^{1/2}$	Empirical fitting
D	<i>Average MG size</i>	n/a	mm	Model specific

The geometric constant of proportionality, C , is primarily considered as the influence of defects, as other geometrical characteristics are constant across meta-crystals (aside from the polycrystal-like architecture, which are accounted for in K/\sqrt{D}). The influence of defects depends on the deformation behaviour of struts, the base material behaviour, and the type and quantity of defects. Assuming pin-jointed structures, stretching-dominated lattices carry equal axial loads in all its members when compressed [16], however, studies have shown that struts parallel to the loading direction carry a significantly greater load [171,231]. FE models in this study reaffirm this and the highest stressed struts are generally ones parallel to the loading direction (Appendix E). As such, the influence of defects increases as struts are more aligned to loading direction. However, since defects near the free surface are more influential (deformation by elastic buckling and plastic hinge (Figure 54) [352]), and the surface roughness and geometrical accuracy improves as struts are more aligned to the build direction (also loading direction), the influence of defects is minimised. Furthermore, the influence of defects was assumed to be similar for all meta-crystals as the angle of lattice orientation in each MG with respect to the loading direction was the same (to negate the effect of strut orientation); as such, differences in the defects between builds are due to the statistical deviation from the fabrication process, not the MG design. Assuming constant C for all meta-crystals, linear fitting of the normalised 0.2% proof stress against $1/\sqrt{D}$ in Figure 52b determined KC to be 208 and $C(\sigma_{0,S} + k/\sqrt{d} + \alpha M G b \sqrt{200/\pi \lambda_c^2})$ to be 164 MPa for the as-printed meta-crystals. Comparing with the previously calculated value for the

material's yield strength implies that $C = 0.23$ and $K = 892 \text{ MPa} \cdot \text{m}^{1/2}$ (for the as-printed meta-crystals).

After heat-treatment, the strengthening contribution from the precipitates needs to be considered. Although the heat-treatment was designed with a short annealing time to preserve the dislocation substructure at the cell boundaries, this was not observed; therefore, the strengthening contributions from the solidification cells were considered to be negligible after heat treatment. The heat-treatment did however homogenise the chemical segregation and dissolves the Laves phase, allowing a higher volume fraction of γ' and γ'' to be precipitated. The stress required to overcome precipitates depends on its size; shearing is more favourable for smaller precipitates and bowing is more favourable for larger ones. While the strengthening from γ'' is generally larger than γ' [353], the larger volume fraction of γ' precipitates observed (Figure 56) makes their strengthening contributions non-negligible. As such, the influence of γ' and γ'' precipitates in this study are assumed to be equal and are considered together. The critical γ'/γ'' precipitate radius that determines if the precipitates are sheared was shown elsewhere to be 12 nm [351], which is marginally less than the average radius of 12.5 nm observed in this study. While this suggests that similar amounts of bowing and shearing can be expected with a normal distribution of precipitate size, a more accurate size distribution function from the Lifshitz-Slyozov-Wagner theory [354] suggests that 58% of precipitates are sheared when the mean precipitate radius equals to the critical radius. With more observed evidence of precipitate shearing (Figure 56i), as consistent with similarly sized γ'/γ'' observed elsewhere [355], shearing of γ'/γ'' is assumed to be the sole mechanism for precipitate deformation in this study for simplicity. The strengthening contribution from the precipitates can therefore be described by Eq. 6.7 [351], where f_p is the volume fraction of precipitates and k_c is an empirically determined constant.

$$\sigma_p^{shear} = k_c M G \sqrt{3 f_p / 2 \pi} \quad (6.7)$$

Appending Eq. 6.7 to Eq. 6.6 gives the complete description of the strengthening contributions from the hierarchical structures in heat-treated IN718 meta-crystals, Eq. 6.8.

$$\sigma_y/\bar{\rho} = C(\sigma_{0_S} + k/\sqrt{d} + \alpha MGb\sqrt{200/\pi\lambda_c^2} + k_c MG\sqrt{3f_p/2\pi} + K/\sqrt{D}) \quad (6.8)$$

Table 8 | Additional parameters for heat-treated IN718.

Parameters	Definition	Value	Units	References
k_c	<i>Calibration constant</i>	10.5	-	Calibrated
f_p	<i>Volume fraction of γ'/γ''</i>	0.21	-	SEM analysis
K	<i>Architected polycrystal coefficient</i>	892	MPa · mm ^{1/2}	Empirical fitting

Similar to the as-printed condition, the base material's yield strength after heat-treatment can be calculated from $\sigma_{0_S} + k/\sqrt{d} + k_c MG\sqrt{3f_p/2\pi}$ using the values mentioned previously in addition to the values in Table 8. Using the experimentally obtained yield stress of the base material (1226 ± 22 MPa), the calibration constant, k_c , was determined to be 10.5. From the linear fitting of the yield strength versus $1/\sqrt{D}$ in Figure 52b and the theoretically calculated value for the yield stress, C and K are calculated to be 0.25 and 1250 MPa · m^{1/2}, respectively. As heat treatment (without hot isostatic pressure) should not affect the processing defects, the geometric factor C should remain unchanged. Very similar C values for the as-printed and heat-treated conditions confirms that the influence of defects did not significantly change after heat-treatment.

6.5. Discussions

The strengthening effects of the MGs architecture were more significant after heat-treatment, as indicated by the larger K value. The larger K value more likely indicates that the architecture and the microstructure were synergistically strengthening the meta-crystal. Macroscopic yielding leads to shear deformation in each MG (Figure 53a-c), on the {200} plane as previously identified in such lattices [301], and form plastic hinges in the struts on the shear plane (Figure 53d). The struts in the localised deformation band first buckled as the critical buckling stress is lower than the yield stress, as determined using Johnson's parabolic formula for less slender struts (Appendix H). Immediately following buckling, plastic hinges occurred in the strut at the buckled locations identified in Figure 53d. Such plastic deformation results in intrinsic precipitation hardening due to interaction between dislocations and γ' and γ'' in individual struts,

making deformed struts stronger. Stronger struts increase the strengthening effects of the MGs in two ways. Firstly, the strength of the MG boundary was shown to increase with the strut connectivity at the boundary [298], therefore more boundaries increases the meta-crystals' strength. Additionally, since planes of struts buckling lead to lateral translations, an aggregate of MGs resist macroscopic compression by requiring the formation of localised deformation bands in each MG. Therefore, more MGs leads to more struts deforming, and increasing the struts' strength therefore collectively enhances the meta-crystals' strength.

The constitutive equation Eqn. 7 allows a deconvolution of the strengthening contribution from each source for the as-printed and heat-treated meta-crystals with increasing number of MGs (Figure 57a and b). While the solidification cells account for a large fraction of the strength in as-printed meta-crystals, replacing them with γ'/γ'' precipitates by heat-treatment provided a significant improvement in strength in the heat-treated meta-crystals (Figure 57 b versus a). It may be worthwhile to modify the heat-treatment regime to preserve the solidification cell structures while still precipitating the γ' and γ'' (as reported in bulk samples [179]). A shorter annealing time may be required due to the much larger surface-to-volume ratio of lattice struts compared to bulk specimens. The relative contribution of the MG architecture became more prominent with increasing number of MGs, particularly in the heat-treated meta-crystals; the contribution from the MG architecture in the heat-treated 32 MG meta-crystal is greater than that of the grain boundaries and the solidification cells in the as-printed meta-crystals (Figure 57a and b). Potential increase in grain boundary strengthening can be achieved via site specific control of the printing parameters. Selecting the appropriate border/downskin processing parameters to promote finer grains and suitable texture [14] near the free surface may be effective in improving the strength of struts.

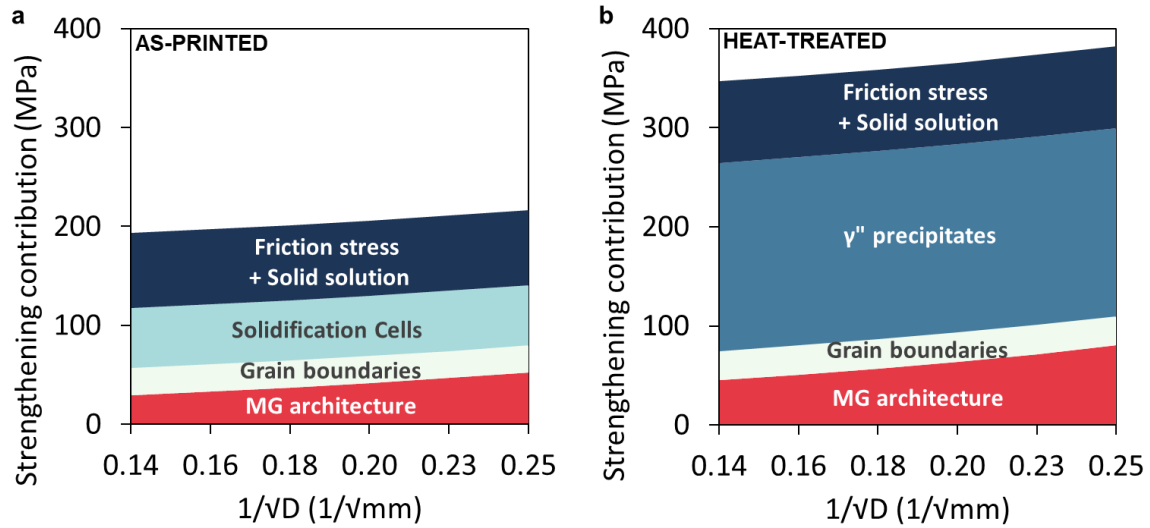


Figure 57 | Strength contributions induced by fractal structure sources. a, b, Breakdown of the strengthening contributions from the hierarchical features in the as-printed and heat-treated meta-crystals with increasing number of MGs (based on Eq. 6.8).

In addition to the increase in strength, the MG architecture more notably minimises the stress drop from the initial collapse and improves the mechanical stability thereafter (Figure 52). Doing so without compromising the strength provides the meta-crystals with an exceptional energy absorption capacity. The MG architecture minimises the stress drop by homogenising the deformation shear band in the structure (Figure 51c and Figure 53). However, a less homogenised deformation was seen after the heat-treatment for the same MG architecture. While the heat-treated 16 MGs meta-crystal still appreciably improved on the stress drop and energy absorption performance from the 1 MG meta-crystal (Figure 52d and e), it was less effective in eliminating the stress drop compared to the as-printed meta-crystals. The heat-treatment reduced the elongation to failure (Appendix C) which increased occurrences of strut fractures in the shear band (Figure 53). Heat-treated struts also shows less intrinsic hardening. A smaller difference between the peak and yield strength of the heat-treated meta-crystals (Figure 51a and b, Figure 52b and c), and the smaller variation in the hardness measured in the strut (Figure 52f), both suggests premature fracture of struts. Strut fractures prevented the stress distribution to the surroundings (Figure 51c and d, and Figure 53e and f) which reduces the strengthening from the MGs there. Nevertheless, the MG architecture reduces the

detrimental effect of the low elongation to failure, to enable significant increase in energy absorption capacity in combination with the high strength.

The energy absorption capacity of heat-treated meta-crystals can be further improved by minimising the premature fracture. This can be achieved by improving the surface finish and elongation to failure of struts. The surface finish of additively manufactured lattice struts have been successfully improved elsewhere in post-processing by electrochemical polishing [156]. The proposed method reduces the surface roughness caused by the partially melted particles and the profile caused by balling and staircases, which resulted in almost double the compressive strength and energy absorption of 316L stainless steel BCC lattices. Similar effectiveness shown with 4130 steel and AlSi10Mg lattices indicates potential for application to other alloys such as IN718. The elongation to failure of struts may be improved with a more appropriate heat-treatment environment. Characterisation of the meta-crystals in this study revealed a thin layer of oxide (Appendix G) which may have detrimental effects, in particular in promoting crack initiation. Heat-treatment in a fully inert atmosphere or in a high vacuum environment will prevent the formation of oxides, thus increasing the elongation to failure of struts. Additionally, alternative architected strengthening features (such as meta-precipitates or meta-phases inspired by the metallurgical precipitation and multiphase hardening, respectively) can be adopted in meta-crystals. Similar fractal-like meta-precipitates can be included to possibly guide and tailor deformation shear bands to prevent catastrophic collapse in meta-crystals and further enhance the strength.

6.6. Conclusions

Heat-treated IN718 Polycrystal-like meta-crystals in this study displayed an excellent combination of strength and energy absorption capacity owing to synergistic strengthening features across multiple length-scales. The strengthening sources were characterised and analysed to help deconvoluting the strengthening contributions and the development of the constitutive law to describe polycrystal-like meta-crystals. Fractal-like boundary strengthening features from the MG architecture, crystalline grains, and solidification cells dominantly control the behaviour of the as-printed meta-

crystals. After a solution annealing + ageing heat-treatment, strengthening from γ'/γ'' precipitates became much more prominent and significantly increased the strength of the base material and the meta-crystals. The heat-treatment increased the yield strength of all the meta-crystals. The separate effect of heat treatment on the strength improvement was revealed in the 1 MG meta-crystal with 87.4% strength increase, but with a significant loss in strength after plastic yielding due to decrease in the ductility of the base material. Larger stress drops in the heat-treated condition correlate with increased occurrences of strut fractures. Such loss was mitigated and almost eliminated by the polycrystal-like architecture. The heat-treated 16 MGs meta-crystals reduced the loss in strength from ~75% to ~30% and eliminated the loss in strength entirely in the as-printed condition. The significant reduction in the stress drop resulted in 23.4% and 35.6% increases in the energy absorption from the 1 MG to the 16 MGs meta-crystals in the as-printed and heat-treated conditions, respectively. The combination of strength and energy absorption capacity enabled by the synergistic strengthening of the material and the polycrystal-like architecture demonstrated the potential of the meta-crystal approach to design lightweight, but high strength and damage tolerant materials. This presents an opportunity to explore other crystal-inspired architected strengthening features for high performance applications.

Blank

Chapter 7

Conclusions and Future Work

7.1. Conclusions

This study investigated the mechanical behaviours of metallic polycrystal-like meta-crystals, with the lattice architecture containing differently oriented domains analogous to crystalline grains. The study separately analysed the influence of features at different length scale to elucidate their contributions to the mechanical behaviour of meta-crystals, before analysing the combined synergistic strengthening effects.

Chapter 4 investigated the influence of the processing defects on the efficacy of the polycrystal-like architecture. Quasi-static compression tests of as-printed Ti-6Al-4V meta-crystals containing 1, 2, 4, 8, 16, 32, 64 MGs revealed that the polycrystal-like architecture slightly increased the strength and the energy absorption capacity of the meta-crystals but were mostly overwhelmed by the influence of defects. DIC analysis showed that the localised deformation bands were not affected by the MG boundary. Struts prematurely fracture causing progressive crumpling of lattice planes which prevented the MG boundary deflecting and distributing the deformation bands. The premature fracture of struts was attributed to a combination of the brittleness of as-printed Ti-6Al-4V with the significance of the processing defects. The processing defects characterised by x-CT and SE imaging showed that lack-of-fusions near the surface were the most significant. Two options were explored to increase the efficacy of the meta-crystals: 1.) an annealing heat-treatment to reduce the internal stresses and to transform the acicular α' martensitic microstructure to a typical $\alpha+\beta$ microstructure and 2.) increase

the strut diameter to reduce the stress concentration effect of the notch-like surface lack-of-fusion. The heat treatment reduced the relative loss in strength and the mechanical stability in the plateau region, but at the expense of the normalised peak strength. Therefore, no improvements to the energy absorption capacity were obtained. Increasing the strut diameter significantly improved the normalised peak strength, highlighting the reduced roles of the processing defects (reduced stress concentration from notch-like defects), although the initial stress drop remained significant. There were also some improvements in the efficacy of the MG architecture with increasing the strut diameter. Combining both approaches obtained a noticeable improvement, suggesting the importance of the base material's properties in accommodating the surface defects on the struts. The normalised peak strengths of the annealed meta-crystals remained comparable to the as-printed meta-crystals, while the stress drop reduced and the efficacy of the MG architecture increased, leading to a significant increase in the energy absorption capacity with increasing the number of MGs.

Chapter 5 investigated the effect of the base material on the mechanical behaviour of meta-crystals fabricated from different base alloys such as IN718, Ti-6Al-4V, and 316L. The yield strength of the 1 MG meta-crystal is proportional to the yield strength of the base material, conforming to the Gibson-Ashby model. The yield strength and energy absorption capacity increased with more MGs for all the base materials, with IN718 showing the most significant increase followed by 316L then Ti-6Al-4V. This is due to the differences in the intrinsic deformation behaviour and the tolerance to processing defects of the base material. Base materials with higher ductility and work-hardening were more tolerant to defects, which prevented premature fracture of struts, enabling the strengthening effects of the architecture and resulting in homogeneous deformation throughout the structure. The study demonstrated that the appropriate combination of the metallurgical microstructure and the polycrystal-like architectural design allows for significant strengthening of the meta-crystals. While Ti-6Al-4V meta-crystals exhibited high strengths, the low elongation to failure and work hardening amplified the influence of the processing defects which suppressed the strengthening of the architecture. For 316L meta-crystals, the base material has excellent ductility in as-printed condition. There were virtually insignificant stress drops after the initial yielding and, therefore, it was

not necessary to introduce the polycrystal-like structure to reduce the post-yield stress reduction. However, IN718 meta-crystals exhibited an extremely promising compressive mechanical response. With an excellent combinations of yield strength and ductility, the 4 and 8 MGs meta-crystals exhibited both high yield and plateau stresses of approximately 300 MPa.

Chapter 6 developed on the findings obtained in the previous two studies. By understanding the interplay between the processing defects and the base material properties on the deformation behaviour, IN718 was determined to be an outstanding candidate of the base material to enable a synergistic strengthening induced by both metallurgical microstructure and architected mesostructures to achieve a high strength and excellent damage tolerance for lightweight polycrystal-like meta-crystals. IN718 meta-crystals containing 1, 2, 4, 8, 16, and 32 MGs were investigated in this study. The stress drop in the as-printed meta-crystals were successfully eliminated with the 32 MGs meta-crystals, while also increasing the yield strength by 12.6% from the 1 MG meta-crystal. The solution annealing and ageing heat treatments enabled precipitation strengthening in the meta-crystals. The heat treatment significantly increased the yield strength of the 1 MG meta-crystal (62.4%) but worsened the initial loss in strength (increase from 38% to 75%). However, increasing the number of MGs to 16 significantly minimised the stress drop by 30%. The heat-treated 16 meta-crystals also showed a 97.5% increase in yield strength and a 33.5% increase in the energy absorption capacity compared to the as-printed 1 MG meta-crystal. The properties of the heat-treated IN718 were able to accommodate the processing defects and enable the synergistic strengthening of the heat treatment and the architecture, resulting in an exceptional peak strength and energy absorption capacity of the meta-crystals. The strengthening contributions at each length scale were also deconvoluted for the development of a theoretical model for the strength of polycrystal-like meta-crystals, providing a basis for designing high-strength meta-crystals in the future. It was shown that the contributions from the γ' and γ'' precipitates and the MG architecture were the most significant in the heat-treated 32 MGs meta-crystals, while the contributions from the solidification cells and the MG architecture were the most significant in the as-printed 32 MGs meta-crystals.

7.2. Recommendations for future works

The work completed in this study has elucidated the influences of various hierarchical features on the compressive mechanical behaviours of polycrystal-like meta-crystals. The study identified several avenues to explore in the future to realise the potential of the meta-crystal approach in developing lightweight, high-strength and damage-tolerant materials. These recommendations are mainly for polycrystal-like meta-crystals. Certainly, there are numerous potential studies relating to other crystal-inspired architectures such as meta-precipitates or multi-phase meta-crystals; the presence of lattice domains with different lattice parameters or lattice topologies to the matrix lattice was shown to affect the deformation behaviour in PLA meta-crystals. For example, stronger and stiffer meta-precipitates which disrupt the propagation of the localised deformation bands can be combined with the polycrystal-like architecture. With known deformation behaviour in polycrystal-like meta-crystals, meta-precipitates can be strategically positioned in each meta-grains to further strengthen the meta-crystals and better control the shear band activities (Figure 58).

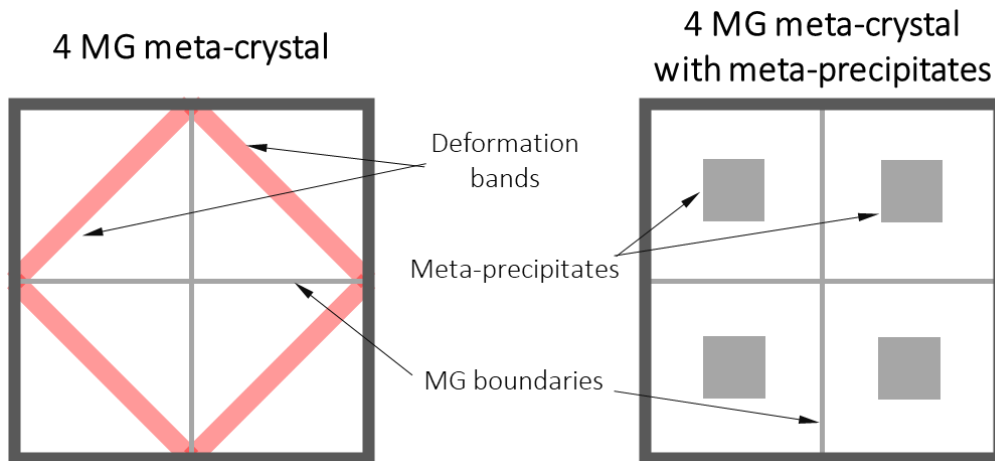


Figure 58 | Potential combination of the polycrystal-like architecture with meta-precipitates to disrupt the known location of the localised deformation bands.

The polycrystal-like architecture designs were kept mostly consistent in this study, i.e., the MGs were similarly oriented to the loading direction, adjacent MGs were similarly misoriented to each other, only vertical and horizontal MG boundaries were used, etc. This is to deconvolute the effect of the MG size and the influence of other length scale

features. However, with better understanding of the synergistic strengthening in the hierarchical structure, it would be interesting to investigate different polycrystal-like architectures. It is known in metallurgy that different boundary types and grain orientations relative to the loading direction, and misorientation angles also affect the deformation of polycrystals. Therefore, future studies to investigate different boundaries (e.g., twist boundaries, varying the coincident lattice sites, etc.) and the mechanisms in which different MG boundaries interact with the propagating deformation band would deepen our understanding of polycrystal-like meta-crystals.

Another avenue to explore is the behaviour of meta-crystals under different loading conditions. A major objective of the strengthening architecture was to increase the energy absorption capacity of the meta-crystals, which was achieved for quasi-static compression loading. However, energy-absorbing applications tend to be at high strain rates, e.g., car crumple zone, protective helmets, armours, etc. The formation of deformation bands in meta-crystals may vary under higher strain-rate loadings. Additionally, the study could investigate different meta-crystal architectures designed to direct and control the deformation location. This would prove valuable in protective applications where the deformation can be directed away from the subject (i.e., people and critical components). Assessment of the deformation behaviour of meta-crystals under multi-axial stress states is also recommended, which would be more realistic to real-world applications. Finally, the fatigue behaviour is paramount in structural applications and needs to be well understood in order for meta-crystals to be a viable option. Additionally, in case of failure, the MG architecture could potentially impede or resist crack propagation, further extending the life of components that are difficult to repair or replace. Further studies are needed to investigate the deformation behaviour of polycrystal-like meta-crystals in more specific loading conditions.

References

- [1] L.J. Gibson, M.F. Ashby, *Cellular solids: Structure and properties*, Cambridge University Press, 1990. <https://doi.org/10.2277/0521499119>.
- [2] M.A. Arie, M.M. Ohadi, Air-Side Heat Transfer Enhancement Utilizing Design Optimization and an Additive Manufacturing Technique, *J. Heat Transfer*. 139 (2018). <https://doi.org/10.1115/1.4035068>.
- [3] H.E. Burton, N.M. Eisenstein, B.M. Lawless, P. Jamshidi, M.A. Segarra, O. Addison, D.E.T. Shepherd, M.M. Attallah, L.M. Grover, S.C. Cox, The design of additively manufactured lattices to increase the functionality of medical implants, *Mater. Sci. Eng. C*. 94 (2019) 901–908. <https://doi.org/10.1016/j.msec.2018.10.052>.
- [4] J.A. Jackson, M.C. Messner, N.A. Dudukovic, W.L. Smith, L. Bekker, B. Moran, A.M. Golobic, A.J. Pascall, E.B. Duoss, K.J. Loh, C.M. Spadaccini, Field responsive mechanical metamaterials, *Science* (80-.). (2018) 1–10.
- [5] X. Wendy Gu, J.R. Greer, Ultra-strong architected Cu meso-lattices, *Extrem. Mech. Lett.* 2 (2015) 7–14. <https://doi.org/10.1016/j.eml.2015.01.006>.
- [6] S. Daynes, S. Feih, W.F. Lu, J. Wei, Optimisation of functionally graded lattice structures using isostatic lines, *Mater. Des.* 127 (2017) 215–223. <https://doi.org/10.1016/j.matdes.2017.04.082>.
- [7] H. Xu, A. Farag, D. Pasini, Multilevel hierarchy in bi-material lattices with high specific stiffness and unbounded thermal expansion, *Acta Mater.* 134 (2017) 155–166. <https://doi.org/10.1016/j.actamat.2017.05.059>.
- [8] T. Mukherjee, T. Debroy, Mitigation of lack of fusion defects in powder bed fusion additive manufacturing, *J. Manuf. Process.* 36 (2018) 442–449. <https://doi.org/10.1016/j.jmapro.2018.10.028>.
- [9] L.E. Murr, S.M. Gaytan, F. Medina, H. Lopez, E. Martinez, B.I. Machado, D.H. Hernandez, L. Martinez, M.I. Lopez, R.B. Wicker, J. Bracke, Next-generation biomedical implants using additive manufacturing of complex , cellular, (2010) 1999–2032. <https://doi.org/10.1098/rsta.2010.0010>.
- [10] R. Tiwari, R.S. Andhare, A. Shooshtari, M. Ohadi, Development of an additive manufacturing-enabled compact manifold microchannel heat exchanger, *Appl. Therm. Eng.* 147 (2019) 781–788. <https://doi.org/10.1016/j.applthermaleng.2018.10.122>.
- [11] D. Hancock, D. Homfray, M. Porton, I. Todd, B. Wynne, Exploring complex high heat flux geometries for fusion applications enabled by additive manufacturing, *Fusion Eng. Des.* 136 (2018) 454–460. <https://doi.org/10.1016/j.fusengdes.2018.02.097>.
- [12] T.A. Schaedler, A.J. Jacobsen, A. Torrents, A.E. Sorensen, J. Lian, J.R. Greer, L. Valdevit, W.B. Carter, Ultralight metallic microlattices, *Science* (80-.). 334 (2011) 962–965. <https://doi.org/10.1126/science.1211649>.
- [13] L.R. Meza, S. Das, J.R. Greer, Strong , Lightweight and Recoverable Three-Dimensional Ceramic Nanolattices, *Science* (80-.). 345 (2014) 1322–1327. <https://doi.org/10.1126/science.1255908>.
- [14] R.R. Dehoff, M.M. Kirka, W.J. Sames, H. Bilheux, A.S. Tremsin, L.E. Lowe, S.S. Babu, Site specific control of crystallographic grain orientation through electron beam additive manufacturing, *Mater. Sci. Technol.* 31 (2015) 931–938. <https://doi.org/10.1179/1743284714Y.00000000734>.
- [15] W. Xu, E.W. Lui, A. Pateras, M. Qian, M. Brandt, In situ tailoring microstructure in additively manufactured Ti-6Al-4V for superior mechanical performance, *Acta Mater.* 125 (2017) 390–400. <https://doi.org/10.1016/j.actamat.2016.12.027>.
- [16] V.S. Deshpande, M.F. Ashby, N.A. Fleck, Foam topology: Bending versus stretching dominated architectures, *Acta Mater.* 49 (2001) 1035–1040. [https://doi.org/10.1016/S1359-6454\(00\)00379-7](https://doi.org/10.1016/S1359-6454(00)00379-7).

- [17] C. Ling, A. Cernicchi, M.D. Gilchrist, P. Cardiff, Mechanical behaviour of additively-manufactured polymeric octet-truss lattice structures under quasi-static and dynamic compressive loading, *Mater. Des.* 162 (2019) 106–118. <https://doi.org/10.1016/j.matdes.2018.11.035>.
- [18] T. Tancogne-Dejean, D. Mohr, Stiffness and specific energy absorption of additively-manufactured metallic BCC metamaterials composed of tapered beams, *Int. J. Mech. Sci.* 141 (2018) 101–116. <https://doi.org/10.1016/j.ijmecsci.2018.03.027>.
- [19] Y. Jiang, Q. Wang, Highly Stretchable 3D-architected Mechanical Metamaterials, *Sci. Rep.* (2016) 1–11. <https://doi.org/10.1038/srep34147>.
- [20] R. Pippan, C. Motz, B. Kriszt, B. Zettl, H. Mayer, S. Stanzl-Tschegg, F. Simancik, J. Kovacik, *Handbook of Cellular Materials*, *Handb. Cell. Met.* (2002) 179–241. <https://doi.org/10.1002/3527600558.ch5>.
- [21] R.L. Holloman, V. Deshpande, A.G. Hanssen, K.M. Fleming, J.R. Scully, H.N. Wadley, Tubular aluminium cellular structures: fabrication and mechanical response, *J. Mech. Mater. Struct.* 8 (2013) 65–94. <https://doi.org/10.2140/jomms.2013.8.65>.
- [22] M.-S. Pham, C. Liu, I. Todd, J. Lertthanasarn, Damage-tolerant architected materials inspired by crystal microstructure, *Nature*. (2019). <https://doi.org/10.1038/s41586-018-0850-3>.
- [23] R.J. Haüy, *Essai d'une Théorie sur la Structure des Cristaux*, A Paris : Chez Gougué & Née de la Rochelle, 1784.
- [24] W. Friedrich, P. Knipping, M. Laue, *Interferenz-erscheinungen bei röntgenstrahlen*, Verlag der Königlich-Bayerischen Akademie der Wissenschaften, München, 1912.
- [25] A. Bravais, *Mémoire sur les systèmes formés par des points distribués régulièrement sur un plan ou dans l'espace*, Bachelier, Paris, 1850.
- [26] C. Barrett, T.B. Massalski, *Structure of Metals. Crystallographic methods, principles and data*, Third (rev, Pergamon Press Ltd., Oxford, 1980.
- [27] A.S. Argon, *Strengthening mechanisms in crystal plasticity*, 2007. <https://doi.org/10.1093/acprof:oso/9780198516002.001.0001>.
- [28] G.E. Dieter, *Mechanical metallurgy*, Internatio, McGraw-Hill, Japan, 1984.
- [29] W.D. Callister, *Fundamentals of materials science and engineering*, Second, John Wiley & Sons, 2001. <https://doi.org/10.1017/CBO9781107415324.004>.
- [30] R.D. Heidenreich, W. Shockley, Report on the Strength of Solids, in: *Phys. Soc. London*, London, 1948: p. 57.
- [31] A.H. Cottrell, *Dislocations and plastic flow in crystals*, First, Oxford Clarendon Press, Oxford, UK, 1963.
- [32] R. Peierls, The size of a dislocation, (1997) 273–276. https://doi.org/10.1142/9789812795779_0032.
- [33] F.R.N. Nabarro, Dislocations in a simple cubic lattice, *Proc. Phys. Soc.* 59 (1947) 256–272. <https://doi.org/10.1088/0959-5309/59/2/309>.
- [34] W. Hume-Rothery, H.M. Powell, On the theory of super-lattice structures in alloys, *Zeitschrift Für Krist. Mater.* 91 (1935) 23–47.
- [35] W. Hume-Rothery, B.R. Coles, *Atomic Theory for Students of Metallurgy.*, (1969). <http://qut.eblib.com.au/patron/FullRecord.aspx?p=677866>.
- [36] W. Hume-Rothery, C.W. Haworth, R.E. Smallman, *The structure of metals and alloys*, Institute of Metals and the Institution of Metallurgists, London, 1969.
- [37] A. Cottrell, *An introduction to metallurgy*, (1967). <http://catalog.hathitrust.org/api/volumes/oclc/955909.html>.

- [38] J.W. Martin, Precipitation hardening, Pergamon Press, Oxford; New York, 1968.
- [39] A. Guinier, Structure of Age-Hardened Aluminium-Copper Alloys, *Nature*. 142 (1938) 569–570.
- [40] G.D. Preston, Structure of Age-Hardened Aluminium-Copper Alloys, *Nature*. 142 (1938) 570.
- [41] H. Gleiter, E. Hornbogen, Precipitation hardening by coherent particles, *Mater. Sci. Eng.* 2 (1968) 285–302. [https://doi.org/10.1016/0025-5416\(68\)90047-5](https://doi.org/10.1016/0025-5416(68)90047-5).
- [42] P.B. Hirsch, A. Kelly, Stacking-fault strengthening, *Philos. Mag.* 12 (1965) 881–900. <https://doi.org/10.1080/14786436508228118>.
- [43] M. Furukawa, Y. Miura, M. Nemoto, Strengthening mechanisms in Al–Li alloys containing coherent ordered particles, *Trans. Japan Inst. Met.* 26 (1985) 230–235. <https://doi.org/10.2320/matertrans1960.26.230>.
- [44] V. Gerold, H. Haberkorn, On the Critical Resolved Shear Stress of Solid Solutions Containing Coherent Precipitates, *Phys. Status Solidi*. 16 (1966) 675–684. <https://doi.org/10.1002/pssb.19660160234>.
- [45] R.W. Weeks, S.R. Pati, M.F. Ashby, P. Barrand, The elastic interaction between a straight dislocation and a bubble or a particle, *Acta Metall.* 17 (1969) 1403–1410. [https://doi.org/10.1016/0001-6160\(69\)90002-9](https://doi.org/10.1016/0001-6160(69)90002-9).
- [46] E. Orowan, Symposium on internal stresses in metals and alloys, *Symp. Intern. Stress. Met. Alloy*. (1948) 451.
- [47] A.D. Rollette, U.F. Kocks, A review of the stages of work hardening, *Proc. "Dislocations-93."* (n.d.).
- [48] F.R.N. Nabarro, Z.S. Basinski, D.B. Holt, The plasticity of pure single crystals, *Adv. Phys.* 13 (1964) 193–323. <https://doi.org/10.1080/00018736400101031>.
- [49] Z.S. Basinski, Forest hardening in face centred cubic metals, *Scr. Metall.* 8 (1974) 1301–1307. [https://doi.org/10.1016/0036-9748\(74\)90350-0](https://doi.org/10.1016/0036-9748(74)90350-0).
- [50] G. Langford, M. Cohen, Strain hardening of iron by severe plastic deformation, *ASM Trans. Q.* 62 (1969) 623–38.
- [51] R. Clark, B. Chalmers, Mechanical deformation of aluminium bicrystals, *Acta Metall.* 2 (1954) 80–86. [https://doi.org/10.1016/0001-6160\(54\)90097-8](https://doi.org/10.1016/0001-6160(54)90097-8).
- [52] W. Boas, M.E. Hargreaves, On the inhomogeneity of plastic deformation in the crystals of an aggregate, (1926).
- [53] R. von Mises, Mechanics of plastic shape change of crystals, *J. Appl. Math. Mech.* 8 (1928) 161.
- [54] G.I. Taylor, Plastic strain in metals, *Plast. Strain Met.* (1938) 307–324.
- [55] E.O. Hall, The deformation and ageing of mild steel: III Discussion of results, *Proc. Phys. Soc. Sect. B.* 64 (1951) 747–753. <https://doi.org/10.1088/0370-1301/64/9/303>.
- [56] N.J. Petch, The cleavage strength of polycrystals, *J. Iron Steel Inst.* 174 (1953) 25–28.
- [57] M.F. Ashby, The deformation of plastically non-homogeneous materials, *Philos. Mag.* 21 (1970) 399–424. <https://doi.org/10.1080/14786437008238426>.
- [58] M. Schmidt, N.B. Dahotre, D. Bourell, E. Toyserkani, Laser-based additive manufacturing: Processes and materials, *Opt. Laser Technol.* 139 (2021) 106999. <https://doi.org/10.1016/j.optlastec.2021.106999>.
- [59] J. Beaman, C. Deckard, Selective laser sintering with assisted powder handling, US4938816A, 1990.
- [60] D. Appleyard, Powering up on powder technology, *Met. Powder Rep.* 70 (2015) 285–289. <https://doi.org/10.1016/j.mprp.2015.08.075>.
- [61] J. Kranz, D. Herzog, C. Emmelmann, Design guidelines for laser additive manufacturing of

- lightweight structures in, 14001 (2016). <https://doi.org/10.2351/1.4885235>.
- [62] S. Arabnejad, R. Burnett Johnston, J.A. Pura, B. Singh, M. Tanzer, D. Pasini, High-strength porous biomaterials for bone replacement: A strategy to assess the interplay between cell morphology, mechanical properties, bone ingrowth and manufacturing constraints, *Acta Biomater.* 30 (2016) 345–356. <https://doi.org/10.1016/j.actbio.2015.10.048>.
 - [63] R. Saint, W. Evans, Y. Z. T. Barrett, T.M. Fromhold, E. Saleh, I. Maskery, 3D-printed components for quantum devices, *Sci. Rep.* (2018) 1–9. <https://doi.org/10.1038/s41598-018-26455-9>.
 - [64] A. Bhargav, V. Sanjairaj, V. Rosa, L.W. Feng, J. Fuh YH, Applications of additive manufacturing in dentistry: A review, *J. Biomed. Mater. Res. - Part B Appl. Biomater.* 106 (2018) 2058–2064. <https://doi.org/10.1002/jbm.b.33961>.
 - [65] ASTM F2792-12a, Standard Terminology for Additive Manufacturing Technologies (Withdrawn 2015), West Conshohocken, PA, 2012. <https://www.astm.org/Standards/F2792.htm>.
 - [66] D. Herzog, V. Seyda, E. Wycisk, C. Emmelmann, Additive manufacturing of metals, *Acta Mater.* 117 (2016) 371–392. <https://doi.org/10.1016/j.actamat.2016.07.019>.
 - [67] H. Attar, M. Calin, L.C. Zhang, S. Scudino, J. Eckert, Manufacture by selective laser melting and mechanical behavior of commercially pure titanium, *Mater. Sci. Eng. A.* 593 (2014) 170–177. <https://doi.org/10.1016/j.msea.2013.11.038>.
 - [68] B. Ferrar, L. Mullen, E. Jones, R. Stamp, C.J. Sutcliffe, Gas flow effects on selective laser melting (SLM) manufacturing performance, *J. Mater. Process. Tech.* 212 (2012) 355–364. <https://doi.org/10.1016/j.jmatprotec.2011.09.020>.
 - [69] W.E. Frazier, Metal additive manufacturing: A review, *J. Mater. Eng. Perform.* 23 (2014) 1917–1928. <https://doi.org/10.1007/s11665-014-0958-z>.
 - [70] W.J. Sames, F.A. List, S. Pannala, R.R. Dehoff, S.S. Babu, The metallurgy and processing science of metal additive manufacturing, *Int. Mater. Rev.* 61 (2016) 315–360. <https://doi.org/10.1080/09506608.2015.1116649>.
 - [71] J.P. Kruth, X. Wang, T. Laoui, L. Froyen, Lasers and materials in selective laser sintering, *Assem. Autom.* 23 (2003) 357–371. <https://doi.org/10.1108/01445150310698652>.
 - [72] K.P. Karunakaran, S. Suryakumar, V. Pushpa, S. Akula, Low cost integration of additive and subtractive processes for hybrid layered manufacturing, *Robot. Comput. Integr. Manuf.* 26 (2010) 490–499. <https://doi.org/10.1016/j.rcim.2010.03.008>.
 - [73] K.N. Amato, S.M. Gaytan, L.E. Murr, E. Martinez, P.W. Shindo, J. Hernandez, S. Collins, F. Medina, Microstructures and mechanical behavior of Inconel 718 fabricated by selective laser melting, *Acta Mater.* 60 (2012) 2229–2239. <https://doi.org/10.1016/j.actamat.2011.12.032>.
 - [74] E. Chlebus, T. Kurzynowski, B. Dyba, Microstructure and mechanical behaviour of Ti—6Al—7Nb alloy produced by selective laser melting, *Mater. Charact.* 62 (2011) 3–10. <https://doi.org/10.1016/j.matchar.2011.03.006>.
 - [75] S.N.M. Jenkins, Mechanical properties and structural evaluation of diamond structure Ti6Al4V lattices made by Electron Beam Melting, University of Sheffield, 2017. [http://etheses.whiterose.ac.uk/20954/1/Mechanical properties and structural evaluation of diamond structure Ti6Al4V lattices made by Electron Beam Melting - S N M Jenkins.pdf](http://etheses.whiterose.ac.uk/20954/1/Mechanical%20properties%20and%20structural%20evaluation%20of%20diamond%20structure%20Ti6Al4V%20lattices%20made%20by%20Electron%20Beam%20Melting%20-%20S%20N%20M%20Jenkins.pdf).
 - [76] P.A. Kobryn, E.H. Moore, S.L. Semiatin, Effect of laser power and traverse speed on microstructure, porosity, and build height in laser-deposited Ti-6Al-4V, *Scr. Mater.* 43 (2000) 299–305. [https://doi.org/10.1016/S1359-6462\(00\)00408-5](https://doi.org/10.1016/S1359-6462(00)00408-5).
 - [77] S. Stecker, K. Lachenberg, H. Wang, R. Salo, Advanced Electron Beam Free Form Fabrication Methods & Technology, *Am. Weld. Soc.* 2 (2006) 12. <http://www.aws.org/conferences/abstracts/2006/012.pdf>.

- [78] V.J. Challis, X. Xu, L.C. Zhang, A.P. Roberts, J.F. Grotowski, T.B. Sercombe, High specific strength and stiffness structures produced using selective laser melting, *Mater. Des.* 63 (2014) 783–788. <https://doi.org/10.1016/j.matdes.2014.05.064>.
- [79] R. Cunningham, A. Nicolas, J. Madsen, E. Fodran, M.D. Sangid, A.D. Rollett, R. Cunningham, A. Nicolas, J. Madsen, E. Fodran, M.D. Sangid, A.D. Rollett, R. Cunningham, Analyzing the effects of powder and post- processing on porosity and properties of electron beam melted Ti-6Al-4V of electron beam melted Ti-6Al-4V, *Mater. Res. Lett.* 3831 (2017). <https://doi.org/10.1080/21663831.2017.1340911>.
- [80] S. Tamas-williams, H. Zhao, F. Léonard, F. Derguti, I. Todd, P.B. Prangnell, XCT analysis of the influence of melt strategies on defect population in Ti – 6Al – 4V components manufactured by Selective Electron Beam Melting, *Mater. Charact.* 102 (2015) 47–61. <https://doi.org/10.1016/j.matchar.2015.02.008>.
- [81] G.K.L. Ng, A.E.W. Jarfors, G. Bi, H.Y. Zheng, Porosity formation and gas bubble retention in laser metal deposition, *Appl. Phys. A.* (2009) 641–649. <https://doi.org/10.1007/s00339-009-5266-3>.
- [82] J. Beuth, J. Fox, J. Gockel, C. Montgomery, R. Yang, H. Qiao, P. Reeseewatt, A. Anvari, S. Narra, N. Klingbeil, Process Mapping for Qualification Across Multiple Direct Metal Additive Manufacturing Processes, (n.d.) 655–665.
- [83] R.R. Dehoff, M.M. Kirka, F.A.L. Iii, K.A. Unocic, W.J. Sames, Crystallographic texture engineering through novel melt strategies via electron beam melting : Inconel 718, *Mater. Sci. Technol.* 31 (2015) 939–944. <https://doi.org/10.1179/1743284714Y.0000000697>.
- [84] S.K. Everton, M. Hirsch, P. Stravroulakis, R.K. Leach, A.T. Clare, Review of in-situ process monitoring and in-situ metrology for metal additive manufacturing, *Mater. Des.* 95 (2016) 431–445. <https://doi.org/10.1016/j.matdes.2016.01.099>.
- [85] M.H. Farshidianfar, F. Khodabakhshi, A. Khajepour, A.P. Gerlich, Closed-loop control of microstructure and mechanical properties in additive manufacturing by directed energy deposition, *Mater. Sci. Eng. A.* 803 (2021) 140483. <https://doi.org/10.1016/j.msea.2020.140483>.
- [86] I. Jeon, L. Yang, K. Ryu, H. Sohn, Online melt pool depth estimation during directed energy deposition using coaxial infrared camera , laser line scanner , and artificial neural network, *Addit. Manuf.* 47 (2021) 102295. <https://doi.org/10.1016/j.addma.2021.102295>.
- [87] S.L. Campanelli, G. Casalino, N. Contuzzi, A. Angelastro, A.D. Ludovico, Analysis of the molten/solidified zone in selective laser melted parts, in: *SPIE 8963, High-Power Laser Mater. Process. Lasers, Beam Deliv. Diagnostics, Appl. III*, 2014. <https://doi.org/10.1117/12.2042170>.
- [88] M.H. Farshidianfar, A. Khajepour, A.P. Gerlich, Effect of real-time cooling rate on microstructure in Laser Additive Manufacturing, *J. Mater. Process. Tech.* 231 (2016) 468–478. <https://doi.org/10.1016/j.jmatprotec.2016.01.017>.
- [89] I. Yadroitsev, I. Yadroitsava, P. Bertrand, I. Smurov, Factor analysis of selective laser melting process parameters and geometrical characteristics of synthesized single tracks, *Rapid Prototyp. J.* 3 (2012) 201–208. <https://doi.org/10.1108/13552541211218117>.
- [90] R. Fabbro, Scaling laws for the laser welding process in keyhole mode, *J. Mater. Process. Tech.* 264 (2019) 346–351. <https://doi.org/10.1016/j.jmatprotec.2018.09.027>.
- [91] K. V Yang, P. Rometsch, T. Jarvis, J. Rao, S. Cao, C. Davies, X. Wu, Porosity formation mechanisms and fatigue response in Al-Si-Mg alloys made by selective laser melting, *Mater. Sci. Eng. A.* 712 (2018) 166–174. <https://doi.org/10.1016/j.msea.2017.11.078>.
- [92] S. Pal, I. Drstvensek, T. Brailij, Physical Behaviour of Materials in Selective Laser Melting Process, *DAAAM Int. Sci. B.* (2018) 239–256. <https://doi.org/10.2507/daaam.scibook.2018.21>.
- [93] Y. Liu, J. Zhang, Z. Pang, W. Wu, Investigation into the influence of laser energy input on selective laser melted thin-walled parts by response surface method, *Opt. Lasers Eng.* 103 (2018) 34–45.

- <https://doi.org/10.1016/j.optlaseng.2017.11.011>.
- [94] T. Furumoto, K. Egashira, K. Munekage, S. Abe, Experimental investigation of melt pool behaviour during selective laser melting by high speed imaging, *CIRP Ann. - Manuf. Technol.* 67 (2018) 253–256. <https://doi.org/10.1016/j.cirp.2018.04.097>.
 - [95] L.E. Criales, M. Ar, B. Lane, S. Moylan, A. Donmez, Laser powder bed fusion of nickel alloy 625 : Experimental investigations of effects of process parameters on melt pool size and shape with spatter, *Int. J. Mach. Tools Manuf.* 121 (2017) 22–36. <https://doi.org/10.1016/j.ijmachtools.2017.03.004>.
 - [96] H. Shipley, D. McDonnell, M. Culleton, R. Coull, R. Lupoi, G.O. Donnell, D. Trimble, Optimisation of process parameters to address fundamental challenges during selective laser melting of Ti-6Al-4V: A review, *Int. J. Mach. Tools Manuf.* 128 (2018) 1–20. <https://doi.org/10.1016/j.ijmachtools.2018.01.003>.
 - [97] T.T. Roehling, S.S.Q. Wu, S.A. Khairallah, J.D. Roehling, S.S. Soezeri, M.F. Crumb, M.J. Matthews, Modulating laser intensity profile ellipticity for microstructural control during metal additive manufacturing, *Acta Mater.* 128 (2017) 197–206. <https://doi.org/10.1016/j.actamat.2017.02.025>.
 - [98] H. Gu, H. Gong, D. Pal, K. Rafi, T. Starr, B. Stucker, Influences of Energy Density on Porosity and Microstructure of Selective Laser Melted 17- 4PH Stainless Steel, (n.d.) 474–489.
 - [99] L. Hitzler, M. Merkel, W. Hall, A. Ochsner, A Review of Metal Fabricated with Laser- and Powder-Bed Based Additive Manufacturing Techniques : Process , Nomenclature , Materials , Achievable Properties , and its Utilization in the Medical Sector, *Adv. Eng. Mater.* 1700658 (2018) 1–28. <https://doi.org/10.1002/adem.201700658>.
 - [100] S. Cao, Z. Chen, C. Voon, S. Lim, K.U.N. Yang, Q. Jia, T.O.M. Jarvis, D. Tomus, X. Wu, Defect, Microstructure, and Mechanical Property of Ti-6Al-4V Alloy Fabricated by High-Power Selective Laser Melting, *JOM.* 69 (2017) 2684–2692. <https://doi.org/10.1007/s11837-017-2581-6>.
 - [101] Z. Xiang, M. Yin, G. Dong, X. Mei, G. Yin, Modeling of the thermal physical process and study on the reliability of linear energy density for selective laser melting, *Results Phys.* 9 (2018) 939–946. <https://doi.org/10.1016/j.rinp.2018.03.047>.
 - [102] K.G. Prashanth, S. Scudino, T. Maity, J. Das, J. Eckert, Is the energy density a reliable parameter for materials synthesis by selective laser melting ?, *Mater. Res. Lett.* 3831 (2017). <https://doi.org/10.1080/21663831.2017.1299808>.
 - [103] D. Rosenthal, Mathematical Theory of Heat Distribution during Welding and Cutting, *Weld. J.* 20 (1941) 220–234.
 - [104] M. Seifi, A. Salem, J. Beuth, O. Harrysson, J.J. Lewandowski, Overview of Materials Qualification Needs for Metal Additive Manufacturing, *Jom.* 68 (2016) 747–764. <https://doi.org/10.1007/s11837-015-1810-0>.
 - [105] J.J. Lewandowski, M. Seifi, Metal Additive Manufacturing: A Review of Mechanical Properties, *Annu. Rev. Mater. Res.* 46 (2016) 151–186. <https://doi.org/10.1146/annurev-matsci-070115-032024>.
 - [106] J. Lertthanasarn, C. Liu, M.S. Pham, Synergistic effects of crystalline microstructure, architected mesostructure, and processing defects on the mechanical behaviour of Ti6Al4V meta-crystals, *Mater. Sci. Eng. A.* (2021). <https://doi.org/10.1016/j.msea.2021.141436>.
 - [107] J. V Gordon, S.P. Narra, R.W. Cunningham, H. Liu, H. Chen, R.M. Suter, J.L. Beuth, A.D. Rollett, Defect structure process maps for laser powder bed fusion additive manufacturing, *Addit. Manuf.* 36 (2020) 101552. <https://doi.org/10.1016/j.addma.2020.101552>.
 - [108] B. Zhang, Y. Li, Q. Bai, Defect Formation Mechanisms in Selective Laser Melting: A Review, *Chinese J. Mech. Eng. (English Ed.)* 30 (2017) 515–527. <https://doi.org/10.1007/s10033-017-0121-5>.
 - [109] R. Cunningham, S.P. Narra, C. Montgomery, J. Beuth, A.D. Rollett, Synchrotron-Based X-ray Microtomography Characterization of the Effect of Processing Variables on Porosity Formation in

- Laser Power-Bed Additive Manufacturing of Ti-6Al-4V, *J. Mater.* 69 (2017) 2–7. <https://doi.org/10.1007/s11837-016-2234-1>.
- [110] F.H. Kim, S.P. Moylan, Literature Review of Metal Additive Manufacturing Defects, *NIST Adv. Manuf. Ser.* 100 (2018) 1–17. <http://nvlpubs.nist.gov/nistpubs/ams/NIST.AMS.100-16.pdf>.
 - [111] A. du Plessis, I. Yadroitsava, I. Yadroitsev, Effects of defects on mechanical properties in metal additive manufacturing: A review focusing on X-ray tomography insights, *Mater. Des.* 187 (2020) 108385. <https://doi.org/10.1016/j.matdes.2019.108385>.
 - [112] L. Zhuo, B. Song, R. Li, Q. Wei, C. Yan, Y. Shi, Effect of element evaporation on the microstructure and properties of CuZnAl shape memory alloys prepared by selective laser melting, *Opt. Laser Technol.* 127 (2020) 106164. <https://doi.org/10.1016/j.optlastec.2020.106164>.
 - [113] X. Lu, M. Chiumenti, M. Cervera, H. Tan, X. Lin, S. Wang, Warpage Analysis and Control of Thin-Walled Structures Manufactured by Laser Powder Bed Fusion, *Metals (Basel)*. 11 (2021).
 - [114] X. Lu, X. Lin, M. Chiumenti, M. Cervera, Y. Hu, X. Ji, Residual stress and distortion of rectangular and S-shaped Ti-6Al-4V parts by Directed Energy Deposition: Modelling and experimental calibration, *Addit. Manuf.* 26 (2019) 166–179. <https://doi.org/10.1016/j.addma.2019.02.001>.
 - [115] J. Cao, M.A. Gharghouri, P. Nash, Finite-element analysis and experimental validation of thermal residual stress and distortion in electron beam additive manufactured Ti-6Al-4V build plates, *J. Mater. Process. Tech.* 237 (2016) 409–419. <https://doi.org/10.1016/j.jmatprotec.2016.06.032>.
 - [116] P. Vora, K. Mumtaz, I. Todd, N. Hopkinson, AlSi12 in-situ alloy formation and residual stress reduction using anchorless selective laser melting, *Addit. Manuf.* 7 (2015) 12–19. <https://doi.org/10.1016/j.addma.2015.06.003>.
 - [117] Y.J. Liu, Z. Liu, Y. Jiang, G.W. Wang, Y. Yang, L.C. Zhang, Gradient in microstructure and mechanical property of selective laser melted AlSi10Mg, *J. Alloys Compd.* 735 (2018) 1414–1421. <https://doi.org/10.1016/j.jallcom.2017.11.020>.
 - [118] A. Du Plessis, I. Yadroitsava, D. Kouprianoff, I. Yadroitsev, Numerical and experimental study of the effect of artificial porosity in a lattice structure manufactured by laser based fusion, *Solid Free. Fabr. Proc.* (2018). <https://doi.org/10.13140/RG.2.2.28115.84007>.
 - [119] M. Suard, G. Martin, P. Lhuissier, R. Dendievel, F. Vignat, J.J. Blandin, F. Villeneuve, Mechanical equivalent diameter of single struts for the stiffness prediction of lattice structures produced by Electron Beam Melting, *Addit. Manuf.* 8 (2015) 124–131. <https://doi.org/10.1016/j.addma.2015.10.002>.
 - [120] C. Yan, L. Hao, A. Hussein, P. Young, D. Raymont, Advanced lightweight 316L stainless steel cellular lattice structures fabricated via selective laser melting, *Mater. Des.* 55 (2014) 533–541. <https://doi.org/10.1016/j.matdes.2013.10.027>.
 - [121] D. Brandão, J. Gumpinger, A.D. Brandão, J.G. Tommaso, M. Ghidini, Fatigue Properties Of Additively Manufactured AlSi10Mg – Surface Fatigue Of AlSi10Mg on Additively Treatment Effect, *Procedia Struct. Integr.* 7 (2017) 58–66. <https://doi.org/10.1016/j.prostr.2017.11.061>.
 - [122] U. Zerbst, M. Madia, C. Klinger, D. Bettge, Y. Murakami, Defects as a root cause of fatigue failure of metallic components . II: Non-metallic inclusions, *Eng. Fail. Anal.* 98 (2019) 228–239. <https://doi.org/10.1016/j.engfailanal.2019.01.054>.
 - [123] U. Zerbst, M. Madia, C. Klinger, D. Bettge, Y. Murakami, D.- Berlin, Defects as a root cause of fatigue failure of metallic components . I: Basic aspects, *Eng. Fail. Anal.* 97 (2019) 777–792. <https://doi.org/10.1016/j.engfailanal.2019.01.055>.
 - [124] I. Yadroitsev, P. Krakhmalev, I. Yadroitsava, Qualification of Ti6Al4V ELI Alloy Produced by Laser Powder Bed Fusion for Biomedical Applications, *JOM.* 70 (2018) 372–377. <https://doi.org/10.1007/s11837-017-2655-5>.
 - [125] M. Tang, P.C. Pistorius, J.L. Beuth, Prediction of lack-of-fusion porosity for powder bed fusion &

- Addit. Manuf. 14 (2017) 39–48. <https://doi.org/10.1016/j.addma.2016.12.001>.
- [126] Q. Guo, C. Zhao, M. Qu, L. Xiong, L.I. Escano, In-situ characterization and quantification of melt pool variation under constant input energy density in laser powder bed fusion additive manufacturing process, Addit. Manuf. 28 (2019) 600–609. <https://doi.org/10.1016/j.addma.2019.04.021>.
 - [127] G. Mohr, S.J. Altenburg, K. Hilgenberg, Effects of inter layer time and build height on resulting properties of 316L stainless steel processed by laser powder bed fusion, Addit. Manuf. 32 (2020) 101080. <https://doi.org/10.1016/j.addma.2020.101080>.
 - [128] H. Gong, K. Rafi, H. Gu, G.D.J. Ram, T. Starr, B. Stucker, Influence of defects on mechanical properties of Ti–6Al–4V components produced by selective laser melting and electron beam melting, Mater. Des. 86 (2015) 545–554. <https://doi.org/10.1016/j.matdes.2015.07.147>.
 - [129] J. Stef, A. Poulon-quintin, A. Redjaimia, J. Ghanbaja, O. Ferry, M. De Sousa, M. Gouné, Mechanism of porosity formation and influence on mechanical properties in selective laser melting of Ti–6Al–4V parts, Mater. Des. 156 (2018) 480–493. <https://doi.org/10.1016/j.matdes.2018.06.049>.
 - [130] P. Krakhmalev, G. Fredriksson, I. Yadroitsava, N. Kazantseva, A. du Plessis, I. Yadroitsev, Deformation behaviour and microstructure of Ti6Al4V manufactured by SLM, 9th Int. Conf. Photonic Technol. - LANE 2016. 83 (2016) 778–788. <https://doi.org/10.1016/j.phpro.2016.08.080>.
 - [131] N.O. Larrosa, W. Wang, N. Read, M.H. Loretto, C. Evans, J. Carr, U. Tradowsky, M.M. Attallah, P.J. Withers, Linking microstructure and processing defects to mechanical properties of selectively laser melted AlSi10Mg alloy, Theor. Appl. Fract. Mech. 98 (2018) 123–133. <https://doi.org/10.1016/j.tafmec.2018.09.011>.
 - [132] L.B. Malefane, W.B. du Preez, M. Maringa, A. du Plessis, Tensile and high cycle fatigue properties of annealed ti6al4v (eli) specimens produced by direct metal laser sintering, South African J. Ind. Eng. 29 (2018) 299–311.
 - [133] J. Zhao, M. Easton, M. Qian, M. Leary, M. Brandt, Effect of building direction on porosity and fatigue life of selective laser melted AlSi12Mg alloy, Mater. Sci. Eng. A. 729 (2018) 76–85. <https://doi.org/10.1016/j.msea.2018.05.040>.
 - [134] T. Ronneberg, C.M. Davies, P.A. Hooper, Revealing relationships between porosity, microstructure and mechanical properties of laser powder bed fusion 316L stainless steel through heat treatment, Mater. Des. 189 (2020) 108481. <https://doi.org/10.1016/j.matdes.2020.108481>.
 - [135] W. Shifeng, L. Shuai, W. Qingsong, C. Yan, Z. Sheng, S. Yusheng, Effect of molten pool boundaries on the mechanical properties of selective laser melting parts, J. Mater. Process. Tech. 214 (2014) 2660–2667. <https://doi.org/10.1016/j.jmatprotec.2014.06.002>.
 - [136] J. Trapp, A.M. Rubenchik, G. Guss, M.J. Matthews, In situ absorptivity measurements of metallic powders during laser powder-bed fusion additive manufacturing, Appl. Mater. Today. 9 (2017) 341–349. <https://doi.org/10.1016/j.apmt.2017.08.006>.
 - [137] W.E. King, H.D. Barth, V.M. Castillo, G.F. Gallegos, J.W. Gibbs, D.E. Hahn, C. Kamath, A.M. Rubenchik, Observation of keyhole-mode laser melting in laser powder-bed fusion additive manufacturing, J. Mater. Process. Tech. 214 (2014) 2915–2925. <https://doi.org/10.1016/j.jmatprotec.2014.06.005>.
 - [138] T. Debroy, S.A. David, Physical processes in fusion welding, Rev. Mod. Phys. 67 (1995).
 - [139] M. Saunders, X marks the spot - find the ideal process parameters for your metal AM parts, Renishaw Featur. Artic. 44 (2019) 1–11. <https://www.renishaw.com/en/additive-manufacturing-feature-articles-41148>.
 - [140] L.N. Carter, M.M. Attallah, R.C. Reed, Laser Powder Bed Fabrication of Nickel-Base Superalloys : Influence of Parameters ; Characterisation , Quantification and Mitigation of Cracking, Superalloys 2012 12th Int. Symp. Superalloys. (2012) 577–586.

- [141] S. Kou, A criterion for cracking during solidification, *Acta Mater.* 88 (2015) 366–374. <https://doi.org/10.1016/j.actamat.2015.01.034>.
- [142] S. Kou, A Simple Index for Predicting the Susceptibility to Solidification Cracking, *Weld. J.* 94 (2015).
- [143] B. Dovguy, M. Simonelli, M. Pham, Alloy design against the solidification cracking in fusion additive manufacturing : an application to a FeCrAl alloy, (2021). <https://doi.org/10.1080/21663831.2021.1922945>.
- [144] Y. Chen, K. Zhang, J. Huang, S. Reza, E. Hosseini, Z. Li, Characterization of heat affected zone liquation cracking in laser additive manufacturing of Inconel 718, *JMADE.* 90 (2016) 586–594. <https://doi.org/10.1016/j.matdes.2015.10.155>.
- [145] M.G. Collins, A.J. Ramirez, J.C. Lippold, An Investigation of Ductility Dip Cracking in Nickel-Based Weld Metals — Part II, *Weld. Res.* (2003) 348–354.
- [146] M.J. Donachie, S.J. Donachie, *Superalloys: A technical guide*, Second, ASM International, 2002.
- [147] M.D. Rowe, Ranking the Resistance of Wrought Superalloys to Strain-Age Cracking, *Weld. J.* (2006) 27–34.
- [148] P.A.A. Khan, T. Debroy, Alloying Element Vaporization and Weld Pool Temperature during Laser Welding of AISI 202 Stainless Steel, *Metall. Trans. B.* 15 (1984) 641–644.
- [149] T. Mukherjee, J.S. Zuback, A. De, T. DebRoy, Printability of alloys for additive manufacturing, *Sci. Rep.* 6 (2016) 1–8. <https://doi.org/10.1038/srep19717>.
- [150] A. Dareh, S. Nafisi, R. Hashemi, H. Ebendorff-heidepriem, Effective post processing of SLM fabricated Ti-6Al-4 V alloy : Machining vs thermal treatment, *J. Manuf. Process.* 68 (2021) 1031–1046. <https://doi.org/10.1016/j.jmapro.2021.06.035>.
- [151] G. Kasperovich, J. Hausmann, Improvement of fatigue resistance and ductility of TiAl6V4 processed by selective laser melting, *J. Mater. Process. Technol.* 220 (2015) 202–214. <https://doi.org/10.1016/j.jmatprotec.2015.01.025>.
- [152] L. Denti, A. Sola, On the Effectiveness of Different Surface Finishing Techniques on A357 . 0 Parts Produced by Laser-Based Powder Bed Fusion : Surface Roughness and Fatigue Strength, (2019). <https://doi.org/10.3390/met9121284>.
- [153] Y. Zhang, J. Li, S. Che, Y. Tian, Electrochemical Polishing of Additively Manufactured Ti–6Al–4V Alloy, *Met. Mater. Int.* 26 (2020) 783–792. <https://doi.org/10.1007/s12540-019-00556-0>.
- [154] D. Landolt, Fundamental aspects of electropolishing, *Electrochem. Acta.* (1987).
- [155] S. Habibzadeh, L. Li, D. Shum-tim, E.C. Davis, S. Omanovic, Electrochemical polishing as a 316L stainless steel surface treatment method : Towards the improvement of biocompatibility, *Corros. Sci.* 87 (2014) 89–100. <https://doi.org/10.1016/j.corsci.2014.06.010>.
- [156] S. Chang, A. Liu, C.Y.A. Ong, L. Zhang, X. Huang, Y.H. Tan, L. Zhao, L. Li, J. Ding, Highly effective smoothening of 3D-printed metal structures via overpotential electrochemical polishing, *Mater. Res. Lett.* 7 (2019) 282–289. <https://doi.org/10.1080/21663831.2019.1601645>.
- [157] H. V Atkinson, S. Davies, Fundamental Aspects of Hot Isostatic Pressing : An Overview, *Metall. Mater. Trans. A. m* (2000).
- [158] S. Tammas-Williams, P.J. Withers, I. Todd, P.B. Prangnell, The Effectiveness of Hot Isostatic Pressing for Closing Porosity in Titanium Parts Manufactured by Selective Electron Beam Melting, *Metall. Mater. Trans. A Phys. Metall. Mater. Sci.* 47 (2016) 1939–1946. <https://doi.org/10.1007/s11661-016-3429-3>.
- [159] A. Plessis, P. Rossouw, Investigation of Porosity Changes in Cast Ti6Al4V Rods After Hot Isostatic Pressing, *J. Mater. Eng. Perform.* 24 (2015) 3137–3141. <https://doi.org/10.1007/s11665-015-1580-4>.

- [160] W. Tillmann, C. Schaak, J. Nellesen, M. Schaper, M.E. Aydinöz, K. Hoyer, Hot isostatic pressing of IN718 components manufactured by selective laser melting, *Addit. Manuf.* 13 (2017) 93–102. <https://doi.org/10.1016/j.addma.2016.11.006>.
- [161] N.T. Aboulkhair, N.M. Everitt, I. Ashcroft, C. Tuck, Reducing porosity in AlSi10Mg parts processed by selective laser melting, *Addit. Manuf.* 1 (2014) 77–86. <https://doi.org/10.1016/j.addma.2014.08.001>.
- [162] M. Simonelli, Y.Y. Tse, C. Tuck, On the texture formation of selective laser melted Ti-6Al-4V, *Metall. Mater. Trans. A Phys. Metall. Mater. Sci.* 45 (2014) 2863–2872. <https://doi.org/10.1007/s11661-014-2218-0>.
- [163] M. Jin, A. Piglione, B. Dovggy, E. Hosseini, P.A. Hooper, S.R. Holdsworth, M.S. Pham, Cyclic plasticity and fatigue damage of CrMnFeCoNi high entropy alloy fabricated by laser powder-bed fusion, *Addit. Manuf.* 36 (2020) 101584. <https://doi.org/10.1016/j.addma.2020.101584>.
- [164] Y.M. Wang, T. Voisin, J.T. Mckeown, J. Ye, N.P. Calta, Z. Li, Z. Zeng, Y. Zhang, W. Chen, T.T. Roehling, R.T. Ott, M.K. Santala, P.J. Depond, M.J. Matthews, A. V Hamza, T. Zhu, Additively manufactured hierarchical stainless steels with high strength and ductility, *Nat. Mater.* 17 (2018). <https://doi.org/10.1038/NMAT5021>.
- [165] X.A. Hu, G. Le Zhao, F.C. Liu, W.X. Liu, Microstructure and mechanical behavior of Inconel 625 alloy processed by selective laser melting at high temperature up to 1000 °C, *Rare Met.* 39 (2020) 1181–1189. <https://doi.org/10.1007/s12598-019-01321-3>.
- [166] T.M. Pollock, A.J. Clarke, S.S. Babu, Design and Tailoring of Alloys for Additive Manufacturing, *Metall. Mater. Trans. A* 51 (n.d.) 6000–6019. <https://doi.org/10.1007/s11661-020-06009-3>.
- [167] A.T. Clare, R.S. Mishra, M. Merklein, H. Tan, I. Todd, L. Chechik, J. Li, M. Bambach, Alloy design and adaptation for additive manufacture, *J. Mater. Process. Technol.* 299 (2022). <https://doi.org/10.1016/j.jmatprotec.2021.117358>.
- [168] M. Simonelli, Y.Y. Tse, C. Tuck, The formation of $\alpha + \beta$ microstructure in as-fabricated selective laser melting of Ti-6Al-4V, *J. Mater. Res.* 29 (2014) 2028–2035. <https://doi.org/10.1557/jmr.2014.166>.
- [169] L. Thijs, K. Kempen, J. Kruth, J. Van Humbeeck, Fine-structured aluminium products with controllable texture by selective laser melting of pre-alloyed AlSi10Mg powder, *Acta Mater.* 61 (2013) 1809–1819.
- [170] J. Akram, P. Chalavadi, D. Pal, B. Stucker, Understanding grain evolution in additive manufacturing through modeling, *Addit. Manuf.* 21 (2018) 255–268. <https://doi.org/10.1016/j.addma.2018.03.021>.
- [171] G. Wang, X. Chen, C. Qiu, On the macro- and micro-deformation mechanisms of selectively laser melted damage tolerant metallic lattice structures, *J. Alloys Compd.* 852 (2021) 156985. <https://doi.org/10.1016/j.jallcom.2020.156985>.
- [172] M.S. Pham, B. Dovggy, P.A. Hooper, C.M. Gourlay, A. Piglione, The role of side-branching in microstructure development in laser powder-bed fusion, *Nat. Commun.* 11 (2020) 1–12. <https://doi.org/10.1038/s41467-020-14453-3>.
- [173] Q. Jia, D. Gu, Selective laser melting additive manufacturing of Inconel 718 superalloy parts: Densification, microstructure and properties, *J. Alloys Compd.* 585 (2014) 713–721. <https://doi.org/10.1016/j.jallcom.2013.09.171>.
- [174] A. Piglione, B. Dovggy, C. Liu, C.M. Gourlay, P.A. Hooper, M.S. Pham, Printability and microstructure of the CoCrFeMnNi high-entropy alloy fabricated by laser powder bed fusion, *Mater. Lett.* 224 (2018) 22–25. <https://doi.org/10.1016/j.matlet.2018.04.052>.
- [175] F. Yan, W. Xiong, E.J. Faierson, Grain Structure Control of Additively Manufactured Metallic Materials, *Metals (Basel)*. (2017) 1–11. <https://doi.org/10.3390/ma10111260>.
- [176] Z. Sun, X. Tan, S. Tor, W.Y. Yeong, Selective laser melting of stainless steel 316L with low porosity and high build rates, *JMADE*. 104 (2016) 197–204. <https://doi.org/10.1016/j.matdes.2016.05.035>.

- [177] D. Wang, C. Song, Y. Yang, Y. Bai, Investigation of crystal growth mechanism during selective laser melting and mechanical property characterization of 316L stainless steel parts, *JMADE*. 100 (2016) 291–299. <https://doi.org/10.1016/j.matdes.2016.03.111>.
- [178] N. Dumontet, D. Connétable, B. Malard, B. Viguier, Elastic properties of the α' martensitic phase in the Ti-6Al-4V alloy obtained by additive manufacturing, *Scr. Mater.* 167 (2019) 115–119. <https://doi.org/10.1016/j.scriptamat.2019.03.042>.
- [179] T.G. Gallmeyer, S. Moorthy, B.B. Kappes, M.J. Mills, B. Amin-Ahmadi, A.P. Stebner, Knowledge of process-structure-property relationships to engineer better heat treatments for laser powder bed fusion additive manufactured Inconel 718, *Addit. Manuf.* 31 (2020) 100977. <https://doi.org/10.1016/j.addma.2019.100977>.
- [180] K.T. Makiewicz, Development of Simultaneous Transformation Kinetics Microstructure Model with Application to Laser Metal Deposited Ti - 6Al - 4V and Alloy 718, The Ohio State University, 2013.
- [181] Y. Tian, D. Mcallister, H. Colijn, M. Mills, D. Farson, M. Nordin, S. Babu, Rationalization of Microstructure Heterogeneity in INCONEL 718 Builds Made by the Direct Laser Additive Manufacturing Process, *Metall. Mater. Trans. A.* (2014). <https://doi.org/10.1007/s11661-014-2370-6>.
- [182] W.J. Sames, R.R. Dehoff, Thermal effects on microstructural heterogeneity of Inconel 718 materials fabricated by electron beam melting, *J. Mater. Res.* (2014). <https://doi.org/10.1557/jmr.2014.140>.
- [183] S. Ghose, S. Babu, R.J. Van Arkel, K. Nai, P.A. Hooper, J.R.T. Jeffers, The influence of laser parameters and scanning strategies on the mechanical properties of a stochastic porous material, *Mater. Des.* 131 (2017) 498–508. <https://doi.org/10.1016/j.matdes.2017.06.041>.
- [184] L.N. Carter, C. Martin, P.J. Withers, M.M. Attallah, The influence of the laser scan strategy on grain structure and cracking behaviour in SLM powder-bed fabricated nickel superalloy, *J. Alloys Compd.* 615 (2014) 338–347. <https://doi.org/10.1016/j.jallcom.2014.06.172>.
- [185] J.D. Hunt, Steady State Columnar and Equiaxed Growth of Dendrites and Eutectic, *Mater. Sci. Eng.* 65 (1984) 75–83.
- [186] P. Karimi, E. Sadeghi, J. Ålgårdh, J. Olsson, Tailored grain morphology via a unique melting strategy in electron beam-powder bed fusion, *Mater. Sci. Eng. A.* 824 (2021). <https://doi.org/10.1016/j.msea.2021.141820>.
- [187] K. Carolin, H. Helmer, A. Bauereiß, R.F. Singer, Tailoring the grain structure of IN718 during selective electron beam melting, *MATEC Web Conf.* 08001 (2014). <https://doi.org/10.1051/mateconf/20141408001>.
- [188] N. Raghavan, S. Simunovic, R. Dehoff, A. Plotkowski, J. Turner, M. Kirka, S. Babu, Localized melt-scan strategy for site specific control of grain size and primary dendrite arm spacing in electron beam additive, *Acta Mater.* 140 (2017) 375–387. <https://doi.org/10.1016/j.actamat.2017.08.038>.
- [189] L. Thijs, M. Luz, M. Sistiaga, R. Wauthle, Q. Xie, J. Kruth, J. Van Humbeeck, Strong morphological and crystallographic texture and resulting yield strength anisotropy in selective laser melted tantalum, *Acta Mater.* 61 (2013) 4657–4668.
- [190] T. Ishimoto, K. Hagihara, K. Hisamoto, S. Sun, T. Nakano, Crystallographic texture control of beta-type Ti-15Mo-5Zr-3Al alloy by selective laser melting for the development of novel implants with a biocompatible low Young's modulus, *Scr. Mater.* 132 (2017) 34–38. <https://doi.org/10.1016/j.scriptamat.2016.12.038>.
- [191] G.P. Dinda, A.K. Dasgupta, J. Mazumder, Texture control during laser deposition of nickel-based superalloy, *Scr. Mater.* 67 (2012) 503–506. <https://doi.org/10.1016/j.scriptamat.2012.06.014>.
- [192] G.W. Milton, A. V. Cherkaev, Which elasticity tensors are realizable?, *J. Eng. Mater. Technol. Trans. ASME*. 117 (1995) 483–493. <https://doi.org/10.1115/1.2804743>.
- [193] M. Kadic, T. Bückmann, N. Stenger, M. Thiel, M. Wegener, On the practicability of pentamode

- mechanical metamaterials, *Appl. Phys. Lett.* 100 (2012). <https://doi.org/10.1063/1.4709436>.
- [194] T. Buckmann, M. Thiel, M. Kadic, R. Schittny, M. Wegener, An elasto-mechanical unfeelability cloak made of pentamode metamaterials, *Nat. Commun.* (2014) 1–6. <https://doi.org/10.1038/ncomms5130>.
 - [195] Y. Chen, T. Li, F. Scarpa, L. Wang, Lattice Metamaterials with Mechanically Tunable Poisson ' s Ratio for Vibration Control, *Phys. Rev. Appl.* 024012 (2017) 1–11. <https://doi.org/10.1103/PhysRevApplied.7.024012>.
 - [196] L. Cabras, M. Brun, I. Meccanica, P. Armi, I.- Cagliari, A class of auxetic three-dimensional lattices, (n.d.) 1–24.
 - [197] M.A. Arie, A.H. Shooshtari, M.M. Ohadi, Experimental characterization of an additively manufactured heat exchanger for dry cooling of power plants, *Appl. Therm. Eng.* 129 (2018) 187–198. <https://doi.org/10.1016/j.applthermaleng.2017.09.140>.
 - [198] K.L. Kirsch, K.A. Thole, Heat Transfer and Pressure Loss Measurements in Additively Manufactured Wavy Microchannels, *J. Turbomach.* (2017). <https://doi.org/10.1115/1.4034342>.
 - [199] D. Saltzman, M. Bichnevicius, S. Lynch, T.W. Simpson, E.W. Reutzel, C. Dickman, R. Martukanitz, Design and evaluation of an additively manufactured aircraft heat exchanger, *Appl. Therm. Eng.* 138 (2018) 254–263. <https://doi.org/10.1016/j.applthermaleng.2018.04.032>.
 - [200] J. Alexandersen, O. Sigmund, K. Erik, B. Stefanov, Design of passive coolers for light-emitting diode lamps using topology optimisation, *Int. J. Heat Mass Transf.* 122 (2018) 138–149. <https://doi.org/10.1016/j.ijheatmasstransfer.2018.01.103>.
 - [201] K.J. Byers, C. Barr, Metal Additive Manufactured Freeform Antenna, *IEEE Antennas Wirel. Propag. Lett.* 17 (2018) 2104–2108.
 - [202] G. Scotti, P. Kanninen, V. Matilainen, A. Salminen, Stainless steel micro fuel cells with enclosed channels by laser additive manufacturing, *Energy.* 106 (2016) 475–481. <https://doi.org/10.1016/j.energy.2016.03.086>.
 - [203] J. Vovrosh, G. Voulazeris, P.G. Petrov, J. Zou, Y. Gaber, L. Benn, D. Woolger, M.M. Attallah, V. Boyer, K. Bongs, Additive manufacturing of magnetic shielding and ultra- high vacuum flange for cold atom sensors, *Sci. Rep.* (2018) 1–10. <https://doi.org/10.1038/s41598-018-20352-x>.
 - [204] R.A. Parham, R.L. Gray, *The Chemistry of Solid Wood*, American Chemical Society, 1984. <https://doi.org/10.1021/ba-1984-0207.ch001>.
 - [205] J. Bauer, L.R. Meza, T.A. Schaedler, R. Schwaiger, X. Zheng, L. Valdevit, Nanolattices: An Emerging Class of Mechanical Metamaterials, *Adv. Mater.* 29 (2017) 1–26. <https://doi.org/10.1002/adma.201701850>.
 - [206] S. Torquato, L. V Gibiansky, M.J. Silva, Effective mechanical and transport properties of cellular solids, *Int. J. Mech. Sci.* 40 (1998) 71–82.
 - [207] X. Wang, T.J. Lu, Optimized acoustic properties of cellular solids Optimized acoustic properties of cellular solids, *J. Acoust. Soc. Am.* 756 (2016). <https://doi.org/10.1121/1.427094>.
 - [208] L.J. Gibson, T. Street, B.C. Vancouver, Deformation and energy absorption diagrams for cellular solids, *Acta Metall.* 32 (1984) 1963–1975.
 - [209] Z. Jia, F. Liu, X. Jiang, L. Wang, Engineering lattice metamaterials for extreme property, programmability, and multifunctionality, *J. Appl. Phys.* 127 (2020). <https://doi.org/10.1063/5.0004724>.
 - [210] M.. Ashby, The properties of foams and lattices, *Philos. Trans. R. Soc. A Math. Phys. Eng. Sci.* 364 (2006) 15–30. <https://doi.org/10.1098/rsta.2005.1678>.
 - [211] M.F. Ashby, *Cellular Ceramics: Structure, Manufacturing, Properties and Applications*, John Wiley & Sons, 2006.

- [212] M. Leary, M. Mazur, H. Williams, E. Yang, A. Alghamdi, B. Lozanovski, X. Zhang, D. Shidid, L. Farahbod-sternahl, G. Witt, I. Kelbassa, P. Choong, M. Qian, M. Brandt, Inconel 625 lattice structures manufactured by selective laser melting (SLM): Mechanical properties , deformation and failure modes, *Mater. Des.* 157 (2018) 179–199. <https://doi.org/10.1016/j.matdes.2018.06.010>.
- [213] L. Xiao, W. Song, C. Wang, H. Tang, Q. Fan, N. Liu, J. Wang, Mechanical properties of open-cell rhombic dodecahedron titanium alloy lattice structure manufactured using electron beam melting under dynamic loading, *Int. J. Impact Eng.* 100 (2017) 75–89. <https://doi.org/10.1016/j.ijimpeng.2016.10.006>.
- [214] J. Kadkhodapour, H. Montazerian, A.C. Darabi, A. Zargarian, S. Schmauder, The relationships between deformation mechanisms and mechanical properties of additively manufactured porous biomaterials, *J. Mech. Behav. Biomed. Mater.* 70 (2017) 28–42. <https://doi.org/10.1016/j.jmbbm.2016.09.018>.
- [215] Z. Alomar, F. Concli, A Review of the Selective Laser Melting Lattice Structures and Their Numerical Models, *Adv. Eng. Mater.* 22 (2020) 1–17. <https://doi.org/10.1002/adem.202000611>.
- [216] K.J. Maloney, C.S. Roper, A.J. Jacobsen, W.B. Carter, L. Valdevit, T.A. Schaedler, Microlattices as architected thin films: Analysis of mechanical properties and high strain elastic recovery, *APL Mater.* 1 (2013). <https://doi.org/10.1063/1.4818168>.
- [217] L.R. Meza, G.P. Phlipot, C.M. Portela, A. Maggi, L.C. Montemayor, A. Comella, D.M. Kochmann, J.R. Greer, Reexamining the mechanical property space of three-dimensional lattice architectures, *Acta Mater.* (2017). <https://doi.org/10.1016/j.actamat.2017.08.052>.
- [218] B. Kriszt, B. Foroghi, K. Faure, H.P. Degischer, Behaviour of aluminium foam under uniaxial compression, *Mater. Sci. Technol.* 16 (2000) 792–796. <https://doi.org/http://dx.doi.org/10.1179/026708300101508450>.
- [219] C. Yan, L. Hao, A. Hussein, P. Young, J. Huang, W. Zhu, Microstructure and mechanical properties of aluminium alloy cellular lattice structures manufactured by direct metal laser sintering, *Mater. Sci. Eng. A.* 628 (2015) 238–246. <https://doi.org/10.1016/j.msea.2015.01.063>.
- [220] I. Maskery, A.O. Aremu, M. Simonelli, C. Tuck, R.D. Wildman, I.A. Ashcroft, R.J.M. Hague, Mechanical Properties of Ti-6Al-4V Selectively Laser Melted Parts with Body-Centred-Cubic Lattices of Varying cell size, *Exp. Mech.* 55 (2015) 1261–1272. <https://doi.org/10.1007/s11340-015-0021-5>.
- [221] L. Euler, Thoughts on the elements of bodies, *Mem. Prussian Acad. Sci. Berlin.* (1746).
- [222] N. Rivier, Statistical crystallography structure of random cellular networks, *Philos. Mag. B Phys. Condens. Matter; Stat. Mech. Electron. Opt. Magn. Prop.* 52 (1985) 795–819. <https://doi.org/10.1080/13642818508240637>.
- [223] L.J. Gibson, Cellular Solids, *MRS Bull.* (2003) 270–274.
- [224] J.C. Maxwell, On the calculation of the equilibrium and stiffness of frames, *London, Edinburgh, Dublin Philos. Mag. J. Sci.* 27 (1864) 294–299. <https://doi.org/10.1080/14786446408643668>.
- [225] J.D. Renton, The beam-like behavior of space trusses, *AIAA J.* 22 (1984) 273–280. <https://doi.org/10.2514/3.8379>.
- [226] T. Tarnai, Simultaneous static and kinematic indeterminacy of space trusses with cyclic symmetry, *Int. J. Solids Struct.* 16 (1980) 347–359. [https://doi.org/10.1016/0020-7683\(80\)90087-6](https://doi.org/10.1016/0020-7683(80)90087-6).
- [227] C.R. Calladine, Buckminster fuller’s “tensegrity” structures and Clerk Maxwell’s rules for the construction of stiff frames, *Int. J. Solids Struct.* 14 (1978) 161–172. [https://doi.org/10.1016/0020-7683\(78\)90052-5](https://doi.org/10.1016/0020-7683(78)90052-5).
- [228] S. Pellegrino, C.R. Calladine, Matrix analysis of statically and kinematically indeterminate frameworks, *Int. J. Solids Struct.* 22 (1986) 409–428. [https://doi.org/10.1016/0020-7683\(86\)90014-4](https://doi.org/10.1016/0020-7683(86)90014-4).

- [229] J.F. Nye, Physical properties of crystals: their representation by tensors and matrices, Oxford university press, 1985.
- [230] A.N. Norris, Mechanics of elastic networks, *Proc. R. Soc. A Math. Phys. Eng. Sci.* 470 (2014). <https://doi.org/10.1098/rspa.2013.0611>.
- [231] M. Mazur, M. Leary, M. Mcmillan, S. Sun, D. Shidid, M. Brandt, Mechanical properties of Ti6Al4V and AlSi12Mg lattice structures manufactured by Selective Laser Melting (SLM), Elsevier Ltd, 2017. <https://doi.org/10.1016/B978-0-08-100433-3.00005-1>.
- [232] H.D. Carlton, J. Lind, M.C. Messner, N.A. Volkoff-Shoemaker, H.S. Barnard, N.R. Barton, M. Kumar, Mapping local deformation behavior in single cell metal lattice structures, *Acta Mater.* 129 (2017) 239–250. <https://doi.org/10.1016/j.actamat.2017.02.023>.
- [233] T. Tancogne-Dejean, A.B. Spierings, D. Mohr, Additively-manufactured metallic micro-lattice materials for high specific energy absorption under static and dynamic loading, *Acta Mater.* 116 (2016) 14–28. <https://doi.org/10.1016/j.actamat.2016.05.054>.
- [234] M. Smith, Z. Guan, W.J. Cantwell, Finite element modelling of the compressive response of lattice structures manufactured using the selective laser melting technique, *Int. J. Mech. Sci.* 67 (2013) 28–41. <https://doi.org/10.1016/j.ijmecsci.2012.12.004>.
- [235] K. Ushijima, W.J. Cantwell, D.H. Chen, Prediction of the mechanical properties of micro-lattice structures subjected to multi-axial loading, *Int. J. Mech. Sci.* 68 (2013) 47–55. <https://doi.org/10.1016/j.ijmecsci.2012.12.017>.
- [236] Y. Huang, Y. Xue, X. Wang, F. Han, Mechanical behavior of three-dimensional pyramidal aluminum lattice materials, *Mater. Sci. Eng. A.* 696 (2017) 520–528. <https://doi.org/10.1016/j.msea.2017.04.053>.
- [237] R. Gümrük, R.A.W. Mines, Compressive behaviour of stainless steel micro-lattice structures, *Int. J. Mech. Sci.* 68 (2013) 125–139. <https://doi.org/10.1016/j.ijmecsci.2013.01.006>.
- [238] D. Erdeniz, T.A. Schaedler, D.C. Dunand, Deposition-based synthesis of nickel-based superalloy microlattices, *Scr. Mater.* 138 (2017) 28–31. <https://doi.org/10.1016/j.scriptamat.2017.05.027>.
- [239] M.R. O'Masta, L. Dong, L. St-Pierre, H.N.G. Wadley, V.S. Deshpande, The fracture toughness of octet-truss lattices, *J. Mech. Phys. Solids.* 98 (2017) 271–289. <https://doi.org/10.1016/j.jmps.2016.09.009>.
- [240] C. Bonatti, D. Mohr, Large deformation response of additively-manufactured FCC metamaterials: From octet truss lattices towards continuous shell mesostructures, *Int. J. Plast.* 92 (2017) 122–147. <https://doi.org/10.1016/j.ijplas.2017.02.003>.
- [241] Y. Huang, Y. Xue, X. Wang, F. Han, Effect of cross sectional shape of struts on the mechanical properties of aluminum based pyramidal lattice structures, *Mater. Lett.* 202 (2017) 55–58. <https://doi.org/10.1016/j.matlet.2017.05.073>.
- [242] S. Zhu, L. Ma, B. Wang, J. Hu, Z. Zhou, Lattice materials composed by curved struts exhibit adjustable macroscopic stress-strain curves, *Mater. Today Commun.* 14 (2018) 273–281. <https://doi.org/10.1016/j.mtcomm.2018.01.017>.
- [243] E.W. Andrews, G. Gioux, P. Onck, L.J. Gibson, Size effects in ductile cellular solids. Part I : modeling, *Int. J. Mech. Sci.* 43 (2001) 0–1.
- [244] E.W. Andrews, G. Gioux, P. Onck, L.J. Gibson, Size effects in ductile cellular solids. Part II : experimental results, *Int. J. Mech. Sci.* 43 (2001) 0–1.
- [245] S.J.N. Morrish, M. Pedersen, K.F.W. Wong, I. Todd, R. Goodall, Size effects in compression in Electron Beam Melted Ti6Al4V diamond structure lattices, *Mater. Lett.* 190 (2017) 138–142. <https://doi.org/10.1016/j.matlet.2016.12.130>.
- [246] C. Tekoglu, L.J. Gibson, T. Pardoën, P.R. Onck, Size effects in foams: Experiments and modeling, *Prog. Mater. Sci.* 56 (2011) 109–138. <https://doi.org/10.1016/j.pmatsci.2010.06.001>.

- [247] A.O. Aremu, I.A. Maskery, C.J. Tuck, I.A. Ashcroft, R.D. Wildman, R.J.M. Hague, Effects of net and solid skins on self-supporting lattice structures, in: *Conf. Proc. Soc. Exp. Mech. Ser.*, 2016: pp. 83–89. https://doi.org/10.1007/978-3-319-22443-5_10.
- [248] Y. Shen, S. McKown, S. Tsopanos, C.J. Sutcliffe, R.A.W. Mines, W.J. Cantwell, The mechanical properties of sandwich structures based on metal lattice architectures, *J. Sandw. Struct. Mater.* 12 (2010) 159–180. <https://doi.org/10.1177/1099636209104536>.
- [249] R. Gümruk, R.A.W. Mines, S. Karadeniz, Determination of Strain Rate Sensitivity of Micro-struts Manufactured Using the Selective Laser Melting Method, *J. Mater. Eng. Perform.* 27 (2018) 1016–1032. <https://doi.org/10.1007/s11665-018-3208-y>.
- [250] S. Merkt, C. Hinke, J. Bültmann, M. Brandt, Y.M. Xie, Mechanical response of TiAl6V4 lattice structures manufactured by selective laser melting in quasistatic and dynamic compression tests, *J. Laser Appl.* 27 (2015) S17006. <https://doi.org/10.2351/1.4898835>.
- [251] S. McKown, Y. Shen, W.K. Brookes, C.J. Sutcliffe, W.J. Cantwell, G.S. Langdon, G.N. Nurick, M.D. Theobald, The quasi-static and blast loading response of lattice structures, *Int. J. Impact Eng.* 35 (2008) 795–810. <https://doi.org/10.1016/j.ijimpeng.2007.10.005>.
- [252] P.J. Tan, S.R. Reid, J.J. Harrigan, Z. Zou, S. Li, Dynamic compressive strength properties of aluminium foams. Part i - Experimental data and observations, *J. Mech. Phys. Solids.* 53 (2005) 2174–2205. <https://doi.org/10.1016/j.jmps.2005.05.007>.
- [253] M. Mazur, M. Leary, S. Sun, M. Vcelka, D. Shidid, M. Brandt, Deformation and failure behaviour of Ti-6Al-4V lattice structures manufactured by selective laser melting (SLM), *Int. J. Adv. Manuf. Technol.* 84 (2016) 1391–1411. <https://doi.org/10.1007/s00170-015-7655-4>.
- [254] V.S. Deshpande, N.A. Fleck, M.F. Ashby, Effective properties of the octet-truss lattice material, *J. Mech. Phys. Solids.* 49 (2001) 1747–1769. [https://doi.org/10.1016/S0022-5096\(01\)00010-2](https://doi.org/10.1016/S0022-5096(01)00010-2).
- [255] R. Gümruk, R.A.W. Mines, S. Karadeniz, Static mechanical behaviours of stainless steel micro-lattice structures under different loading conditions, *Mater. Sci. Eng. A.* 586 (2013) 392–406. <https://doi.org/10.1016/j.msea.2013.07.070>.
- [256] L. Boniotti, S. Beretta, L. Patriarca, L. Rigoni, S. Foletti, Experimental and numerical investigation on compressive fatigue strength of lattice structures of AlSi7Mg manufactured by SLM, *Int. J. Fatigue.* 128 (2019) 105181. <https://doi.org/10.1016/j.ijfatigue.2019.06.041>.
- [257] M. Speirs, B. Van Hooreweder, J. Van Humbeeck, J.P. Kruth, Fatigue behaviour of NiTi shape memory alloy scaffolds produced by SLM, a unit cell design comparison, *J. Mech. Behav. Biomed. Mater.* 70 (2017) 53–59. <https://doi.org/10.1016/j.jmbbm.2017.01.016>.
- [258] V. Sufiiarov, V. Sokolova, E. Borisov, A. Orlov, A. Popovich, Investigation of accuracy, microstructure and properties of additive manufactured lattice structures, *Mater. Today Proc.* 30 (2019) 572–577. <https://doi.org/10.1016/j.matpr.2020.01.137>.
- [259] E. Hernández-Nava, C.J. Smith, F. Derguti, S. Tamas-Williams, F. Leonard, P.J. Withers, I. Todd, R. Goodall, The effect of defects on the mechanical response of Ti-6Al-4V cubic lattice structures fabricated by electron beam melting, *Acta Mater.* 108 (2016) 279–292. <https://doi.org/10.1016/j.actamat.2016.02.029>.
- [260] C. Yan, L. Hao, A. Hussein, S.L. Bubba, P. Young, D. Raymont, Evaluation of light-weight AlSi10Mg periodic cellular lattice structures fabricated via direct metal laser sintering, *J. Mater. Process. Technol.* 214 (2014) 856–864. <https://doi.org/10.1016/j.jmatprotec.2013.12.004>.
- [261] P. Li, Constitutive and failure behaviour in selective laser melted stainless steel for microlattice structures, *Mater. Sci. Eng. A.* 622 (2015) 114–120. <https://doi.org/10.1016/j.msea.2014.11.028>.
- [262] C. Qiu, S. Yue, N.J.E. Adkins, M. Ward, H. Hassanin, P.D. Lee, P.J. Withers, M.M. Attallah, Influence of processing conditions on strut structure and compressive properties of cellular lattice structures fabricated by selective laser melting, *Mater. Sci. Eng. A.* 628 (2015) 188–197.

<https://doi.org/10.1016/j.msea.2015.01.031>.

- [263] E. Hernández-Nava, C.J. Smith, F. Derguti, S. Tammias-Williams, F. Léonard, P.J. Withers, I. Todd, R. Goodall, The effect of density and feature size on mechanical properties of isostructural metallic foams produced by additive manufacturing, *Acta Mater.* 85 (2015) 387–395. <https://doi.org/10.1016/j.actamat.2014.10.058>.
- [264] D. Barba, C. Alabort, Y.T. Tang, M.J. Viscasillas, R.C. Reed, E. Alabort, On the size and orientation effect in additive manufactured Ti-6Al-4V, *Mater. Des.* 186 (2020) 108235. <https://doi.org/10.1016/j.matdes.2019.108235>.
- [265] C. de Formanoir, M. Suard, R. Dendievel, G. Martin, S. Godet, Improving the mechanical efficiency of electron beam melted titanium lattice structures by chemical etching, *Addit. Manuf.* 11 (2016) 71–76. <https://doi.org/10.1016/j.addma.2016.05.001>.
- [266] S. Banait, X. Jin, M. Campos, M.T. Pérez-prado, Precipitation-induced transition in the mechanical behavior of 3D printed Inconel 718 bcc lattices, *Scr. Mater.* 203 (2021) 114075. <https://doi.org/10.1016/j.scriptamat.2021.114075>.
- [267] P. Delroisse, P.J. Jacques, E. Maire, O. Rigo, A. Simar, Effect of strut orientation on the microstructure heterogeneities in AlSi10Mg lattices processed by selective laser melting, *Scr. Mater.* 141 (2017) 32–35. <https://doi.org/10.1016/j.scriptamat.2017.07.020>.
- [268] X. Li, Y.H. Tan, H.J. Willy, P. Wang, W. Lu, M. Cagirici, C.Y.A. Ong, T.S. Herng, J. Wei, J. Ding, Heterogeneously tempered martensitic high strength steel by selective laser melting and its micro-lattice: Processing, microstructure, superior performance and mechanisms, *Mater. Des.* 178 (2019) 107881. <https://doi.org/10.1016/j.matdes.2019.107881>.
- [269] A. Vyatskikh, S. Delalande, A. Kudo, X. Zhang, C.M. Portela, J.R. Greer, Additive manufacturing of 3D nano-architected metals, *Nat. Commun.* 9 (2018) 593. <https://doi.org/10.1038/s41467-018-03071-9>.
- [270] L.R. Meza, A.J. Zelhofer, N. Clarke, A.J. Mateos, D.M. Kochmann, J.R. Greer, Resilient 3D hierarchical architected metamaterials, *Proc. Natl. Acad. Sci.* 112 (2015) 11502–11507. <https://doi.org/10.1073/pnas.1509120112>.
- [271] S. Lee, M. Jafary-zadeh, D.Z. Chen, Y. Zhang, J.R. Greer, Size Effect Suppresses Brittle Failure in Hollow Cu 60 Zr 40 Metallic Glass Nanolattices Deformed at Cryogenic Temperatures, *Nano Lett.* (2015). <https://doi.org/10.1021/acs.nanolett.5b01034>.
- [272] N.G. Dou, R.A. Jagt, C.M. Portela, J.R. Greer, A.J. Minnich, Ultralow Thermal Conductivity and Mechanical Resilience of Architected Nanolattices, *Nano Lett.* 18 (2018) 4755–4761. <https://doi.org/10.1021/acs.nanolett.8b01191>.
- [273] D. Jang, L.R. Meza, F. Greer, J.R. Greer, Fabrication and deformation of three-dimensional hollow ceramic nanostructures, *Nat. Mater.* 12 (2013) 893–898. <https://doi.org/10.1038/nmat3738>.
- [274] D.M. Dimiduk, Size-affected single-slip behavior of pure nickel microcrystals, *Acta Mater.* 53 (2005) 4065–4077. <https://doi.org/10.1016/j.actamat.2005.05.023>.
- [275] L.L. Li, X.H. An, P.J. Imrich, P. Zhang, Z.J. Zhang, G. Dehm, Z.F. Zhang, Microcompression and cyclic deformation behaviors of coaxial copper bicrystals with a single twin boundary, *Scr. Mater.* 69 (2013) 199–202. <https://doi.org/10.1016/j.scriptamat.2013.04.004>.
- [276] C. Liu, The origin of the boundary strengthening in polycrystal-inspired architected materials, *Nat. Commun.* (n.d.) 1–10. <https://doi.org/10.1038/s41467-021-24886-z>.
- [277] M.L. Montero-sistiaga, M. Godino-martinez, K. Boschmans, J. Kruth, J. Van Humbeeck, K. Vanmeensel, Microstructure evolution of 316L produced by HP-SLM (high power selective laser melting), *Addit. Manuf.* 23 (2018) 402–410. <https://doi.org/10.1016/j.addma.2018.08.028>.
- [278] A. Röttger, J. Boes, W. Theisen, M. Thiele, C. Esen, A. Edelmann, R. Hellmann, Microstructure and

- mechanical properties of 316L austenitic stainless steel processed by different SLM devices, *Int. J. Adv. Manuf. Technol.* (2020) 769–783.
- [279] M.J. Silva, L.J. Gibson, The effects of non-periodic microstructure and defects on the compressive strength of two-dimensional cellular solids, *Int. J. Mech. Sci.* 39 (1997) 549–563. [https://doi.org/10.1016/S0020-7403\(96\)00065-3](https://doi.org/10.1016/S0020-7403(96)00065-3).
 - [280] US Titanium Industry, Titanium Alloys -- Ti6Al4V Grade 5, *AZO Mater.* (2015) 4–7. <https://www.azom.com/article.aspx?ArticleID=1547> (accessed April 11, 2021).
 - [281] Special Metals Corporation, Inconel Alloy 718, *Spec. Met. Corp.* 69 (2020). <https://doi.org/10.31399/asm.ad.ni0762>.
 - [282] AK Steel, 316/316L Stainless Steel, *AK Steel Prod. Data Bull.* (2016). http://www.aksteel.com/sites/default/files/2018-01/316316L201706_2.pdf (accessed April 11, 2021).
 - [283] J.R. Bickford, Automatic Stripe Analysis Tool, *Army Res. Lab.* (2013).
 - [284] P. Lehto, Ultramicroscopy Adaptive domain misorientation approach for the EBSD measurement of deformation induced dislocation sub-structures, *Ultramicroscopy*. 222 (2021) 113203. <https://doi.org/10.1016/j.ultramic.2021.113203>.
 - [285] G. Lütjering, J. Williams, *Titanium*, Springer VBH, Berlin, 2007. <https://doi.org/10.1007/978-3-540-73036-1>.
 - [286] B. Van Hooreweder, J.P. Kruth, Advanced fatigue analysis of metal lattice structures produced by Selective Laser Melting, *CIRP Ann. - Manuf. Technol.* 66 (2017) 221–224. <https://doi.org/10.1016/j.cirp.2017.04.130>.
 - [287] C. Leyens, M. Peters, *Titanium and Titanium Alloys: Fundamentals and Applications*, Wiley-VCH, Weinheim, 2010. <https://doi.org/10.1002/3527602119>.
 - [288] D.A. Hollander, M. Von Walter, T. Wirtz, R. Sellei, B. Schmidt-rohlfing, O. Paar, H. Erli, Structural , mechanical and in vitro characterization of individually structured Ti – 6Al – 4V produced by direct laser forming, 27 (2006) 955–963. <https://doi.org/10.1016/j.biomaterials.2005.07.041>.
 - [289] W.S.W. Harun, M.S.I.N. Kamariah, N. Muhamad, S.A.C. Ghani, F. Ahmad, Z. Mohamed, A review of powder additive manufacturing processes for metallic biomaterials, *Powder Technol.* 327 (2018) 128–151. <https://doi.org/10.1016/j.powtec.2017.12.058>.
 - [290] W. Xu, M. Brandt, S. Sun, J. Elambasseril, Q. Liu, K. Latham, K. Xia, M. Qian, Additive manufacturing of strong and ductile Ti-6Al-4V by selective laser melting via in situ martensite decomposition, *Acta Mater.* 85 (2015) 74–84. <https://doi.org/10.1016/j.actamat.2014.11.028>.
 - [291] G. Gong, J. Ye, Y. Chi, Z. Zhao, Z. Wang, G. Xia, X. Du, H. Tian, H. Yu, C. Chen, Research status of laser additive manufacturing for metal: a review, *J. Mater. Res. Technol.* 15 (2021) 855–884. <https://doi.org/10.1016/j.jmrt.2021.08.050>.
 - [292] T. Vilaro, C. Colin, J.D. Bartout, As-Fabricated and Heat-Treated Microstructures of the Ti-6Al-4V Alloy Processed by Selective Laser Melting, (n.d.). <https://doi.org/10.1007/s11661-011-0731-y>.
 - [293] L. Facchini, A. Molinari, K. Wissenbach, Ductility of a Ti-6Al-4V alloy produced by selective laser melting of prealloyed powders, 6 (2010) 450–459. <https://doi.org/10.1108/13552541011083371>.
 - [294] C. Qiu, N.J.E. Adkins, M.M. Attallah, Microstructure and tensile properties of selectively laser-melted and of HIPed laser-melted Ti – 6Al – 4V, *Mater. Sci. Eng. A.* 578 (2013) 230–239. <https://doi.org/10.1016/j.msea.2013.04.099>.
 - [295] G. Del Guercio, M. Galati, A. Saboori, P. Fino, L. Iuliano, Microstructure and Mechanical Performance of Ti-6Al-4V Lattice Structures Manufactured via Electron Beam Melting (EBM): A Review, *Acta Metall. Sin. (English Lett.)* 33 (2020) 183–203. <https://doi.org/10.1007/s40195-020-00998-1>.

- [296] A. Alghamdi, D. Downing, M. McMillan, M. Brandt, M. Qian, M. Leary, Experimental and numerical assessment of surface roughness for Ti6Al4V lattice elements in selective laser melting, *Int. J. Adv. Manuf. Technol.* 105 (2019) 1275–1293. <https://doi.org/10.1007/s00170-019-04092-4>.
- [297] L. Thijs, F. Verhaeghe, T. Craeghs, J. Van Humbeeck, J. Kruth, A study of the microstructural evolution during selective laser melting of Ti – 6Al – 4V, *Acta Mater.* 58 (2010) 3303–3312. <https://doi.org/10.1016/j.actamat.2010.02.004>.
- [298] C. Liu, J. Lertthanasarn, M. Pham, The origin of the boundary strengthening in polycrystal-inspired architected materials, (n.d.).
- [299] Y. Amani, S. Dancette, P. Delroisse, A. Simar, E. Maire, Compression behavior of lattice structures produced by selective laser melting: X-ray tomography based experimental and finite element approaches, *Acta Mater.* 159 (2018) 395–407. <https://doi.org/10.1016/j.actamat.2018.08.030>.
- [300] M. Hamidi Nasab, S. Romano, D. Gastaldi, S. Beretta, M. Vedani, Combined effect of surface anomalies and volumetric defects on fatigue assessment of AlSi7Mg fabricated via laser powder bed fusion, *Addit. Manuf.* 34 (2020) 100918. <https://doi.org/10.1016/j.addma.2019.100918>.
- [301] C. Liu, J. Lertthanasarn, M.-S. Pham, Revealing the origins of shear band activity and boundary strengthening in polygrain-like architected materials, (2020). <https://arxiv.org/abs/2011.02424> (accessed November 6, 2020).
- [302] J.B. Johnson, C.W. Bryan, F.E. Turneaure, The theory and practice of modern framed structures, 6th ed., John Wiley & Sons, New York, USA, 1897.
- [303] M.S. Pham, B. Dovggy, P.A. Hooper, Twinning induced plasticity in austenitic stainless steel 316L made by additive manufacturing, *Mater. Sci. Eng. A.* 704 (2017) 102–111. <https://doi.org/10.1016/j.msea.2017.07.082>.
- [304] A.I. Kahveci, G.E. Welsch, Effect of oxygen on the hardness and alpha/beta phase ratio of Ti6Al4V alloy, *Scr. Metall.* 20 (1986) 1287–1290. [https://doi.org/10.1016/0036-9748\(86\)90050-5](https://doi.org/10.1016/0036-9748(86)90050-5).
- [305] Q. Yu, L. Qi, T. Tsuru, R. Traylor, D. Rugg, J.W. Morris, M. Asta, D.C. Chrzan, A.M. Minor, Origin of dramatic oxygen solute strengthening effect in titanium, *Science* (80-.). 347 (2015) 635–639. <https://doi.org/10.1126/science.1260485>.
- [306] C. Qiu, M. Al Kindi, A.S. Aladawi, I. Al Hatmi, A comprehensive study on microstructure and tensile behaviour of a selectively laser melted stainless steel, *Sci. Rep.* 8 (2018) 1–16. <https://doi.org/10.1038/s41598-018-26136-7>.
- [307] A. Suzuki, K. Sekizawa, M. Liu, N. Takata, M. Kobashi, Effects of Heat Treatments on Compressive Deformation Behaviors of Lattice-Structured AlSi10Mg Alloy Fabricated by Selective Laser Melting, *Adv. Eng. Mater.* 21 (2019) 1–9. <https://doi.org/10.1002/adem.201900571>.
- [308] R. Wauthle, B. Vrancken, B. Beynaerts, K. Jorissen, J. Schrooten, J.P. Kruth, J. Van Humbeeck, Effects of build orientation and heat treatment on the microstructure and mechanical properties of selective laser melted Ti6Al4V lattice structures, *Addit. Manuf.* 5 (2015) 77–84. <https://doi.org/10.1016/j.addma.2014.12.008>.
- [309] K. Prasad, R. Sarkar, P. Ghosal, V. Kumar, M. Sundararaman, High temperature low cycle fatigue deformation behaviour of forged IN 718 superalloy turbine disc, *Mater. Sci. Eng. A.* 568 (2013) 239–245. <https://doi.org/10.1016/j.msea.2012.12.069>.
- [310] I. Yadroitsev, P. Krakhmalev, I. Yadroitsava, Selective laser melting of Ti6Al4V alloy for biomedical applications : Temperature monitoring and microstructural evolution, *J. Alloys Compd.* 583 (2014) 404–409. <https://doi.org/10.1016/j.jallcom.2013.08.183>.
- [311] E. Akca, A. Gursel, A Review on Superalloys and IN718 Nickel-Based INCONEL Superalloy, *Period. Eng. Nat. Sciences.* (2015). <https://doi.org/10.21533/pen.v3i1.43>.
- [312] R. Cozar, D.A. Pineau, Morphology of γ' and γ'' Precipitates and Thermal Stability of Inconel 718

Type Alloys, Metall. Trans. 4 (1973).

- [313] M. Sundararaman, P. Mukhopadhyay, S. Banerjee, Some Aspects of the Precipitation of Metastable Intermetallic Phases in INCONEL 718, Metall. Mater. Trans. A. 23 (1992).
- [314] J. Belan, High frequency fatigue test of IN718 alloy – microstructure and fractography evaluation, Metalurgija. 54 (2015).
- [315] D. Deng, R. Lin, H. Brodin, J. Moverare, Microstructure and mechanical properties of Inconel 718 produced by selective laser melting: Sample orientation dependence and effects of post heat treatments, Mater. Sci. Eng. A. 713 (2018) 294–306. <https://doi.org/10.1016/j.msea.2017.12.043>.
- [316] D. Deng, Additively Manufactured Inconel 718: Microstructures and Mechanical Properties, 2018. <http://liu.diva-portal.org/smash/get/diva2:1177201/FULLTEXT02.pdf%0Ahttps://doi.org/10.3384/lic.diva-144491%0Ahttp://liu.diva-portal.org/smash/get/diva2:1177201/PREVIEW01.png%0Ahttp://urn.kb.se/resolve?urn=urn:nbn:se:liu:diva-144491>.
- [317] R. Krakow, D.N. Johnstone, A.S. Eggeman, D. Hünert, M.C. Hardy, C.M.F. Rae, P.A. Midgley, On the crystallography and composition of topologically close-packed phases in ATI 718Plus®, Acta Mater. 130 (2017) 271–280. <https://doi.org/10.1016/j.actamat.2017.03.038>.
- [318] H.K. Rafi, N. V Karthik, H. Gong, T.L. Starr, B.E. Stucker, Microstructures and Mechanical Properties of Ti6Al4V Parts Fabricated by Selective Laser Melting and Electron Beam Melting, 22 (2013) 3872–3883. <https://doi.org/10.1007/s11665-013-0658-0>.
- [319] Q. Zhang, Effect of Heat Treatment on Microstructure Evolution and Mechanical Properties of Selective Laser Melted Inconel 718 Alloy, J. Mater. Eng. Perform. 28 (2019) 5376–5386. <https://doi.org/10.1007/s11665-019-04309-3>.
- [320] Z. Wang, K. Guan, M. Gao, X. Li, X. Chen, X. Zeng, The microstructure and mechanical properties of deposited-IN718 by selective laser melting, J. Alloys Compd. 513 (2012) 518–523. <https://doi.org/10.1016/j.jallcom.2011.10.107>.
- [321] Z. Sun, X. Tan, Simultaneously enhanced strength and ductility for 3D-printed stainless steel 316L by selective laser melting, NPG Asia Mater. (2018) 127–136. <https://doi.org/10.1038/s41427-018-0018-5>.
- [322] L. Huynh, J. Rotella, M.D. Sangid, Fatigue behavior of IN718 microtrusses produced via additive manufacturing, Mater. Des. 105 (2016) 278–289. <https://doi.org/10.1016/j.matdes.2016.05.032>.
- [323] A.A. Martin, N.P. Calt, J.A. Hammons, S.A. Khairallah, M.H. Nielsen, R.M. Shuttlesworth, N. Sinclair, M.J. Matthews, J.R. Jeffries, T.M. Willey, J.R.I. Lee, Ultrafast dynamics of laser-metal interactions in additive manufacturing alloys captured by in situ X-ray imaging, Mater. Today Adv. 1 (2019) 100002. <https://doi.org/10.1016/j.mtadv.2019.01.001>.
- [324] S. Coeck, M. Bisht, J. Plas, F. Verbist, Prediction of lack of fusion porosity in selective laser melting based on melt pool monitoring data, Addit. Manuf. 25 (2019) 347–356. <https://doi.org/10.1016/j.addma.2018.11.015>.
- [325] M.R. Alkahari, T. Furumoto, T. Ueda, A. Hosokawa, R. Tanaka, M.S. Abdul Aziz, Thermal conductivity of metal powder and consolidated material fabricated via selective laser melting, Key Eng. Mater. 523–524 (2012) 244–249. <https://doi.org/10.4028/www.scientific.net/KEM.523-524.244>.
- [326] C. Liu, J. Lertthanasarn, M.-S. Pham, Revealing the origins of shear band activity and boundary strengthening in polygrain-like architected materials, (2020). <http://arxiv.org/abs/2011.02424> (accessed November 6, 2020).
- [327] E. Liverani, A. Fortunato, A. Ascari, Characterization of Lattice Structures for Additive Manufacturing of Lightweight Mechanical Components, in: Proc. ASME 2017 Manuf. Sci. Eng. Conf., 2017. <https://doi.org/10.1115/MSEC2017-2835>.

- [328] G. Meyer, F. Brenne, T. Niendorf, C. Mittelstedt, Influence of the Miniaturisation Effect on the Effective Stiffness of Lattice Structures in Additive Manufacturing, *Metals* (Basel). (2020) 1–18.
- [329] J. Lertthanasarn, C. Liu, M.S. Pham, Influence of the base material on the mechanical behaviors of polycrystal-like meta-crystals, *J. Micromechanics Mol. Phys.* 2150004 (2021) 1–25. <https://doi.org/10.1142/S2424913021500041>.
- [330] S.J. Hong, W.P. Chen, T.W. Wang, A Diffraction Study of the γ'' Phase in INCONEL 718 Superalloy, *Metall. Mater. Trans. A* 32 (2001).
- [331] D. Gustafsson, J. Moverare, S. Johansson, M. Hörnqvist, Fatigue crack growth behaviour of Inconel 718 with high temperature hold times, *Procedia Eng.* 2 (2010) 1095–1104. <https://doi.org/10.1016/j.proeng.2010.03.118>.
- [332] R. Scholz, R. Matera, Proton irradiation creep of Inconel 718 at 300 ° C, *J. Nucl. Mater.* 287 (2000) 414–417.
- [333] J.M. Pereira, B.A. Lerch, Effects of heat treatment on the ballistic impact properties of Inconel 718 for jet engine fan containment applications, *Int. J. Impact Eng.* 25 (2001) 715–733.
- [334] R.E. Schafrik, D.D. Ward, J.R. Groh, Application of alloy 718 in GE aircraft engines: past, present and next five years, *Proc. Int. Symp. Superalloys Var. Deriv.* 1 (2001) 1–11. https://doi.org/10.7449/2001/superalloys_2001_1_11.
- [335] H. Chandler, *Heat Treater's Guide: Practices and Procedures for Nonferrous Alloys*, ASM International, 1996.
- [336] H. Qi, M. Azer, A. Ritter, Studies of Standard Heat Treatment Effects on Microstructure and Mechanical Properties of Laser Net Shape Manufactured Inconel 718, *Metall. Mater. Trans. A* 2 (n.d.). <https://doi.org/10.1007/s11661-009-9949-3>.
- [337] M. Terock, U. Glatzel, Mechanical and Microstructural Investigation of Nickel-Based Superalloy IN718 Manufactured by Selective Laser Melting (SLM), *Adv. Eng. Mater.* (2015) 1099–1105. <https://doi.org/10.1002/adem.201500158>.
- [338] W.M. Tucho, P. Cuvillier, A. Sjolyst-Kverneland, V. Hansen, Microstructure and hardness studies of Inconel 718 manufactured by selective laser melting before and after solution heat treatment, *Mater. Sci. Eng. A* 689 (2017) 220–232. <https://doi.org/10.1016/j.msea.2017.02.062>.
- [339] E. Chlebus, K. Gruber, B. Ku, J. Kurzac, T. Kurzynowski, Effect of heat treatment on the microstructure and mechanical properties of Inconel 718 processed by selective laser melting, *Mater. Sci. Eng. A* 639 (2015) 647–655. <https://doi.org/10.1016/j.msea.2015.05.035>.
- [340] W. Huang, J. Yang, H. Yang, G. Jing, Z. Wang, X. Zeng, Heat treatment of Inconel 718 produced by selective laser melting: Microstructure and mechanical properties, *Mater. Sci. Eng. A* 750 (2019) 98–107. <https://doi.org/10.1016/j.msea.2019.02.046>.
- [341] Y.T. Chen, A.C. Yeh, M.Y. Li, S.M. Kuo, Effects of processing routes on room temperature tensile strength and elongation for Inconel 718, *Mater. Des.* 119 (2017) 235–243. <https://doi.org/10.1016/j.matdes.2017.01.069>.
- [342] H. Lei, C. Li, J. Meng, H. Zhou, Y. Liu, X. Zhang, P. Wang, D. Fang, Evaluation of compressive properties of SLM-fabricated multi-layer lattice structures by experimental test and μ -CT-based finite element analysis, *Mater. Des.* 169 (2019) 107685. <https://doi.org/10.1016/j.matdes.2019.107685>.
- [343] K. Hazeli, B.B. Babamiri, J. Indeck, A. Minor, H. Askari, Microstructure-topology relationship effects on the quasi-static and dynamic behavior of additively manufactured lattice structures, *Mater. Des.* 176 (2019) 107826. <https://doi.org/10.1016/j.matdes.2019.107826>.
- [344] Z. Xiao, Y. Yang, R. Xiao, Y. Bai, C. Song, D. Wang, Evaluation of topology-optimized lattice structures manufactured via selective laser melting, *Mater. Des.* 143 (2018) 27–37. <https://doi.org/10.1016/j.matdes.2018.01.023>.

- [345] S. Yuan, C.K. Chua, K. Zhou, 3D-Printed Mechanical Metamaterials with High Energy Absorption, *Adv. Mater. Technol.* 4 (2019) 1–9. <https://doi.org/10.1002/admt.201800419>.
- [346] H.N.G. Wadley, N.A. Fleck, A.G. Evans, Fabrication and structural performance of periodic cellular metal sandwich structures, *Compos. Sci. Technol.* 63 (2003) 2331–2343. [https://doi.org/10.1016/S0266-3538\(03\)00266-5](https://doi.org/10.1016/S0266-3538(03)00266-5).
- [347] Z.G. Zhu, Q.B. Nguyen, F.L. Ng, X.H. An, X.Z. Liao, P.K. Liaw, S.M.L. Nai, J. Wei, Hierarchical microstructure and strengthening mechanisms of a CoCrFeNiMn high entropy alloy additively manufactured by selective laser melting, *Scr. Mater.* 154 (2018) 20–24. <https://doi.org/10.1016/j.scriptamat.2018.05.015>.
- [348] M.R. Staker, D.L. Holt, The dislocation cell size and dislocation density in copper deformed at temperatures between 25 and 700°C, *Acta Metall.* 20 (1972) 569–579.
- [349] U.F. Kocks, H. Mecking, Physics and phenomenology of strain hardening: the FCC case, *Prog. Mater. Sci.* 48 (2003) 171–273. [https://doi.org/10.1016/S0079-6425\(02\)00003-8](https://doi.org/10.1016/S0079-6425(02)00003-8).
- [350] R.W. Kozar, A. Suzuki, W.W. Milligan, J.J. Schirra, M.F. Savage, T.M. Pollock, Strengthening mechanisms in polycrystalline multimodal nickel-base superalloys, *Metall. Mater. Trans. A Phys. Metall. Mater. Sci.* 40 (2009) 1588–1603. <https://doi.org/10.1007/s11661-009-9858-5>.
- [351] M. Fisk, J.C. Ion, L.E. Lindgren, Flow stress model for IN718 accounting for evolution of strengthening precipitates during thermal treatment, *Comput. Mater. Sci.* 82 (2014) 531–539. <https://doi.org/10.1016/j.commatsci.2013.10.007>.
- [352] L. Dong, V. Deshpande, H. Wadley, Mechanical response of Ti-6Al-4V octet-truss lattice structures, *Int. J. Solids Struct.* 60 (2015) 107–124. <https://doi.org/10.1016/j.ijsolstr.2015.02.020>.
- [353] M.C. Chaturvedi, Y. Han, Effect of particle size on the creep rate of superalloy Inconel 718, *Mater. Sci. Eng.* 89 (1987) 7–10. [https://doi.org/10.1016/0025-5416\(87\)90264-3](https://doi.org/10.1016/0025-5416(87)90264-3).
- [354] E. Nembach, G. Neite, Precipitation hardening of superalloys by ordered γ' -particles, *Prog. Mater. Sci.* 29 (1985) 177–319. [https://doi.org/10.1016/0079-6425\(85\)90001-5](https://doi.org/10.1016/0079-6425(85)90001-5).
- [355] L. Feng, D. Lv, R.K. Rhein, J.G. Goiri, M.S. Titus, A. Van der Ven, T.M. Pollock, Y. Wang, Shearing of γ' particles in Co-base and Co-Ni-base superalloys, *Acta Mater.* 161 (2018) 99–109. <https://doi.org/10.1016/j.actamat.2018.09.013>.

Appendices

Appendix A. MATLAB script for determining compressive properties of meta-crystals from load-displacement data.

```
%% For analysing compression data of lattices
% Set up - ALL REQUIRED
clear all
Name = 'BST508AXX'; % Name of current set of lattices
data = ['C:\Users\ ' Name ' _Load-Extension.xlsx']; % Comp data file
props = ['C:\Users\ ' Name ' _Properties.xlsx']; % Properties data file
trim_tol = 0; % tolerance value for zeroing displacement

%% Data import and clean up
% COMPRESSION DATA
% Data format:
% Name | Model 1 | | Model 2 | | Model 3 | ...
% Extens | Load | | Extens | Load | | Extens | Load | ...
% 'values'.....

importdata = readcell(data); % import data
Dim = size(importdata); % obtain size of imported data
datasize = [Dim(1)-2 Dim(2)]; % Dim(2) is number of datasets
raw = zeros(datasize); % Pure extension-load data
for i=1:Dim(2)
    raw(:, i) = [importdata{3:end, i}];
end
% raw (isnan(raw)) = 0; % Replaces NaN with 0

% zero displacement
raw_trimmed = zeros(Dim(1), Dim(2));
for j=2:2:Dim(2)
    for i=1:Dim(1)
        if raw(i,j) < trim_tol % Tolerance value for trimming disp
        else
            raw_trimmed(1:end-1-i,j-1:j) = raw(i:end,j-1:j); % assign only
values above the tolerance to the trimmed matrix
            %trim(j/2) = raw(i,j-1);
            break
        end
    end
end
end

raw_trimmed(raw_trimmed==0) = NaN; % Replaces zeroes with NaN

% PHYSICAL PROPERTIES
% Data format:
% | Model 1 | Model 2 | Model 3 | ...
% | Height | Height | Height | ...
% | Width | Width | Width | ...
% | Depth | Depth | Depth | ...
% | Mass | Mass | Mass | ...

importprops = readcell(props); % import data

LatSize = zeros(3,Dim(2)/2);
for i=1:Dim(2)/2
    LatSize(:,i) = [importprops{2:4,i}]; % Height, width, depth of
lattices in mm
end
```

```

LatMass = [importprops{5,:}]; % Mass of lattices in grams

LatDens = zeros(1,Dim(2)/2);
for i=1:Dim(2)/2
    LatDens(i) = LatMass(i)/(LatSize(1,i)*LatSize(2,i)*LatSize(3,i));
end

if Name(3) == 'I' % Material density in g/mm3
    dens = 0.00822; % In718
elseif Name(3) == 'T'
    dens = 0.00443; % Ti64
elseif Name(3) == 'S'
    dens = 0.00799; % 316L
else
    msg = msgbox('Name not recognised','Error!');
end

RelDens = LatDens/dens; % Relative density

%% Organise Stress-strain

Normalise = questdlg('Normalise data by relative density?');

% Convert raw data to stress-strain
SS = zeros(size(raw_trimmed,1),size(raw_trimmed,2));
for i=1:2:Dim(2)
    SS(:,i) = raw_trimmed(:,i)./LatSize(1).*100; % Strain (%)
    if Normalise(1) == 'N' % Stress
        SS(:,i+1) = raw_trimmed(:,i+1)./(LatSize(2)*LatSize(3));
    elseif Normalise(1) == 'Y' % Normalised stress
        SS(:,i+1) = (raw_trimmed(:,i+1)./(LatSize(2)*LatSize(3)))/RelDens((i+1)/2);
    else
        break
    end
end

%% Plot stress-strain
hold on

for i=1:2:Dim(2)-1
    plot(SS(:,i),SS(:,i+1), 'LineWidth',2);
end
leg_label = {'1 MG','2 MGs','4 MGs','8 MGs','16 MGs','32 MGs','64 MGs'};
legend(leg_label(1:Dim(2)/2),'Location','SouthEast')
xlabel('Strain (%)')
set(gca,'FontSize',22)
title(Name);
if Normalise(1) == 'N'
    ylabel('Stress (MPa)');
elseif Normalise(1) == 'Y'
    ylabel('Normalised Stress (MPa)');
else
end

% Find values of max stress and strain for each model
just_stress = SS(:,2:2:Dim(2));
max_stress_ind = max(just_stress,[],1,'omitnan');
max_stress_all = max(max_stress_ind);

just_strain = SS(:,1:2:Dim(2)-1);
max_strain_ind = max(just_strain,[],1,'omitnan');
max_strain_all = max(max_strain_ind);

xlim([0 max_strain_all*1.1]);
ylim([0 max_stress_all*1.1]);

```

```

hold off

% Calculates densification strain (empirical, from cellular solids textbook)

idx = zeros(1,Dim(2)/2);
strain_d = zeros(1, Dim(2)/2);           % Densification strain
c = 1.6;                                % constant for strain_d (og = 1.4)

%% Toughness

for i=1:Dim(2)
    for j=1:20
        if isnan(SS(j,i)) == 1
            SS(j,i) = 0;
        else
            end
        end
    end
end

% Calculates area under curve up to a given strain
tough_strain = 50;                       %calculates up to this strain %
tough_range = zeros(1, Dim(2)/2);

for ts_MG=1:size(tough_range, 2)
    for ts_S=1:size(SS, 1)
        if SS(ts_S, (ts_MG*2)-1)>=tough_strain
            tough_range(1, ts_MG) = ts_S;           %index in SS at
tough_strain
            break
        else
            %do nothing
        end
    end
end
end

hold on
toughness = zeros(Dim(1),Dim(2)/2);
toughness(toughness==0) = NaN;
for i=1:Dim(2)/2
    %toughness(1:tough_range(i),i) = cumtrapz(SS(1:tough_range(i),(i*2)-
1)/100,SS(1:tough_range(i),i*2));
    toughness(1:tough_range(i),i) = cumtrapz((SS(1:tough_range(i),(i*2)-
1)/100),SS(1:tough_range(i),i*2));
    plot(SS(:,(i*2)-1), toughness(:,i), 'LineWidth', 2);
end
legend
hold off

leg_label = {'1 MG','2 MGs','4 MGs','8 MGs','16 MGs','32 MGs','64 MGs'};
legend(leg_label(1:Dim(2)/2),'Location','SouthEast')
set(gca,'FontSize',22)
ylabel('Cumulative Energy Absorbed (MJ.m-3)');
xlabel('Strain');
title(Name);
xlim([0 tough_strain]);

energy_absorbed=zeros(1, ts_MG);
for m=1:ts_MG
    energy_absorbed(m) = max(toughness(:,m));
end

if Dim(2)/2 == 3
    barX = categorical({'1', '2', '4'});
    barX = reordercats(barX, {'1', '2', '4'});
elseif Dim(2)/2 == 4
    barX = categorical({'1', '2', '4', '8'});
    barX = reordercats(barX, {'1', '2', '4', '8'});
elseif Dim(2)/2 == 5

```

```

        barX = categorical({'1', '2', '4', '8', '16'});
        barX = reordercats(barX, {'1', '2', '4', '8', '16'});
elseif Dim(2)/2 == 6
    barX = categorical({'1', '2', '4', '8', '16', '32'});
    barX = reordercats(barX, {'1', '2', '4', '8', '16', '32'});
else
    barX = categorical({'1', '2', '4', '8', '16', '32', '64'});
    barX = reordercats(barX, {'1', '2', '4', '8', '16', '32', '64'});
end

bar(barX, energy_absorbed);
title(Name);
ylabel(['Energy absorbed up to ' num2str(tough_strain) '% strain (MJ.m-3)']);
xlabel('Number of Metagrain');

hold off

%% Hardening/Softening

grad_SS = zeros(Dim(1),2,Dim(2)/2);
bin_size = 0.2;
grad_SS_map = zeros(Dim(1),Dim(2)/2); % maps grad_SS to SS

for i=1:10
    for j=1:Dim(2)
        if isnan(SS(i,j))==1
            SS(i,j)=0;
        else
            end
        end
    end
end

for j=1:Dim(2)/2 % loop through all models
    delta_strain = SS(1,(j*2)-1);
    count=1;
    grad_count=2;
    for i=2:size(SS,1) % loop through all datapoints
        delta_strain = delta_strain+SS(i,(j*2)-1)-SS(i-1,(j*2)-1);
        %incrementally increase delta_strain
        if delta_strain >= bin_size % binning strain according to bin_size
            grad_SS(grad_count,1,j) = SS(count,(2*j)-1)+delta_strain; % stores
            the strain every 1% intervals
            grad_SS(grad_count,2,j) = (SS(i,j*2)-SS(count,j*2))/...
                (SS(i,(j*2)-1)-SS(count,(j*2)-1)); % change in
            stress/change in strain
            count = i; % change count to index of previous %
            grad_SS_map(grad_count-1,j) = i;
            grad_count = grad_count+1;
            delta_strain = delta_strain-bin_size; % resets change in strain
        end
        count
        %delta_strain = 0;
        elseif delta_strain > max_strain_ind(j)
            break
        else
            % do nothing
        end
    end
end

end

grad_SS(grad_SS==0) = NaN;
grad_SS(1,(:,)) = 0;
hold on
for i=1:Dim(2)/2
    plot(grad_SS(:,1,i),grad_SS(:,2,i),'LineWidth',1.5);
end
y=[0,0;max_strain_all,0];
plot(y(:,1),y(:,2),'--k','LineWidth',1);

```

```

hold off
leg_label = {'1 MG','2 MGs','4 MGs','8 MGs','16 MGs','32 MGs','64 MGs'};
legend(leg_label(1:Dim(2)/2),'Location','SouthEast')
set(gca,'FontSize',22)
ylim([-100 100])
xlabel('Strain (%)')
ylabel('dstress/dstrain')
title(Name);

% Plot same as above with moving average

grad_SS(grad_SS==0) = NaN;
grad_SS(1, :, :) = 0;

gradSS_mov = movmean(grad_SS,8,3);

hold on
for i=1:Dim(2)/2
    plot(gradSS_mov(:,1,i),gradSS_mov(:,2,i),'LineWidth',1);
end
y=[0,0;max_strain_all,0];
plot(y(:,1),y(:,2),'--k','LineWidth',1);
hold off
leg_label = {'1 MG','2 MGs','4 MGs','8 MGs','16 MGs','32 MGs','64 MGs'};
legend(leg_label(1:Dim(2)/2),'Location','SouthEast')
set(gca,'FontSize',22)
ylim([-100 100])
xlabel('Strain (%)')
ylabel('dstress/dstrain - 8pts moving average')
title(Name);

%% Stress drop

% Determine peak stress

peak = zeros(4,Dim(2)/2);
for j=1:Dim(2)/2
    for i=2:size(grad_SS,1)
        if grad_SS(i,2,j)<0 && grad_SS(i+1,2,j)<0 && grad_SS(i+2,2,j)<0 % 3
            consecutive negative gradients
                peak(1,j) = i; % corresponding index in
grad_SS
                peak(2,j) = grad_SS_map(i,j); % temporary corresponding
index in SS
                [peak(4,j),temp_i] = max(SS(peak(2,j)...
                    -50:peak(2,j)+50,2*j)); % search max stress % +-50
indexes
                peak(2,j) = peak(2,j)-51+temp_i; % real index in SS
                peak(3,j) = SS(peak(2,j),(j*2)-1); % corresponding strain in
grad_SS
                peak(4,j) = SS(peak(2,j),j*2); % peak stress
                break
            else
                % do nothing
            end
        end
    end
end

% Determine stress at 1st drop

trough = zeros(4,Dim(2)/2);
for j=1:Dim(2)/2
    for i=peak(1,j):size(grad_SS,1)
        if grad_SS(i,2,j)>0 && grad_SS(i+1,2,j)>0 && grad_SS(i+2,2,j)>0 % 3
            consecutive positive gradients
                trough(1,j) = i; % corresponding index in
grad_SS

```

```

        trough(2,j) = grad_SS_map(i,j); % temporary corresponding
index in SS
        [trough(4,j),temp_i] = min(SS(trough(2,j)...
        -50:trough(2,j)+50,2*j)); % search max stress % +-50
indexes
        trough(2,j) = trough(2,j)-51+temp_i; % real index in SS
        trough(3,j) = SS(trough(2,j),(j*2)-1); % corresponding
strain in grad_SS
        trough(4,j) = SS(trough(2,j),j*2); % trough stress
        break
    else
        % do nothing
    end
end
end

% Quantify stress drop
% rows: 1)magnitude 2)percentage 3)strain range 4)ave drop gradient
% 5)Drop rate (MPa/s) 6)'score' = [range/drop fraction] (maximise)
drop = zeros(5, Dim(2)/2);

for j=1:Dim(2)/2
    drop(1,j) = peak(4,j)-trough(4,j);
    drop(2,j) = 100*drop(1,j)/peak(4,j);
    drop(3,j) = trough(3,j)-peak(3,j);
    drop(4,j) = -drop(1,j)/drop(3,j);
    drop(5,j) = (drop(1,j)*0.001)/(drop(3,j)/100);
    drop(6,j) = drop(3,j)/(drop(2,j)/100);
end

% Plot dual y bar charts

% Datasets on left axis. Add zeros(1,(Dim(2)/2))' according to number of
datasets
left_axis = [drop(2,:) ', zeros(1,(Dim(2)/2)) '];
% Dataset on right axis. Mind the order of the data
right_axis = [zeros(1,(Dim(2)/2)) ', drop(5,:) '];
% Plot left then right
hold on
cats = {'1','2','4','8','16','32','64'};
order = {'1','2','4','8','16','32','64'};
x_axis = categorical(cats(1:(Dim(2)/2)),order,'Ordinal',true);
yyaxis left
bar(x_axis,left_axis, 0.4);
ylabel('First stress drop (%)');
yyaxis right
bar(x_axis(1:(Dim(2)/2)),right_axis,0.4);
ylabel('Stress drop rate (MPa/s)');
hold off
xlabel('Number of Metagrain');
title(Name);

% max(toughness,[],1,'omitnan')

%% E modulus and Proof-stress

% calculates the E modulus of the current dataset

% Let user pick starting point
waitfor(msgbox('Click midpoint of linear region', 'E modulus calculation'));
E_midpoint = zeros(3,Dim(2)/2); %row1: strain%, row2: stress, row3:index
minR2 = 0.9997;
initial_range = 10; % strain range around E midpoint in
percent of 0 to strain at peak stress

for p=1:Dim(2)/2

```

```

%plot SS of current MG
figure
plot(SS(:, (2*p)-1), SS(:, (2*p)), 'LineWidth', 2);
xlabel('Strain (%)');
ylabel('Normalised Stress (MPa)');
xlim([0 max(peak(3,:))*1.5]);
ylim([0 max(peak(4,:))*1.1]);
title(p);

%click on midpoint
[X,Y]=ginput(1);

% Find the nearest point to selection
h = gco();
hx = h.XData;
hy = h.YData;
d = sqrt((X-hx).^2 + (Y-hy).^2);
[~,minIdx] = min(d);
E_midpoint(1:3,p)=[SS(minIdx, (2*p)-1);SS(minIdx, (2*p));minIdx];
close

end

%assume strain at peak stress is 2x midpoint
% Finds the midpoint between the strain at peak stress and zero
% Find strain range

b=zeros(3,1,Dim(2)/2); % b(1, :, :) is the y intercept, b(2, :, :) is
the slope
b(3,1,:) = 1; % b(3,1,:) is the current r-squared value,
initialise at 1
SS_E_strain= zeros(2,3,Dim(2)/2); % [low-limit strain, mid-strain, high-
limit strain; low-i, mid-i, high-i; MG]
SS_E_range=zeros(1,1,Dim(2)/2);

iterate = 1;

% pick start point

%*** set intial range in percent

sr = initial_range/200; % converts to decimal and halved

for MG=1:Dim(2)/2 % Calculates slope and y-intercept of
linear region within acceptable r-squared
while b(3,1,MG)>minR2 % Finds the strain range in which the r-
squared value is above the limit
iterate = Dim(2)/2;
% for MG=1:Dim(2)/2 %obtain index of lower,
midpoint, upper strain range
% calculates strain range [low mid high]
if b(3,1,MG)>minR2
% SS_E_strain(1, :, MG) = [midpoint minus strain range
midpoint midpoint plus strain range]
SS_E_strain(1, :, MG) = [E_midpoint(1, MG) -
(sr*E_midpoint(1, MG)*2) E_midpoint(1, MG)
E_midpoint(1, MG)+(sr*E_midpoint(1, MG)*2)];
for i=1:2*E_midpoint(3, MG) %from 1 to
peak stress index in SS
if SS(i, (2*MG)-1)<SS_E_strain(1,1,MG) %if strain is
less than lower strain limit do nothing %do nothing
else
SS_E_strain(2,1,MG) = i; %when strain
is larger, store index as lower limit index
break
end
end
end

```

```

        for j=SS_E_strain(2,1,MG):2*E_midpoint(3,MG) %from index of
low strain limit to index of peak stress
        if SS(j,(2*MG)-1)<SS_E_strain(1,2,MG) %if strain is
lower than midpoint strain do nothing
            %do nothing
        else
            SS_E_strain(2,2,MG) = j; %when strain
is larger, store index as midpoint index
            break
        end
    end
    for k=SS_E_strain(2,2,MG):2*E_midpoint(3,MG) %from index of
midpoint strain to index of peak stress
    if SS(k,(2*MG)-1)<SS_E_strain(1,3,MG) %if strain is
lower than upper limit strain do nothing
        %do nothing
    else
        SS_E_strain(2,3,MG) = k; %when strain
is larger, store index as upper limit index
        break
    end
end
else
    %do nothing
end
% extract 10% strain range about midpoint as x y
%
    if SS_E_range==0 % loop on initial run only
        SS_E_range(1,1,MG)=SS_E_strain(2,3,MG)-SS_E_strain(2,1,MG); %range
of indexes
        % E_x_y_MG(:, :, MG) = [max(SS_E_range), 2]; % (strain, stress, MG)
        % b=zeros(3,1,Dim(2)/2);
        % else
        % do nothing
        % end

% for MG2=1:Dim(2)/2 %stores stress-strain from
between the limits in SS_x_y_MG
% if b(3,1,MG)>minR2
    E_x_y_MG(1:SS_E_range(1,1,MG)+1, :, MG) =
SS([SS_E_strain(2,1,MG):...
    SS_E_strain(2,3,MG)], [(2*MG)-1:(2*MG)]); %stress and
strain from lower to upper strain limit
% else
% do nothing
% end
% end

E_x_y_MG(E_x_y_MG==0) = NaN; %change all 0 values to NaN

% Runs initial linear fitting for strains within 10% of midpoint
% Calculates R-squared and store in 3rd row of b
% y2=(x.*b(2))+b(1);
% R2=1-sum((y-y2).^2)/sum((y-mean(y)).^2);

% for MG3=1:Dim(2)/2 %calculates the r-squared
value from stress-strain
% if b(3,1,MG3)>minR2
    b(1:2,1,MG) = [ones(SS_E_range(1,1,MG)+1,1)
E_x_y_MG([1:SS_E_range(1,1,MG)+1],1,MG)]...
    \E_x_y_MG([1:SS_E_range(1,1,MG)+1],2,MG);
    b(3,1,MG)=1-sum((E_x_y_MG([1:SS_E_range(1,1,MG)+1],2,MG)-...
(E_x_y_MG([1:SS_E_range(1,1,MG)+1],1,MG).*b(2,1,MG)+b(1,1,MG))).^2)/...
    sum((E_x_y_MG([1:SS_E_range(1,1,MG)+1],2,MG)-...
    mean(E_x_y_MG([1:SS_E_range(1,1,MG)+1],2,MG))).^2);
    sr = sr+0.01; %increase strain range by 2%

```



```

        if sr>0.4                                %if strain range is larger than 80%,
break
        sr = sr-0.02;
        msgbox('strain range exceeded limit (80%)')
        return
    else
        %do nothing
    end
end
end

E_modulus(1:Dim(2)/2,1) = b(2,1,:)*100;

%plot SS with E
hold on
for i=1:2:Dim(2)-1
    plot(SS(:,i),SS(:,i+1), 'LineStyle','--');
end
leg_label = {'1 MG','2 MGs','4 MGs','8 MGs','16 MGs','32 MGs','64 MGs'};
legend(leg_label(1:Dim(2)/2),'Location','SouthEast')
xlabel('Strain (%)')
set(gca,'FontSize',22)
title(Name);
ylabel('Normalised Stress (MPa)');
xlim([0 max(peak(3,:))*1.5]);
ylim([0 max(peak(4,:))*1.1])

for emod=1:Dim(2)/2
    plot(E_x_y_MG([1:SS_E_range(1,1,emod)+1],1,emod),...

(E_x_y_MG([1:SS_E_range(1,1,emod)+1],1,emod).*b(2,1,emod)+b(1,1,emod)) ...
        , 'LineWidth',2);
end

hold off

% Proof Stress

% find x intercept, adjust 0.2% proof, extrapolate to SS intercept
% y=mx+c --> m=b(2), c=B(1) --> y=0, x=-b(1)/b(2)

x_int(1:Dim(2)/2)=(-1*b(1,1,:))./b(2,1,:);
proof_strain=x_int+0.2;
intersections=zeros(1,2,Dim(2)/2);
proof_stress=zeros(Dim(2)/2,1);

%creates E parallels
for EP=1:Dim(2)/2
    c=-b(2,1,EP)*proof_strain(EP);
    x_points=linspace(proof_strain(EP),E_midpoint(1,EP)*3,1000);
    E_parallel(:, :,EP)=[x_points' (x_points'*b(2,1,EP))+c];

    %finds the intercept - downloaded from Mathworks
    %NS (2021). Curve intersections
    %(https://www.mathworks.com/matlabcentral/fileexchange/22441-curve-
intersections),
    %MATLAB Central File Exchange. Retrieved February 16, 2021.
    %...Preliminary stuff
    hF = @le;
    x1 = SS(:, (2*EP)-1); x2 = E_parallel(:,1,EP)';
    y1 = SS(:, (2*EP)); y2 = E_parallel(:,2,EP)';
    dx1 = diff(x1); dy1 = diff(y1);
    dx2 = diff(x2); dy2 = diff(y2);

    %...Determine 'signed distances'
    S1 = dx1.*y1(1:end-1) - dy1.*x1(1:end-1);
    S2 = dx2.*y2(1:end-1) - dy2.*x2(1:end-1);

```

```

d_x1=bsxfun(@times,dx1,y2)-bsxfun(@times,dy1,x2);
D1=bsxfun(@minus,d_x1(:,1:end-1),S1).*bsxfun(@minus,d_x1(:,2:end),S1);
d_x2=(bsxfun(@times,y1,dx2)-bsxfun(@times,x1,dy2))';
D2=bsxfun(@minus,d_x2(:,1:end-1),S2').*bsxfun(@minus,d_x2(:,2:end),S2');

C1 = feval(hF,D1,0);
C2 = feval(hF,D2,0)';

%...Obtain the segments where an intersection is expected
[i,j] = find(C1 & C2);
if isempty(i),P = zeros(2,0);return; end;

%...Transpose and prepare for output
i=i'; dx2=dx2'; dy2=dy2'; S2 = S2';
L = dy2(j).*dx1(i) - dy1(i).*dx2(j);
i = i(L~=0); j=j(L~=0); L=L(L~=0); %...Avoid divisions by 0

%...Solve system of eqs to get the common points
P = unique([dx2(j).*S1(i) - dx1(i).*S2(j), ...
            dy2(j).*S1(i) - dy1(i).*S2(j)]./[L L], 'rows');
if size(P,1)>size(intersections,1)
    intersections(size(P,1),2,EP)=0;
else %do nothing
end
intersections(1:size(P,1),:,EP)=P;
proof_stress(EP,1)=max(intersections(:,2,EP));

end

hold on

for psp=1:Dim(2)/2
    plot(E_parallel(:,1,psp),E_parallel(:,2,psp))
end

hold off

%% Adjust x_int to be 0 strain and plot SS

adjusted_SS=SS;
for i=1:2:Dim(2)
    adjusted_SS(:,i)=adjusted_SS(:,i)-x_int((i+1)/2);
end

hold on

for i=1:2:Dim(2)-1
    plot(adjusted_SS(:,i),adjusted_SS(:,i+1), 'LineWidth',2);
end
leg_label = {'1 MG','2 MGs','4 MGs','8 MGs','16 MGs','32 MGs','64 MGs'};
legend(leg_label(1:Dim(2)/2),'Location','SouthEast')
xlabel('Strain (%)')
set(gca,'FontSize',22)
title(Name);
if Normalise(1) == 'N'
    ylabel('Stress (MPa)');
elseif Normalise(1) == 'Y'
    ylabel('Normalised Stress (MPa)');
else
end

% Find values of max stress and strain for each model
just_adj_stress = adjusted_SS(:,2:2:Dim(2));
max_adj_stress_ind = max(just_adj_stress,[],1,'omitnan');
max_adj_stress_all = max(max_adj_stress_ind);

just_adj_strain = adjusted_SS(:,1:2:Dim(2)-1);

```

```

max_adj_strain_ind = max(just_adj_strain,[],1,'omitnan');
max_adj_strain_all = max(max_adj_strain_ind);

xlim([0 max_adj_strain_all*1.1]);
ylim([0 max_adj_stress_all*1.1]);

hold off

```

Appendix B. MATLAB script for calculating the strut diameter from ImageJ data.

```

%% Subroutine for calculating the minimum strut diameter from xCT data

% Crop out single strut and extract 2 sets of data
% Data format
% 1.) The centre of mass of all slices. .csv file ending in com
%      slice | Area | X | Y          coord system top-left, origin 0,0
% 2.) The outline coordintaes of all slices. .txt file ending in outline
%      X | Y | slice | intensity    coord system bottom-left, origin 0,0

%% Set up - REQUIRED
clear all
Name = 'BST505A08V';          % Name of current set of lattices

% Data import and formatting

com = ['C:\Users'...
      '\Strut Diameter\Data\' Name 'com.csv']; % centre of mass data file
outline = ['C:\Users\'...
          '\Strut Diameter\Data\' Name 'outline.txt']; % outline data file
imginfo = ['C:\Users\Jump\OneDrive\Desktop\Work\Uni\Manuscripts'...
          '\Paper 1 - Effect of print quality\Strut Diameter\Data\' Name
          'image.txt']; % image info data file

importcom = readcell(com);      % import centre of mass
importoutline = readcell(outline); % import outline
importinfo = readcell(imginfo); % image info

% Tidy up data - remove area from 1 and intensity from 2. Reorg 2 in to 3d
% comdata(slices,2) = [x y]
% outlinedata(points on boundary,2,slices) = [X; Y ; slice]
% shift data so origin on 1,1 rather than 0,0

slices = length(importcom)-1;
comdata = [cell2mat(importcom(2:end, 3)) cell2mat(importcom(2:end, 4))];
comdata = comdata+1;
importoutline = cell2mat(importoutline);
importinfo = cell2mat(importinfo(1:4,2));

k=0;
for i=1:slices
    j=1;
    while importoutline(j+k,3) == i-1
        outlinedata(j,1:2,i) = importoutline(j+k,1:2)+1;
        j=j+1;
        if j+k>size(importoutline,1)
            break
        else
            %do nothing
        end
    end
    k=k+j-1;
end

% Change coordinate system of comdata so origin is at bottom-left

```

```

% x remains the same, y is upside down

outlinedata(outlinedata == 0) = NaN;
comdata(:,2) = importinfo(2)-comdata(:,2);

% Make outline coordinates relative to corresponding c.o.m coordinates

mappedoutline = zeros(size(outlinedata, 1), 4, slices);
for i=1:slices
    mappedoutline(:,1:2,i) = outlinedata(:,1:2,i)-comdata(i,:);
end

% Calculate distance from origin and angle from x-axis using com as origin
% Mag stored in 3rd column and angle stored in 4th column of outlinedata

for k=1:slices
    for i=1:size(mappedoutline,1)
        if isnan(mappedoutline(i,1,k)) == 1
            break
        else
            mappedoutline(i,3,k) =
sqrt((mappedoutline(i,1,k)^2)+(mappedoutline(i,2,k)^2));
            mappedoutline(i,4,k) =
atan(mappedoutline(i,2,k)/mappedoutline(i,1,k));
            if mappedoutline(i,1,k)>=0 && mappedoutline(i,2,k)>=0 % +ve
x and y
                %do nothing
            elseif mappedoutline(i,1,k)<0 && mappedoutline(i,2,k)>=0 % -ve
x and +ve y
                mappedoutline(i,4,k) = pi+mappedoutline(i,4,k);
            elseif mappedoutline(i,1,k)<0 && mappedoutline(i,2,k)<0 % -ve
x and y
                mappedoutline(i,4,k) = pi+mappedoutline(i,4,k);
            elseif mappedoutline(i,1,k)>=0 && mappedoutline(i,2,k)<0 % +ve
x and -ve y
                mappedoutline(i,4,k) = (2*pi)+mappedoutline(i,4,k);
            end
        end
    end
end

% Pair opposite boundary points (difference of pi rad) and sum distances

mindiameter = zeros(1,5,slices); % x1|y1|x2|y2|distance
for k=1:slices % loop through all slices
    i=1; % set up for each slice
    currenti=1;
    imax=0;
    for i2=1:size(mappedoutline,1) % find the number of ~isnan in
current slice
        if ~isnan(mappedoutline(i2,1,k))
            imax=imax+1;
        else
            end
        end
    currentmindist = 1000;
    while i<=imax % loop through all ~isnan
        currentminangle = 10;
        for i3=1:imax % compare current i with
all i in slice
            if abs(abs(mappedoutline(i3,4,k)-mappedoutline(currenti,4,k))-
pi)>currentminangle % loop through all pair and find the closest to 180deg
                %do nothing
            else
                if
(mappedoutline(i3,3,k)+mappedoutline(currenti,3,k))<currentmindist && ...

```

```

        abs(abs(mappedoutline(i3,4,k)-
mappedoutline(currenti,4,k))-pi)<0.05 % compare to current min distance. If
smaller store in mindiameter
        mindiameter(1,1:2,k)=mappedoutline(currenti,1:2,k);
        mindiameter(1,3:4,k)=mappedoutline(i3,1:2,k);

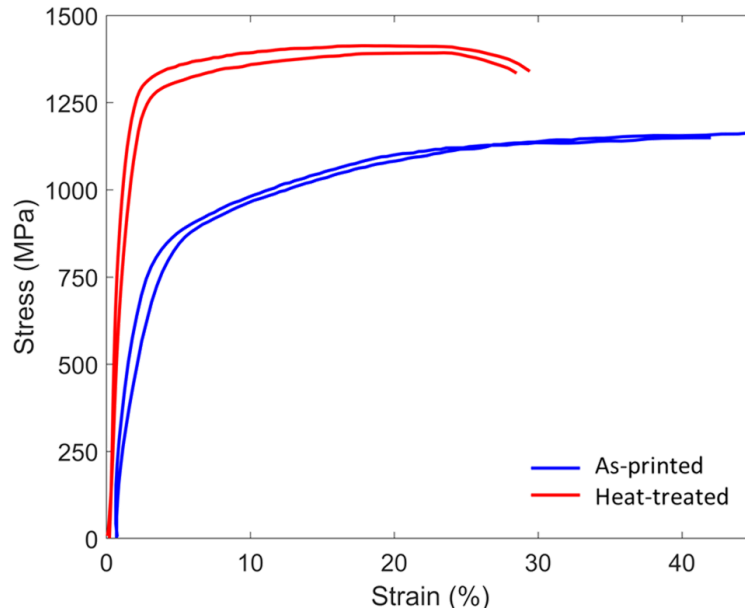
mindiameter(1,5,k)=mappedoutline(currenti,3,k)+mappedoutline(i3,3,k);

currentmindist=mappedoutline(currenti,3,k)+mappedoutline(i3,3,k);
        else
            %do nothing
        end
        currentminangle=abs(mappedoutline(i3,4,k)-
mappedoutline(currenti,4,k)-pi);
        end
    end
    i=i+1;
    currenti=currenti+1;
end

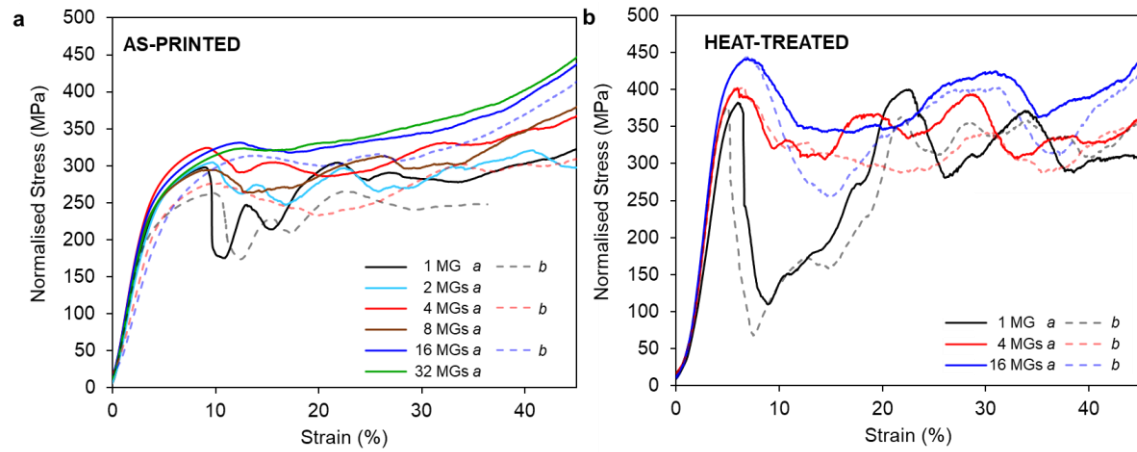
end

```

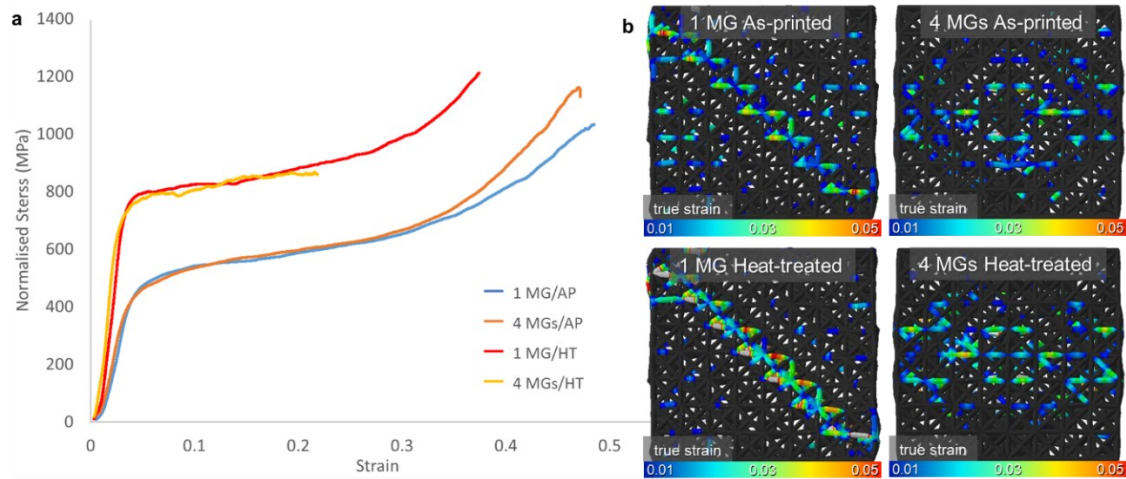
Appendix C. Tensile stress-strain response of bulk IN718 tested in the as-printed and heat-treated condition. IN718 samples fabricated using the same printing parameters and tested according to the **ISO 189201** standard. The heat-treatment condition was identical to that subjected to the meta-crystals.



Appendix D. Stress-strain response of the as-printed and heat-treated meta-crystals with varying number of meta-grains. **a**, as-printed meta-crystals containing 1, 2, 4, 8, 16, and 32 MGs and **b**, heat-treated meta-crystals containing 1, 4, and 16 MGs showing good repeatability in the compressive stress strain response.

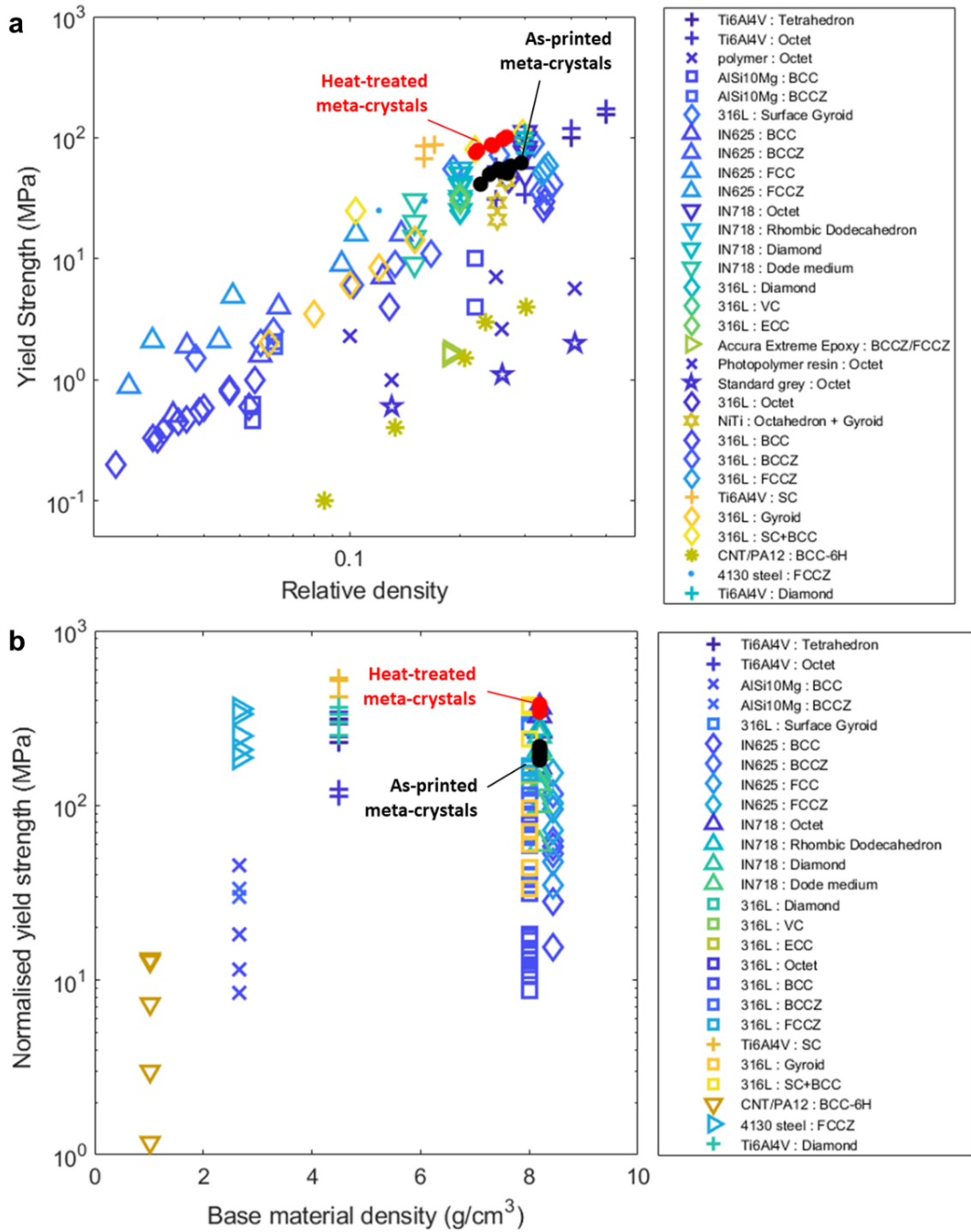


Appendix E. Finite Element Modelling of meta-crystals. **a**, Normalised stress-strain curves of as-printed and heat-treated meta-crystals with 1 and 4 MGs obtained from the FE simulation. **b**, True strain contour maps highlighting strain localisation at peak stress for the as-printed and heat-treated 1 and 4 MGs meta-crystals.

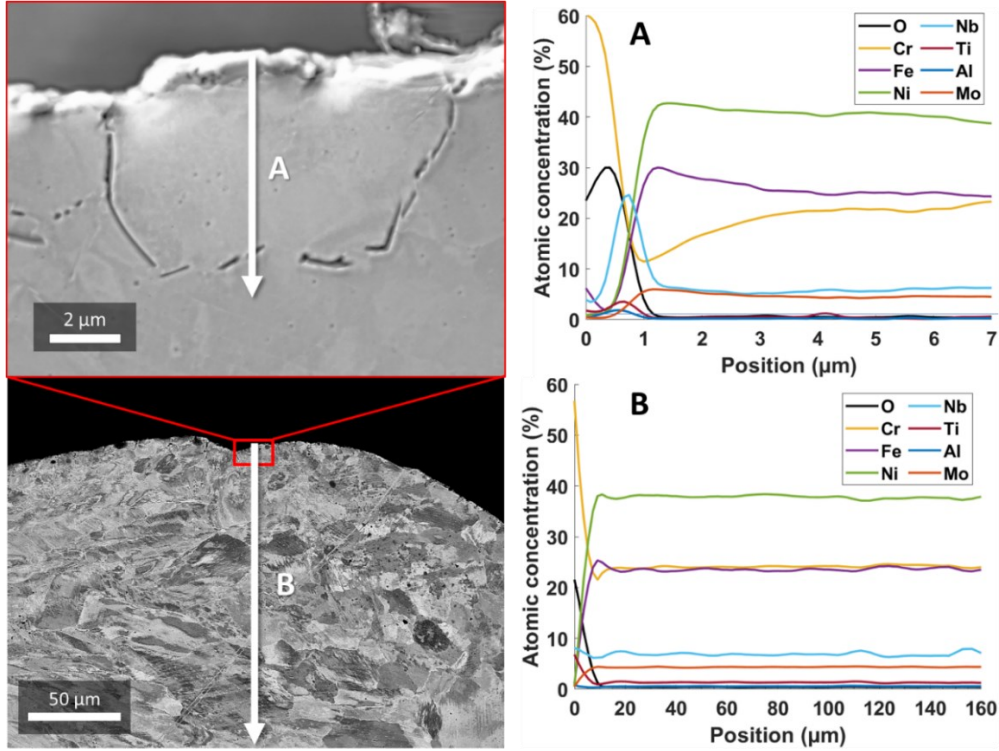


Appendix F. Comparison of meta-crystals with other lattice structures reported in literature. **a**, Plot of the normalised compressive yield strength versus the relative density and **b**, the normalised compressive

yield strength versus the density of the base material. In both plots the symbol represents the base material and the colour represents the unit cell topology.



Appendix G. Oxidation of meta-crystals from heat-treatment. XRD showing chemical segregation near the surface (top) and in the bulk (bottom) of the strut as a result of heat-treatment. Enrichment of O and Cr and depletion of the remaining elements between 0-1 μm from the free surface. Nb peaked at the interface between the oxide layer and the bulk structure.



Appendix H. Calculation of buckling stress in IN718 meta-crystals.

Strut buckling stress is determined by the Johnson's parabolic formula (Eq. 2) as the slenderness ratio (l/r , where l is the length and r is the radius of gyration) is less than the transition slenderness ratio, R_{trans} (as determined by Eq. 1). E is the elastic modulus, $K = 0.9$ is a constant dependant on the end constraints, and σ_y is the yield strength. The slenderness ratio of $\langle 001 \rangle$ struts is 25 and $R_{trans} = 49.5$ and 61.9 for the as-printed and heat-treated conditions.

$$R_{trans} = \sqrt{\frac{2\pi^2 E}{K^2 \sigma_y}} \quad (6.9)$$

$$\sigma_{crit} = \frac{P_{crit}}{A} = \sigma_y - \left(\frac{\sigma_y K L}{2\pi r} \right)^2 \left(\frac{1}{E} \right) \quad (6.10)$$

The stress required for buckling are 658.8 MPa and 1126.1 MPa for the as-printed and heat-treated conditions, respectively.